

Graph Neural Network Flavour Tagging and Boosted Higgs Measurements at the LHC

Samuel John Van Stroud
University College London

Submitted to University College London in fulfilment
of the requirements for the award of the
degree of **Doctor of Philosophy**

March 23, 2023

Declaration

I, Samuel John Van Stroud confirm that the work presented in this thesis is my own. Where information has been derived from other sources, I confirm that this has been indicated in the thesis.

Samuel Van Stroud

Abstract

This thesis presents investigations into the challenges of, potential improvements to, and the application of b -jet identification to study the Higgs boson at the ATLAS experiment at the Large Hadron Collider (LHC). A focus is placed on the high transverse momentum regime, which is a critical region in which to study the Standard Model, but within which successful b -jet identification becomes difficult.

As b -jet identification relies on the successful reconstruction of charged particle trajectories (tracks), the tracking performance is investigated and potential improvements are assessed. Track reconstruction becomes increasingly difficult at high transverse momentum due to the increased multiplicity and collimation of tracks, and also due to the presence of displaced tracks that may occur as the result of the decay of a long-flying b -hadron. The investigations revealed that the track quality selections applied during track reconstruction are suboptimal for tracks inside high transverse momentum b -jets, motivating future studies into the optimisation of these cuts.

To improve b -tagging performance two novel techniques are employed: the classification of the origin of tracks and the application of graph neural networks. An algorithm has been developed to classify the origin of tracks, which allows a more optimal collection of tracks to be selected for use in other algorithms. A graph neural network (GNN) jet flavour tagger has also been developed. This tagger requires only tracks and jet variables as inputs, making a break from previous algorithms, which relied on the outputs of several other

algorithms. This model is trained to simultaneously predict the jet flavour, track origins, and track-pair compatibility (i.e. vertexing), and demonstrates markedly improvements in b -tagging performance, both at low and high transverse momenta. The closely related task of c-jet identification also benefits from these methods.

Analysis of high transverse momentum $H \rightarrow b\bar{b}$ decays, where the Higgs boson is produced in association with a vector boson, was also performed using 139 fb^{-1} of 13 TeV proton-proton collision data from Run 2 of the LHC. The analysis is described, with a focus on the detailed modelling studies performed by the author. The analysis measured provided first measurements in this channel of the Higgs boson production in two high transverse momentum regions.

Impact Statement

This thesis details research in experimental particle physics. The primary contributions are on the improvement of the data analysis algorithms which are used to process proton-proton collisions induced within the ATLAS detector at the Large Hadron Collider (LHC), and the analysis of candidate Higgs boson events.

The primary outcome of the research is an advancement of knowledge about how the Universe works on the most fundamental level, encoded for example in the improved measurement of the fundamental constants for the Standard Model, or in the observation of previously unseen particles or interactions. Although this kind of knowledge doesn't always have an immediate and direct relevance for society, potential applications are impossible to rule out and could have a very large impact further in the future, as has been seen with previous advancements in fundamental science.

The research does find indirect application in the form of associated technological developments that have transferable application within different fields. The cutting-edge techniques developed at CERN for ATLAS and the LHC have found many spin-off applications elsewhere in society, for example the World Wide Web, high-field magnet technology in MRI, touch-screen technology and cloud computing. Fundamental physics, as a proposer of novel and difficult problems, can therefore be seen as a way to generate innovative technologies.

Working in the field also helps to train skilled researchers, which can be redeployed to other areas of society to tackle various problems. In this thesis advanced statistical and data science methods are

deployed. Such methods currently find wide and varied use in many fields. The training of such highly skilled individuals, has a sustained and significant positive economic impact.

Finally, the work carried at ATLAS and the LHC is widely publicised – support of and interest in fundamental physics research helps to generate excitement about science and technology, and educate people about how the Universe works. This in turn attracts people into the area, propagating the benefits described above.

Acknowledgements

Firstly I give thanks to my supervisor Tim Scanlon for all the guidance and support he has offered over the course of this doctorate. Tim has always been consistent with clear explanations and sound advice throughout the last four years. I would also like to thank everyone I've worked with at ATLAS and at UCL. In particular I have Jonathan Shlomi to thank for the fruitful collaboration on advancements in flavour tagging. I would also like to thank Brian Moser and Hannah Arnold for their patient support during the course of the VH , $H \rightarrow b\bar{b}$ analysis. I'm grateful to everyone I've worked with in the ATLAS Flavour Tagging and Tracking groups, in particular to Gabriel Facini, Valerio Dao, Bingxuan Liu and Francesco Di Bello for their guidance, and Dan Guest for his fastidious merge request reviews. This thesis was made in L^AT_EX 2 _{ε} using the “heptesis” class [1].

Contents

1	Introduction	12
2	Theoretical Framework	14
2.1	The Standard Model	14
2.1.1	Quantum Electrodynamics	15
2.1.2	Quantum Chromodynamics	17
2.1.3	The Electroweak Sector	18
2.2	The Higgs Mechanism	19
2.2.1	Electroweak Symmetry Breaking	20
2.2.2	Fermionic Yukawa Coupling	23
2.2.3	Higgs Sector Phenomenology	25
3	The Large Hadron Collider and the ATLAS Detector	28
3.1	The Large Hadron Collider	29
3.2	Coordinate System & Collider Definitions	30
3.2.1	ATLAS Coordinate System	31
3.2.2	Track Parameterisation	32
3.2.3	Hadron Collider Definitions	32
3.3	The ATLAS Detector	36
3.3.1	Inner Detector	37
3.3.2	Calorimeters	40
3.3.3	Muon Spectrometer	42
3.3.4	The Trigger	43
3.4	Reconstructed Physics Objects	44
3.4.1	Tracks	44
3.4.2	Vertices	48
3.4.3	Jets	49
3.4.4	Leptons	51

3.4.5	Missing Transverse Momentum	53
3.5	<i>b</i> -tagging Algorithms	53
3.5.1	Common Definitions	54
3.5.2	Low-level Algorithms	54
3.5.3	High-level Algorithms	55
4	Tracking and Flavour Tagging at High p_T	56
4.1	Datasets	56
4.2	<i>b</i> -hadron Reconstruction	57
4.2.1	Decay Topology	57
4.2.2	Challenges	60
4.3	Investigations into High p_T <i>b</i> -hadron Tracking Improvements	64
4.3.1	Shared Hits	64
4.3.2	Global χ^2 Fitter Outlier Removal	64
4.4	Conclusion	67
5	Track Classification MVA	69
5.1	Machine Learning Background	69
5.1.1	Neural Networks	71
5.1.2	Training with Gradient Descent	73
5.2	Track Truth Origin Labelling	73
5.3	Fake Track Identification Tool	74
5.3.1	Model Inputs	76
5.3.2	Model Hyperparameters	78
5.3.3	Results	79
5.4	<i>b</i> -hadron Track Identification	80
5.5	Combined Approach	80
5.6	Conclusion	82
6	Graph Neural Network Flavour Tagger	84
6.1	Motivation	84
6.2	Graph Neural Network Theory	86
6.3	Experimental Setup	88
6.3.1	Datasets	88
6.4	Model Architecture	89
6.4.1	Model Inputs	89

6.4.2	Auxiliary Training Objectives	91
6.4.3	Architecture	92
6.4.4	Training	96
6.5	Results	97
6.5.1	<i>b</i> -tagging Performance	98
6.5.2	<i>c</i> -tagging Performance	100
6.5.3	Ablations	103
6.5.4	Inclusion of Low-Level Vertexing Algorithms	105
6.5.5	Jet Display Diagrams	105
6.5.6	Vertexing Performance	107
6.5.7	Track Classification Performance	113
6.6	Further Studies	115
6.6.1	Looser Track Selection	115
6.6.2	High Level Trigger	116
6.6.3	High Luminosity LHC	116
6.7	Conclusion	119
7	Boosted VHbb Analysis	123
7.1	Analysis Overview	124
7.1.1	Object Reconstruction	125
7.1.2	Event Selection	127
7.1.3	Control Regions	128
7.1.4	Background Composition	128
7.1.5	Data & Simulated Samples	131
7.1.6	Overview of Systematic Uncertainties	131
7.2	Experimental Uncertainties	133
7.3	Background Modelling	134
7.3.1	Truth Tagging	135
7.3.2	Sources of Systematic Modelling Uncertainties	135
7.3.3	Implementation of Variations	137
7.3.4	Vector Boson + Jets Modelling	138
7.3.5	Diboson Modelling	144
7.3.6	$t\bar{t}$ and single-top Modelling	146
7.3.7	Signal Modelling	147

7.4 Statistical Treatment	148
7.4.1 Likelihood Function	149
7.4.2 Background Normalisations	152
7.4.3 Asimov Dataset & Expected Results	152
7.5 Results	152
7.5.1 Post-fit Results	153
7.5.2 Observed Signal Strength & Significance	157
7.5.3 Impact of Systematics	159
7.5.4 STXS Interpretation	163
7.6 Conclusion	163
8 Conclusion	166
8.1 Summary	166
8.2 Future Work	167
Bibliography	169
List of figures	184
List of tables	197

² Chapter 1

³ Introduction

- ⁴ This thesis describes various efforts in improving the understanding of the Higgs
⁵ boson and its coupling to heavy flavour quarks, primarily through the improvement
⁶ of the algorithms used to reconstruct and analyse jets. The thesis is structured in
⁷ the following manner:
- ⁸ Chapter 2 describes the theoretical foundations of the work presented in the rest of
⁹ the thesis.
- ¹⁰ Chapter 3 describes the ATLAS detector and the CERN accelerator complex. Details
¹¹ of reconstructed physics objects are also provided.
- ¹² Chapter 4 provides an overview of the reconstruction of charged particle tracks
¹³ (tracking) and identification of jets containing b -hadrons (b -tagging) at ATLAS, and
¹⁴ studies into the challenges of high transverse momentum b -tagging.
- ¹⁵ Chapter 5 describes the development of an algorithm to predict the origins of tracks.
¹⁶ The tool is used to improve b -tagging performance by the identification and removal
¹⁷ of fake tracks before their input to the b -tagging algorithms.
- ¹⁸ Chapter 6 introduces a novel monolithic approach to b -tagging using graph neural
¹⁹ networks and auxiliary training objectives.
- ²⁰ Chapter 7 describes the measurement of the associated production of a Higgs boson
²¹ decaying into a pair of b -quarks at high transverse momentum.
- ²² Chapter 8 contains some concluding remarks.

²³ The author's contribution to the work presented in this thesis is as follows.

²⁴ **Tracking:** The author was an active member of the Cluster and Tracking in Dense
²⁵ Environments group throughout their PhD, starting with their qualification task
²⁶ on the understanding of tracking performance at high transverse momentum. The
²⁷ author played a key role in software r22 validation studies for the tracking group,
²⁸ including the validation of the quasi-stable particle interaction simulation and the
²⁹ radiation damage Monte-Carlo simulation. The author helped design and improve
³⁰ several tracking software frameworks, and contributed to heavy flavour tracking
³¹ efficiency studies in dense environments. The author developed a tool to identify
³² and reject fake-tracks, which is being investigated for use in the upcoming tracking
³³ paper.

³⁴ ***b*-tagging:** The author has been an active member of the Flavour Tagging group
³⁵ since September 2014. The author played a key role in investigating the performance
³⁶ of the low level taggers at high transverse momentum and led studies into the
³⁷ labelling and classification of track origins. Based on work by Jonathan Shlomi [2],
³⁸ the author helped develop a new flavour tagging algorithm which offers a large
³⁹ performance improvement with respect to the current state of the art. The author
⁴⁰ was the primary editor of a public note associated with this work [3], which will
⁴¹ also be further developed in an upcoming paper. The author also contributed to
⁴² the proliferation of the new algorithm to the trigger, High Luminosity LHC, and
⁴³ $X \rightarrow bb$ use cases. The author also played a key role in software r22 validation
⁴⁴ studies for the Flavour Tagging group, including the validation of the quasi-stable
⁴⁵ particle interaction simulation. The author maintains and contributes to various
⁴⁶ software frameworks used in the Flavour Tagging group, including as lead developer
⁴⁷ of three packages, to create training datasets, pre-process samples for algorithm
⁴⁸ studies and a framework for training graph neural networks, and contributes to group
⁴⁹ documentation.

⁵⁰ **Higgs:** The author was an active member of the Boosted VHbb analysis group. The
⁵¹ author performed various studies deriving systematic uncertainties for the $V+jets$
⁵² and diboson backgrounds. The author also produced and maintained samples, ran fit
⁵³ studies and cross checks, and gave the diboson unblinding approval talk to the Higgs
⁵⁴ group. The author also contributed to the development of the analysis software.

55 **Chapter 2**

56 **Theoretical Framework**

57 The Standard Model (SM) of particle physics is the theory describing all known
58 elementary particles and their interactions via three of the four fundamental forces.

59 Developed by merging the successful theories of quantum mechanics and relativity
60 in the second half of the 20th century, the SM's position today at the centre of our
61 understanding of the nature of the Universe is firmly established by an unparalleled
62 level of agreement between the model predictions and experimental results [4, 5].

63 The SM has predicted the discovery of the top and bottom quarks [6–8], the W
64 and Z bosons [9], and the tau neutrino [10]. The last missing piece of the SM to be
65 discovered was the Higgs boson, first theorised in the 1960s [11–13], and eventually
66 observed at the LHC in 2012 [14, 15]. After its discovery, much ongoing work has
67 been carried out performing detailed measurements of its mass and interactions with
68 other particles.

69 In this chapter, an overview of the SM is given in Section 2.1, and a more detailed
70 discussion of the Higgs sector and Higgs phenomenology is provided in Section 2.2.

71 **2.1 The Standard Model**

72 The SM is formulated in the language of Quantum Field Theory (QFT). In this
73 framework, particles are localised excitations of corresponding quantum fields, which
74 are operator-valued distributions across spacetime.

75 Central to QFT is the Lagrangian density which describes the kinematics and
 76 dynamics of a field. Observations of conserved quantities are linked, via Noether's
 77 theorem, to symmetries which are expressed by the Lagrangian. Alongside Global
 78 Poincaré symmetry, the SM Lagrangian observes a local non-Abelian $SU(3)_C \otimes$
 79 $SU(2)_L \otimes U(1)_Y$ gauge symmetry. Gauge symmetries leave observable properties of
 80 the system unchanged when the corresponding gauge transformations are applied
 81 to the fields. The full Lagrangian of the SM can be broken up into distinct terms
 82 corresponding to the different sectors, as in Eq. (2.1). An overview of each sector is
 83 given in the following chapters.

$$\mathcal{L}_{\text{SM}} = \mathcal{L}_{\text{EW}} + \mathcal{L}_{\text{QCD}} + \mathcal{L}_{\text{Higgs}} + \mathcal{L}_{\text{Yukawa}} \quad (2.1)$$

84 The SM provides a mathematical description of how three of the four fundamental
 85 forces interact with the matter content of the Universe. The particle content of the
 86 SM consists of spin-1/2 fermions, listed in Table 2.1, and integral spin bosons listed
 in Table 2.2.

Generation	Leptons			Quarks		
	Flavour	Mass [MeV]	Charge [e]	Flavour	Mass [MeV]	Charge [e]
First	e	0.511	-1	u	2.16	$2/3$
	ν_e	$< 1.1 \times 10^{-6}$	0	d	4.67	$-1/3$
Second	μ	105.7	-1	c	1.27×10^3	$2/3$
	ν_μ	< 0.19	0	s	93.4	$-1/3$
Third	τ	1776.9	-1	t	173×10^3	$2/3$
	ν_τ	< 18.2	0	b	4.18×10^3	$-1/3$

Table 2.1: The fermions of the SM [16]. Three generations of particles are present. Also present (unlisted) are the antiparticles, which are identical to the particles up to a reversed charge sign.

87

88 2.1.1 Quantum Electrodynamics

89 Quantum electrodynamics (QED) is the relativistic quantum theory which describes
 90 the interactions between the photon and charged matter. Consider a Dirac spinor
 91 field $\psi = \psi(x)$ and its adjoint $\bar{\psi} = \psi^\dagger \gamma^0$, where ψ^\dagger denotes the Hermitian conjugate

Name	Symbol	Mass [GeV]	Charge [e]	Spin
Photon	γ	$< 1 \times 10^{-27}$	$< 1 \times 10^{-46}$	1
Charged Weak boson	W^\pm	80.377 ± 0.012	± 1	1
Neutral Weak boson	Z	91.1876 ± 0.0021	0	1
Gluon	g	0	0	1
Higgs	H	125.25 ± 0.17	0	0

Table 2.2: The bosons of the SM [16]. The photon, weak bosons and gluons are gauge bosons arising from gauge symmetries, and carry the four fundamental forces of the SM. The recently discovered Higgs boson is the only fundamental scalar particle in the SM.

of ψ . The field ψ describes a fermionic spin-1/2 particle, for example an electron. The Dirac Lagrangian density is

$$\mathcal{L}_{\text{Dirac}} = \bar{\psi}(i\cancel{\partial} - m)\psi, \quad (2.2)$$

where $\cancel{\partial} = \gamma^\mu \partial_\mu$ denotes the contraction with the Dirac gamma matrices γ^μ (summation over up-down pairs of indices is assumed). Application of the Euler-Lagrange equation on Eq. (2.2) yields the Dirac equation

$$(i\cancel{\partial} - m)\psi = 0. \quad (2.3)$$

Suppose some fundamental symmetry that requires invariance under a local $U(1)$ gauge transformation

$$\psi \rightarrow \psi' = \psi e^{-iq\alpha(x)}, \quad (2.4)$$

where α varies over every spacetime point x . Under this transformation, the Dirac equation transforms as

$$(i\cancel{\partial} - m)\psi e^{-iq\alpha(x)} + q\cancel{\partial}\alpha(x)\psi e^{-iq\alpha(x)} = 0. \quad (2.5)$$

For the Dirac equation to remain invariant under the transformation in Eq. (2.4), a new field A_μ which transforms as $A_\mu \rightarrow A'_\mu = A_\mu + \partial_\mu\alpha(x)$ must be added. The transformed interaction term

$$-q\cancel{A}\psi \rightarrow -q\cancel{A}\psi e^{-iq\alpha(x)} - q\cancel{\partial}\alpha(x)\psi e^{-iq\alpha(x)} \quad (2.6)$$

104 will then cancel the asymmetric term in Eq. (2.5) as required. The $U(1)$ invariant
105 Lagrangian can therefore be constructed by adding an interaction between the ψ
106 and A_μ fields to Eq. (2.2). For completeness, the kinetic term for the new field A_μ
107 is also added in terms of $F_{\mu\nu} = \partial_\mu A_\nu - \partial_\nu A_\mu$, which is trivially invariant under the
108 transformation in Eq. (2.4). The interaction term is typically absorbed into the
109 covariant derivative $D_\mu = \partial_\mu + iqA_\mu$, thus named as it transforms in the same way as
110 the field ψ . Collecting these modifications to Eq. (2.2) yields the QED Lagrangian

$$\mathcal{L}_{\text{QED}} = -\frac{1}{4}F_{\mu\nu}F^{\mu\nu} + \bar{\psi}(iD^\mu - m)\psi. \quad (2.7)$$

111 The quadratic term $A_\mu A^\mu$ is not invariant and therefore the field A_μ must be massless.
112 Requiring invariance under local $U(1)$ gauge transformations necessitated the addition
113 of a new field A_μ , interpreted as the photon field, which interacts with charged matter.
114 In the SM, the QED Lagrangian is absorbed into the electroweak sector, discussed
115 in Section 2.1.3.

116 2.1.2 Quantum Chromodynamics

117 Quantum Chromodynamics (QCD) is the study of quarks, gluons and their interac-
118 tions. Quarks and gluons carry colour charge, which comes in three kinds, called
119 red, green and blue. While the $U(1)$ symmetry group in Section 2.1.1 was Abelian,
120 the QCD Lagrangian is specified by requiring invariance under transformations from
121 the non-Abelian $SU(3)$ group, making it a Yang-Mills theory [17] which requires the
122 addition of self-interacting gauge fields. The infinitesimal $SU(3)$ group generators
123 are given by $T_a = \lambda_a/2$, where λ_a are the eight Gell-Mann matrices. These span the
124 space of infinitesimal group transformations and do not commute with each other,
125 instead satisfying the commutation relation

$$[T_a, T_b] = if_{abc}T_c, \quad (2.8)$$

126 where f_{abc} are the group's structure constants. Consider the six quark fields $q_k = q_k(x)$.
127 Each flavour of quark q_k transforms in the fundamental triplet representation, in
128 which each component of the triplet corresponds to the colour quantum number
129 for red, green and blue colour charged respectively. $G_{\mu\nu}^a$ are the eight gluon field

130 strength tensors, one for each generator T_a , defined as

$$G_{\mu\nu}^a = \partial_\mu A_\nu - \partial_\nu A_\mu - g_s f^{abc} A_\mu^b A_\nu^c, \quad (2.9)$$

131 where A_μ^a are the gluon fields and g_s is the strong coupling constant. The covariant
132 derivative is written as

$$D_\mu = \partial_\mu + i g_s T_a A_\mu^a. \quad (2.10)$$

133 The full QCD Lagrangian is then given by

$$\mathcal{L}_{\text{QCD}} = -\frac{1}{4} G_{\mu\nu}^a G_a^{\mu\nu} + q_k (i \not{D} - m_k) q_k. \quad (2.11)$$

134 Cubic and quartic terms of the gauge fields A_μ^a appear in the Lagrangian, leading to
135 the gluon's self interaction.

136 The QCD coupling constant g_s varies, or “runs”, with energy. At lower energy scales
137 (and corresponding larger distance scales) the interaction is strong. This leads to
138 quark confinement, whereby an attempt to isolate individual colour-charged quarks
139 requires so much energy that additional quark-antiquark pairs are produced. At
140 higher energy scales (and corresponding smaller distance scales), asymptotic freedom
141 occurs as the interactions become weaker, allowing perturbative calculations to be
142 performed. Hadrons are bound states of quarks. They are invariant under $SU(3)$
143 gauge transformations (i.e. are colour-charge neutral, or *colourless*).

144 2.1.3 The Electroweak Sector

145 The weak and electromagnetic forces are unified in the Glashow-Weinberg-Salam
146 (GWS) model of electroweak interaction [18–20]. The Lagrangian is specified by
147 requiring invariance under the symmetry group $SU(2)_L \otimes U(1)_Y$, as motivated by a
148 large amount of experimental data. Here, $SU(2)_L$ is referred to as weak isospin and
149 $U(1)_Y$ as weak hypercharge.

150 The generators of $SU(2)_L$ are $T_a = \sigma_a/2$, where σ_a are the three Pauli spin matrices
151 which satisfy the commutation relation

$$[T_a, T_b] = i\varepsilon_{abc}T_c. \quad (2.12)$$

152 The generator of $U(1)_Y$ is $Y = 1/2$. Each generator corresponds to a gauge field,
153 which, after symmetry breaking (discussed in Section 2.2), give rise to the massive
154 vector bosons, W^\pm and Z , and the massless photon. The massive vector bosons
155 are the carriers of the weak force. Due to the mass of the force carriers, the weak
156 force has a short range and so it appears weak even though its intrinsic strength is
157 comparable to that of QED.

158 The charge operator Q can be written as a combination of the third $SU(2)_L$ generator
159 and the $U(1)_Y$ generator as in

$$Q = T_3 + Y. \quad (2.13)$$

160 The weak force violates parity conservation [21–23], i.e. invariance under parity
161 transformations (mirror reflections). Only left handed fermions participate in the
162 weak interaction. Since there is no other force through which neutrinos interact with
163 other particles, there are no right handed neutrinos in the Standard Model.

164 2.2 The Higgs Mechanism

165 The Brout-Englert-Higgs mechanism (henceforth just the “Higgs mechanism”) is the
166 process through which the fundamental particles of the SM acquire mass [11–13].
167 Experimentally it was known that the weak force had a low effective strength, which
168 was suggestive of a massive mediating gauge particle. However, directly adding
169 mass to the weak gauge bosons violates the non-Abelian symmetry of the SM.
170 Instead, the gauge bosons gain mass through the interaction with a scalar Higgs
171 field which results from the spontaneous breakdown of symmetry as discussed in
172 Section 2.2.1. Similarly, the Higgs mechanism gives mass to the fermions, as discussed
173 in Section 2.2.2. Section 2.2.3 described some basic phenomenology of the Higgs
174 particle relevant to hadron colliders.

¹⁷⁵ 2.2.1 Electroweak Symmetry Breaking

¹⁷⁶ Spontaneous symmetry breaking (SSB) is a key part of the Higgs mechanism. It
¹⁷⁷ is the transition of a physical system from a state of manifest symmetry to a state
¹⁷⁸ of hidden, or *broken*, symmetry. In particular, this applies to physical systems
¹⁷⁹ where the Lagrangian observes some symmetry, but the lowest energy vacuum states
¹⁸⁰ do not exhibit that same symmetry. In other words, the symmetry is broken for
¹⁸¹ perturbations around the vacuum state.

¹⁸² Consider the case in which the gauge fields from the local $SU(2)_L \otimes U(1)_Y$ symmetry
¹⁸³ group (discussed in Section 2.1.3) are coupled to a complex scalar field $\phi = \phi(x)$,
¹⁸⁴ transforms as a weak isospin doublet. Omitting the kinetic term of the gauge fields,
¹⁸⁵ and writing $\phi^2 \equiv \phi^\dagger \phi$, the Lagrangian is

$$\mathcal{L}_{\text{Higgs}} = (D_\mu \phi)^\dagger (D^\mu \phi) - [\mu^2 \phi^2 + \lambda \phi^4], \quad (2.14)$$

¹⁸⁶ where the covariant derivative is given by

$$D_\mu = \partial_\mu + igA_\mu^a T^a + ig'B_\mu, \quad (2.15)$$

¹⁸⁷ and T^a are the generators of $SU(2)$. The potential term $V(\phi)$ is made up of a
¹⁸⁸ quadratic and quartic term in the scalar field ϕ , which each contain an arbitrary
¹⁸⁹ parameter, respectively λ and μ . The quartic term gives the field self-interaction, and
¹⁹⁰ cannot be negative as this would lead to a potential that was unbounded from below.
¹⁹¹ The quadratic term can be positive or negative. In the case where the quadratic term
¹⁹² is positive, it is interpreted as a mass term for the scalar field. By choosing $\mu^2 < 0$
¹⁹³ the field becomes unphysical due to its negative mass. The shape of the potential in
¹⁹⁴ this case is shown in Fig. 2.1. Note that in the case of the Standard Model, the scalar
¹⁹⁵ field ϕ is a complex doublet, and so the corresponding potential is 5-dimensional.
¹⁹⁶ In order to obtain a physical interpretation of the Lagrangian in Eq. (2.14) for the
¹⁹⁷ case where $\mu^2 < 0$, the field ϕ is expanded around the vacuum state. The vacuum
¹⁹⁸ expectation value (VEV) is the expected value of the field ϕ which minimises the
¹⁹⁹ potential $V(\phi)$ (equivalently the expected value of the field operator ϕ when the
²⁰⁰ system is in a vacuum state, $|\langle \phi \rangle_0|^2 \equiv |\langle 0 | \phi | 0 \rangle|^2 \equiv \phi_0^2$). Minimising the potential

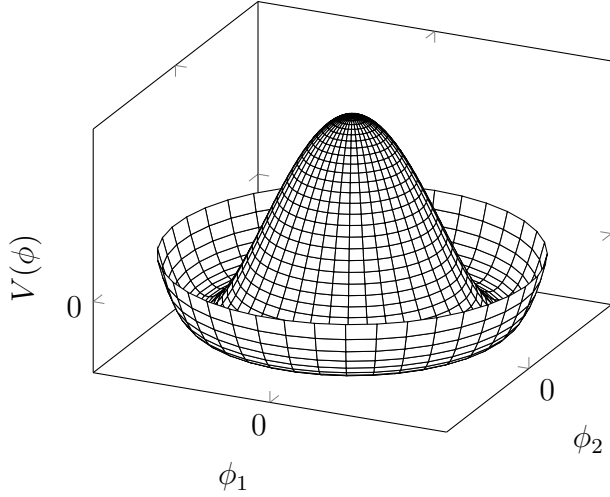


Figure 2.1: The Higgs potential $V(\phi)$ of the complex scalar field singlet $\phi = \phi_1 + i\phi_2$, with a choice of $\mu^2 < 0$ leading to a continuous degeneracy in the true vacuum states. A false vacuum is present at the origin.

201 gives a VEV of

$$\phi_0^2 = -\mu^2/\lambda = v^2. \quad (2.16)$$

202 Due to the shape of the potential in Fig. 2.1, there is a degeneracy in the direction
203 that the complex doublet ϕ points. As all the different vacuum states minimise
204 the potential and therefore yield identical physics, one can arbitrarily choose the
205 state to lie along the second component of the doublet. Application of Eq. (2.13)
206 shows this choice is manifestly invariant under the charge operator. This allows
207 the identification of the unbroken subgroup $U(1)_Q$, under which the ground state is
208 invariant. The generator of $U(1)_Q$ is the charge operator Q .

209 Adding the particle content back to the theory by expanding the field around the
210 vacuum state, and making a transformation to the unitary gauge to remove unphysical
211 Nambu-Goldstone modes (which arise in the context of global symmetries [24, 25]),
212 yields

$$\phi = \frac{1}{\sqrt{2}} \begin{bmatrix} 0 \\ v + H \end{bmatrix}, \quad (2.17)$$

where H is a real scalar field, the *true vacuum* Higgs field. Substituting this into Eq. (2.14) and identifying physical fields from the quadratic terms of linear combinations of unphysical fields, one can write the physical fields W_μ^\pm , Z_μ and A_μ in terms of the original fields A_μ^a and B_μ . This gives

$$W_\mu^\pm = \frac{1}{\sqrt{2}}(A_\mu^1 \mp iA_\mu^2) \quad \begin{bmatrix} A_\mu \\ Z_\mu \end{bmatrix} = \begin{bmatrix} \cos \theta_W & \sin \theta_W \\ -\sin \theta_W & \cos \theta_W \end{bmatrix} \begin{bmatrix} B_\mu \\ A_\mu^3 \end{bmatrix}. \quad (2.18)$$

where θ_W is the weak mixing angle defined by

$$\cos \theta_W = \frac{g}{\sqrt{g^2 + g'^2}}. \quad (2.19)$$

The corresponding masses of the now massive vector bosons can be read off as

$$m_W = \frac{1}{2}gv \quad m_Z = \frac{m_W}{\cos \theta_W}, \quad (2.20)$$

while the photon remains massless. The Higgs mass is $m_H = v\sqrt{\lambda} = \mu$.

This is the Higgs mechanism. It maintains the renormalisability and unitarity of the SM whilst allowing the weak vector bosons to acquire mass. In summary, an unphysical complex scalar field ϕ with a nonzero VEV leads to spontaneous symmetry breaking. Due to the non-Abelian symmetry breaking, would-be massless Nambu-Goldstone modes, which arise after expansion around the true vacuum state, are cancelled out by making a local gauge transformation to the unitary gauge, and instead are absorbed by the vector bosons, allowing them to acquire mass.

This sector of the SM contains four fundamental parameters that must be determined from experiment. These can be specified by the Lagrangian parameters g , g' , v and λ or the physically measurable parameters m_Z , $\sin \theta_W$, m_H and e . In the local neighbourhood around the true vacuum, the macroscopic symmetry of the system is not realised, and therefore the physical particles do not obey the original symmetry. However, information about the symmetry is retained through some additional constraints on the parameters of the theory. Prior to symmetry breaking, the potential contained two terms and two constants. After symmetry breaking there are three terms but still only two constants that relate these terms. This is the vestige of the original symmetry.

237 Spontaneous symmetry breaking has modified the original symmetry group of the SM
238 $SU(2)_L \times U(1)_Y \rightarrow SU(3)_C \otimes U(1)_Q$. Three broken generators from the symmetry
239 group $SU(2)_L \times U(1)_Y$ have been absorbed into the definition of the physical weak
240 vector bosons, giving them mass. The same methodology can be used to generate
241 the fermion masses, as shown in the next section.

242 2.2.2 Fermionic Yukawa Coupling

243 Adding the masses of the fermions by hand breaks the gauge invariance of the
244 theory. Instead, we can use a Yukawa coupling between the fermion fields and the
245 Higgs field in order to generate mass terms after spontaneous electroweak symmetry
246 breakdown [19]. In this way, the fermion masses are determined by both the respective
247 couplings to the Higgs field and the VEV of the Higgs field itself, which sets the
248 basic mass scale of the theory.

249 The Higgs field ϕ transforms as an $SU(2)$ doublet with $Y = 1/2$, as does the left-
250 handed fermion field ψ_L . The right-handed fermion field ψ_R transforms as an $SU(2)$
251 singlet.

252 Charged Lepton Masses

253 The renormalisable and gauge invariant coupling between a fermionic field ψ and a
254 scalar Higgs field ϕ can be written as

$$\mathcal{L}_{\text{Yukawa}} = -g_f(\bar{\psi}_L \phi \psi_R + \bar{\psi}_R \phi^\dagger \psi_L). \quad (2.21)$$

255 where $\psi_L = (\nu_L, e_L)$ and $\psi_R = e_R$ for the first generation leptons. After spontaneous
256 symmetry breaking (see Section 2.2.1), the scalar Higgs field in unitary gauge
257 Eq. (2.17) consists of a VEV and the true vacuum Higgs field H . Substituting this
258 in to Eq. (2.21) yields

$$\mathcal{L}_{\text{Yukawa}} = -\frac{v g_e}{\sqrt{2}} \bar{e} e - \frac{g_e}{\sqrt{2}} \bar{e} H e, \quad (2.22)$$

259 using $\bar{e} e = (\bar{e}_L + \bar{e}_R)(e_L + e_R) = \bar{e}_L e_R + \bar{e}_R e_L$. The VEV component of ϕ provides
260 the first term in Eq. (2.22) which is quadratic in the electron field, and can therefore

261 be identified as the electron mass term. An interaction term between the electron
 262 field e and the true vacuum Higgs field H is also present. Mass is generated for the
 263 other charged lepton generations in the same way.

264 **Quark Masses**

265 The down-type quarks acquire their mass analogous to the leptons, with $\psi_L = (u_L, d_L)$
 266 and $\psi_R = d_R$ for the first quark generation. Mass is generated for the up-type quarks
 267 using the conjugate field to ϕ which transforms under $SU(2)$ as a doublet with
 268 $Y = -1/2$. The conjugate field $\tilde{\phi}$ is constructed as

$$\tilde{\phi} = i\sigma_2 \phi^\dagger = \begin{bmatrix} 0 & 1 \\ -1 & 0 \end{bmatrix} \begin{bmatrix} \phi_1^\dagger \\ \phi_2^\dagger \end{bmatrix} = \frac{1}{\sqrt{2}} \begin{bmatrix} v + H \\ 0 \end{bmatrix}, \quad (2.23)$$

269 and transforms in the same way as ϕ . This field can be used to write an additional
 270 Yukawa coupling which provides mass for the up-type quarks in a similar way as
 271 before.

$$\mathcal{L}_{\text{Yukawa}}^{\text{up}} = -g_q (\bar{\psi}_L \tilde{\phi} \psi_R + \bar{\psi}_R \tilde{\phi}^\dagger \psi_L) \quad (2.24)$$

272 Considering the first generation of up-type quarks with $\psi_L = (u_L, d_L)$ and $\psi_R = u_R$,
 273 substitution into Eq. (2.24) yields

$$\mathcal{L}_{\text{Yukawa}}^{\text{up}} = -\frac{vg_u}{\sqrt{2}} \bar{u}u - \frac{g_u}{\sqrt{2}} \bar{u}Hu. \quad (2.25)$$

274 The Yukawa terms mix quarks of different generations. Physical particles are detected
 275 in their mass eigenstates q , which diagonalise the mass matrix, but interact via the
 276 weak interaction according to their weak eigenstates \tilde{q} , which are superpositions
 277 of the mass eigenstates. This feature of the weak sector leads to mixing between
 278 different generations of quarks. Quark mixing can be expressed using the Cabibbo-
 279 Kobayashi-Maskawa (CKM) matrix, which specifies the strength of flavour-changing
 280 weak currents. The entries in the matrix are enumerated as

$$\begin{bmatrix} \tilde{d} \\ \tilde{s} \\ \tilde{b} \end{bmatrix} = \begin{bmatrix} V_{ud} & V_{us} & V_{ub} \\ V_{cd} & V_{cs} & V_{cb} \\ V_{td} & V_{ts} & V_{tb} \end{bmatrix} \begin{bmatrix} d \\ s \\ b \end{bmatrix}, \quad (2.26)$$

281 where the size of the elements $|V_{pq}|^2$ measures the probability of a transition between
282 states p and q .

283 2.2.3 Higgs Sector Phenomenology

284 As previously discussed in this chapter, the Higgs field plays a key role in the SM
285 by giving mass to fundamental particles. The strength of the coupling between
286 the Higgs field and another particle is proportional to that particle's mass. This
287 fact dictates which production mechanisms and decay modes are dominant at the
288 LHC. The cross sections for different production mechanisms at a centre of mass
289 energy $\sqrt{s} = 13 \text{ TeV}$ are shown as a function of the Higgs mass m_H in Fig. 2.2. At
290 leading order in QCD, Higgs boson production occurs mainly through four modes,
291 shown in Fig. 2.3. The dominant production mode is gluon-gluon fusion ($pp \rightarrow H$),
292 which is predominantly mediated by a virtual top quark loop. Vector boson fusion
293 ($pp \rightarrow qqH$) is the second most likely production mechanism, in which a pair of
294 W or Z bosons fuse to produce a Higgs after being radiated by two quarks. Next
295 most common is the associated production of a Higgs boson and a vector boson
296 ($pp \rightarrow VH$), in which a pair of quarks fuse to produce a single W or Z boson which
297 radiates a Higgs. The final of the four leading production modes is top quark fusion,
298 in which two gluons each radiate a quark-antiquark pair, and a quark from each pair
299 fuses to produce a Higgs boson.

300 Although gluon-gluon fusion is the dominant production mode, for hadronic decays
301 of the Higgs boson the associated production with a vector boson has the advantage
302 of leading to a more distinct signature due to the likelihood of the vector bosons
303 decaying leptons. Leptons provide a clean signals to detect and trigger on.

304 Since the Higgs boson couples proportional to mass, decays to heavier particles are
305 favoured. The branching ratios of different Higgs boson decay modes are shown
306 as a function of m_H in Fig. 2.4. Approximately 58% of the time the Higgs boson
307 decays to a pair of b -quarks, the dominant decay mode. The next most likely decay
308 mode is to a pair of W bosons, which occurs approximately 20% of the time. After
309 the b -quark, the next heaviest fermions are the tau lepton and the c -quark, decays
310 to pairs of these particles happen approximately an order of magnitude less often.
311 Decays to pairs of vector bosons are via a virtual off shell Higgs boson only. While
312 the $H \rightarrow \gamma\gamma$ and $H \rightarrow ZZ$ branching ratios are small compared with fermionic decay

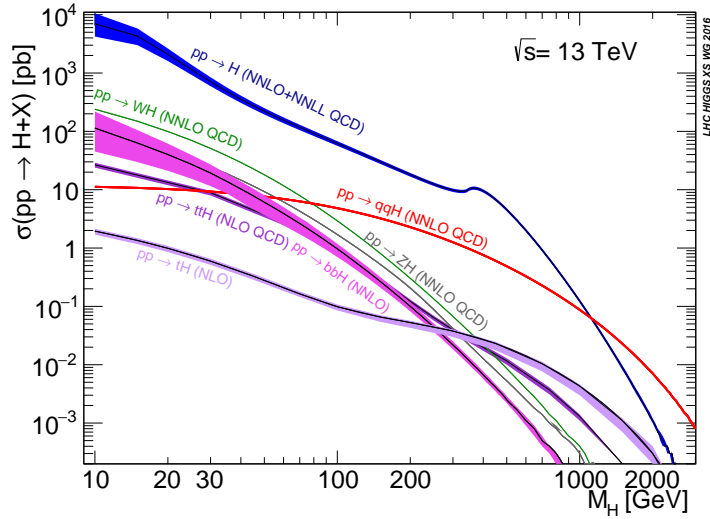


Figure 2.2: Higgs boson production cross sections as a function of Higgs mass (m_H) at $\sqrt{s} = 13 \text{ TeV}$ [26]. Uncertainties are shown in the shaded bands. At $m_H = 125 \text{ GeV}$, Higgs boson production is dominated by gluon-gluon fusion, vector boson fusion, associated production with vector bosons, and top quark fusion.

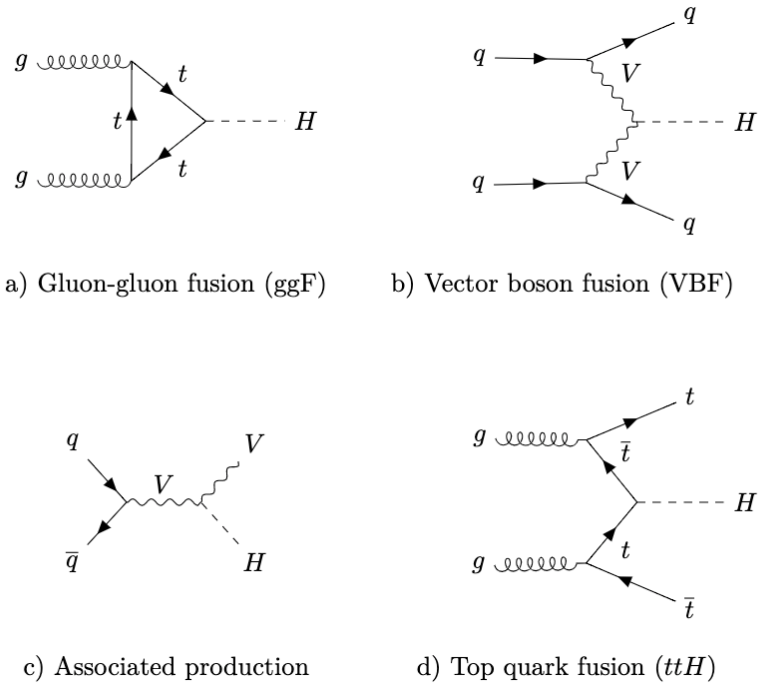


Figure 2.3: Diagrams for the four main Higgs boson production modes at the LHC for a Higgs mass $m_H = 125 \text{ GeV}$ at a centre of mass energy $\sqrt{s} = 13 \text{ TeV}$.

³¹³ modes (around 0.2% for $H \rightarrow \gamma\gamma$), these decay channels were instrumental in the
³¹⁴ initial discovery of the Higgs due to the low level of background processes which
³¹⁵ mimic the final state [14, 15].

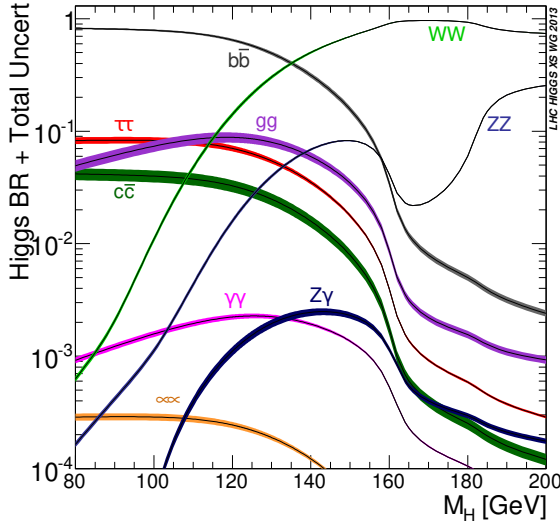


Figure 2.4: Higgs boson branching ratios as a function of Higgs mass (m_H) at $\sqrt{s} = 13$ TeV [26]. Uncertainties are shown in the shaded bands. At $m_H = 125$ GeV, the Higgs predominantly decays to a pair of b -quarks, around 58% of the time. The leading subdominant decay mode is to a pair of W bosons.

³¹⁶ This thesis presents a measurement of the Higgs bosons production rate using events
³¹⁷ with a Higgs boson produced in association with vector boson and decaying to a pair
³¹⁸ of b -quarks, i.e. $pp \rightarrow VH(b\bar{b})$. The $H \rightarrow b\bar{b}$ decay mode directly probes the Higgs
³¹⁹ coupling to fermions, and more specifically to the bottom quark. This coupling was
³²⁰ first observed in 2018 [27, 28]. Ongoing work measuring the coupling strengths, in
³²¹ particular in the high energy regime, is the focus of the analysis presented in this
³²² thesis in Chapter 7.

323 Chapter 3

324 The Large Hadron Collider and the
325 ATLAS Detector

326 Since the completion of its construction in 2008, the Large Hadron Collider (LHC) [29]
327 at CERN has extended the frontiers of particle physics through significant increases
328 in centre of mass energy and luminosity compared with previous collider experiments.
329 The LHC accelerates bunches of protons around a 27 km ring until they are travelling
330 just 3 m s^{-1} slower than the speed of light, at which point they are made to collide.
331 The proton bunches travel round the ring 11,000 times per second in two concentric
332 beams, which are guided by superconducting magnets cooled using liquid helium to
333 -271.3°C (1.9 K). The beams travel in opposite directions around the ring and are
334 crossed at four locations so that collisions between protons can take place. Around
335 these collision points four specialised detectors, ALICE [30], CMS [31], LHCb [32] and
336 ATLAS [33], are located to capture information about the products of the collisions.

337 In this chapter, a brief overview of the LHC and the accelerator complex at CERN
338 is given in Section 3.1. The coordinate system used at the ATLAS detector and
339 other common definitions are introduced in Section 3.2. An overview of the different
340 detector systems is provided in Section 3.3, and finally descriptions of various
341 commonly used reconstructed objects is given in Section 3.4.

³⁴² 3.1 The Large Hadron Collider

³⁴³ The LHC is operated in multi-year *runs* during which beams of protons are circulated
³⁴⁴ and collided. Between runs there are periods of shutdown while the accelerator and
³⁴⁵ detector machinery is maintained and upgraded. Run 1 began in 2010 when the LHC
³⁴⁶ collided proton bunches, each containing more than 10^{11} particles, 20 million times
³⁴⁷ per second, providing 7 TeV proton-proton collisions at instantaneous luminosities
³⁴⁸ of up to $2.1 \times 10^{32} \text{ cm}^{-2} \text{ s}^{-1}$. The centre-of-mass energy was increased to 8 TeV
³⁴⁹ in 2012. Over the course of Run 1, 26.4 fb^{-1} of usable integrated luminosity was
³⁵⁰ recorded. Run 2, which spanned 2015–2018, further increased the proton-proton
³⁵¹ collision energy to 13 TeV. During Run 2 the bunch spacing was reduced, leading
³⁵² to a collision rate of 40 MHz. Over the course of Run 2 a total usable integrated
³⁵³ luminosity of 139 fb^{-1} was recorded. 2022 marked the beginning of Run 3 which,
³⁵⁴ with a higher center of mass energy and peak luminosity, is expected to culminate in
³⁵⁵ an approximate tripling of the dataset size. A summary of key information about
³⁵⁶ each run is listed in Table 3.1.

Period	Year	\sqrt{s} [TeV]	$\langle \mu \rangle$	Bunch spacing [ns]	Luminosity [$\text{cm}^{-2} \text{ s}^{-1}$]
Run 1	2010–2012	7–8	18	50–150	8×10^{33}
Run 2	2015–2018	13	34	25	$1\text{--}2 \times 10^{34}$
Run 3	2022–2025	13.6	50	25	2×10^{34}

Table 3.1: Overview of the different LHC runs [34,35]. The average number of interactions per bunch-crossing is denoted as $\langle \mu \rangle$ (see Section 3.2.3), and is here averaged over the entire run. The luminosity is the peak instantaneous luminosity. Numbers for Run 3 are preliminary and are only provided to give an indication of expected performance.

³⁵⁷ An overview of the accelerator complex at CERN is shown in Fig. 3.1. The LHC is
³⁵⁸ at the final stage of a chain of accelerators which incrementally step-up the energy
³⁵⁹ of incoming protons. The first accelerator is Linac2 (which has been replaced by
³⁶⁰ Linac4 in 2020), a linear accelerator which accelerates negative hydrogen ions to an
³⁶¹ energy of 160 MeV. Upon leaving Linac4, the ions are stripped of both electrons
³⁶² and the resulting protons are fed into the Proton Synchrotron Booster (PSB), which
³⁶³ increases the energy of the protons to 2 GeV. The protons leaving the PSB are passed
³⁶⁴ to the Proton Synchrotron (PS), which increases the energy to 26 GeV, and then
³⁶⁵ from the PS to the Super Proton Synchrotron (SPS) which further increases the

366 energy to 450 GeV. Finally, the proton beams are injected in the LHC where they
 367 are accelerated to their final energy of 6.5 TeV (for Run 2).

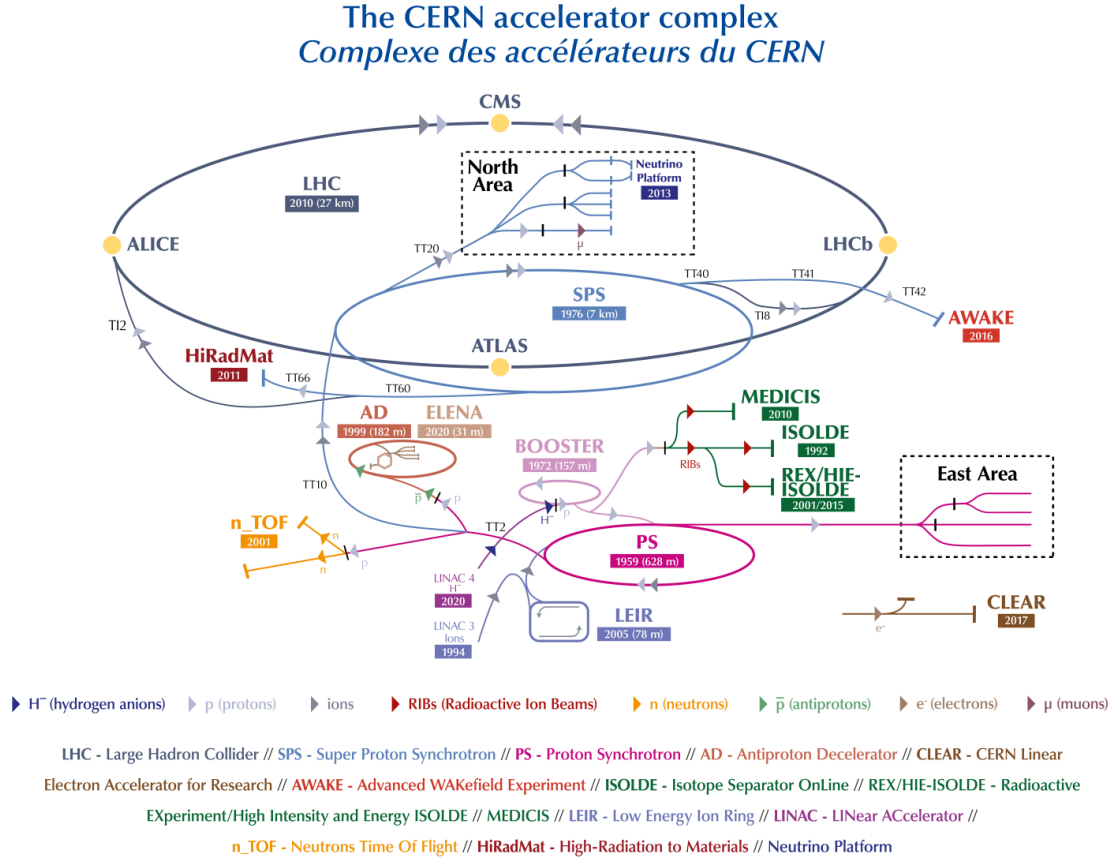


Figure 3.1: An overview of the CERN accelerator complex [36]. The LHC is fed by a series of accelerators starting with Linac2 (or Linac4 from 2020). Next are the Proton Synchrotron Booster, the Proton Synchrotron, and finally the Super Proton Synchrotron which injects protons into the LHC.

368 3.2 Coordinate System & Collider Definitions

369 In Section 3.2.1, the coordinate system used at ATLAS is introduced. The parame-
 370 terisation used for specifying the trajectory of charged particle tracks is described in
 371 Section 3.2.2, and definitions for some frequently occurring concepts and quantities
 372 is provided in Section 3.2.3.

³⁷³ 3.2.1 ATLAS Coordinate System

³⁷⁴ The origin of the coordinate system used by ATLAS is the nominal interaction point
³⁷⁵ in the centre of the detector. As shown in Fig. 3.2, the z -axis points along the
³⁷⁶ direction of the beam pipe, while the x -axis points from the interaction point to the
³⁷⁷ centre of the LHC ring, and the y -axis points upwards. The transverse plane lies
³⁷⁸ in x - y while the longitudinal plane lies along the z -axis. A cylindrical coordinate
³⁷⁹ system with coordinates (r, ϕ) is used in the transverse plane, where r is the radius
³⁸⁰ from the origin and ϕ is the azimuthal angle around the z -axis.

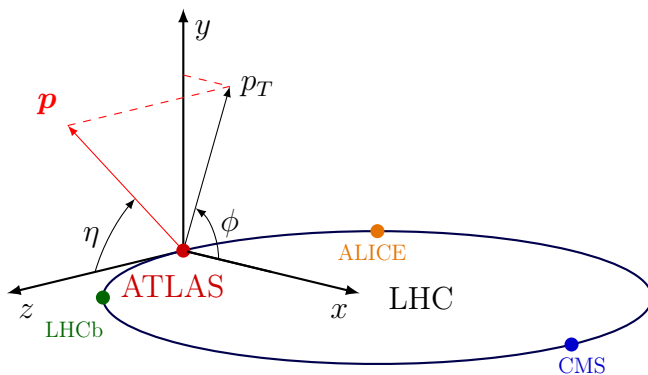


Figure 3.2: The coordinate system used at the ATLAS detector, showing the locations of the four main experiments located at various points around the LHC. The 3-vector momentum $\mathbf{p} = (p_x, p_y, p_z)$ is shown by the red arrow. Reproduced from Ref. [37].

³⁸¹ The polar angle θ is commonly specified in terms of the pseudorapidity η , defined as

$$\eta = -\ln \left[\tan \left(\frac{\theta}{2} \right) \right]. \quad (3.1)$$

³⁸² The pseudorapidity is a convenient quantity to work with as differences in η are
³⁸³ invariant under Lorentz boosts.

³⁸⁴ The transverse momentum p_T of an object is the sum in quadrature of the momenta
³⁸⁵ in the transverse plane

$$p_T = \sqrt{p_x^2 + p_y^2}. \quad (3.2)$$

386 Angular distance between two objects is measured in units of ΔR and is defined as

$$\Delta R = \sqrt{(\Delta\eta)^2 + (\Delta\phi)^2}, \quad (3.3)$$

387 where $\Delta\eta$ and $\Delta\phi$ are the differences in pseudorapidity and azimuthal angle between
388 the two objects.

389 3.2.2 Track Parameterisation

390 The trajectories of charged particle tracks are parameterised as a helix which is fully
391 specified using five parameters: $(d_0, z_0, \phi, \theta, q/p)$. The transverse and longitudinal
392 impact parameters (IP) d_0 and z_0 specify the closest approach of the trajectory of a
393 particle to an given origin, where the hard scatter primary vertex (see Section 3.4.2)
394 is used in this thesis. ϕ and θ are the azimuthal and polar angles respectively, and
395 q/p is the measured charge on the track¹ divided by the scalar 3-momentum. Fig. 3.3
396 shows each of these parameters diagrammatically.

397 Impact parameter significances are defined as the IP divided by its corresponding
398 uncertainty, $s(d_0) = d_0/\sigma(d_0)$ and $s(z_0) = z_0/\sigma(z_0)$. When used in flavour tagging
399 (see Chapter 4), track IP significances are lifetime signed according to the track's
400 direction with respect to the jet axis and the primary vertex [39]. The signed IP
401 significances is positive if the track crosses the jet axis in front of the primary vertex
402 and negative if the crossing is behind the primary vertex.

403 3.2.3 Hadron Collider Definitions

404 Cross Section

405 The cross section σ is closely related to the probability of an interaction between
406 two colliding particles, and is analogous to an effective cross-sectional area of the
407 particles. The cross section of a process depends on the transition matrix element
408 and a phase space integral. At hadron colliders such as the LHC, the proton-proton

¹Reconstructed charged particles are assumed to have a charge of ± 1 .

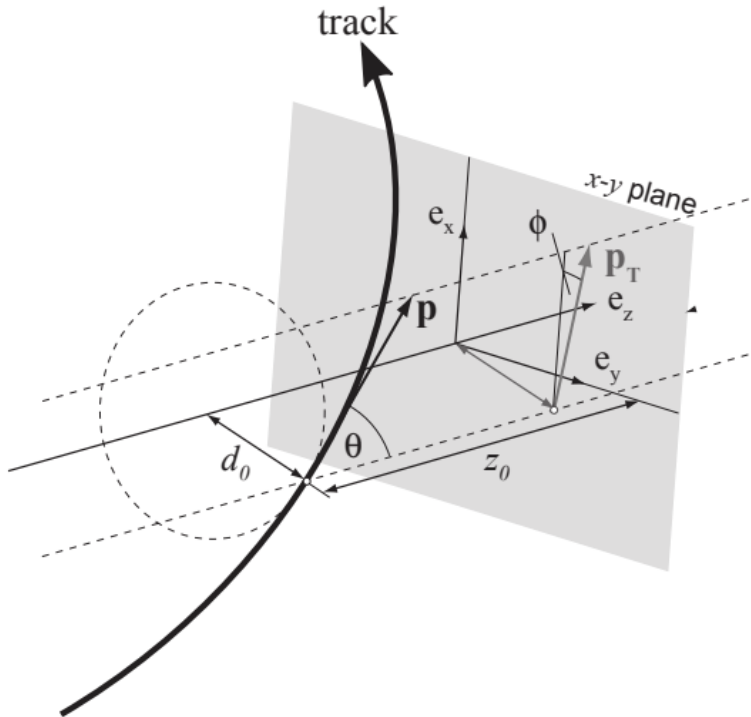


Figure 3.3: The track parameterisation used at the ATLAS detector. Five coordinates $(d_0, z_0, \phi, \theta, q/p)$ are specified, defined at the track's point of closest approach to the nominal interaction point at the origin of the coordinate system. The figure shows the three-momentum \mathbf{p} and the transverse momentum p_T (defined in Eq. (3.2)). The basis vectors e_x , e_y and e_z are also shown. Reproduced from Ref. [38].

⁴⁰⁹ cross section can be factorised as

$$\sigma(pp \rightarrow X) \approx \text{PDFs} \cdot \text{partonic cross section.} \quad (3.4)$$

⁴¹⁰ The partonic cross section can be calculated at high energies such as those found at
⁴¹¹ the LHC, while the parton distribution functions (PDFs) have to be extracted from
⁴¹² experimental results.

⁴¹³ Luminosity

⁴¹⁴ The total number of proton-proton collisions N is related to the total pp cross σ
⁴¹⁵ section by the integrated luminosity L , as in

$$N = \sigma L = \sigma \int \mathcal{L} dt. \quad (3.5)$$

⁴¹⁶ The instantaneous luminosity \mathcal{L} relates the cross section to the number of collisions
⁴¹⁷ per unit time. For two colliding bunched proton beams, it is defined as

$$\mathcal{L} = \frac{1}{\sigma} \frac{dN}{dt} = \frac{fn_1 n_2}{4\pi \sigma_x \sigma_y}, \quad (3.6)$$

⁴¹⁸ where n_1 and n_2 are the number of protons in the colliding bunches, f is the bunch
⁴¹⁹ crossing frequency, and σ_x and σ_y are the rms width of the beam in the horizontal
⁴²⁰ and vertical directions.

⁴²¹ The total luminosity recorded over the course of Run 2 is shown in Fig. 3.4. In
⁴²² total, 139 fb^{-1} of usable physics data was collected over the three-year run. The
⁴²³ uncertainty on the total integrated luminosity is 1.7% [40].

⁴²⁴ Pile-up

⁴²⁵ At the centre of the ATLAS detector, bunches of more than 10^{11} protons are collided.
⁴²⁶ Each bunch-crossing is called an *event*. There is generally one hard proton-proton
⁴²⁷ scatter per event. Additional interactions are typically relatively soft ($low-p_T$) and
⁴²⁸ are known as *pile-up*. Pile-up from interactions within the same bunch-crossing is
⁴²⁹ known as *in-time* pile-up while residual signatures from previous bunch-crossings
⁴³⁰ is known as *out-of-time* pile-up. The number of pile-up interactions is denoted μ ,

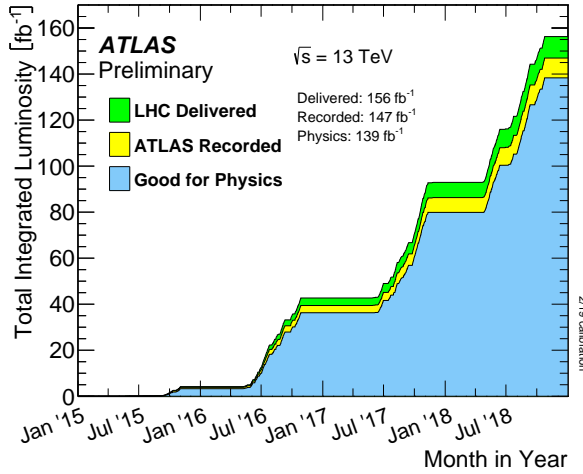


Figure 3.4: Delivered, recorded, and usable integrated luminosity as a function of time over the course of Run 2 [35]. A total of 139 fb^{-1} of collision data is labelled as good for physics, meaning all sub-detector systems were operating nominally.

431 which is often given as a time-averaged value $\langle \mu \rangle$. Histograms showing the number of pile-up interactions over the course of Run 2 are shown in Fig. 3.5.

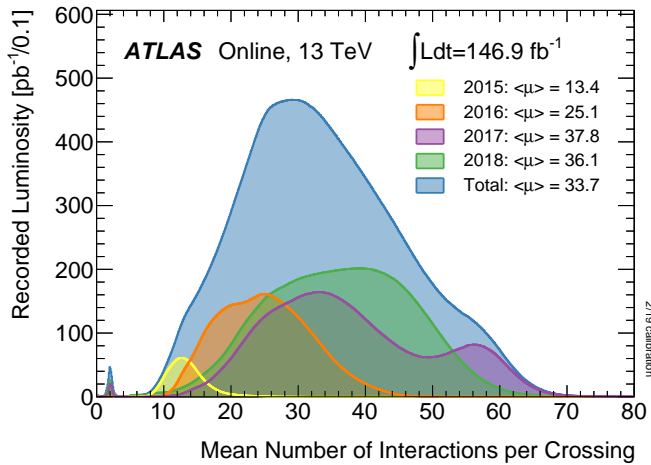


Figure 3.5: Average pile-up profiles measured by ATLAS during Run 2 [35].

⁴³³ 3.3 The ATLAS Detector

⁴³⁴ The ATLAS² detector is made up of several specialised sub-detectors which are
⁴³⁵ arranged concentrically around the nominal interaction point at the centre of the
⁴³⁶ detector, as shown in Fig. 3.6. The detector is designed to cover nearly the entire solid
⁴³⁷ angle around the collision point. In this section a brief overview of each sub-detector
⁴³⁸ is given, in order of increasing radial distance from the point of collision. The inner
⁴³⁹ tracking detector is described in Section 3.3.1, the electromagnetic and hadronic
⁴⁴⁰ calorimeters in Section 3.3.2, the muon spectrometer in Section 3.3.3, and finally the
⁴⁴¹ trigger is described in Section 3.3.4. More complete information on the detector can
⁴⁴² be found in Ref. [33], while an overview of physics performance is given in [41].

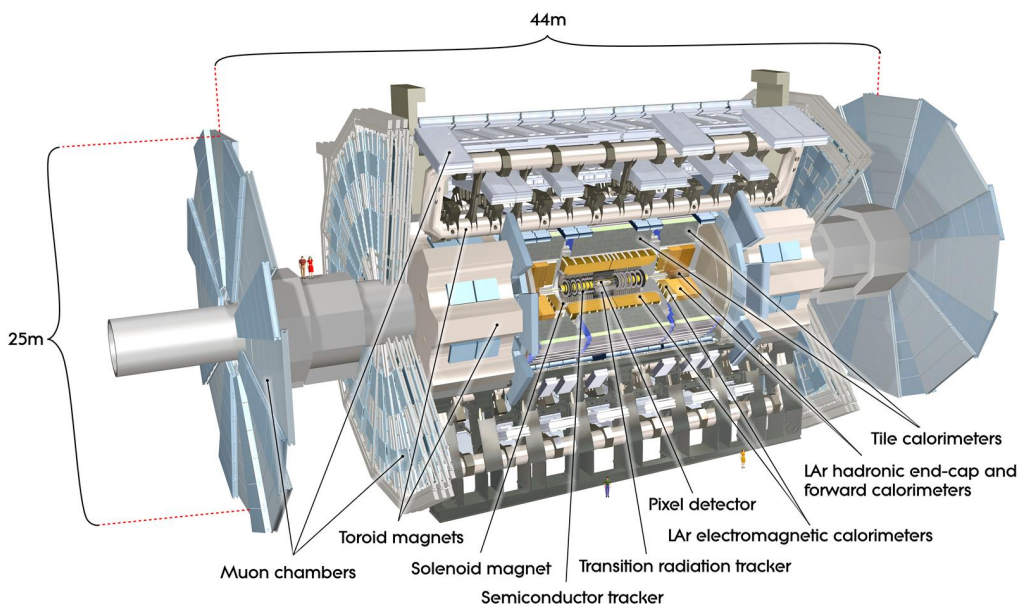


Figure 3.6: A 3D model of the entire ATLAS detector [42]. Cutouts to the centre of the detector reveal the different sub-detectors which are arranged in concentric layers around the nominal interaction point.

²A Toroidal LHC ApparatuS.

443 3.3.1 Inner Detector

444 The inner-detector system (ID) provides high-resolution charged particle trajectory
445 tracking in the range $|\eta| < 2.5$. The ID is immersed in a 2 T axial magnetic field,
446 produced by a superconducting solenoidal magnet, which enables the measurement
447 of particle momentum and charge. After Run 3, the ID will be replaced by the
448 ITk [43, 44].

449 The inner detector is made up of several sub-systems, shown in Figs. 3.7 and 3.8.
450 The high-granularity silicon pixel detector covers the innermost region and typically
451 provides four space-point measurements per track. It is followed by the silicon
452 microstrip tracker (SCT), which usually provides a further four space-point measure-
453 ments (8 hits) per track. These silicon detectors are complemented by the Transition
454 Radiation Tracker (TRT), which enables radially extended track reconstruction up
455 to $|\eta| = 2.0$ and typically provides 33 (38) additional hits in the barrel (end-cap).

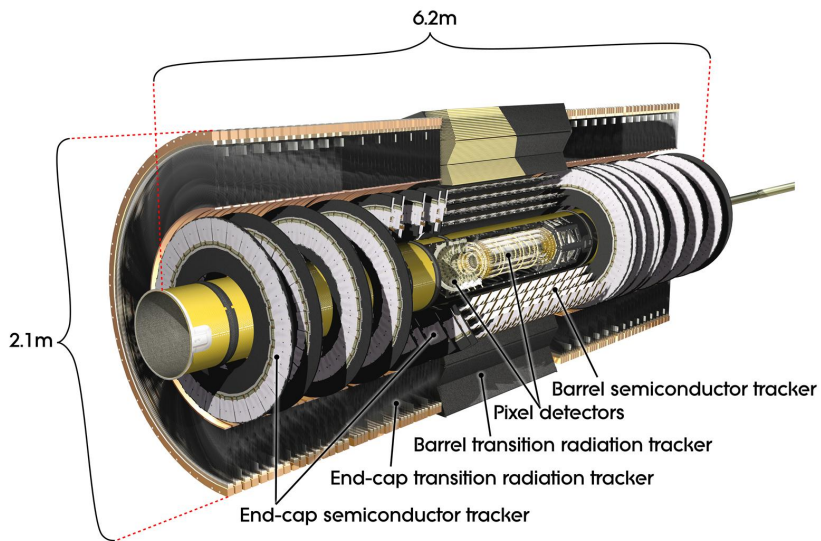


Figure 3.7: A 3D model of the ATLAS ID showing the pixel, SCT and TRT sub-detectors [45].

456 The target inverse momentum resolution for the combined ID measurement is
457 parameterised as a function of the track transverse momentum and polar angle [41].

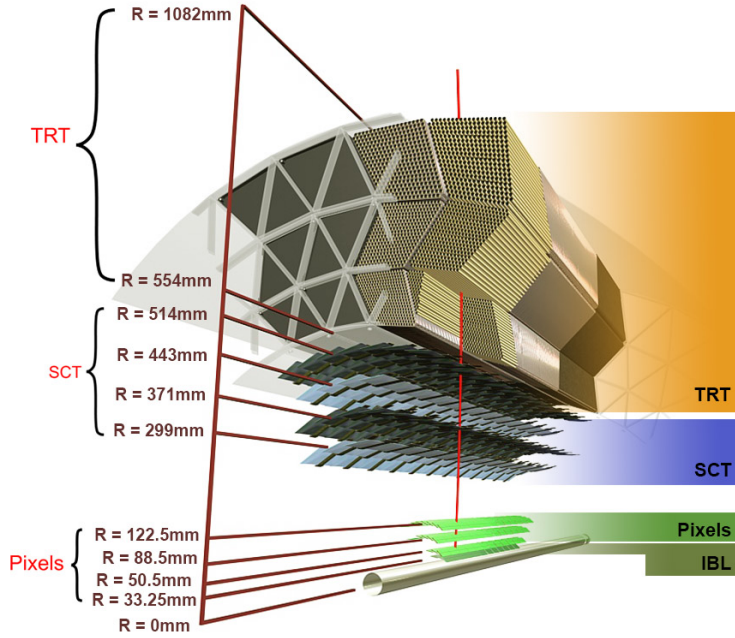


Figure 3.8: A cross-sectional view of the ATLAS ID, with the radii of the different barrel layers shown [38].

⁴⁵⁸ The parameterisation is given by

$$\sigma(1/p_T) = 0.36 \oplus \frac{13}{p_T \sin \theta} \text{ TeV}^{-1}, \quad (3.7)$$

⁴⁵⁹ where \oplus denotes a sum in quadrature. For low- p_T tracks (e.g. $p_T \approx 500 \text{ MeV}$) in the
⁴⁶⁰ central region this corresponds to a relative error of approximately 0.01%. Meanwhile
⁴⁶¹ for high- p_T tracks (e.g. $p_T \approx 100 \text{ GeV}$) in the central region this corresponds to
⁴⁶² a relative error of approximately 4%. The momentum resolution generally good
⁴⁶³ enough to correctly identify the sign of the charge on particles up to the highest
⁴⁶⁴ energies expected at the LHC. The transverse impact parameter resolution $\sigma(d_0)$ is
⁴⁶⁵ parameterised similarly as

$$\sigma(d_0) = 11 \oplus \frac{115}{p_T \sin \theta} \mu\text{m}. \quad (3.8)$$

⁴⁶⁶ Typical uncertainties for the transverse IP resolution are 230 μm and 11 μm for low
⁴⁶⁷ and high- p_T tracks in the central region, respectively.

468 Pixel Detector

469 The silicon pixel detector is comprised of four cylindrical barrels at increasing radii
 470 from the beamline, and four disks on each side. The innermost barrel layer is the
 471 insertable B-layer (IBL), shown in Fig. 3.9. The IBL was installed before Run 2 [46,47]
 472 and lies approximately just 33 mm from the beam axis. The second-to-innermost layer
 473 is often referred to as the B-layer. The specification of the pixel detector determines
 474 the impact parameter resolution and the ability to reconstruct primary and secondary
 475 vertices. The detector is required to have a high granularity (i.e. resolution) to
 476 maintain the low occupancy required to resolve nearby particles. Individual pixels
 477 are $50\text{ }\mu\text{m}$ in the transverse direction $R\phi$ and $400\text{ }\mu\text{m}$ in the longitudinal z direction
 478 ($250\text{ }\mu\text{m}$ for the IBL). Cluster positions have a resolution of approximately $10\text{ }\mu\text{m}$ in
 479 $R\phi$ and $100\text{ }\mu\text{m}$ in z .

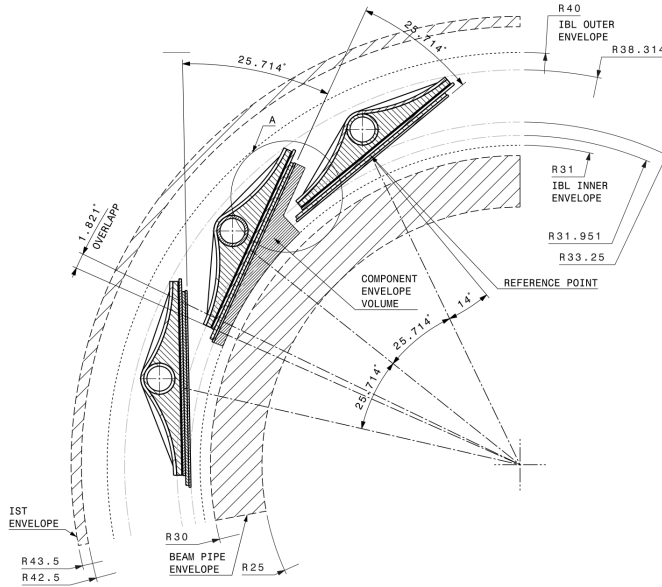


Figure 3.9: A schematic cross-sectional view of the ATLAS IBL [46].

480 Semi-Conductor Tracker (SCT)

481 The SCT is made up of four concentric barrel layers in the central region, and nine
 482 disks in each end-cap. Each layer is itself made of a pair of silicon microstrip layers,
 483 with a small stereo angle (20 mrad) between the two layers enabling the z -coordinate

484 to be measured from a pair of strip measurements. The SCT typically provides
485 four precision space-point measurements (eight strip measurements) per track in
486 the barrel region. These have intrinsic uncertainties of $17\text{ }\mu\text{m}$ in the transverse
487 direction $R\phi$, and $580\text{ }\mu\text{m}$ in the longitudinal direction z [48]. The measurements
488 provide a contribution to the measurement of charged particle momentum and impact
489 parameter.

490 **Transition Radiation Tracker (TRT)**

491 The TRT is a straw-tube tracker which complements the higher-resolution silicon-
492 based tracks by offering a larger number of hits per track (typically more than 30)
493 and a long lever arm, which aids the accurate measurement of particle momentum.
494 It is made up of approximately 300 000 drift tubes with a diameter of 4 mm which
495 are filled with an argon/xenon gas mixture. The walls of each tube are electrically
496 charged, and a thin conducting wire runs along the center. When a charged particle
497 traverses a tube, it ionises the gas and the resulting liberated electrons drift along
498 the electric field to the wire, where an associated charge is registered. In the barrel
499 the straws run parallel to the z -axis and therefore the TRT only provides tracking
500 information in $R\phi$. Straws are arranged radially in the end-caps. The resulting
501 two-dimensional space-points have a resolution of approximately $120\text{ }\mu\text{m}$. The spaces
502 between the straws are filled with a polymer which encourages the emission of
503 transition radiation, aiding electron identification.

504 **3.3.2 Calorimeters**

505 The calorimeter system measures the energy of incident particles over the range
506 $|\eta| < 4.9$. There are two main sub-systems: the electromagnetic calorimeter (ECal),
507 which focuses on the measurement of electrons and photons, and the hadronic
508 calorimeter (HCal), which measures the energy of hadrons. A schematic view of the
509 calorimeter system is shown in Fig. 3.10. Upon entering the calorimeter, incident
510 particles will interact with the detector material to produce a shower of secondary
511 particles with reduced energies. The charge deposited in this process is measured to
512 reconstruct the energy of the initial incident particle. The two calorimeter sub-systems

513 must provide strong containment of showering particles to prevent punch-through of
 514 EM and hadronic particles to the HCal and muon systems respectively.

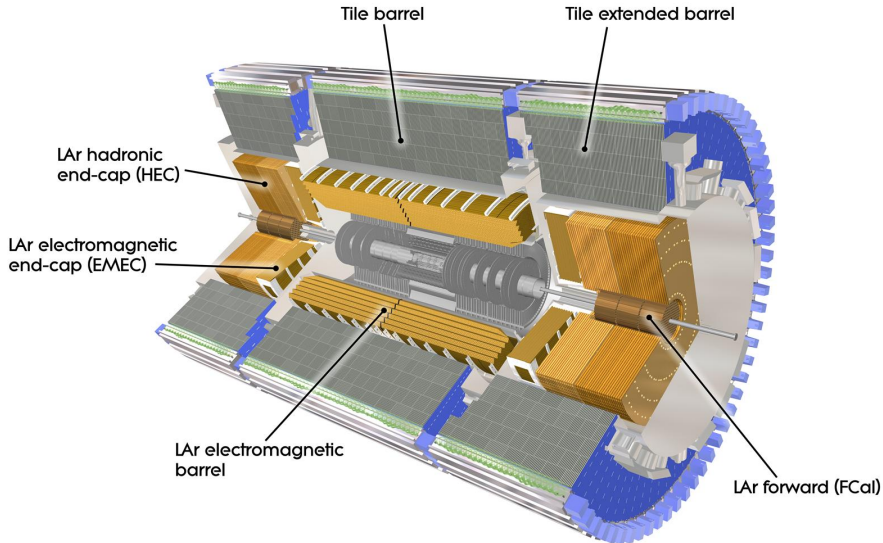


Figure 3.10: The ATLAS calorimeters [49]. The ECal uses LAr-based detectors, while the HCal uses mainly scintillating tile detectors. In the forward region the HCal also includes the LAr hadronic end-caps.

515 Liquid Argon (LAr) Electromagnetic Calorimeter

516 The more granular lead/liquid-argon ECal covers the region $|\eta| < 3.2$ and is split
 517 into barrel (covering $|\eta| < 1.475$) and end-cap (covering $1.375 < |\eta| < 3.2$) regions.
 518 EM calorimetry works by encouraging electrons and photons to interact with electric-
 519 cally charged particles in detector material via bremsstrahlung ($e \rightarrow e\gamma$) and pair
 520 production ($\gamma \rightarrow e^+e^-$). The EM calorimeter uses lead absorber plates to initiate
 521 EM showers, resulting in secondary particles which ionise the surrounding liquid
 522 argon. The charge is collected on copper electrodes and read out. The accordion
 523 geometry of the ECal allows for a full coverage in ϕ without any azimuthal cracks.
 524 The energy resolution of the LAr calorimeter is made up of a sampling and a constant
 525 term, which are summed in quadrature to produce the overall energy resolution. The
 526 sampling term contributes approximately $10\%/\sqrt{E}$, while the constant term adds an
 527 additional 0.7%. Photons with moderate transverse energy $E_T \approx 50$ GeV have an

528 overall energy resolution of at most 1.6% over most of the pseudorapidity range. At
 529 lower $E_T \approx 10 \text{ GeV}$, the resolution is degraded to approximately 5%. The resolution
 530 measurements are obtained from test beam data [41].

531 **Hadronic Tile Calorimeter**

532 In the central barrel region with $|\eta| < 1.7$, the HCal uses a tile calorimeter with
 533 steel as an absorbing material, and scintillating tiles as the active material. Two
 534 copper/liquid-argon calorimeter end-caps are also used. Incident hadrons interact
 535 via the strong and electromagnetic forces with the absorber material, mainly losing
 536 energy due to multiple inelastic nuclear collisions. The active material captures the
 537 resulting electrons and photons to measure the energy of the incident hadron.
 538 The hadronic energy resolution of the HCal is parameterised as a function of the
 539 hadron's transverse energy

$$\sigma(E_T)/E_T = 50\%/\sqrt{E_T} \oplus 3\%, \quad (3.9)$$

540 corresponding to a energy resolution of 11% (6.5%) for a hadron with E_T of approxi-
 541 mately 10 GeV (50 GeV) [50].

542 **3.3.3 Muon Spectrometer**

543 Due to their higher mass, muons easily pass unimpeded through the ID and calorime-
 544 ters and therefore require specialised detectors for their measurement. The Muon
 545 Spectrometer (MS) is made up of dedicated tracking and triggering hardware, as
 546 shown in Fig. 3.11. The precision tracking system uses three layers of monitored drift
 547 tubes with a barrel region covering $|\eta| < 1.2$ and end-caps covering $1 < |\eta| < 2.7$.
 548 The inner layers of the end-caps use cathode strip chambers to better cope with the
 549 high occupancy in the forward region. The trigger system is comprised of resistive
 550 plate chambers in the barrel region covering $|\eta| < 1.0$ and thin gap chambers in
 551 the end-cap regions covering $1 < |\eta| < 2.4$. A set of three superconducting air-core
 552 toroidal magnets, each made up of eight coils, is used in each of the barrel and
 553 end-caps to deflect the muons as they pass through the MS, allowing their momentum
 554 and charge to be measured from the direction and magnitude of curvature. The

555 toroidal magnets generate a field which is largely orthogonal to the muon trajectories
 556 which allows for maximum deflection. The transverse momentum resolution (mea-
 557 sured for combined ID and muon tracks, see Section 3.4.4) has been measured to be
 558 approximately 1.7% in the central region for muons from J/ψ decays, increasing to
 2.3% for muons in the forward regions [51].

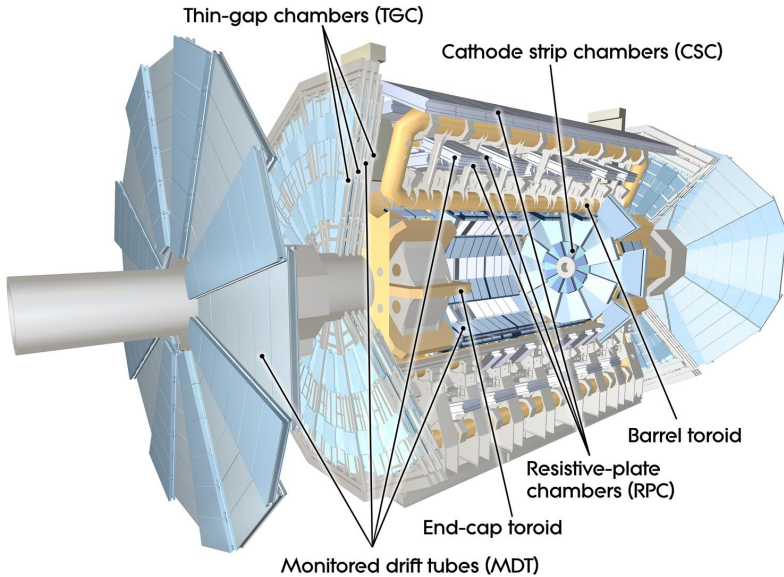


Figure 3.11: The ATLAS muon spectrometer [52].

559

560 3.3.4 The Trigger

561 The 25 ns bunch spacing used over the course of Run 2 corresponds to a bunch-
 562 crossing or event rate of 40 MHz (see Table 3.1). If the full information for the
 563 detector was written out for each event, this would correspond to the generation
 564 of 60 TB of data each second. This is more than can be feasibly read out from the
 565 hardware, processed and stored, requiring the use of a trigger system which quickly
 566 makes a decision about whether or not an event is potentially interesting and should
 567 be kept for further analysis. The trigger system is comprised of two levels which
 568 aim to identify various signatures, such as electrons, muons, taus, photons, and jets
 569 (including b -jets), as well as events with large total or missing transverse energy. The
 570 hardware-based Level-1 (L1) trigger uses coarse information from the calorimeters
 571 and MS to accept events at an average rate of 100 kHz approximately 2.5 μ s after the

572 event. After the L1 trigger, the software-based High Level Trigger (HLT) makes use
573 of 40 000 CPU cores to make a final selection on surviving events in approximately a
574 few hundred milliseconds. The final event read-out rate is approximately 1.2 kHz,
575 corresponding to 1.2 GB s^{-1} of permanent data storage. More information is provided
576 in [53].

577 3.4 Reconstructed Physics Objects

578 Event reconstruction is the process of analysing the output from the detector to
579 determine the type and properties of particles present in an event. The reconstructed
580 event provides information about the underlying physics process that led to these
581 observable final state particles. Events passing the trigger selection (described in
582 Section 3.3.4) undergo offline reconstruction, which makes use of the full information
583 from the detector. Reconstruction and analysis of events relies on the extensive
584 ATLAS software stack, see Ref. [54] for more information.

585 Several different reconstructed objects are used for physics analyses. Objects relevant
586 to this thesis are described below.

587 3.4.1 Tracks

588 The reconstructed trajectories of charged particles are referred to as *tracks*. Tracks
589 are reconstructed from the energy depositions (called *hits*) left by the particles as
590 they traverse the inner detector. Tracks are used in the reconstruction of other
591 objects, including vertices and jets, so their accurate reconstruction is a critical
592 task. A comprehensive introduction to ATLAS tracking is available in Ref. [55],
593 while specific optimisations for dense environments are detailed in Refs. [56, 57]. An
594 overview of track reconstruction is given below.

595 Space-point Formation (Clustering)

596 When a charged particle traverses a silicon layer, charge can be collected in more
597 than one pixel or strip. This is due to the incident angle of the particles with respect
598 to the sensor, and also the drift of electrons between sensors caused by the magnetic

599 field. Clusters (also called *hits* or *space-points*) are formed by clustering neighbouring
600 pixels or strips and estimating locations of space-points using the shape and energy
601 distribution of the clusters.

602 **Track Finding**

603 Space-points are used to build track seeds. These are groups of three hits which
604 are geometrically compatible with being part of a track segment. A combinatorial
605 Kalman filter (KF) is used to build track candidates by extending track seeds. The
606 filter can create multiple track candidates per seed, with bifurcations along the track
607 occurring when more than one compatible space-point exists on a given layer. In
608 this way, the KF creates an excess of *track candidates*, which are only required to
609 satisfy basic quality requirements. Track candidates are allowed to reuse or *share*
610 hits freely (a single hit may be used by multiple track candidates). Typically, the
611 presence of shared hits is a predictor of a bad track due to the high granularity of
612 the ATLAS tracking detectors. At this stage, there can also be a large number of
613 incorrect hits assigned to otherwise good tracks, and additionally large numbers of
614 *fake* tracks, which are comprised of a majority of wrong hits and do not correspond
615 to the trajectory of any one physical particle (*fake* tracks are defined as those where
616 the majority of associated hits do not originate from one single truth particle, see
617 Eq. (5.5)). The low quality of tracks at this stage necessitates an ambiguity solving
618 step, in which candidates are cleaned, and the highest quality track are selected.

619 **Ambiguity Solving**

620 Ambiguity solving was introduced as part of the ATLAS New Tracking effort [55],
621 which was intended to improve track reconstruction performance in dense envi-
622 ronments. In the ambiguity solver, track candidates are processed individually in
623 descending order of a track score. The track score quantifies the likelihood of the
624 track corresponding to the trajectory of a real particle. Scoring uses a number of
625 variables, including the number and positions of hits (preferring hits in more precise
626 regions of the detector), the transverse momentum of the track and the track fit
627 quality. The track fit quality describes the quality of the track as the χ^2 divided
628 by the number degrees of freedom on the track. A preference for high transverse

629 momentum tracks promotes the successful reconstruction of the more physically
 630 interesting energetic particles, and suppresses the large number of wrong hits assigned
 631 to low momentum tracks. The ambiguity solver also penalises tracks with missing
 632 hits on the innermost detector layers.

633 During the processing of a track candidate, the track is cleaned (whereby problematic
 634 hits are removed), and, if the resulting track satisfies the quality selection criteria, a
 635 high precision fit of the track parameters using the surviving hits is performed. The
 636 high precision fit makes full use of all available information, and uses an updated
 637 position and uncertainty estimate for each cluster obtained from a Neural Network
 638 (NN) [58]. If the track has reached this stage without being rejected by passing various
 639 quality requirements, it is re-scored and returned to the list of track candidates. If
 640 the same track is then processed again without requiring modification, it is added to
 641 the final track collection. Track candidates that fall below certain quality threshold
 642 are rejected. This selection does allow for the possibility of a track having small
 643 number of shared hits, as detailed in Table 3.2.

Parameter	Selection
p_T	$> 500 \text{ MeV}$
$ \eta $	< 2.5
$ d_0 $	$< 3.5 \text{ mm}$
$ z_0 \sin \theta $	$< 5 \text{ mm}$
Silicon hits	≥ 8
Shared silicon hits	< 2
Silicon holes	< 3
Pixel holes	< 2

Table 3.2: Quality selections applied to tracks, where d_0 is the transverse IP of the track, z_0 is the longitudinal IP with respect to the PV and θ is the track polar angle (see Section 3.2.2 for the IP definitions). Silicon hits are hits on the pixel and SCT layers. Shared hits are hits used on multiple tracks which have not been classified as split by the cluster-splitting neural networks [57]. A hole is a missing hit, where one is expected, on a layer between two other hits on a track.

644 Neural Network Cluster Splitting

645 As part of track cleaning, shared hits are classified by a NN to determine if they are
 646 compatible with the characteristic features of a merged cluster [56, 58]. A merged
 647 cluster is one made up of a combination of energy deposits from more than one
 648 particle, which have become merged due to the closeness of the associated particles
 649 and the limited resolution of the detector. It is common for clusters to become
 650 merged in dense environments, as discussed in Section 4.2. If the cluster is predicted
 651 to be merged it is labelled as being freely shareable, or *split*. Hits not compatible
 652 with the merged hypothesis can still be shared by a limited number of tracks, but
 653 come with a penalty for the track which may hinder its acceptance into the final
 track collection.

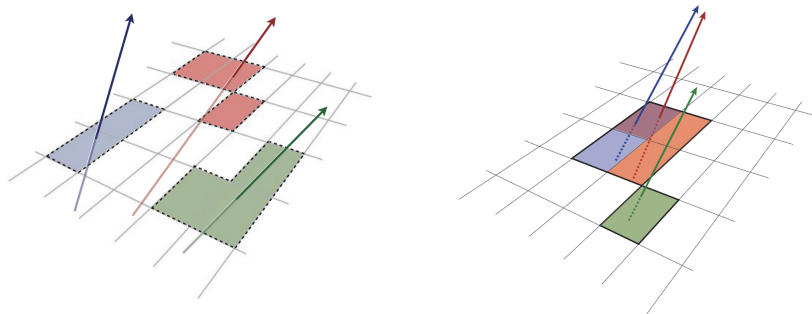


Figure 3.12: Particles (left) which have enough separation will leave charge depositions which are resolved into separate clusters. Sufficiently close particles (right) can lead to merged clusters. Their combined energy deposits are reconstructed as a single merged cluster [57].

654

655 Pseudotracking

656 Pseudotracking uses Monte Carlo truth information to group together all the hits
 657 left by each truth particle. Each collection of hits which, as a unit, satisfies basic
 658 quality requirements is directly used in a full resolution track fit. If the track fit is
 659 successful, a “pseudotrack” track is created and stored. If the track fit fails, or the
 660 collection of hits does not pass the basic quality requirements (for example because
 661 of a lack of hits) then the particle is said to be un-reconstructable. In this way,
 662 pseudotracking performance represents the ideal reconstruction performance given

the ATLAS detector, with perfect hit-to-track association and track reconstruction efficiency. The approach was introduced in Ref. [59] as a way to obtain a fast approximation of tracking reconstruction for simulated data, however the technique has become a useful tool for studying tracking performance in general [56].

3.4.2 Vertices

Groups of reconstructed tracks can be examined to determine whether the particles originated from a common spatial point of origin. This occurs when proton-proton collisions take place (primary vertices), when a particle decays or radiates, and also as a result of interaction with the detector material (secondary vertices). Vertex reconstruction is made up of two stages. First, vertex finding takes place, which is the process of grouping tracks into compatible vertices. Second, vertex fitting combines information from compatible tracks to reconstruct the physical properties of the vertex, such as mass and position.

Primary Vertices

Each proton-proton interaction happens at a *primary vertex* (PV). Primary vertices are iteratively reconstructed with tracks using the iterative vertex finder (IVF) [60]. The *hard scatter vertex* of an event is chosen as the primary vertex whose associated tracks have the largest sum of transverse momentum squared, $\Sigma(p_T^2)$.

Secondary Vertices

Secondary vertices (SV) occur when a particle radiates or decays at a sufficient distance from the primary vertex to be resolved from the primary vertex (see Section 4.2.1). Two widely used secondary vertexing tools are used within ATLAS: SV1 and JetFitter [61, 62]. Each attempts to reconstruct secondary vertices inside a jet using the tracks associated to that jet (see Section 3.4.3 for more information about track association). SV1 by design attempts to reconstruct only a single inclusive vertex per jet. This inclusive vertex groups all b -hadron decay products, including tracks from the b -hadron decay itself and tracks from $b \rightarrow c$ decays. The second tool, JetFitter attempts to resolve each displaced vertex inside the jet, such

691 that secondary vertices from b -hadron decays are reconstructed separately to tertiary
 692 vertices from $b \rightarrow c$ decay chains.

693 3.4.3 Jets

694 Jets are an aggregate reconstructed object corresponding to a collection of collimated
 695 stable particles which results from the presence of a quark or gluon. Jets are built
 696 by clustering constituent objects (e.g. tracks or calorimeter clusters) using a jet
 697 finding algorithm, for example the anti- k_t algorithm [63], which is implemented in
 698 FASTJET [64].

699 Objects can be associated to jets in one of two ways. The first is via a geometrical
 700 matching in ΔR (see) The second is via a ghost association [65], where the object is
 701 assigned a negligible momentum and re-clustered into the jet after its formation.

702 Jets from pile-up interactions are suppressed using the Jet Vertex Tagger (JVT)
 703 algorithm, which uses the transverse momenta of tracks to identify jets from pile-up
 704 interactions [66].

705 EMTopo Jets

706 EMTopo jets are reconstructed from noise-suppressed topological clusters (topoclus-
 707 ters) of calorimeter energy depositions [67]. The clustering uses the energy significance
 708 of each cell, defined as

$$S_{\text{cell}} = \frac{E_{\text{cell}}}{\sigma_{\text{noise, cell}}}, \quad (3.10)$$

709 where E_{cell} is the energy measured in a given calorimeter cell, and $\sigma_{\text{noise, cell}}$ is the
 710 expected level of noise on the cell (e.g. from pile-up interactions). Topoclusters are
 711 formed from a seed cell with a large S_{cell} , and expanded by iteratively adding neigh-
 712 bouring cells with a sufficiently large energy significance. Collections of topoclusters
 713 are then clustered into a jet using the anti- k_t algorithm with a radius parameter of
 714 0.4 (small- R jets) or 1.0 (large- R jets). More information, including information on
 715 the calibration of the topocluster jet energy scale, is available in Ref. [67].

716 Particle Flow Jets

717 Particle-flow (PFlow) jets are reconstructed from particle-flow objects [68] using
718 the anti- k_t algorithm with a radius parameter of 0.4. Particle-flow objects integrate
719 information from both the ID and the calorimeters, improving the energy resolution
720 at high transverse momenta and reducing pile-up contamination. The PFlow jet
721 energy scale is calibrated according to Ref. [69].

722 Large- R Jets

723 Large- R jets have a radius parameter $R = 1.0$ and are built by clustering topological
724 calorimeter clusters using the anti- k_t algorithm [70]. The large radius parameter
725 is especially useful for containing the decay products of a boosted Higgs boson, as
726 discussed in Chapter 7. Due to their large size, large- R jets benefit from a grooming
727 procedure called trimming which remove soft contaminants inside the jet [71, 72].
728 Trimming aims to remove jet constituents from pile-up and the underlying event,
729 which helps to improve the jet mass resolution and its robustness to varying levels
730 of pile-up. The jet mass is computed using a combination of information from the
731 calorimeters and ID, and a calibration to data is applied [73].

732 Track-jets

733 Track-jets are built by clustering tracks using the anti- k_t clustering algorithm. They
734 are associated to large- R jets as sub-jets and used to identify large- R jets containing
735 b -hadrons. The radius parameter is allowed to vary with transverse momentum such
736 that a broader cone (up to $R = 0.4$) is used for low- p_T track-jets and a narrower
737 cone (down to $R = 0.02$) for high- p_T track-jets [74, 75]. The narrower cone is better
738 suited to clustering highly collimated jet constituents at high- p_T .

739 Jet Flavour Labels

740 Jet flavour labels are assigned to small- R jets according to the presence of a truth
741 hadron within $\Delta R(\text{hadron}, \text{jet}) < 0.3$ of the jet axis. If a b -hadron is found the jet is
742 labelled a b -jet. In the absence of a b -hadron, if a c -hadron is found the jet is called

⁷⁴³ a c -jet. If no b - or c -hadrons are found, but a τ is found in the jet, it is labelled as a
⁷⁴⁴ τ -jet, else it is labelled as a light-jet.

⁷⁴⁵ PFlow jets are used to train the algorithms discussed in Chapter 5 and Chapter 6.

⁷⁴⁶ Jet Track Association

⁷⁴⁷ Tracks are associated to small- R jets using a ΔR association cone, the width of which
⁷⁴⁸ decreases as a function of jet p_T , with a maximum cone size of $\Delta R \approx 0.45$ for jets
⁷⁴⁹ with $p_T = 20$ GeV and minimum cone size of $\Delta R \approx 0.25$ for jets with $p_T > 200$ GeV.
⁷⁵⁰ If a track is within the association cones of more than one jet, it is assigned to the
⁷⁵¹ jet which has a smaller $\Delta R(\text{track}, \text{jet})$.

⁷⁵² 3.4.4 Leptons

⁷⁵³ Electrons and muons leave characteristic signatures that are picked up in the ECal
⁷⁵⁴ and MS respectively. The reconstruction of both types of charged lepton is briefly
⁷⁵⁵ outlined below.

⁷⁵⁶ Electrons

⁷⁵⁷ A diagrammatic view of electron reconstruction is shown in Fig. 3.13. Electrons
⁷⁵⁸ candidates are reconstructed by matching PV-compatible³ inner detector tracks
⁷⁵⁹ to topological calorimeter clusters. The track-cluster matching criteria takes into
⁷⁶⁰ account the significant energy loss of the electron due to bremsstrahlung. If a match
⁷⁶¹ is found, a refit of the track is performed using the Gaussian Sum Filter (GSF) [76],
⁷⁶² which better handles trajectory reconstruction in the presence of bremsstrahlung.
⁷⁶³ Various identification criteria are then applied to the candidates using a likelihood-
⁷⁶⁴ based (LH) method to improve purity. These include requirements on the track
⁷⁶⁵ quality and cluster matching, the shape of electromagnetic shower in the ECal,
⁷⁶⁶ leakage into the HCal, and the amount of transition radiation detected in the TRT.
⁷⁶⁷ Isolation criteria with respect to other nearby ID tracks and calorimeter clusters may
⁷⁶⁸ also be applied. A full description can be obtained from Ref. [77].

³The ID track associated with the electron is required to satisfy $d_0/s(d_0) < 5$ and $z_0 \sin \theta < 0.5$ mm.

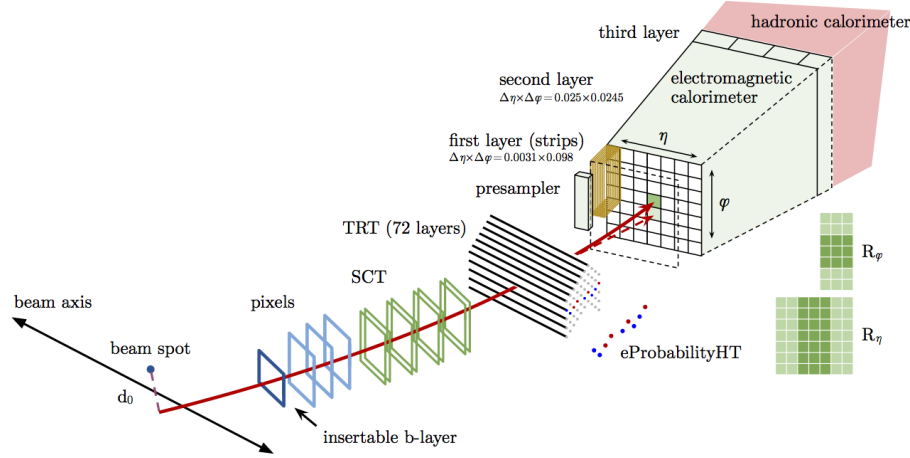


Figure 3.13: A sketch of electron reconstruction using the ATLAS detector [77]. Electron reconstruction makes use of the entire ID and the calorimeters.

769 Muons

770 Muon reconstruction makes use of the dedicated MS (see Section 3.3.3), the tracks
 771 from the ID, and the presence of characteristic signatures in the calorimeters. Muon
 772 tracks (i.e. a track reconstructed in the MS) are reconstructed by connecting straight-
 773 line track segments, which are identified via a Hough transform, and combined into
 774 a approximately parabolic trajectory. Finally, a global χ^2 fit is performed, taking
 775 into account possible interactions between the muon and the detector material. A
 776 reconstructed muon is called *combined* if it can be matched successfully to an to
 777 an ID track. Combined muons undergo a further fit with the combined ID and MS
 778 hits, with the energy loss due to the traversal of the calorimeters being taking into
 779 account.

780 After reconstruction, candidate undergo an identification processes which helps to
 781 efficiently identify prompt muons whilst rejecting background signals (e.g. non-
 782 prompt muons from pion and kaon decays, the punch-through of a hadron from the
 783 calorimeter, or the semi-leptonic decay of a heavy flavour hadron). Combined muon
 784 identification takes into account discrepancies in the p_T and charge measurements
 785 in the MS and ID, and the χ^2 of the combined track fit. Selections on the number
 786 of hits in the ID and MS are also applied. At the medium identification working
 787 point, approximately 96% of prompt muons with $20 \text{ GeV} < p_T < 100 \text{ GeV}$ are

788 successfully identified. On top of the identification requirements, a number of
789 isolation requirements can also be applied to further suppress background signals.

790 More information on muon reconstruction, identification and isolation can be found
791 in Ref. [51].

792 3.4.5 Missing Transverse Momentum

793 An imbalance in the final state transverse momentum can occur as a result of
794 incomplete measurement of the final state particles. In particular, neutrinos are
795 not measured by the detector and contribute to the missing transverse momentum
796 $\mathbf{E}_T^{\text{miss}}$. Incomplete detector acceptance and inaccuracies in the reconstruction of the
797 final state can also contribute to the missing transverse momentum of an event. In
798 order to calculate the missing transverse momentum, the negative vector sum of
799 the momentum of all photons, leptons and small- R jets with $p_T > 20 \text{ GeV}$ is taken.
800 The momenta of tracks associated to the primary vertex are also taken into account.
801 The magnitude of $\mathbf{E}_T^{\text{miss}}$ is written E_T^{miss} . More information about missing transverse
802 momentum reconstruction is provided in [78].

803 3.5 b -tagging Algorithms

804 Many ATLAS analyses rely on flavour tagging, which is the identification of jets
805 containing heavy flavour (HF) hadrons (b -hadrons and c -hadrons) as opposed to
806 those containing only light-flavour hadrons or gluons. In particular, b -tagging is the
807 identification of jets originating only from b -hadrons (i.e. b -jets). Flavour tagging
808 is a critical component of the physics programme of the ATLAS experiment. It is
809 of crucial importance for the study of the Standard Model (SM) Higgs boson and
810 the top quark, which decay preferentially to b -quarks [79, 80], and additionally for
811 several Beyond the Standard Model (BSM) resonances that readily decay to heavy
812 flavour quarks [81].

813 In this section some common definitions used in flavour tagging are given in Sec-
814 tion 3.5.1, followed by a description of the various b -jet identification algorithms
815 (also called *taggers*) used in ATLAS in Sections 3.5.2 and 3.5.3.

816 3.5.1 Common Definitions

817 Each flavour tagging algorithm outputs a discriminant value that can be used to
 818 select jets of the signal flavour. The efficiency of a flavour tagging algorithm is
 819 defined as the fraction of signal jets which are correctly identified by the tagger.
 820 Given N^{signal} signal jets, $N_{\text{tagger}}^{\text{signal}}$ of which have passed the algorithm's selection and
 821 $N_{\text{untagger}}^{\text{signal}}$ of which have not, the efficiency is given by

$$\varepsilon = \frac{N_{\text{tagged}}^{\text{signal}}}{N_{\text{tagged}}^{\text{signal}} + N_{\text{untagged}}^{\text{signal}}}. \quad (3.11)$$

822 Meanwhile the *fake rate* is defined as the efficiency for a background class to be
 823 selected, i.e.

$$\text{fake rate} = \frac{N_{\text{tagged}}^{\text{background}}}{N_{\text{tagged}}^{\text{background}} + N_{\text{untagged}}^{\text{background}}}. \quad (3.12)$$

824 The *rejection power* of the model is quantified for a given background as the reciprocal
 825 of the fake rate, i.e.

$$\text{rejection power} = \frac{1}{\text{fake rate}}. \quad (3.13)$$

826 A *fixed-cut working point* (WP) defines the corresponding selection applied to the
 827 tagging discriminant in order to achieve a given efficiency on the inclusive $t\bar{t}$ sample.

828 3.5.2 Low-level Algorithms

829 The low-level algorithms are the first step in the b -tagging process. They take inputs
 830 information about the jet and its associated tracks and reconstruct distinct features
 831 of the experimental signature of heavy flavour jets. The low-level algorithms are a
 832 combination of manually optimised reconstruction algorithms, for example SV1 and

833 JetFitter which reconstruct displaced decay vertices (see Section 3.4.2) and IPxD
 834 which discriminates based on track IPs, and trained machine learning models such
 835 as RNNIP and DIPS which use IP and hit information from a variable number of
 836 tracks [82, 83].

837 3.5.3 High-level Algorithms

838 The high-level algorithms combine the outputs of the independently optimised low-
 839 level algorithms using a multivariate approach to produce a discriminant value for
 840 each jet. For example the MV2c10 algorithm, used in the analysis described in
 841 Chapter 7, consists of a boosted decision tree which combines the outputs of IPxD,
 842 SV1 and JetFitter [61, 84, 85]. The working point is tuned to achieve an average b -jet
 843 efficiency of 70% on simulated $t\bar{t}$ events. At this efficiency working point, rejection
 844 factors for c -jets and light-jets are approximately 9 and 304 respectively.

845 The current ATLAS flavour tagger, DL1r [85], is part of a series of taggers that
 846 use a deep neural network to combine the outputs of the low-level algorithms. The
 847 low-level algorithms used by the different high-level taggers DL1, DL1r and DL1d is
 848 shown in Fig. 3.14.

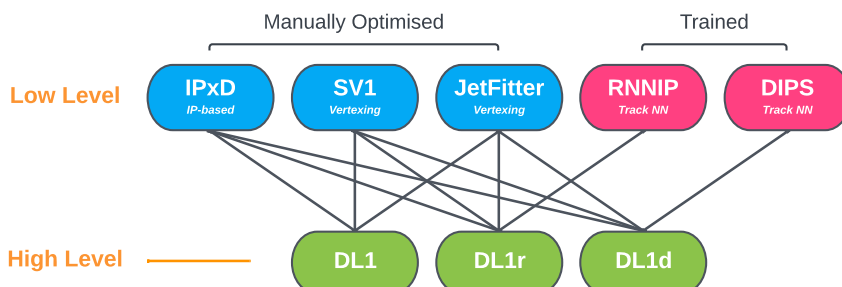


Figure 3.14: An overview of different high and low level taggers used in ATLAS. The low level taggers are IPxD, SV1 and JetFitter, and RNNIP and DIPS [61, 62, 82, 83]. The outputs of these taggers are fed into the high-level taggers DL1, DL1r and DL1d [85, 86].

849 **Chapter 4**

850 **Tracking and Flavour Tagging at
851 High p_T**

852 The various flavour tagging algorithms (introduced in Section 3.5) work by identi-
853 fying the unique signatures of heavy flavour (HF) jets (b - and c -jets). Ultimately,
854 the tagging algorithms use input information about the reconstructed jet and its
855 associated tracks. Successful b -tagging therefore relies on the efficient and accurate
856 track reconstruction, especially for tracks corresponding to the products of HF decays.
857 In this chapter studies investigating the challenges facing track reconstruction and
858 flavour tagging at high- p_T are discussed.

859 The chapter is structured as follows. In Section 4.1 an introduction to the datasets
860 used in this thesis is given. The unique signatures of b -jets are outlined in Section 4.2.
861 A summary of the challenges facing tracking and b -tagging at high transverse mo-
862 mentum is provided in Section 4.2.2. Some preliminary investigations into improving
863 tracking in the high- p_T regime are investigated in Section 4.3. In Section 4.4 the
864 conclusions of this chapter are given.

865 **4.1 Datasets**

866 This thesis makes extensive use of two simulated datasets which are described in this
867 section. The datasets are made up of simulated SM $t\bar{t}$ and BSM Z' events initiated by
868 proton-proton collisions at a center of mass energy $\sqrt{s} = 13$ TeV. The Z' sample is
869 constructed in such a manner that it has a relatively flat jet p_T spectrum up to 5 TeV

and decays democratically to equal numbers of b -, c - and light-jets. The generation of the simulated event samples includes the effect of multiple pp interactions per bunch crossing with an average pile-up of $\langle \mu \rangle = 40$, which includes the effect on the detector response due to interactions from bunch crossings before or after the one containing the hard interaction.

The $t\bar{t}$ events are generated using the POWHEGBox v2 generator [87–90] at next-to-leading order with the NNPDF3.0NLO [91] set of parton distribution functions (PDFs). The h_{damp} parameter¹ is set to 1.5 times the mass of the top-quark (m_{top}) [92], with $m_{\mathrm{top}} = 172.5$ GeV. The events are interfaced to PYTHIA 8.230 [93] to model the parton shower, hadronisation, and underlying event, with parameters set according to the A14 tune [94] and using the NNPDF2.3LO set of PDFs [95]. Z' events are generated with PYTHIA 8.2.12 with the same tune and PDF set. The decays of b - and c -hadrons are performed by EVTGEN v1.6.0 [96]. Particles are passed through the ATLAS detector simulation [97] based on GEANT4 [98].

Jets are required to have a pseudorapidity $|\eta| < 2.5$ and $p_{\mathrm{T}} > 20$ GeV. Additionally, a standard selection using the JVT tagger (see Section 3.4.3) at the tight working point is applied to jets with $p_{\mathrm{T}} < 60$ GeV and $|\eta| < 2.4$ in order to suppress pile-up contamination [66].

4.2 b -hadron Reconstruction

This section outlines the typical detector signature of a b -hadron in Section 4.2.1 and discusses some associated reconstruction difficulties in Section 4.2.2.

4.2.1 Decay Topology

b -hadrons are quasi-stable bound states of a bottom quark and one or more lighter quarks. Collectively, these are the B -mesons (e.g. $B^+ = u\bar{b}$, $B^0 = d\bar{b}$) and baryons (e.g. $\Lambda_b^0 = udb$). After a b -quark is produced as the result of a proton-proton collision, they quickly hadronise. The hadronisation process is hard – around 70–80% of

¹The h_{damp} parameter is a resummation damping factor and one of the parameters that controls the matching of POWHEG matrix elements to the parton shower and thus effectively regulates the high- p_{T} radiation against which the $t\bar{t}$ system recoils.

896 the b -quark's momentum is passed to the b -hadron, with the rest being radiated
 897 as prompt hadronisation or fragmentation particles. See Ref. [99] for a more in
 898 depth discussion on hadronisation and the closely related process of fragmentation.
 899 Henceforth the combined hadronisation and fragmentation products will be referred
 900 to collectively as fragmentation.

901 b -hadrons are interesting objects of study due to their relatively long proper lifetimes
 902 $\tau \approx 1.5$ ps [100]. This lifetime corresponds to a proper decay length $c\tau \approx 450$ μm . In
 903 the rest frame of the detector, the typical b -hadron travels a distance

$$d = \gamma\beta c\tau \approx \gamma c\tau \quad (4.1)$$

904 before decaying, where in the high energy limit $\gamma = E_b/m_b$ and $\beta = v/c = 1$.

905 For a 50 GeV b -hadron, this gives $d \approx 4.5$ mm, which is displaced enough to be
 906 resolved from the primary vertex. Meanwhile for a 1 TeV b -hadron, $d \approx 90$ mm –
 907 well beyond the radius of the first pixel layer (the IBL) which is situated at a radius
 908 of approximately 33 mm from the center of the detector (the distance varies due
 909 to the interleaved structure) Fig. 4.1 shows how the mean decay radius varies as a
 910 function of b -hadron p_T . This significant displacement is characteristic of b -jets and
 911 makes it possible to reconstruct secondary vertices (SV) at the b -hadron decay point.

912 b -hadrons decay weakly to on average four or five collimated stable particles [101].
 913 These particles, along with any other fragmentation particles, are reconstructed in
 914 the detector as a jet. A b -jet has several characteristic features which differentiate it
 915 from light-jets. The primary feature is the presence of a high mass secondary vertex
 916 that is significantly displaced from the primary vertex. Reconstruction of these
 917 vertices from tracks with common points of spatial origin is a common approach
 918 used in the identification of b -jets.

919 Additional signatures of b -hadrons are as follows. Associated tracks and SVs can
 920 have a large transverse impact parameter d_0 as a result of the b -hadron displacement
 921 (as shown in Fig. 4.2). Since it is common for the b -hadron to decay to a c -hadron
 922 with non-negligible lifetime, tertiary vertices can be found within b -jets resulting
 923 from $b \rightarrow c$ decay chains. Additionally, as the b - or c -hadron decays semileptonically
 924 in approximately 40% of cases [16], the presence of a reconstructed electron or muon
 925 inside a jet gives information about the jet flavour.

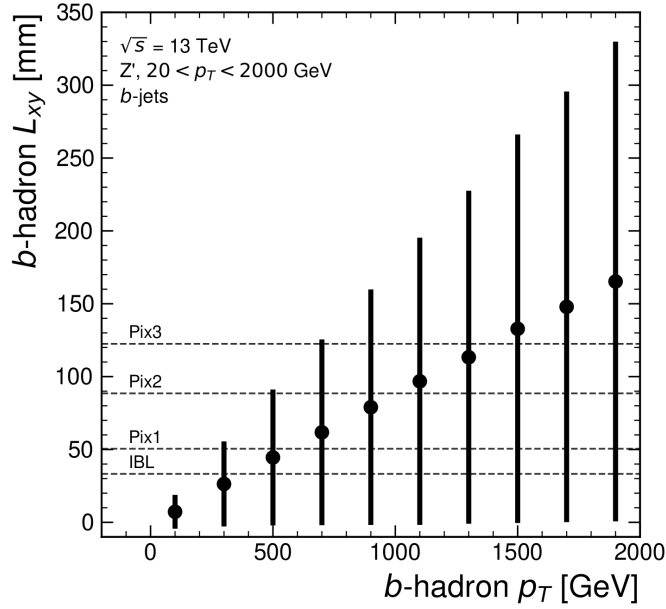


Figure 4.1: The truth b -hadron decay radius L_{xy} as a function of truth transverse momentum p_T for reconstructed b -jets in Z' events. Error bars show the standard deviation. The pixel layers are shown in dashed horizontal lines.

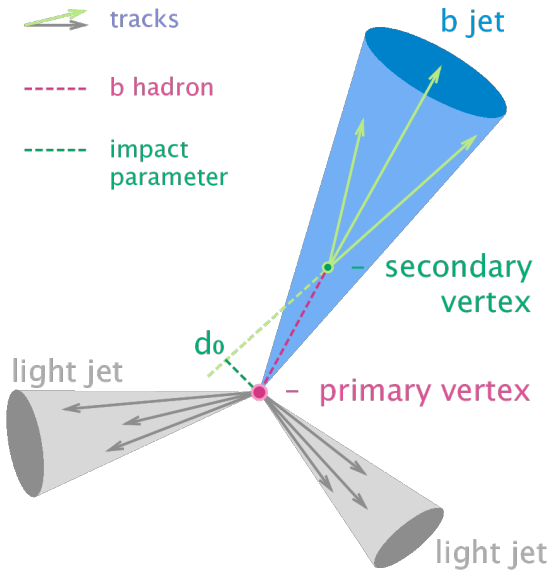


Figure 4.2: Diagram of a typical b -jet (blue) which has been produced in an event alongside two light jets (grey) [102]. The b -hadron has travelled a significant distance (pink dashed line) from the primary interaction point (pink dot) before its decay. The large transverse impact parameter d_0 is a characteristic property of the trajectories of b -hadron decay products.

926 These signatures are primarily identified using tracks associated to jets, or using re-
927 constructed electrons or muons, which also rely on tracks as discussed in Section 3.4.4.
928 As such, efficient and accurate track reconstruction is essential for high performance
929 flavour tagging.

930 **4.2.2 Challenges**

931 As discussed, a necessary requirement for successful b -tagging is the efficient and
932 accurate reconstruction of the charged particle trajectories in the jet. For high p_T
933 jets ($p_T > 200$ GeV) this task becomes difficult due to a combination of effects. As
934 the b -jet energy increases, the multiplicity of the fragmentation products inside the
935 jet increases, while the multiplicity of the products of the weak decay is unaffected.
936 The “signal” tracks (those from the weak decay of the b -hadron) therefore become
937 significantly outnumbered. Both fragmentation and b -hadron weak decay products
938 also become increasingly collimated as their inherited transverse momentum increases.
939 This is compounded by the increased decay length of b -hadrons (and c -hadrons) at
940 high- p_T , which means that the decay products have less of an opportunity to diverge
941 before reaching the first tracking layers of the detector (shown in Fig. 4.3). If the
942 weak decay of the b -hadron takes place close enough to a detector layer, or if the
943 particles are otherwise sufficiently collimated, charge deposits left by nearby particles
944 may not be resolved individually, instead being reconstructed as merged clusters [57].

945 As discussed in Section 3.4.1, merged clusters are generally rare, and so shared
946 hits generally predict bad tracks and are correspondingly penalised during track
947 reconstruction. However, in the core of high p_T b -jets the density of particles is high
948 enough that the probability of cluster merging increases dramatically. Successful
949 reconstruction of such tracks requires the presence of shared hits to be effectively
950 dealt with but in the standard reconstruction the presence of these can end up
951 impairing the successfully reconstruction of the track. Furthermore, decays may also
952 take place inside the tracking detectors themselves, which at best leads to missing
953 measurements on the most sensitive detector layers, and at worst can lead to wrong
954 inner layer hits being added to displaced tracks, since the reconstruction process
955 penalises tracks without inner layer hits.

956 The above effects create two related, but distinct problems for b -tagging. The first
957 part is a drop in track reconstruction efficiency. The presence of shared and missing

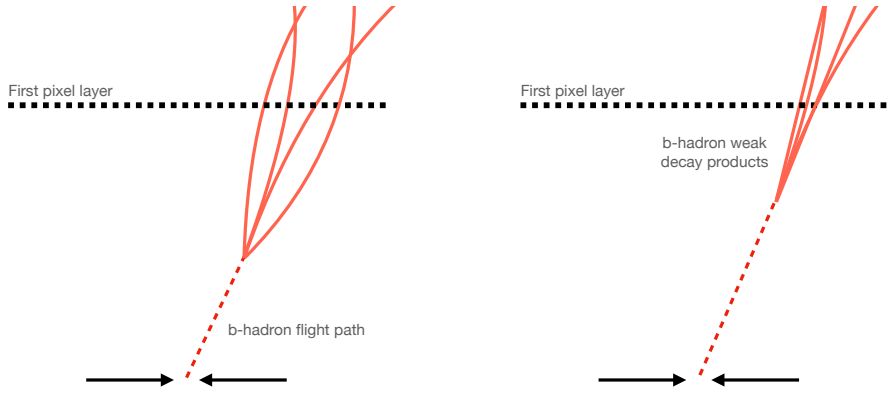


Figure 4.3: At lower p_T (left) the decay length of the b -hadron is on average reduced, and the decay tracks are less collimated. At higher p_T (right) the b -hadron decay length increases and the resulting decay tracks are more collimated and have less distance over which to diverge before reaching detector elements. As a result, the ID may be unable to resolve charged depositions from different particles, resulting merged clusters.

958 hits reduces a track's score in the ambiguity solver meaning that higher ranking, but
 959 potentially worse, track candidates are processed first and take ownership of the hits.
 960 This can make it difficult for otherwise reasonable b -hadron decay tracks to meet
 961 the ambiguity solver's stringent track quality requirements, leading to their rejection
 962 at this stage and an overall decrease in the b -hadron decay track reconstruction
 963 efficiency. As shown in Fig. 4.4, this can result in a large drop in reconstruction
 964 efficiency for b -hadron decay products of up to 50% for at $p_T = 2 \text{ TeV}$.

965 The second part of the problem is that, due to the high multiplicity of clusters
 966 available for assignment in the vicinity of the typical high- p_T b -hadron decay track,
 967 and also given the strong positive bias of the ambiguity solver towards those tracks
 968 with pixel measurements in each layer (especially the innermost IBL measurement),
 969 many b -hadron decay tracks are assigned incorrect inner layer hits. This is only a
 970 problem for those decay products which were produced within the pixel detector
 971 as a result of a significantly displaced b -hadron decay, and so do not have a correct
 972 hit available for assignment. Fig. 4.5 shows the number of hits as a function of the
 973 reconstructed track p_T for fragmentation tracks and tracks from the weak decay
 974 of the b -hadron. The baseline tracks represent the standard reconstruction setup,
 975 while the pseudotracks represent the ideal tracking setup as outlined in Section 3.4.1.
 976 Hit multiplicities on the pseudotracks decrease at high p_T due to the flight of the

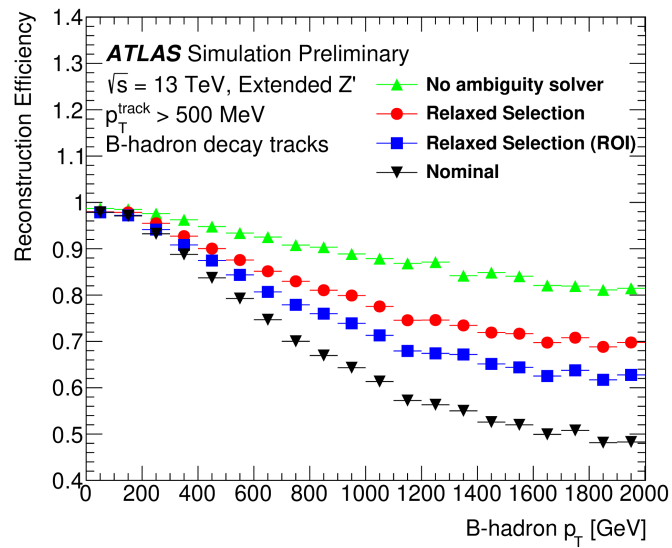


Figure 4.4: b -hadron decay track reconstruction efficiency as a function of truth b -hadron p_T [103]. Nominal track reconstruction is shown in black, while the track reconstruction efficiency for track candidates (i.e. the pre-ambiguity solver efficiency) is shown in green. For high- p_T b -hadrons, the ambiguity solver is overly aggressive in its removal of b -hadron decay tracks. Suggestions for the improvement of the track reconstruction efficiency in this regime by the loosening of cuts in the ambiguity solver are shown in blue and red.

977 b -hadron before its decay. The baseline tracks have more hits than the pseudotracks,
 978 indicating that they are being incorrectly assigned additional hits on the inner layers
 979 of the detector.

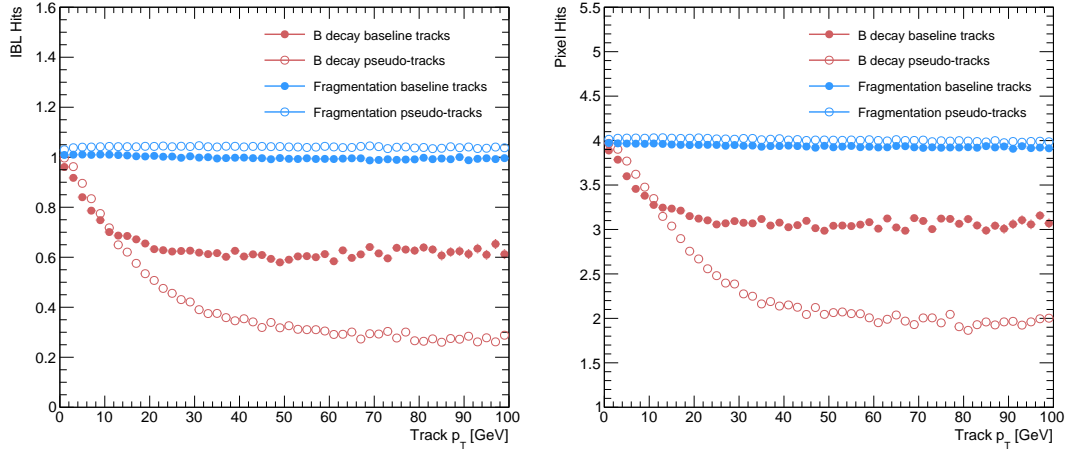


Figure 4.5: Hit multiplicities on the IBL (left) and the pixel layers (right) as a function of the p_T of the reconstructed track for tracks in jets in a Z' sample at $\sqrt{s} = 13$ TeV. Tracks from the weak decay of the b -hadron are shown in red, while fragmentation tracks (which are prompt) are in blue. Baseline tracks are those produced in the standard reconstruction described in Section 3.4.1, while pseudotracks represent the ideal performance of the ATLAS detector and are described in Section 3.4.1.

980 These incorrect hits may skew the parameters of the track, which can in turn lower
 981 the performance of the downstream b -tagging algorithms. In particular, b -tagging
 982 algorithms rely heavily on the transverse impact parameter significance $s(d_0)$ of the
 983 track (see Section 3.2.2). The quality of this measurement is expected to be adversely
 984 affected by wrong inner-layer hits on the track. Furthermore, multiple tracks sharing
 985 an incorrect hit can lead to the creation of spurious secondary vertices, which can
 986 cause further problems for the b -tagging algorithms.

987 The combination of the effects described makes reconstructing tracks in the core
 988 of high p_T b -jets particularly challenging. The reduced reconstruction efficiency of
 989 b -hadron decay tracks and incorrectly assigned hits is thought to be the primary
 990 cause of the observed drop in b -tagging efficiency at high energies, however further
 991 study is required to determine which effect may dominate.

992 4.3 Investigations into High p_T b -hadron Tracking 993 Improvements

994 In Section 4.3.1 pseudotracks, a key tool for studying the ideal tracking performance
995 of the ATLAS detector, are used to study the shared hit requirements on tracks in
996 the dense cores of high- p_T b -jets. Section 4.3.2 details a study which investigated
997 modifying the global track fitter to improve reconstruction performance in this
998 regime.

999 4.3.1 Shared Hits

1000 The ambiguity solver is not run for pseudotracks. However, if the standard track
1001 collection is produced alongside the pseudotracks, then cluster splitting neural
1002 networks will be run for the standard tracks, and the resulting classification of
1003 clusters will be propagated to hits on pseudotracks. This quirk allows one to study
1004 the inefficiencies of the cluster splitting process, and relatedly to determine whether
1005 shared hit cuts in the ambiguity solver are too loose or too tight. The fraction of hits
1006 that are shared for the IBL and the B-layer is shown in Fig. 4.6. The shared hits on
1007 pseudotracks represent correctly assigned hits from merged clusters that were not
1008 able to be classified as split by the cluster splitting neural networks. As such, these
1009 represent the number of shared hits the ambiguity solver should aim to allow given
1010 the current performance of the cluster splitting algorithm. For shared hits on the IBL
1011 for particles produced before the IBL, the baseline selection appears to be successful
1012 in disallowing excessive numbers of shared hits. However, the ambiguity solver fails to
1013 limit shared hits for those particles produced after the IBL, reflecting the previously
1014 discussed problem of displaced tracks picking up incorrect hits. Meanwhile, it is clear
1015 that for the B-layer, the ambiguity solver is being overly aggressive in its rejection of
1016 shared hits.

1017 4.3.2 Global χ^2 Fitter Outlier Removal

1018 As part of the track fit an outlier removal procedure is run in which suspicious hits
1019 are identified and removed. This section documents ongoing studies into improving

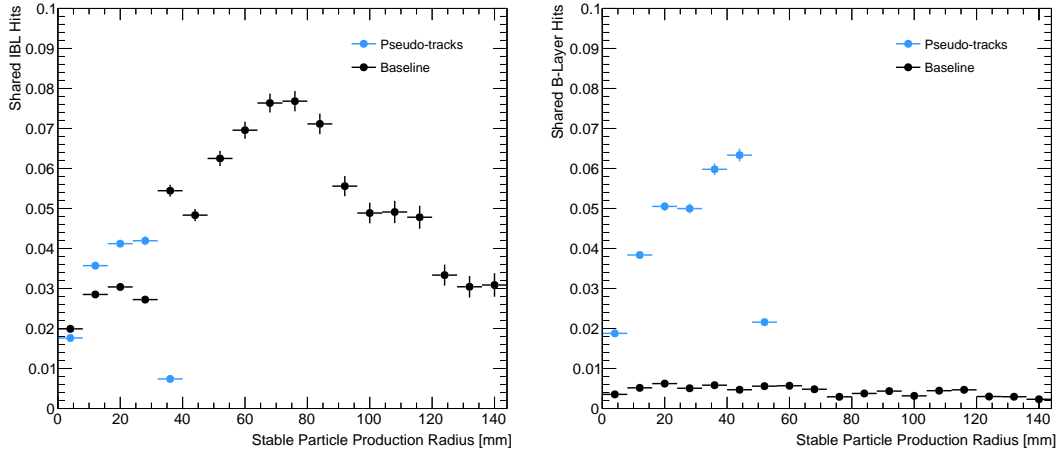


Figure 4.6: The fraction of IBL (left) and B-layer (right) hits which are shared on b -hadron decay tracks as a function of the production radius of the b -hadron decay product for tracks in jets in a Z' sample at $\sqrt{s} = 13$ TeV. Pseudotrack represent the ideal performance given the ATLAS detector, see Section 3.4.1.

1020 hit-to-track assignment by using the Global χ^2 Fitter (GX2F) to identify and prevent
 1021 incorrect hits from being assigned to tracks during the track fit. This is in contrast
 1022 to a previously investigated approach [104] which attempted to identify and remove
 1023 incorrect hits after the reconstruction of the track.

1024 The GX2F code, as a relatively low-level component of track reconstruction, has
 1025 not undergone significant modification for several years, and was originally only
 1026 optimised in the context of prompt, isolated tracks. Since then, a new tracking
 1027 sub-detector, the IBL, was installed. The motivation for looking at the GX2F is that
 1028 this change may require the re-optimisation of the GX2F code, and in particular the
 1029 outlier removal procedure. Further motivation for this approach comes from the low
 1030 rate of labelled outliers in baseline tracking, in contrast to the relatively higher rate
 1031 of tracks with an incorrect IBL hit.

1032 Implementation

1033 The outlier removal procedure for the pixel detector is described in this section.
 1034 The hits on the track are looped over in order of increasing radial distance to the
 1035 beam pipe. For each hit, errors $\sigma(m_i)$ on the measurement of the transverse and
 1036 longitudinal coordinates are calculated. These errors are dependent on the sub-

1037 detector which recorded the measurement (some sub-detectors are more precise than
1038 others). Additionally, a residual displacement $r_i = m_i - x_i$ between the predicted
1039 position of the track x_i (inclusive of the current measurement), and the position of
1040 the hit itself, m_i , is calculated. The pull p_i on the track state due to the current
1041 measurement is calculated according to

$$p_i = \frac{m_i - x_i}{\sqrt{\sigma(m_i)^2 - \sigma(x_i)^2}} \quad (4.2)$$

1042 This pull is computed for the transverse and longitudinal coordinates of the mea-
1043 surement, and the maximum of the two is selected and checked to see if it exceeds
1044 a certain selection threshold. If it does, the hit will be removed if the track also
1045 exceeds a threshold on the total χ^2/n , where n is the number of degrees of freedom
1046 on the track. The results of varying the outlier selection and χ^2/n thresholds are
1047 described below.

1048 Selection Optimisation

1049 A systematic variation of the outlier selection and χ^2/n thresholds has been carried
1050 out. Both thresholds were reduced in fixed step sizes of 0.25 for the outlier selection
1051 threshold and 1 for the χ^2/n threshold. The results for the best performing selections
1052 are discussed below. The value of the outlier selection threshold was reduced from 4
1053 down to 1.75, a change which affects the silicon layers (the TRT has separate outlier
1054 removal logic). Furthermore, a specific cut for the IBL was introduced, and after
1055 optimisation is set to 1.25. The second threshold on the track χ^2/n was also reduced
1056 from 7 to 4. Finally, instead of taking the maximum of the pulls in the longitudinal
1057 and transverse directions, a quadrature sum is taken of these two values and used.
1058 This variation is labelled “Mod GX2F” and was found to improve performance.

1059 The results are shown in Fig. 4.7 and demonstrate a reduction in wrong hit assignment
1060 whilst also improving slightly the rate at which good hits are assigned to tracks. For
1061 a 1 TeV track, the rate to assign good hits to the track increases by approximately
1062 10%, while the rate to assign incorrect hits decreases by approximately 16%. The
1063 improvements are also observed when looking inclusively in all tracks, which avoids
1064 the need for a specific b -jet region-of-interest selection.

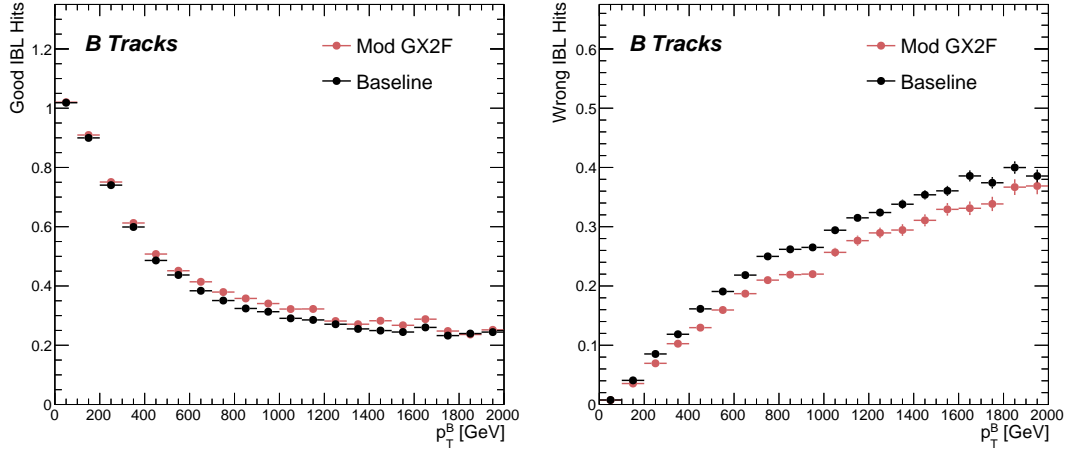


Figure 4.7: The average number of good (left) and wrong (right) IBL hits as a function of b -hadron p_T for tracks using baseline tracking (black) and the modified version of the outlier removal procedure (red).

1065 An improvement, though modest, of all track parameter resolutions and pulls is
 1066 observed. The improvement for the transverse impact parameter pull is shown in
 1067 Fig. 4.8. The results demonstrate an improvement in hit assignment, unchanged
 1068 reconstruction efficiency, and modest improvement in track parameter resolutions
 1069 and pulls. In addition, the truth match probability of tracks is unchanged, suggesting
 1070 that there is no increase in fake track rates. The changes are expected to have a
 1071 negligible impact on computational resources.

1072 4.4 Conclusion

1073 In this section, the difficulties facing efficient and accurate track reconstruction,
 1074 and hence performant b -tagging, have been outlined. The ambiguity solver, which
 1075 attempts to clean or reject tracks which have an excessive number of shared hits,
 1076 is shown to be overly aggressive in the removal of b -hadron decay product track
 1077 candidates. The ambiguity solving process relies on a complicated pre-defined
 1078 selection which has not been optimised for high transverse momentum b -hadron
 1079 track reconstruction. These conclusions have motivated further ongoing studies into
 1080 the improvement of the track reconstruction in dense environments and the high- p_T
 1081 regime, such as those in Ref. [103].

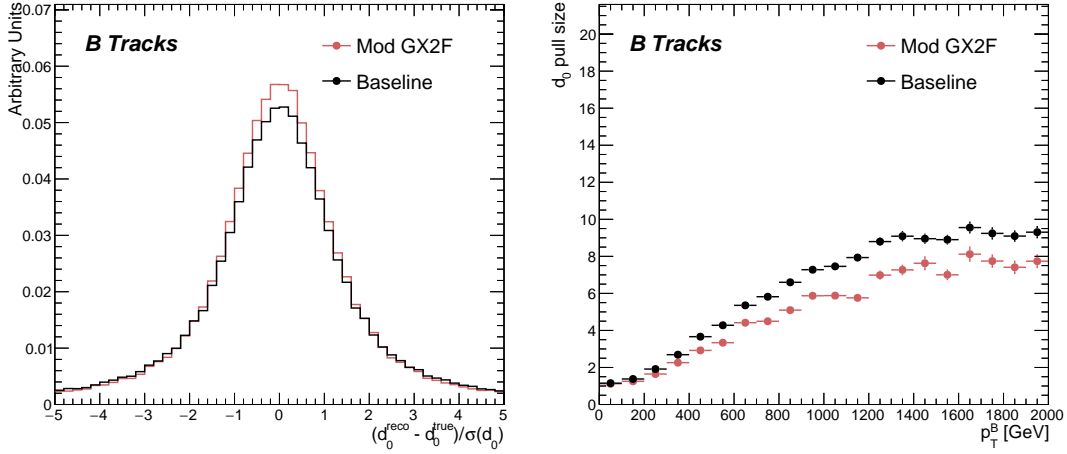


Figure 4.8: (left) b -hadron decay track d_0 pulls ($d_0/s(d_0)$) for baseline and modified GX2F tracks. (right) The absolute value of the d_0 pull as a function of the truth b -hadron transverse momentum.

1082 An optimisation of the outlier removal process in the global χ^2 fitter was carried out.
 1083 The results of the optimisation show that more aggressive removal of outlier hits can
 1084 lead to fewer wrong hits being assigned to tracks, and improvements in the pulls of
 1085 the track parameters.

1086 Future Work

1087 The studies were carried out in Release 21 of the ATLAS software, and need to be
 1088 reproduced using the newer Release 22 to confirm the results against other changes
 1089 in the baseline tracking configuration. It is also necessary to study the impact of
 1090 the improved outlier removal on the downstream b -tagging algorithms. Thanks to
 1091 the all-in-one flavour tagging approach described in Chapter 6, this will in future be
 1092 easier to study.

1093 As there are some known data-MC discrepancies, fine tuned optimisation such as the
 1094 work presented here presents an opportunity to over-optimize the tracking algorithms
 1095 on MC. As such, further studies validating the improved outlier removal procedure
 1096 on data are required.

1097 **Chapter 5**

1098 **Track Classification MVA**

1099 This chapter details work on implementing a multivariate algorithm (MVA) to predict
1100 the truth origin of reconstructed tracks. An introduction to formalisms of machine
1101 learning is given in Section 5.1. In Section 5.2, the truth origin label is defined,
1102 and in Section 5.3 these labels are used to train a machine learning model that can
1103 effectively discriminate between good and fake tracks. Several studies motivated this
1104 work by demonstrating that at high p_T , b -tagging performance was degraded by the
1105 presence of large numbers of poorly reconstructed or fake tracks. If an algorithm
1106 could be trained to detect fake tracks, these could be removed before their input to
1107 the b -tagging algorithms with the aim of improving performance. In addition, other
1108 groups that are sensitive to the presence of fake tracks would also benefit from this
1109 work.

1110 **5.1 Machine Learning Background**

1111 Over the past few decades, machine learning (ML) techniques have become increas-
1112 ingly popular in High Energy Physics experiments due the increased volumes of
1113 high-dimensional data and improvements in the techniques used (in particular deep
1114 learning). Machine learning is the process by which a computer program uses data
1115 to learn suitable parameters for a predictive model. This is opposed to explicitly
1116 providing instructions on how to perform a task. A subfield known as *supervised*
1117 *learning* is used in this work, and consists of exposing a model to a large number of
1118 labelled examples in order to extract relationships between the input data and their

1119 labels. These relationships are often complex, and explicitly programmed rules can
1120 fail to fully capture the relationships between inputs and outputs.

1121 In the simplest case, a set of m labelled training examples $S = \{(x_1, y_1), \dots, (x_m, y_m)\}$
1122 is collected. Each element (x_i, y_i) consists of a input vector $x_i \in \mathbb{R}^{\text{input}}$, and the
1123 corresponding label y_i . In classification problems, these labels are integer *class labels*
1124 $y_i \in \{0, \dots, N - 1\}$, where N is the number of classes, which specify which of a
1125 pre-determined set of categorical classes the training example belongs to. The rest
1126 of the discussion in this chapter is limited to binary classification problems ($N = 2$).
1127 The two classes are often referred to as signal ($y_i = 1$) and background ($y_i = 0$),
1128 which need to be separated. Collecting sufficient and suitable data is one of the
1129 primary challenges of machine learning, as such data is not always readily available.
1130 Fortunately, sophisticated tools to simulate particle collisions have already been
1131 developed by the scientific community [105, 106]. These tools play a key role in
1132 generating a suitably large amount of labelled data which is used to train algorithms.
1133 More detail on the input datasets is given in Section 4.1.

1134 After obtaining suitable training data, the next step is to define a model. Given an
1135 input domain $\mathbb{R}^{\text{input}}$ and an output domain $(0, 1)$, the model $f_\theta : \mathbb{R}^{\text{input}} \rightarrow (0, 1)$ is a
1136 parameterised functional mapping from input space to output space. Given an input
1137 example x_i and a set of parameters θ , the model outputs a prediction $\hat{y}_i \in (0, 1)$ for
1138 the true label y_i , as in

$$f_\theta(x_i) = \hat{y}_i. \quad (5.1)$$

1139 The output \hat{y}_i is in the interval $(0, 1)$ so as to be interpreted as the probability that
1140 the input example x_i belongs to the signal class. The parameters θ of the model are
1141 randomly initialised, and the model is designed to be expressive enough to correctly
1142 map the inputs x_i to the outputs y_i given a reasonable optimisation of the parameters.
1143 To perform this optimisation, the model is then trained, which amounts to showing
1144 the model a series of labelled training examples and modifying the parameters of the
1145 model based on its ability to correctly predict the labels.

5.1.1 Neural Networks

1146 Neural networks (NNs) are a common choice for the machine learning model f since
1148 they have the ability to approximate any function [107] and are easy to train via
1149 backpropagation [108].

1150 Artificial Neurons

1151 The basic functional component of a NN is the *artificial neuron* or node, which is
1152 loosely inspired by a mathematical model of a biological neuron [109, 110]. A diagram
1153 of an artificial neuron is shown in Fig. 5.1. Each neuron is defined by its parameters
1154 or *weights* θ and a choice of activation function. Each neuron takes a fixed number
1155 of inputs and computes the dot product of the input and weight vectors $x^T\theta$ and
1156 additionally adds a constant bias term θ_0 . This term plays the role of a trainable
1157 constant value that is independent of the inputs.

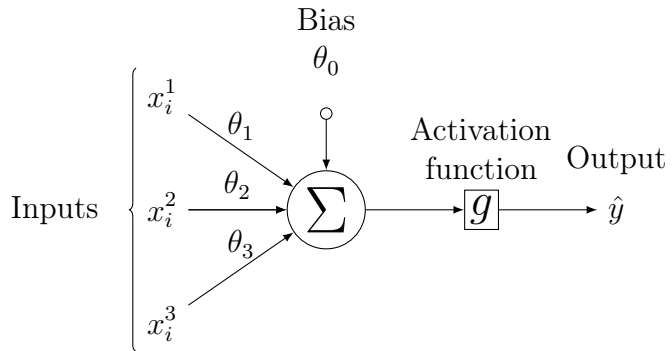


Figure 5.1: A diagram displaying the logical flow of a single neuron with three inputs x_i^j . Each input is multiplied by a weight θ_j , and the resulting values are summed. A bias term θ_0 is added, and the result z is passed to an activation function. Each neuron can be thought of as a logistic regression model.

1158 The output of the dot product and bias term z is fed into an activation function
1159 $g(z)$. The activation function has several uses, most notably acting as a source of
1160 non-linearity and bounding the output of the neuron. Some common activation
1161 functions (sigmoid, tanh, ReLU and SiLU) [111, 112] are shown in Fig. 5.2. The choice
1162 of activation function can have implications for the performance and convergence of
1163 the network, since the gradient of $g(z)$ is used to compute the weight updates during

1164 training. This is also why input data is typically normalised to have zero mean and
1165 unity variance [113].

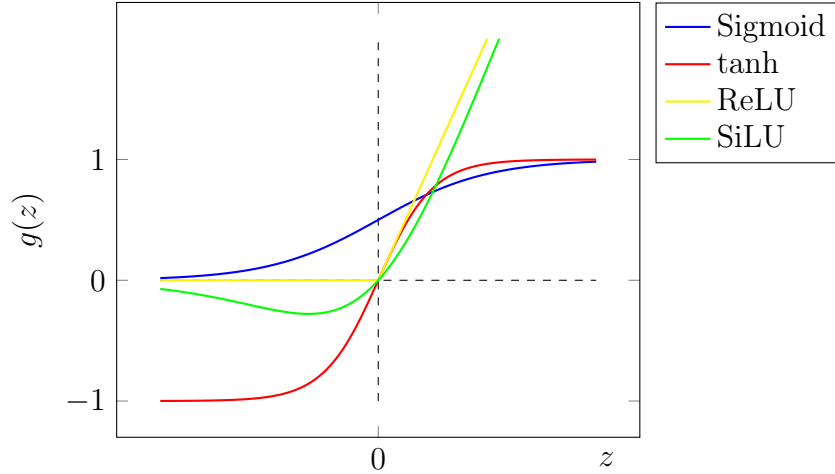


Figure 5.2: The output of several common choices for the activation function $g(z)$ of an artificial neuron. The input z is the output of the dot product between the activation and the weights, plus a bias term.

1166 **Networks**

1167 Several neurons are linked together in layers to form a neural network. The inputs
1168 are propagated layer-by-layer through the network until reaching the final output
1169 layer. The number of layers and neurons per layer are important hyperparameters
1170 (those parameters which are not optimised as part of the training process) which
1171 influence the performance of the model. In the case of binary classification, the final
1172 output layer generally consists of a single neuron with a sigmoid activation

$$g(z) = \frac{1}{1 + e^{-z}}, \quad (5.2)$$

1173 where z is the output from the dot product of the inputs and the weights, plus the
1174 bias term. This value is bounded between zero and one allowing the final output to
1175 be interpreted as the probability that the input sample belongs to the signal class.
1176 NNs have the crucial property of being differentiable functions, which facilitates the
1177 training process described in the next section.

5.1.2 Training with Gradient Descent

A training algorithm is used to optimise the weights and biases of a NN after exposure to the training data. The training algorithm works by minimising a loss function L , which quantifies the error in the model's predictions. NNs are commonly trained using backpropagation in combination with a variant of the stochastic gradient descent algorithm to iteratively update the model parameters. In binary classification problems, the binary cross entropy given in Eq. (5.3) loss is often used.

$$L(x_i, \theta) = y_i \ln[f_\theta(x_i)] + (1 - y_i) \ln[1 - f_\theta(x_i)] \quad (5.3)$$

Since the model f is differentiable, a correction for each parameter θ_i can be computed by taking the partial derivative of L with respect to the parameter. Updated parameters θ'_i are calculated by updating the original parameter in the direction which reduces the loss.

$$\theta'_i = \theta_i - \alpha \frac{\partial L}{\partial \theta_i} \quad (5.4)$$

The hyperparameter α is known as the *learning rate* and dictates the size of the step taken in the direction of the slope. The errors for each parameter are efficiently calculated using the backpropagation algorithm [108]. The process of updating weights is repeated until the weights are judged to have converged, which means the network is trained. In practice, small batches of the input data are shown to the network at a time. For each batch the average loss is calculated and the network's weights are updated. There are many extensions and variations of the gradient descent algorithm. This work uses the Adam optimiser which adds momentum to the weight updates (dampening oscillations) and an adaptive per-parameter learning rate [114].

5.2 Track Truth Origin Labelling

Crucial to supervised learning techniques are the ground truth class labels which the machine learning model is trained to predict. A set of track truth labels which a high degree of granularity have been implemented in the ATLAS software stack, and are listed in Table 5.1. The labelling scheme has been designed to be useful beyond

the classification of good and fake tracks. The origins are determined by analysing the simulated record to determine the physical process that led to the creation of the truth (i.e. simulated) particle which is associated with each reconstructed track. Tracks are associated with truth particles by selecting the particle with the highest *truth-matching probability* (TMP), defined in Eq. (5.5). For a given truth particle, the TMP is a weighted sum of the number of hits on a reconstructed track which are matched to the truth particle N^{match} , divided the total number of hits on the track N^{total} . The weights are sub-detector-dependent and are designed to account for the varying importance of the different ID sub-detectors (based upon their precision) in the reconstruction of a track.

$$\text{TMP} = \frac{10N_{\text{Pix}}^{\text{match}} + 5N_{\text{SCT}}^{\text{match}} + N_{\text{TRT}}^{\text{match}}}{10N_{\text{Pix}}^{\text{total}} + 5N_{\text{SCT}}^{\text{total}} + N_{\text{TRT}}^{\text{total}}} \quad (5.5)$$

For the fake track classification tool, the track truth origins in Table 5.1 are used to construct a binary label by assigning all fake tracks to the background category, and all other tracks as signal. The fake track classifier is then trained to distinguish between these two categories of tracks. Fake tracks are defined using the TMP, with a $\text{TMP} < 0.75$ ¹ giving a track the label of fake. Fake tracks are made up of combinatorial fakes, which are tracks which do not correspond to the trajectory of any truth particle, and poorly reconstructed tracks, which may somewhat resemble the trajectory of a truth particle but due to the presence of some wrong hits on the track will not accurately reproduce the true trajectory. In such cases the fake track can still be identified as having an origin: it is for example possible to have a fake track which is from the decay of a b -hadron.

5.3 Fake Track Identification Tool

The rate of fake tracks increases at high transverse momentum as shown in Fig. 5.3 due to the difficulties in track reconstruction outlined in Section 4.2.2. The performance of b -tagging algorithms is reduced as a direct result of the presence of these tracks as

¹An alternative definition of a fake track as one with $\text{TMP} < 0.5$ is also in use within ATLAS, but 0.75 was used for this study.

Truth Origin	Description
Pile-up	From a pp collision other than the primary interaction
Fake	Created from the hits of multiple particles
Primary	Does not originate from any secondary decay
fromB	From the decay of a b -hadron
fromBC	From a c -hadron decay which itself is from the decay of a b -hadron
fromC	From the decay of a c -hadron which is not from the decay of a b -hadron
OtherSecondary	From other secondary interactions and decays

Table 5.1: Truth origins which are used to categorise the physical process that led to the production of a track. Tracks are matched to charged particles using the truth-matching probability [57]. A truth-matching probability of less than 0.75 indicates that reconstructed track parameters are likely to be mismeasured and may not correspond to the trajectory of a single charged particle. The “OtherSecondary” origin includes tracks from photon conversions, K_S^0 and Λ^0 decays, and hadronic interactions.

1229 shown for SV1 (see Section 3.4.2) in Fig. 5.4, where the efficiency to mistag a light-jet
 1230 decreases by up to 35% at a b -jet efficiency of 35% if such tracks are removed.

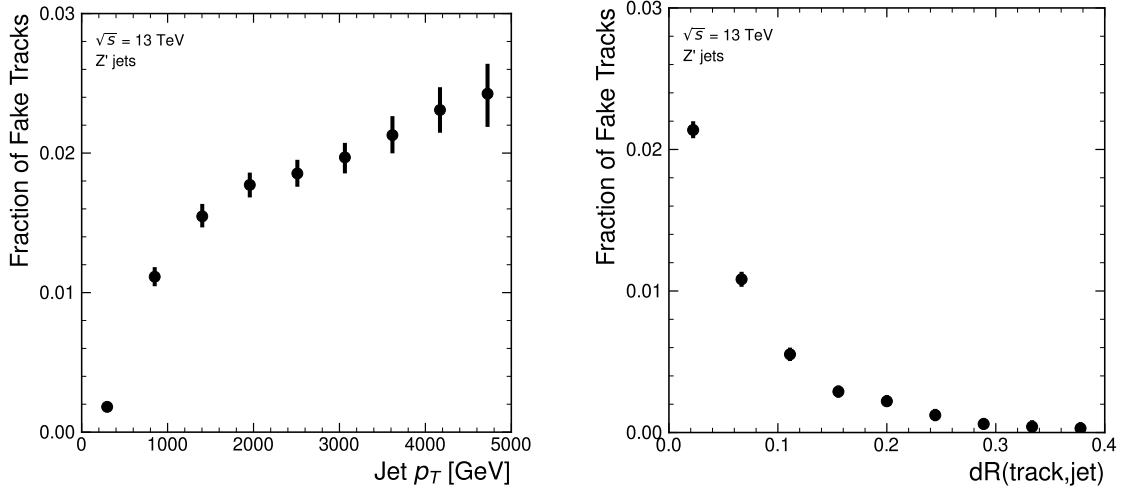


Figure 5.3: Rate of fake tracks as a function of jet transverse momentum (left) and $\Delta R(\text{track},\text{jet})$ (right) for jets in the Z' sample. The rate of fake tracks increases significantly as a function of p_T , and also increases as the distance to the jet axis decreases.

1231 To identify and remove fake tracks, a NN classification tool was trained with all
 1232 non-fake tracks as the signal class and fake tracks as the background class. Inputs to
 1233 the model are described in Section 5.3.1, while fake track removal performance is

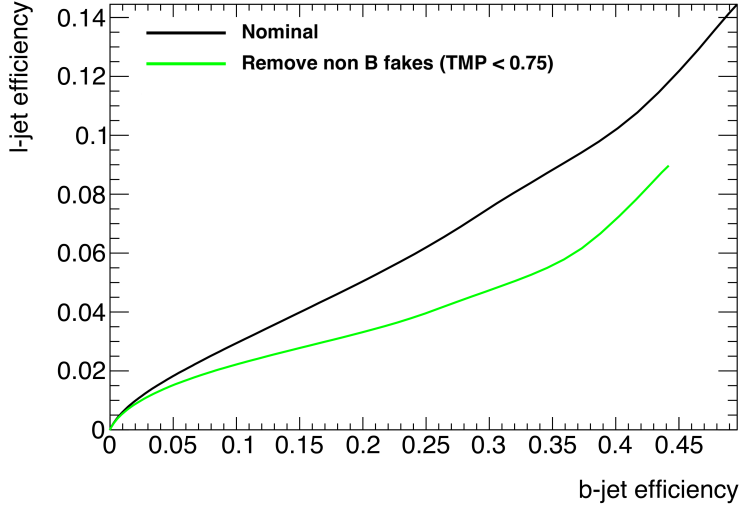


Figure 5.4: The light-jet efficiency of the low level tagger SV1 for jets in the Z' sample with $250 < p_T < 5000$ GeV, as a function of b -jet efficiency. The nominal tracking setup (black) is shown alongside the case where fake tracks which are not from the decay of a b -hadron are removed. The light-jet efficiency is decreased, demonstrating that the presence of fake tracks is detrimental to the algorithm performance.

1234 given in Section 5.3.3. Both models are trained and evaluated using jets from the $t\bar{t}$
 1235 and Z' samples described in Section 4.1

1236 5.3.1 Model Inputs

1237 The fake track MVA is given two jet variables and 20 tracking related variables
 1238 for each track fed into the network. The jet transverse momentum and signed
 1239 pseudorapidity constitute the jet-level inputs, with the track-level inputs listed in
 1240 Table 5.2.

1241 The track parameters and hit pattern are key indicators of whether or not a track
 1242 is fake. The FracRank variable is the ordered index of the tracks that pass the
 1243 ambiguity solver's selection divided by the total number of successfully reconstructed
 1244 tracks in the event. The ambiguity solver processes track candidates iteratively
 1245 in order of an internal score (see Section 3.4.1), and the order in which tracks are
 1246 accepted is preserved. Since tracks with shared hits have lower scores, tracks which
 1247 do not require the removal of shared hits are likely to be processed and accepted

Jet Input	Description
p_T	Jet transverse momentum
η	Signed jet pseudorapidity
Track Input	Description
p_T	Track transverse momentum
ΔR	Angular distance between the track and jet
d_0	Closest distance from the track to the PV in the longitudinal plane
z_0	Closest distance from the track to the PV in the transverse plane
nIBLHits	Number of IBL hits
nPixHits	Number of pixel hits
nSCTHits	Number of SCT hits
nTRTHits	Number of TRT hits
nBLHits	Number of B-layer hits
nIBLShared	Number of shared IBL hits
nIBLSplit	Number of split IBL hits
nPixShared	Number of shared pixel hits
nPixSplit	Number of split pixel hits
nSCTShared	Number of shared SCT hits
r_{first}	Radius of first hit
nDOF	Number of degrees of freedom on the track
FracRank	Ambiguity solver ordering variable

Table 5.2: Input features to the fake track classification NN. Basic jet kinematics, along with information about the reconstructed track parameters and constituent hits are used. Shared hits, are hits used on multiple tracks which have not been classified as split by the cluster-splitting neural networks [57], while split hits are hits used by multiple tracks which have been identified as merged, and therefore split.

1248 earlier on, whereas tracks with shared hits will be processed later and potentially
1249 have their shared hits removed. Hence the FracRank variable gives an indication
1250 of the track quality and how likely it is that hits would have been removed (tracks
1251 processed later on are more likely to have hits removed).

1252 Track selection follows the loose selection described in Ref. [83] and outlined in
1253 Table 3.2, which was found to improve the performance compared to previous tighter
1254 selections, whilst ensuring good resolution of the track’s parameters and a low fake
1255 rate [57]. Inputs are scaled to have a central value of zero and a variance of unity
1256 before training and evaluation.

1257 5.3.2 Model Hyperparameters

1258 Due to the imbalance between the two classes (with fake tracks being relatively
1259 uncommon), a weight was added to the loss function for the background class to
1260 balance their relative weights. The NN was made up of two hidden layers with
1261 220 nodes per layer. The ReLU activation function was used in conjunction with
1262 the Adam optimiser with a learning rate of $1e-3$. Optimisation of the networks
1263 architecture was carried out to ensure optimal performance with a relatively small
1264 number of learnable parameters – 54,000. The model was trained using 40 million
1265 tracks with a further 4 million tracks each used for validation and testing. A full list
1266 of the model hyperparameters is given in Table 5.3.

Hyperparameter	Value
Batch size	2048
Activation	ReLU
Optimiser	Adam
Initial learning rate	$1e-3$
Training epochs	20
Training tracks	40m
Validation tracks	4m
Testing tracks	4m

Table 5.3: Hyperparameter for the track classification model

5.3.3 Results

In order to evaluate the fake track classification tool, a orthogonal test sample of 4 million tracks in jets in the combined $t\bar{t}$ and Z' samples was used. The continuous scalar output from the NN model is interpreted as the probability that a given track is a signal track (i.e. not fake). Fig. 5.5 shows the performance of the fake track classification MVA. The signal and background classes are well separated in the output of the tool. Also shown is a receiver operating characteristic (ROC) curve, which plots the rate of true positives against the rate of false positives over a scan of cut points on the NN output ranging from zero to one. The area under the curve (AUC) gives a summary of the aggregate classification power of the model. The fake track classification tool achieves an AUC of 0.935 for all tracks, which is indicative of a well-performing model. Considering only tracks from b -hadron decays, this value drops slightly to 0.928.

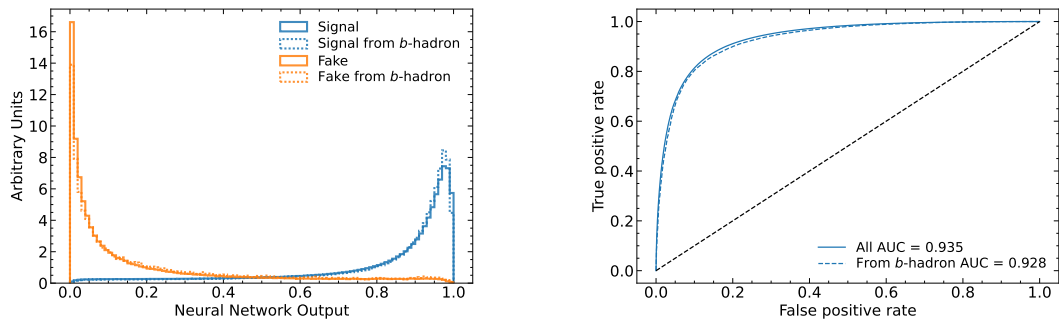


Figure 5.5: (left) Normalised histograms of the fake track classification model output separated for signal and fake tracks, and further separated by those tracks which are from the decay of a b -hadron. (right) The ROC curve for all tracks (solid line) and tracks from the decay of a b -hadron (dashed line). The plots show tracks in the combined $t\bar{t}$ and Z' testing sample. The model is able to successfully discriminate between signal and fake tracks, and shows a very similar performance when looking specifically at tracks from the decay of a b -hadron.

Signal and fake track efficiencies at two different NN output cut points are shown in Table 5.4. The results demonstrate that the tool is effective in retaining 98.8% of signal tracks, while correctly identifying (and therefore enabling the removal of) 45.6% of fake tracks. Table 5.4 also shows that a significant amount of tracks which are labelled as both fake and from the decay of a b -hadron are also removed. This can

1285 happen because fake tracks with $\text{TMP} < 0.75$ are still matched to a truth particle,
1286 which can be the decay product of a b -hadron.

MVA Output Cut	Signal Track Efficiency		Fake Track Efficiency	
	All	From b	All	From b
0.06	98.8%	98.9%	45.6%	39.8%
0.12	97.3%	97.5%	59.4%	53.6%

Table 5.4: Good and fake track selection efficiencies for the combined $t\bar{t}$ and Z' samples. Two working points are defined, cutting on the NN output at 0.06 and 0.12.

1287 5.4 b -hadron Track Identification

1288 After initial tests and investigation, it was found that fake tracks which were the
1289 result of b -hadron decays actually aided b -tagging performance, as demonstrated in
1290 Fig. 5.7. The application of a single tool which removed all fake tracks was therefore
1291 not optimal. A second tool was therefore trained in the same manner as the first,
1292 this one was designed to distinguish between those tracks which were from the decay
1293 of a b -hadron (FromB and FromBC in Table 5.1) and those which were not (all other
1294 truth origins). Fake tracks which were from the decay of a b -hadron were included in
1295 the signal class. The b -hadron decay track MVA was trained using the same setup
1296 as described above, with the same tracks, input variables, and training procedure.
1297 The performance of the model to separate b -hadron decay tracks from other tracks
1298 is shown in Fig. 5.6. Using a selection WP of 0.1, the model can retain 98.5% of
1299 b -hadron tracks and reject 46.2% of tracks not from the decay of a b -hadron. In
1300 Section 5.5, this model is used in conjunction with the fake track identification MVA
1301 to identify and remove fake tracks which are not from the decay of a b -hadron.

1302 5.5 Combined Approach

1303 A 2-dimensional cut was then used to only reject those tracks that had a high
1304 probability of being fake, and also a low probability of being a b -hadron decay track.
1305 The results of the combined approach are provided in Table 5.5, which shows that

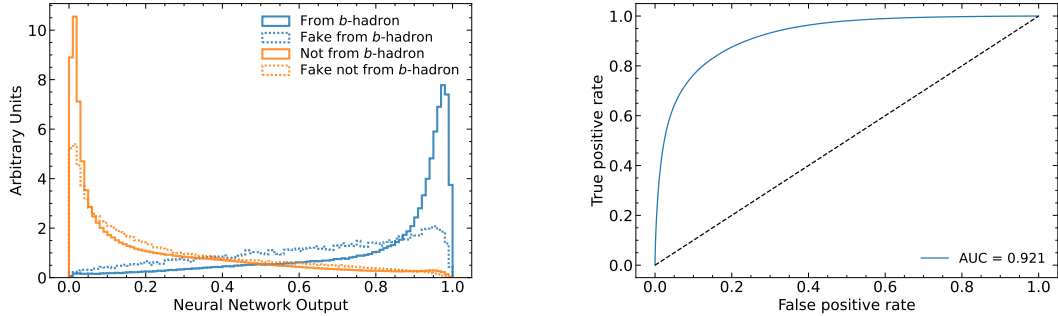


Figure 5.6: (left) Normalised histogram of the b -hadron track identification model output separated for tracks from the decay of a b -hadron and tracks from other sources. The two groups are further separated into those tracks which are fake. (right) The ROC curve for all tracks (solid line). The plots show tracks in the combined $t\bar{t}$ and Z' testing sample.

1306 for the working point “A”, 98.6% of b -hadron decay tracks (both good and fake) are
 1307 retained, while 50.7% of fake tracks which are not from b -hadron decays are rejected.

WP	Fake MVA Cut	b -hadron Decay MVA Cut	Retained b -hadron Tracks	Fake non- b -hadron Tracks Rejected
A	0.5	0.4	98.6%	50.7%
B	0.6	0.5	97.5%	62.0%

Table 5.5: Cut values for the fake and b -hadron decay track MVAs for the two defined working points. Working point “B” cuts more aggressively on the MVA outputs than WP “A”, removing more fake tracks but resulting in an increased loss of signal tracks (which here are all b -hadron decay tracks).

1308 The light-jet efficiency of SV1 is successfully reduced when using the combined tools
 1309 to remove fake tracks that are not from a b -hadron decay, as shown in Fig. 5.7. At a
 1310 b -jet efficiency of 70%, the light-jet mistag rate for jets with $250 < p_T < 400$ GeV
 1311 is reduced from 0.054 to 0.044, a relative improvement of approximately 20%. For
 1312 jets with $400 < p_T < 1000$ GeV the mistage rate drops from 0.1 to 0.08 for a similar
 1313 relative improvement of 20%. The performance of the fake track removal approach
 1314 was also tested for the other low level vertexing algorithm – JetFitter. A similar level
 1315 of improvement in the light-jet mistag rate was observed with a reduction of up to a
 1316 20% reduction for both low- and high- p_T jets in the Z' sample achieved. Together,
 1317 these results demonstrate that by identifying and removing fake tracks which are not

the result of the weak decay of a b -hadron, the performance of the low level tagging algorithms can be improved by an amount which is comparable to the improvement that would be observed if the tracks were selected at truth level1.

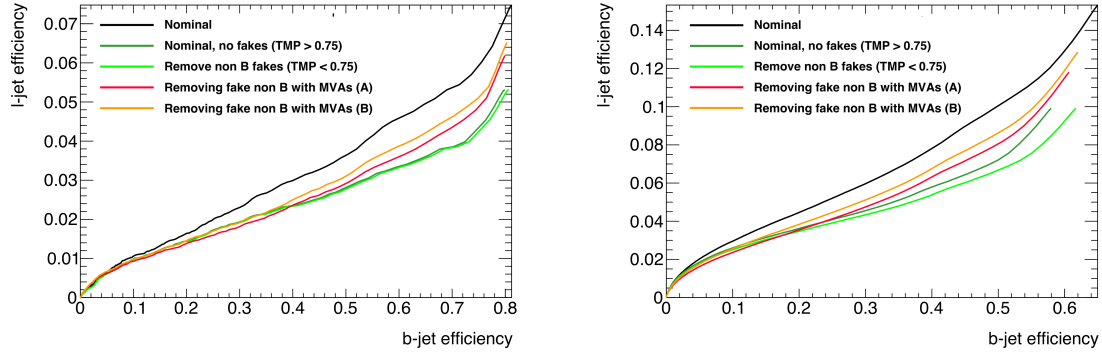


Figure 5.7: The effect of applying the fake track identification algorithm together with the b -hadron decay track identification on the jet tagging performance of SV1 for jets in the Z' sample with $250 \text{ GeV} < p_T < 400 \text{ GeV}$ (left) and $400 \text{ GeV} < p_T < 1 \text{ TeV}$ (right). The nominal SV1 light-jet rejection (black) is compared to two working points of fake track removal, labelled “A” (red) and “B” (orange), which represent two different 2D working points of the track classification tools. Removal of fake tracks based on truth information is shown by the green curves.

5.6 Conclusion

Fake tracks, which are prevalent in the core of high p_T jets, have an adverse impact on b -tagging performance. A ML tool to identify fake tracks has been developed, which can be used to limit the number of fake tracks being input to the b -tagging algorithms. An advantage of the approach is that the continuous output of the model allows for the tuning of good and fake track identification efficiencies. Since it was found that b -hadron decay tracks can also be poorly reconstructed and thus marked as fake, it was deemed necessary also to train a second algorithm to detect b -hadron decay tracks so that the removal of these tracks could be avoided. Removing fake and non- b decay tracks in this way was found to improve the light-jet mistagging rate of SV1 and JetFitter by up to 20% at high transverse momentum. The improvement achieved using the classification tools was in general comparable with that achieved when using the truth information to remove the fake tracks not from the decay of a b -hadron.

1335 Future Work

1336 While removing tracks prior to their input to the low level tagging algorithms is
1337 shown here to be beneficial, a more performant alternative might be to keep these
1338 tracks but label them as being fake (for example using the output of the classification
1339 tool), and allow the tagging algorithms to take this into consideration. This is not
1340 straightforward with manually optimised taggers such as SV1 and JetFitter, but is
1341 possible with more advanced taggers as described in Chapter 6.

1342 Tools which identify the origin of a given track have other potential uses. One
1343 application is to isolate a relatively pure sample of fake tracks which can be used
1344 to estimate the fake track rate in data, which would be useful for estimating the
1345 uncertainty on fake track modelling. Another application is to use the b -hadron
1346 track identification tool to improve the track-to-jet association. Both applications
1347 are currently under investigation.

1348 The approach here works on a track-by-track basis, but a more sophisticated approach
1349 would consider the correlations between the tracks inside a jet. Also left for future
1350 work is to simultaneously train a single tool which discriminates between all the
1351 truth origins listed in Table 5.1. Such a tool would be useful as a general purpose
1352 multiclass classifier. An algorithm which takes both these aspects into consideration
1353 is discussed in Chapter 6.

₁₃₅₄ **Chapter 6**

₁₃₅₅ **Graph Neural Network Flavour
Tagger**

₁₃₅₇ This chapter introduces GN1, a novel ML-based flavour tagging algorithm based on
₁₃₅₈ graph neural networks (GNNs). In Section 6.1, an overview of the approach used
₁₃₅₉ for GN1 is given. An introduction to the theory of GNNs is provided in Section 6.2.
₁₃₆₀ Details of the experimental setup are provided in Section 6.3, while the architecture
₁₃₆₁ of GN1 is specified in Section 6.4.3. In Section 6.4.4, the training procedure is
₁₃₆₂ described, and in Section 6.5 the results are shown.

₁₃₆₃ **6.1 Motivation**

₁₃₆₄ GN1 is a monolithic approach to flavour tagging as illustrated in Fig. 6.1. As opposed
₁₃₆₅ to the existing approach to flavour tagging described in Chapter 4, which relies
₁₃₆₆ on a two tiered approach requiring the use of both low- and high-level algorithms,
₁₃₆₇ GN1 takes as inputs information directly from an unordered variable number of
₁₃₆₈ tracks as input, and predicts the jet flavour without requiring outputs from the
₁₃₆₉ intermediate low-level algorithms. In addition to predicting the flavour of the jet, the
₁₃₇₀ model predicts which physical processes produced the various tracks, and groups the
₁₃₇₁ tracks into vertices. These auxiliary training objectives provide valuable additional
₁₃₇₂ information about the contents of the jet and enhance the performance of the primary
₁₃₇₃ flavour prediction task. The use of GNNs offers a natural way to classify jets with

1374 variable numbers of unordered associated tracks (see Section 6.2), while allowing for
1375 the inclusion of auxiliary training objectives [2, 115].

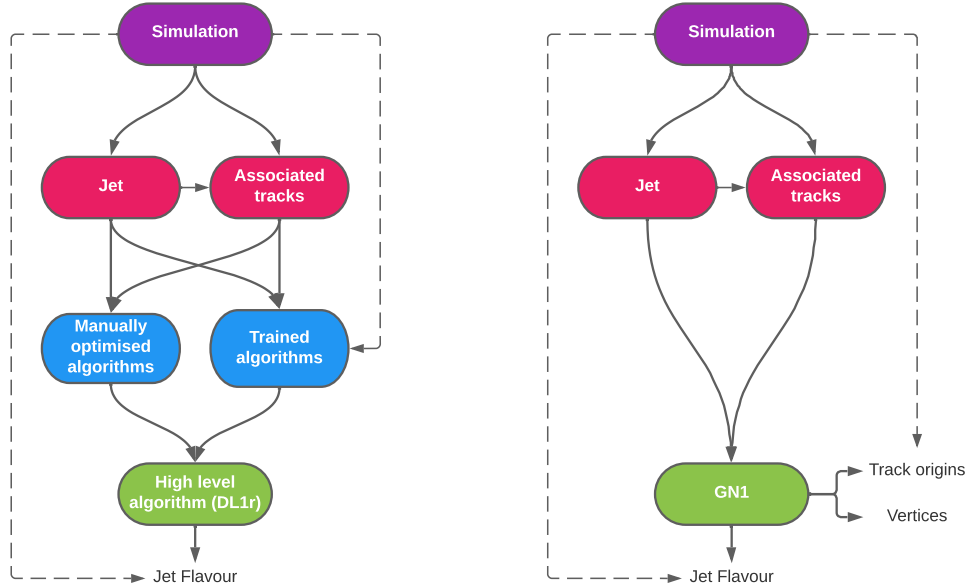


Figure 6.1: Comparison of the existing flavour tagging scheme (left) and GN1 (right). The existing approach utilises low-level algorithms (shown in blue), the outputs of which are fed into a high-level algorithm (DL1r). Instead of being used to guide the design of the manually optimised algorithms, additional truth information from the simulation is now being used as auxiliary training targets for GN1. The solid lines represent reconstructed information, whereas the dashed lines represent truth information [3].

1376 The current flavour tagging algorithms utilise a two-tired approach, with five low
1377 level algorithms feeding intermediate features into the high-level tagger DL1r, which
1378 outputs variables which discriminate between the different jet flavours. In contrast
1379 GN1 consists of only a single neural network, which takes the tracks as inputs along
1380 with some kinematic information about the jet. As a result, it does not depend on
1381 the outputs of any other flavour tagging algorithm. A simple training of the model
1382 fully optimises its parameters, representing a significant simplification with respect to
1383 the optimisation procedure for DL1r. This is particularly important when optimising
1384 the tagger for new regions of phase space (e.g. c -tagging or high- p_T b -tagging), or
1385 when the detector is upgraded or the charged particle reconstruction or selection
1386 algorithms are re-optimised.

1387 GN1 is trained to learn about the internal structure of the jet through the use of two
1388 auxiliary training objectives: the prediction of the underlying physics process from
1389 which each track originated, and the grouping of tracks originating from a common
1390 spatial position (i.e. a common vertex). These auxiliary objectives are meant to
1391 guide the neural network towards a more complete understanding of the underlying
1392 physics inside the jet, thereby removing the need for the low-level algorithms, which
1393 previously contained information about the underlying physics in their design. The
1394 training targets for the primary and auxiliary objectives are extracted from truth
1395 information, as opposed to reconstructed quantities available in both collision data
1396 and simulation.

1397 In this chapter, the following advantages of the GN1 approach will be demonstrated:

- 1398 1. GN1 boasts improved performance with respect to the current ATLAS flavour
1399 tagging algorithms, with significantly larger background rejection rates for a
1400 given signal efficiency. Alternatively the rejection rates can be kept fixed for a
1401 substantial increase in signal efficiency, in particular at high- p_T .
- 1402 2. The same network architecture can be easily optimised for a wider variety of
1403 use cases (e.g. c -jet tagging and high- p_T jet tagging) since there are no low-level
1404 algorithms to retune.
- 1405 3. There are fewer algorithms to maintain.
- 1406 4. Alongside the network's prediction of the jet flavour, the auxiliary vertex and
1407 track origin predictions provide more information on why a jet was (mis)tagged
1408 or not. This information can also have uses in other applications, for instance
1409 to explicitly reconstruct displaced decay vertices or to remove fake tracks.¹

1410 6.2 Graph Neural Network Theory

1411 Graph neural networks are a more sophisticated neural network model (see Sec-
1412 tion 5.1.1) that are designed to operate on graph structured data. A brief introduction
1413 to GNNs is provided in this section following the formalism in Ref. [116].

¹A fake track is defined in this chapter as a track with a truth-matching probability less than 0.5, where the truth-matching probability is defined in Ref. [57].

1414 A graph \mathcal{G} consists of a set of N^n nodes $\mathcal{N} = \{h_i\}_{i=1:N^n}$, a set of N^e edges $\mathcal{E} =$
1415 $\{e_i\}_{i=1:N^e}$, and a global representation u . Each node represents an individual object,
1416 and edges are directed connections between two nodes, called the *sender* and *receiver*
1417 nodes. The connectivity of the graph therefore encodes information about the
1418 relationships between objects that exist in the graph.

1419 A single graph network layer consists of three separate update functions ϕ^e , ϕ^h and
1420 ϕ^u one for each of the nodes, edges, and global graph representation, and similarly
1421 three aggregation functions $\rho^{e \rightarrow h}$, $\rho^{e \rightarrow u}$ and $\rho^{h \rightarrow u}$. The aggregation functions combine
1422 information across different edges or nodes for input into the update functions,
1423 which produce new representations for the nodes, edges and global objects based on
1424 the information in the previous layer and the aggregated information. The update
1425 functions are typically each implemented as a dense feedforward neural network (as
1426 described in Section 5.1.1). The edges e_i are updated by a edge network ϕ^e as in

$$e'_i = \phi^e(e_i, h_s, h_r, u), \quad (6.1)$$

1427 where h_s and h_r are the sender and receiver nodes respectively. The nodes are
1428 updated with a node network ϕ^h as in

$$h'_i = \phi^h(\bar{e}'_i, h_i, u), \quad (6.2)$$

1429 where $\bar{e}'_i = \rho^{e \rightarrow h}(E'_i)$, and E'_i is the set of sender nodes for receiver node h_i . $\rho^{e \rightarrow h}$ is
1430 referred to as the edge aggregation function. The global representation is updated
1431 using the global network ϕ^u as in

$$u' = \phi^u(\bar{e}', \bar{h}', u), \quad (6.3)$$

1432 where \bar{e}' is the aggregation $\rho^{e \rightarrow u}$ over all updated edges e'_i and \bar{h}' is the aggregation
1433 $\rho^{h \rightarrow u}$ over all updated nodes h'_i .

1434 The graph network layer performs a graph convolution, in an analogous way to a
1435 convolutional neural network operating on a grid of pixels. The above description
1436 is general, and not all concrete implementations of GNNs need to implement every
1437 aspect. For example, the global graph representation need not be present, and
1438 it is also possible that no dedicated edge features are present. In such cases the
1439 corresponding update and aggregation functions are not needed. Fig. 6.2 shows two

1440 possible graph network update layers. The layer used in the GN1 model is specified
1441 in more detail in Section 6.4.3.

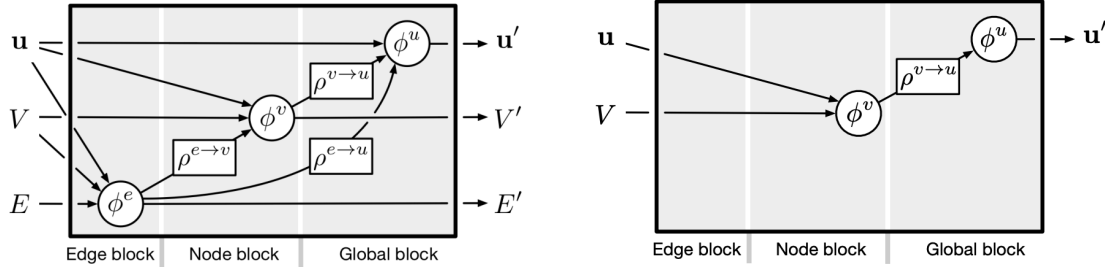


Figure 6.2: The flow of information through a graph neural network layer for (left) a full implementation of the layer and (right) a deep sets model [117]. Reproduced from Ref. [116].

1442 6.3 Experimental Setup

1443 6.3.1 Datasets

1444 The datasets used to train the GN1 tagger are the same as described in Section 4.1.
1445 The training dataset contains 30 million jets, 60% of which are $t\bar{t}$ jets and 40% of
1446 which are Z' jets. In order to evaluate the performance of the model during training,
1447 a statistically independent validation set of 500k jets from both the $t\bar{t}$ and Z' samples
1448 are used. For the testing of the model and the creation of the performance plots,
1449 a further 1 million independent testing jets from each of the $t\bar{t}$ and Z' samples are
1450 used. Before being fed into the model, the track- and jet-level inputs are normalised
1451 to have a mean of zero and a variance of unity. The jet flavour labels are assigned
1452 as described in Section 3.4.3. Truth labelled b -, c - and light-jets are kinematically
1453 re-sampled in p_T and η to ensure identical distributions in these variables.

1454 6.4 Model Architecture

1455 6.4.1 Model Inputs

1456 As inputs, GN1 is fed two kinematic jet variables and an unordered set of up to 40
1457 tracks which have been associated to the jet. If more than 40 tracks are associated
1458 to a given jet, only the first 40 tracks with the largest transverse IP significance $s(d_0)$
1459 (see Section 3.2.2) are fed into the model as inputs. Each track is characterised by 21
1460 variables as detailed in Table 6.1. The kinematic jet variables are the jet transverse
1461 momentum and signed pseudorapidity. For each track, variables containing the
1462 track parameters and uncertainties, and detailed information on the hit content are
1463 provided as inputs to the model.

1464 Dependence of the model on the absolute value of the azimuthal jet angle ϕ is
1465 explicitly removed by providing only the azimuthal angle of tracks relative to the jet
1466 axis. The track pseudorapidity is also provided relative to the jet axis.

1467 Since heavy flavour hadrons can decay semileptonically approximately 40% of the time,
1468 the presence of a reconstructed lepton in the jet carries discriminating information
1469 about the jet flavour. To exploit this, a variant of GN1 called GN1Lep is trained in
1470 addition to the baseline model. The GN1Lep variant is identical to the baseline model,
1471 except for the inclusion an additional track-level input, leptonID, which indicates
1472 if the track was used in the reconstruction of an electron, a muon or neither. The
1473 variable is signed by the charge of the reconstructed lepton. The leptons used in the
1474 definition of the leptonID variable are required to satisfy basic quality requirements.
1475 The muons are required to be combined [118], and the electrons are required to pass
1476 the *VeryLoose* likelihood-based identification working point [119].

1477 The selections applied to the tracks, outlined in Table 3.2, is the same as that used
1478 for the fake track classification MVA described in Chapter 5. However, Section 6.6.1
1479 demonstrates that further relaxation of the track selection requirements may be
1480 warranted.

Jet Input	Description
p_T	Jet transverse momentum
η	Signed jet pseudorapidity
Track Input	Description
q/p	Track charge divided by momentum
$d\eta$	Pseudorapidity of the track, relative to the jet η
$d\phi$	Azimuthal angle of the track, relative to the jet ϕ
d_0	Closest distance from the track to the PV in the longitudinal plane
$z_0 \sin \theta$	Closest distance from the track to the PV in the transverse plane
$\sigma(q/p)$	Uncertainty on q/p
$\sigma(\theta)$	Uncertainty on track polar angle θ
$\sigma(\phi)$	Uncertainty on track azimuthal angle ϕ
$s(d_0)$	Lifetime signed transverse IP significance
$s(z_0)$	Lifetime signed longitudinal IP significance
nPixHits	Number of pixel hits
nSCTHits	Number of SCT hits
nIBLHits	Number of IBL hits
nBLHits	Number of B-layer hits
nIBLShared	Number of shared IBL hits
nIBLSplit	Number of split IBL hits
nPixShared	Number of shared pixel hits
nPixSplit	Number of split pixel hits
nSCTShared	Number of shared SCT hits
nPixHoles	Number of pixel holes
nSCTHoles	Number of SCT holes
leptonID	Indicates if track was used to reconstruct an electron or muon

Table 6.1: Input features to the GN1 model. Basic jet kinematics, along with information about the reconstructed track parameters and constituent hits are used. Shared hits, are hits used on multiple tracks which have not been classified as split by the cluster-splitting neural networks [57], while split hits are hits used on multiple tracks which have been identified as merged. A hole is a missing hit, where one is expected, on a layer between two other hits on a track. The track leptonID is an additional input to the GN1Lep model [3].

6.4.2 Auxiliary Training Objectives

In addition to the jet flavour classification, two auxiliary training objectives are defined. The first auxiliary objective is the prediction of the physical process that gave rise to each track within the jet (i.e. the track origin), while the second is the prediction of track-pair vertex compatibility. Each auxiliary training objective comes with a training target which, similar to the jet flavour label, is a truth labels derived from the simulation. The presence of the auxiliary training objectives improves the jet classification performance as demonstrated in Section 6.5.3.

For the track origin prediction objective, each track is labelled with one of the exclusive categories defined in Table 5.1 of Section 5.2 after analysing the particle interaction (or lack thereof) which led to its formation. Since the presence of different track origins is strongly related to the flavour of the jet, training GN1 to recognise the origin of the tracks provides an additional handle on the classification of the jet flavour. This task may also aid the jet flavour prediction by acting as a form of supervised attention [120] - in detecting tracks from heavy flavour decays the model may learn to pay more attention to these tracks.

The vertexing auxiliary objective makes use of the fact that displaced decays of b - and c -hadrons lead to secondary and tertiary vertices inside the jet, as described in Section 4.2.1. The presence of displaced secondary vertices is not a completely clean signal of a heavy flavour jet, as displaced secondary vertices can also occur in light-jets as a result of material interactions, conversions, and long-lived particle decays (e.g. K_S^0 and Λ^0). For this objective, GN1 predicts a binary label for each pair of tracks in the jet. The label has a value of 1 if the truth particles associated with the two tracks in the pair originated from the same spatial point, and 0 otherwise. To derive the corresponding truth labels for training, truth production vertices within 0.1 mm are merged. Track-pairs where one or both of the tracks in the pair have an origin label of either Pile-up or Fake are assigned a label of 0. Using the pairwise predictions from the model, groups of tracks that have common compatibility can be formed, resulting in the identification of vertices. Two existing low-level tagging algorithms, SV1 and JetFitter (introduced in Section 3.4.2), are currently used to find and reconstruct vertices inside jets and are used as inputs to the existing jet flavour tagger DL1r. The addition of this auxiliary training objective removes the need for inputs from a dedicated secondary vertexing algorithm.

1514 Both of the auxiliary training objectives described here can be considered as “stepping
1515 stones” on the way to classifying the flavour of the jet. By requiring the model to
1516 predict the truth origin of each track and the vertex compatibility of each track-pair,
1517 the model is guided to learn representations of the jet which are connected to the
1518 underlying physics and therefore relevant for classifying the jet flavour.

1519 **6.4.3 Architecture**

1520 A coarse optimisation of the network architecture hyperparameters (for example
1521 number of layers and number of neurons per layer) has been carried out in order
1522 to maximise the flavour tagging performance, but it is likely that further dedicated
1523 optimisation studies could lead to further performance improvements.

1524 The model architecture builds on a previous implementation of a GNN-based jet
1525 tagger [115]. The previous approach was comprised of two separate graph neural
1526 networks with the auxiliary tasks being performed at an intermediate stage after the
1527 first and before the second. This two stage approach was found to be unnecessary and
1528 as such GN1 simplifies the architecture into a single graph neural network with the
1529 auxiliary tasks being performed at the end, alongside the primary jet classification
1530 task. GN1 makes use of a more sophisticated graph neural network layer [121],
1531 which is described in more detail below. The changes significantly improved tagging
1532 performance and also led to a significant reduction in training time.

1533 As inputs, the model takes information about the jet and a number of associated
1534 tracks, as detailed in Section 6.4.1. The jet variables are concatenated with the
1535 variables for each track as shown in Fig. 6.3. The combined jet-track input vectors
1536 are then fed into a per-track initialisation network with three hidden layers, each
1537 containing 64 neurons, and an output layer with a size of 64, as shown in Fig. 6.4. The
1538 track initialisation network is similar to a deep sets model [117], but does not include
1539 a reduction operation (mean or summation) over the output track representations.
1540 The initialisation network allows for initial per-track input processing without the
1541 associated parameter count cost of the graph convolutional layers described below.

1542 The outputs of the track initialisation network are used to populate the nodes of a
1543 fully connected graph, such that each node in the graph neighbours every other node.
1544 Each node h_i in the graph corresponds to a single track in the jet, and is characterised

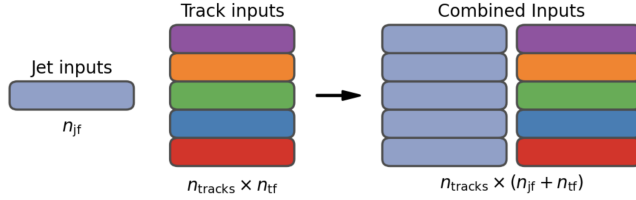


Figure 6.3: The inputs to GN1 are the two jet features ($n_{jf} = 2$), and an array of n_{tracks} , where each track is described by 21 track features ($n_{tf} = 21$). The jet features are copied for each of the tracks, and the combined jet-track vectors of length 23 form the inputs of GN1 [3].

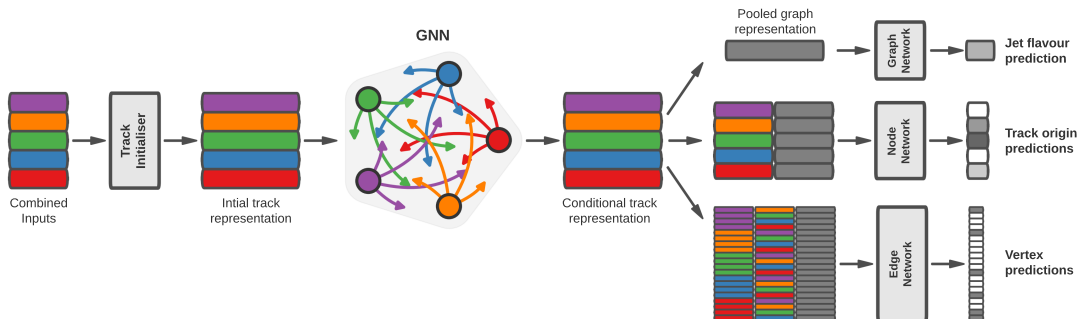


Figure 6.4: The network architecture of GN1. Inputs are fed into a per-track initialisation network, which outputs an initial latent representation of each track. These representations are then used to populate the node features of a fully connected graph network. After the graph network, the resulting node representations are used to predict the jet flavour, the track origins, and the track-pair vertex compatibility [3].

1545 by a feature vector, also called a representation. The per-track output representations
 1546 from the initialisation networks are used as the initial feature vectors of each node
 1547 in the graph. In each layer of the graph network, output node representations h'_i
 1548 are computed by aggregating the features of h_i and neighbouring nodes \mathcal{N}_i using
 1549 a multi-head attention mechanism ($n = 2$) as described in Ref. [121, 122]. First,
 1550 the feature vectors of receiver and sender nodes are fed into two fully connected
 1551 linear layers \mathbf{W}_r and \mathbf{W}_s , to produce an updated representation for each sender and
 1552 receiver node $\mathbf{W}_r h_i$ and $\mathbf{W}_s h_j$. These updated feature vectors are used to compute
 1553 edge scores $e(h_i, h_j)$ for each node pair, as in

$$e(h_i, h_j) = \mathbf{a} \cdot \theta [\mathbf{W}_r h_i + \mathbf{W}_s h_j], \quad (6.4)$$

1554 where, θ is a non-linear activation function, and \mathbf{a} is a learned vector. These edge
 1555 scores are then used to calculate attention weights a_{ij} for each pair of nodes using
 1556 the softmax function over the edge scores

$$a_{ij} = \text{softmax}_j [e(h_i, h_j)]. \quad (6.5)$$

1557 Finally, the updated representations for the receiver nodes h'_i are computed by taking
 1558 the weighted sum over each updated node representation $\mathbf{W}_r h_i$, with weights a_{ij}

$$h'_i = \sigma \left[\sum_{j \in \mathcal{N}_i} a_{ij} \cdot \mathbf{W}_r h_j \right]. \quad (6.6)$$

1559 The set of operations described above constitute a single graph network layer. Three
 1560 such layers are stacked to construct the graph network, representing a balance
 1561 between achieving good performance in a reasonable time and avoiding overtraining
 1562 due to inflation of the parameter count of the model. The final output from the graph
 1563 neural network is a set of per-node (i.e. per-track) feature vectors that are conditional
 1564 representations of each track given the other tracks in the jet. In order to perform

the jet flavour prediction, a flattened global representation of the jet is needed. To produce this, the output track representations are combined using a weighted sum, where the weights are learned during training and therefore act as a form of attention over the different tracks. The flattened outputs from the sum are then fed into a fully connected feedforward neural network with four layers and three outputs, one for each jet flavour. Two other separate fully connected feedforward neural networks are then also used to independently perform the auxiliary classification objectives of GN1. A summary of the different classification networks used for the various training objectives is shown in Table 6.2.

Network	Hidden layers	Output size	Label
Node classification network	128, 64, 32	7	Track origin
Edge classification network	128, 64, 32	1	Track-pair compatibility
Graph classification network	128, 64, 32, 16	3	Jet flavour

Table 6.2: A summary of GN1’s different classification networks used for the various training objectives, adapted from Ref. [3]. The hidden layers column contains a list specifying the number of neurons in each layer. ReLU activation is used through the network [111].

The node classification network predicts the track truth origin as defined in Table 5.1. This network takes as inputs the features from a single output node from the graph network and the global representation of the jet. The node network has three hidden layers containing 128, 64 and 32 neurons respectively, and an output size of seven, corresponding to the seven different truth origins defined in Table 5.1.

The edge classification network is used to predict whether the tracks in the track-pair belong to a common vertex. This network takes as inputs the concatenated representations from each pair of tracks and the global jet representation. Similar to the node network, the edge network has three hidden layers containing 128, 64 and 32 neurons respectively, and a single output, which is used to perform binary classification of the track-pair compatibility. The output predictions for the two auxiliary networks are used for the auxiliary training objectives discussed in Section 6.4.2.

Finally, the graph classification network is used to predict the jet flavour. This network takes only the global jet representation as input. The graph classification

1589 network is comprised of four fully connected hidden layers with 128, 64, 32 and 16
1590 neurons respectively, and has three outputs corresponding to the b -, c - and light-
1591 jet classes. To obtain probability outputs for each task, the outputs from each
1592 classification network are passed through a softmax function.

1593 6.4.4 Training

1594 The full GN1 training procedure minimises the total loss function L_{total} , defined as

$$L_{\text{total}} = L_{\text{jet}} + \alpha L_{\text{vertex}} + \beta L_{\text{track}}. \quad (6.7)$$

1595 This loss is composed of three terms: L_{jet} , the categorical cross entropy loss over the
1596 different jet flavours; L_{vertex} , the binary track-pair compatibility cross entropy loss;
1597 and L_{track} , the categorical cross entropy loss for the track origin prediction. L_{vertex} is
1598 computed via a weighted average over all intra-jet track-pairs in the batch, and L_{track}
1599 is computed by a weighted average over all tracks in the batch, where the weights
1600 are described below.

1601 The different losses converge to different values during training, reflecting differences
1602 in the relative difficulty of the various training objectives. The values of L_{vertex} and
1603 L_{track} are weighted by $\alpha = 1.5$ and $\beta = 0.5$ respectively to ensure they converge to
1604 similar values, giving them an equal weighting towards L_{total} . The values of α and
1605 β are chosen to ensure that L_{jet} converges to a larger value than either L_{vertex} and
1606 L_{track} , which reflects the primary importance of the jet classification objective. It
1607 was found that in practice the overall performance of the model was not sensitive
1608 to modest changes in the loss weights α and β . Pre-training using L_{total} (i.e. on
1609 all tasks) and fine tuning on only the jet classification task also did not improve
1610 performance versus the standard setup, indicating that the auxiliary tasks are not
1611 in direct competition with the jet classification task. As there was a large variation
1612 in the relative abundance of tracks of the different origins, the contribution of each
1613 origin to L_{track} was weighted by the inverse of the frequency of their occurrence. In
1614 vertexing loss L_{vertex} , the class weight for track-pairs where both tracks are from
1615 either a b - or c -hadron was increased by a factor of two as compared with other

1616 track-pairs, to encourage the network to focus on correctly classifying heavy flavour
1617 vertices.

1618 GN1 can be trained with either the node or edge networks (and their corresponding
1619 auxiliary tasks), or both, removed, as discussed in Section 6.5.3. In such cases,
1620 the corresponding losses L_{vertex} and L_{track} are also removed from the calculation
1621 of the overall loss L_{total} . The performance of the resulting models provides a
1622 useful indication of the benefit of including the auxiliary tasks to the primary jet
1623 classification objective.

1624 GN1 was trained for 100 epochs on 4 NVIDIA V100 GPUs. Each epoch takes
1625 approximately 25 mins to complete over the training sample of 30 million jets. The
1626 Adam optimiser [123] with an initial learning rate of $1e-3$, and a batch size of 4000
1627 jets (spread across the 4 GPUs) was used. Typically the validation loss, calculated
1628 on 500k jets, became stable after around 60 epochs. The epoch that minimized the
1629 validation loss was used for evaluation. GN1 has been integrated into the ATLAS
1630 software [54] using ONNX [124]. The test sample jet flavour predictions scores are
1631 computed using the ATLAS software stack as a verification of this process.

1632 6.5 Results

1633 The GN1 tagger is evaluated both as a b -tagging and c -tagging algorithm in Sec-
1634 tion 6.5.1 and Section 6.5.2 respectively. Evaluation is performed separately on
1635 jets in the $t\bar{t}$ sample with $20 < p_T < 250 \text{ GeV}$ and jets in the Z' sample with
1636 $250 < p_T < 5000 \text{ GeV}$. The performance of the model is compared to the DL1r
1637 tagger [85, 86], which has been retrained on 75 million jets from the same samples as
1638 GN1. The input RNNIP tagger [82] to DL1r has not been retrained. As discussed,
1639 each tagger predicts the probability that a jet belongs to the b -, c - and light-classes.
1640 To use the model for b -tagging, these probabilities are combined into a single score
1641 D_b , which is defined as

$$D_b = \log \frac{p_b}{(1 - f_c)p_l + f_c p_c}, \quad (6.8)$$

where f_c is a free parameter that determines the relative weight of p_c to p_l in the score D_b , controlling the trade-off between c - and light-jet rejection performance. The choice of f_c is arbitrary, and is optimised based upon the desired light- vs c -jet rejection performance. This parameter is set to a value of $f_c = 0.018$ for the DL1r model, obtained through an optimisation procedure described in Ref. [85]. Based on a similar optimisation procedure, a value of $f_c = 0.05$ is used for the GN1 models.

A comparison of the b -tagging discriminant D_b between DL1r and GN1 is shown in Fig. 6.5. The shapes of the D_b distributions are generally similar for b -, c - and light-jets between both models, however, GN1 shifts the b -jet distribution to higher values of D_b in the regions with the greatest discrimination. The GN1 c -jet distribution is also shifted to lower values of D_b when compared with DL1r, enhancing the separation and indicating that GN1 is improving c -jet rejection when compared with DL1r.

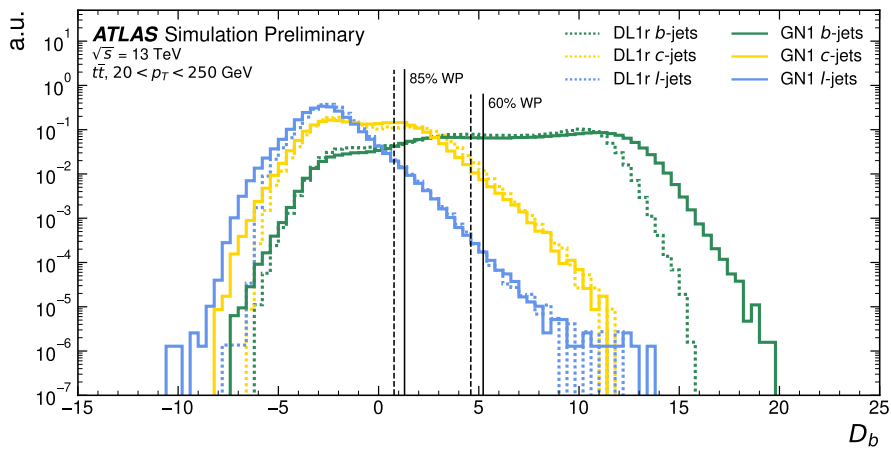


Figure 6.5: Comparison between the DL1r and GN1 b -tagging discriminant D_b for jets in the $t\bar{t}$ sample. The 85% WP and the 60% WP are marked by the solid (dashed) lines for GN1 (DL1r), representing respectively the loosest and tightest WPs typically used by analyses. A value of $f_c = 0.018$ is used in the calculation of D_b for DL1r and $f_c = 0.05$ is used for GN1. The distributions of the different jet flavours have been normalised to unity area [3].

6.5.1 b -tagging Performance

The performance of b -tagging algorithms is quantified by their ability to reject c - and light-jets for a given b -jet selection efficiency WP. In order to compare the b -tagging performance of the different taggers for the b -jet tagging efficiencies in the range

1658 typically used by analyses, the corresponding c - and light-jet rejection rates are
1659 displayed in Figs. 6.6 and 6.7 for jets in the $t\bar{t}$ and Z' samples respectively. Four
1660 standard WPs are defined with b -jet tagging efficiencies of 60%, 70%, 77% and 85%
1661 respectively. These WPs are commonly used by physics analyses depending on their
1662 specific signal and background requirements. The WPs are defined based on jets in
1663 the $t\bar{t}$ sample only. Due to the much higher jet p_T range in the Z' sample, and the
1664 increased difficulty in tagging jets at high- p_T (see Chapter 4), the corresponding b -jet
1665 tagging efficiencies for jets in the Z' sample are lower than the corresponding WPs
1666 calculated in the $t\bar{t}$ sample. For instance the WP cut value computed to provide a
1667 70% b -jet tagging efficiency on the $t\bar{t}$ sample results in a b -jet tagging efficiency of
1668 just $\sim 30\%$ on the Z' sample. In order to account for this, the range of b -jet tagging
1669 efficiencies displayed for plots showing the performance for jets in the Z' sample (for
1670 example Fig. 6.7) is chosen to span the lower efficiencies achieved in the Z' sample
1671 at high- p_T .

1672 For jets in the $t\bar{t}$ sample with $20 < p_T < 250 \text{ GeV}$, GN1 demonstrates considerably
1673 better c - and light-jet rejection when compared with DL1r across the full range of
1674 b -jet tagging efficiencies studied. The relative improvement is strongly dependent
1675 on the b -jet tagging efficiency under study. The largest improvements are found at
1676 lower b -jet tagging efficiencies. At a b -jet tagging efficiency of 70%, the c -jet rejection
1677 improves by a factor of ~ 2.1 while the light-jet rejection improves by a factor of ~ 1.8
1678 with respect to DL1r. For high- p_T jets in the Z' sample with $250 < p_T < 5000 \text{ GeV}$,
1679 GN1 also brings a significant performance improvement with respect to DL1r across
1680 the range of b -jet tagging efficiencies studied. Again, the largest relative improvement
1681 in performance comes at the lower b -jet tagging efficiencies. At a b -jet efficiency of
1682 30%, GN1 improves the c -jet rejection with respect to DL1r by a factor of ~ 2.8 and
1683 the light-jet rejection by a factor of ~ 6 . The performance comparison at lower b -jet
1684 tagging efficiencies is made more difficult due to the increased statistical uncertainties
1685 which result from the high rejection of background.

1686 The GN1Lep variant of GN1 demonstrates further improved performance with respect
1687 to the baseline model. This demonstrates the additional jet flavour discrimination
1688 power provided by the leptonID track input. For jets in the $t\bar{t}$ sample, the relative c -
1689 jet rejection improvement with respect to GN1 at the 70% b -jet WP is approximately
1690 25%. The improvement in light-jet rejection also increases by 40% at the same WP.
1691 For jets in the Z' sample, the relative c -jet rejection (light-jet rejection) performance

1692 with respect to GN1 improves by approximately 10% (25%) at a b -jet tagging
1693 efficiency of 30%.

1694 In general, the performance of all the taggers is strongly dependent on jet p_T , due
1695 to the increased multiplicity and collimation of tracks, and the displaced decays
1696 that result from within the heavy flavour jets (see Chapter 4). Together, they
1697 contribute to a reduced reconstruction efficiency for heavy flavour tracks, and a
1698 general degradation in quality of tracks inside the core of a jet, which in turn reduces
1699 the jet tagging performance. In order to study how the tagging performance changes
1700 as a function of the jet p_T , the b -jet tagging efficiency as a function of p_T for a fixed
1701 light-jet rejection of 100 in each bin is shown in Fig. 6.8. For jets in the $t\bar{t}$ sample,
1702 at a fixed light-jet rejection of 100, GN1 improves the b -jet tagging efficiency by
1703 approximately 4% across all the jet p_T bins. Meanwhile, GN1Lep again demonstrates
1704 improved performance with respect to GN1, in particular at lower p_T . The relative
1705 increase in the b -jet tagging efficiency increases from 4% to 8% with respect to DL1r.
1706 For jets in the Z' sample, GN1 again outperforms DL1r across the entire jet p_T range
1707 studied. The largest relative improvement in performance is found at the highest
1708 transverse momenta of jet $p_T > 2 \text{ TeV}$, and corresponds to an approximate factor of
1709 2 improvement in efficiency with respect to DL1r.

1710 The performance of the model was also evaluated as a function of the average
1711 number of pile-up interactions in the event. No significant dependence of the tagging
1712 performance was observed.

1713 6.5.2 c -tagging Performance

1714 As discussed previously, GN1 does not rely on any inputs from manually optimised
1715 low-level tagging algorithms. Since these algorithms were originally designed and
1716 tuned with the aim of b -tagging, and not c -tagging, the low level tagging algorithms
1717 may perform suboptimally for c -tagging purposes. The tagging of c -jets therefore
1718 presents a compelling use case for GN1. As each of the models is trained with three
1719 output classes, using it as a c -tagging algorithm is trivially analogous to the approach
1720 used for b -tagging. The model output probabilities are combined into a single score
1721 D_c , which is defined similarly to Eq. (6.8) as

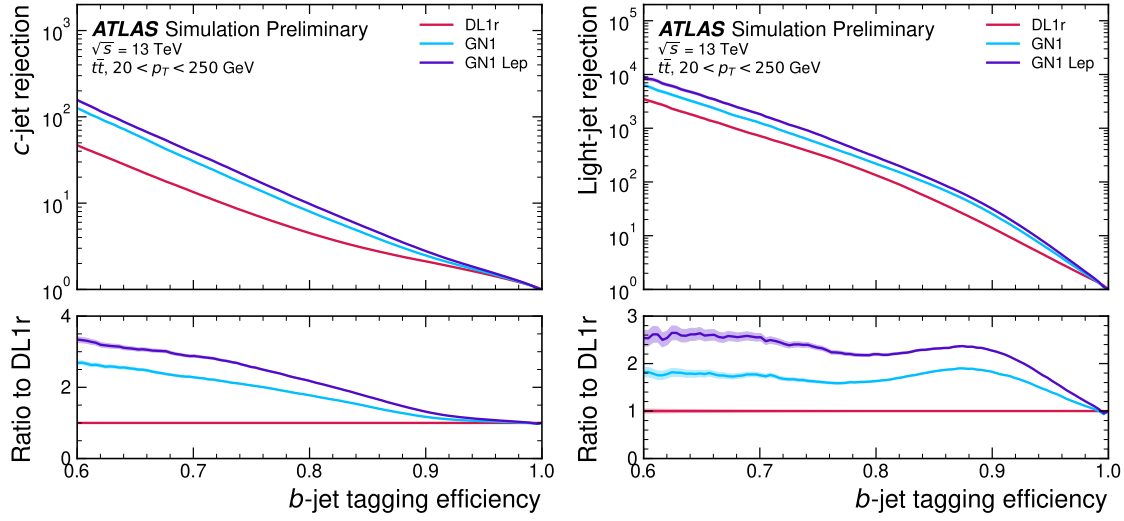


Figure 6.6: The c -jet (left) and light-jet (right) rejections as a function of the b -jet tagging efficiency for jets in the $t\bar{t}$ sample with $20 < p_T < 250 \text{ GeV}$. The ratio with respect to the performance of the DL1r algorithm is shown in the bottom panels. A value of $f_c = 0.018$ is used in the calculation of D_b for DL1r and $f_c = 0.05$ is used for GN1 and GN1Lep. Binomial error bands are denoted by the shaded regions. The x -axis range is chosen to display the b -jet tagging efficiencies usually probed in these regions of phase space [3].

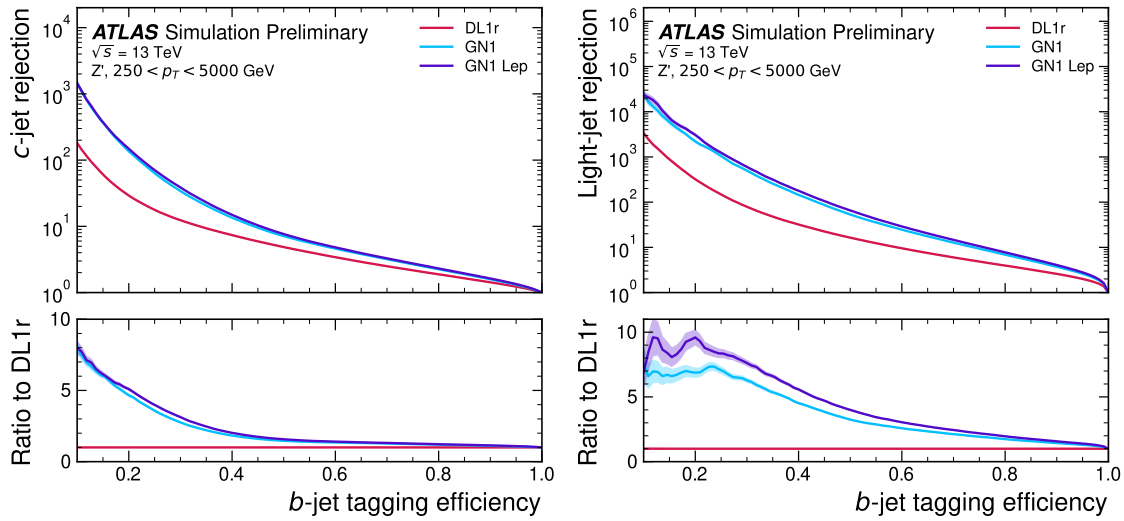


Figure 6.7: The c -jet (left) and light-jet (right) rejections as a function of the b -jet tagging efficiency for jets in the Z' sample with $250 < p_T < 5000 \text{ GeV}$. The ratio with respect to the performance of the DL1r algorithm is shown in the bottom panels. A value of $f_c = 0.018$ is used in the calculation of D_b for DL1r and $f_c = 0.05$ is used for GN1 and GN1Lep. Binomial error bands are denoted by the shaded regions. The x -axis range is chosen to display the b -jet tagging efficiencies usually probed in these regions of phase space [3].

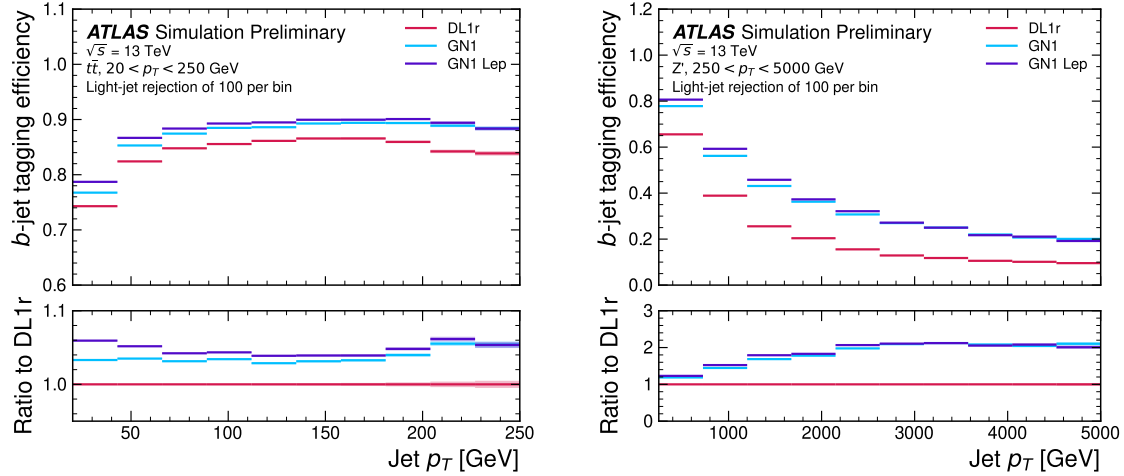


Figure 6.8: The *b*-jet tagging efficiency for jets in the $t\bar{t}$ sample (left) and jets in the Z' sample (right) as a function of jet p_T with a fixed light-jet rejection of 100 in each bin. A value of $f_c = 0.018$ is used in the calculation of D_b for DL1r and $f_c = 0.05$ is used for GN1 and GN1Lep. GN1 demonstrates improved performance with respect to DL1r across the p_T range shown. Binomial error bands are denoted by the shaded regions [3].

$$D_c = \log \frac{p_c}{(1 - f_b)p_l + f_b p_b}. \quad (6.9)$$

A value of $f_b = 0.2$ is used for all models, based on the same optimisation procedure that was used for the *b*-tagging use case. Similar to Section 6.5.1, the different taggers are compared to one another by scanning through a range of *c*-jet tagging efficiencies and plotting the corresponding *b*- and light-jet rejection rates, and the WPs are defined using jets in the $t\bar{t}$ sample. Standard *c*-jet tagging efficiency WPs used by physics analyses are significantly lower than the *b*-tagging WPs in order to maintain reasonable *b*- and light-jet rejection rates. This is reflected in the range of *c*-jet tagging efficiencies used in *c*-tagging plots such as Figs. 6.9 and 6.10. Fig. 6.9 displays the *c*-tagging performance of the models on the jets in the $t\bar{t}$ sample. GN1 is shown to perform significantly better than DL1r. Similar to the *b*-tagging case, the *b*- and light-jet rejection improve most at lower *c*-jet tagging efficiencies, with the *c*-jet rejection (light-jet rejection) improving by a factor 2 (1.6) with respect to DL1r at a *c*-jet tagging efficiency of 25%. GN1Lep again outperforms GN1, though the improvements are more modest than observed for the *b*-tagging use case,

1736 with both the b -jet rejection (light-jet rejection) improving with respect to GN1
1737 by approximately 10% (20%) at the 25% c -jet WP. Fig. 6.10 shows the c -tagging
1738 performance on the jets in the Z' sample with $250 < p_T < 5000$ GeV. Both GN1 and
1739 GN1Lep perform similarly, improving the b -jet rejection by 60% and the light-jet
1740 rejection by a factor of 2 at the 25% c -jet WP.

1741 6.5.3 Ablations

1742 Ablation studies (the removal of certain components of a model in order to study
1743 the impact of that component) are carried out to determine the importance of the
1744 auxiliary training objectives of GN1 to the overall performance. The “GN1 No
1745 Aux” variant retains the primary jet classification objective, but removes both track
1746 classification and vertexing auxiliary objectives and correspondingly only minimises
1747 the jet classification loss. The “GN1 TC” variant includes the track classification
1748 objective but not the vertexing objective. Finally, the “GN1 Vert” includes the
1749 vertexing objective, but not the track classification objective.

1750 For jets in both the $t\bar{t}$ and Z' samples, a general trend is observed that the models
1751 trained without one or both of the auxiliary objectives results in significantly reduced
1752 c - and light-jet rejection when compared with the baseline GN1 model, as shown
1753 in Figs. 6.11 and 6.12. For jets in the $t\bar{t}$ sample, the performance of GN1 No Aux
1754 is similar to DL1r, while GN1 TC and GN1 Vert perform similarly to each other.
1755 For jets in the Z' sample, the GN1 No Aux model shows a clear improvement in c -
1756 and light-jet rejection when compared with DL1r at lower b -jet tagging efficiencies.
1757 Similar to jets in the $t\bar{t}$ sample, GN1 TC and GN1 Vert perform similarly, and bring
1758 large gains in background rejection when compared with GN1 No Aux, but the
1759 combination of both auxiliary objectives yields the best performance.

1760 It is notable that the GN1 No Aux model matches or exceeds the performance of
1761 DL1r without the need for inputs from the low-level algorithms. This indicates that
1762 the performance improvements enabled by the improved neural network architecture
1763 used in GN1 appear to be able to compensate for the removal of the low-level
1764 algorithm inputs. The GN1 TC and GN1 Vert variants each similarly outperform
1765 DL1r, demonstrating that both contribute to the overall high performance of the
1766 baseline model. The overall best performing model is the full version of GN1 trained

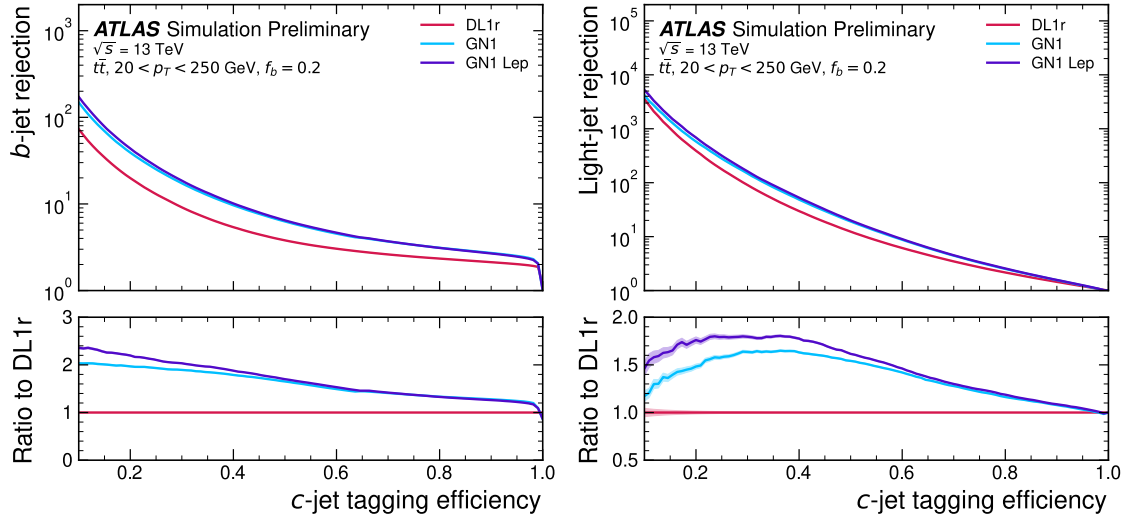


Figure 6.9: The b -jet (left) and light-jet (right) rejections as a function of the c -jet tagging efficiency for $t\bar{t}$ jets with $20 < p_T < 250$ GeV. The ratio to the performance of the DL1r algorithm is shown in the bottom panels. Binomial error bands are denoted by the shaded regions. The x -axis range is chosen to display the c -jet tagging efficiencies usually probed in these regions of phase space [3].

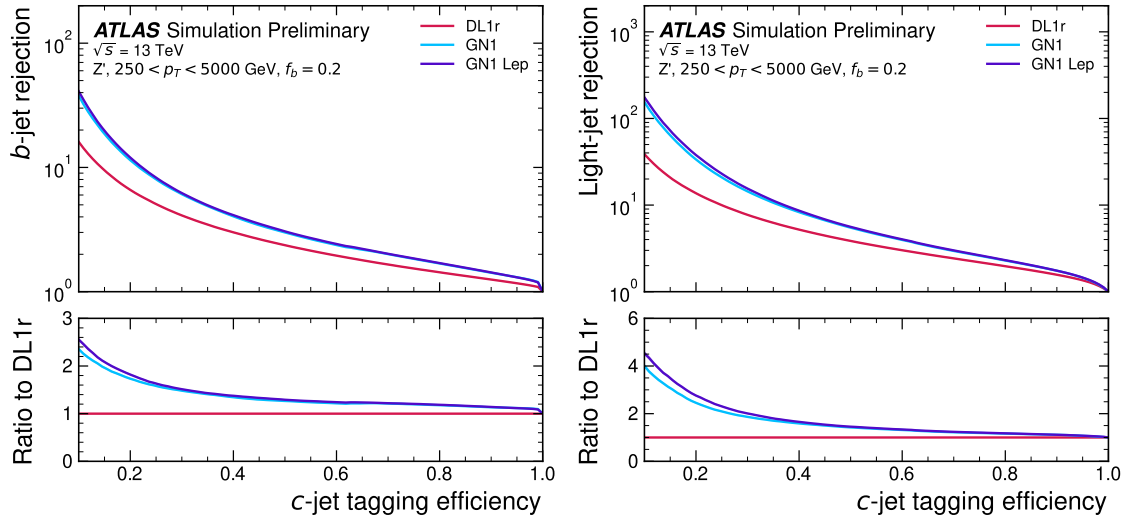


Figure 6.10: The b -jet (left) and light-jet (right) rejections as a function of the c -jet tagging efficiency for Z' jets with $250 < p_T < 5000$ GeV. The ratio to the performance of the DL1r algorithm is shown in the bottom panels. Binomial error bands are denoted by the shaded regions. The x -axis range is chosen to display the c -jet tagging efficiencies usually probed in these regions of phase space [3].

1767 with both auxiliary objective, demonstrating that the two auxiliary objectives are
1768 complementary.

1769 6.5.4 Inclusion of Low-Level Vertexing Algorithms

1770 As already mentioned, GN1 does not include any inputs from the low-level tagging
1771 algorithms, including the vertexing algorithms SV1 and JetFitter [61]. Since these
1772 algorithms are known to play a key role in contributing to the performance of DL1r,
1773 it was studied whether their inclusion in GN1 could result in further performance
1774 improvements. In a dedicated training of GN1, the SV1 and JetFitter tagger outputs
1775 were added to the GN1 jet classification network as an input, similar to how they
1776 are used in DL1r. These outputs include information on the reconstructed vertices,
1777 including the number of vertices, and the properties of the reconstructed vertices.
1778 In addition, if track was used in the reconstruction of a vertex, a corresponding
1779 index to the vertex was included as a track-level inputs to GN1. These indices were
1780 also used to construct an input feature for the edge classification network used to
1781 identify vertices, which was given a value of one if the track-pair were from a common
1782 reconstructed SV1 or JetFitter vertex, and zero otherwise. The jet classification
1783 performance of this GN1 model was not significantly different to the baseline model,
1784 and in some cases the performance was slightly reduced. It was therefore concluded
1785 that GN1 does not benefit from the inclusion of information from SV1 and JetFitter,
1786 indicating that the model is able to reconstruct the relevant information provided
1787 by these low-level algorithms. The study also demonstrates that the model can
1788 function as a highly performant standalone tagger that does not require (beyond
1789 retraining) any manual optimisation to achieve good performance in a wide range
1790 of phase spaces. A dedicated look at the vertexing performance of GN1 with some
1791 comparisons to SV1 and JetFitter is found in Section 6.5.6

1792 6.5.5 Jet Display Diagrams

1793 The auxiliary training objectives of GN1 allow for improved model interpretability,
1794 which is especially important for a monolithic approach as the low level taggers,
1795 which provide useful physical insight, are no longer present. Figs. 6.13 and 6.14
1796 provide example comparisons of the true origin and vertexing information compared

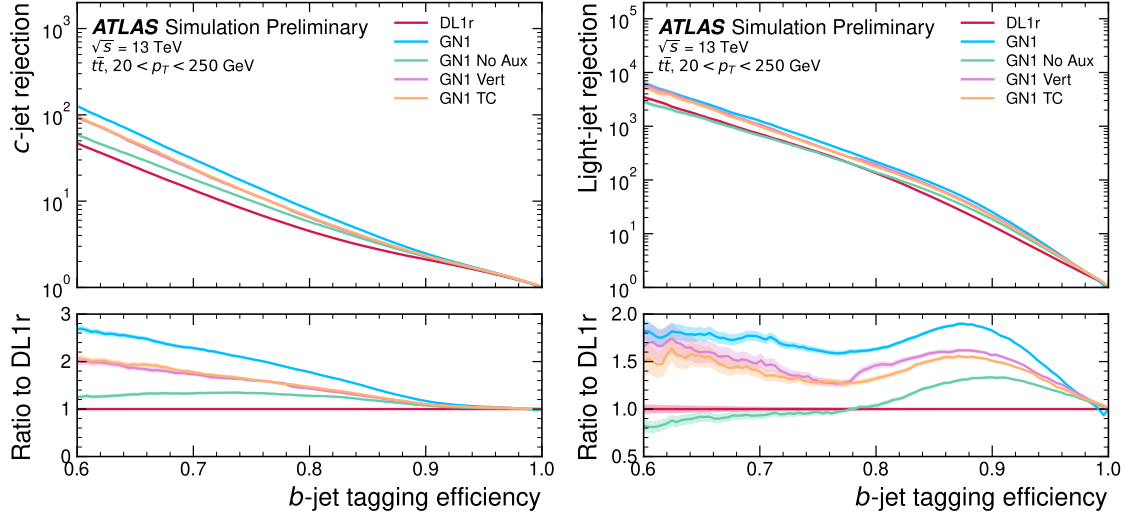


Figure 6.11: The c -jet (left) and light-jet (right) rejections as a function of the b -jet tagging efficiency for $t\bar{t}$ jets with $20 < p_T < 250$ GeV, for the nominal GN1, in addition to configurations where no (GN1 No Aux), only the track classification (GN1 TC) or only the vertexing (GN1 Vert) auxiliary objectives are deployed. The ratio to the performance of the DL1r algorithm is shown in the bottom panels. A value of $f_c = 0.018$ is used in the calculation of D_b for DL1r and $f_c = 0.05$ is used for GN1 [3].

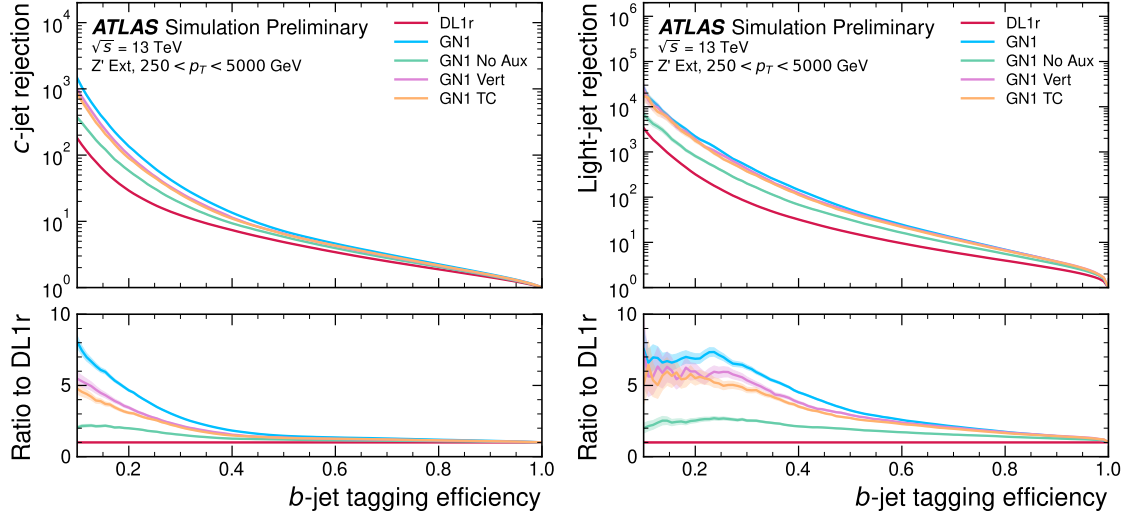


Figure 6.12: The c -jet (left) and light-jet (right) rejections as a function of the b -jet tagging efficiency for Z' jets with $250 < p_T < 5000$ GeV, for the nominal GN1, in addition to configurations where no (GN1 No Aux), only the track classification (GN1 TC) or only the vertexing (GN1 Vert) auxiliary objectives are deployed. The ratio to the performance of the DL1r algorithm is shown in the bottom panels. A value of $f_c = 0.018$ is used in the calculation of D_b for DL1r and $f_c = 0.05$ is used for GN1 [3].

1797 with the predicted values from GN1, SV1 and JetFitter. Such comparisons can be
 1798 used to provide an indication that GN1 reconstructs the correct representation of the
 1799 jet structure, and may also help to identify limitations of the model. In the figures,
 1800 the tracks in the jet are indexed twice on each of the x - and y -axes, and tracks are
 1801 grouped into vertices along with other tracks as indicated by common markings in
 1802 the relevant rows and columns.

1803 In Fig. 6.13, GN1 correctly groups the three primary tracks as having come from the
 1804 primary vertex. The b -hadron and $b \rightarrow c$ -hadron decay vertices are also correctly
 1805 predicted, and the origin of the tracks in each is correct. There is a single OtherSec-
 1806 ondary track which GN1 incorrectly predicts as having come from pile-up. Meanwhile
 1807 SV1 (by design) merges the two heavy flavour decay vertices, but incorrectly includes
 1808 a track from the primary vertex. JetFitter reconstructs two vertices, one which is a
 1809 combination of two tracks from different truth vertices and two other single track
 1810 vertices in each of the heavy flavour vertices. GN1 also predicts the flavour of the jet
 1811 with a high degree of certainty.

1812 Similarly Fig. 6.13 shows that GN1 is also able to relatively accurately predict the
 1813 origin and vertex information of tracks inside a jet. The pile-up tracks and primary
 1814 vertex tracks are correctly identified, and the heavy flavour decay tracks are also
 1815 correctly identified with the exception of one of the b -hadron decay tracks. Again,
 1816 SV1 merges the two heavy flavour decay vertices along with a track from pile-up,
 1817 while JetFitter shows signs of being under-constrained by reconstructing two single
 1818 track vertices, one with a pile-up track and one with a track from a $b \rightarrow c$ -hadron
 1819 decay. While these examples do not give a complete picture of the performance of
 1820 GN1, they do show provide a powerful way to visualise and diagnose the behaviour
 1821 of GN1.

1822 6.5.6 Vertexing Performance

1823 From the track-pair vertex prediction, tracks can be partitioned into compatible
 1824 groups representing vertices through the use of a deterministic clustering algorithm
 1825 (see Ref. [115]). As such, GN1 can perform vertex “finding”, but not vertex “fitting”,
 1826 i.e. the reconstruction of a vertex’s properties, which currently still requires the
 1827 use of a dedicated vertex fitter. In order to study the performance of the different
 1828 vertexing tools, the truth vertex label of the tracks are used.

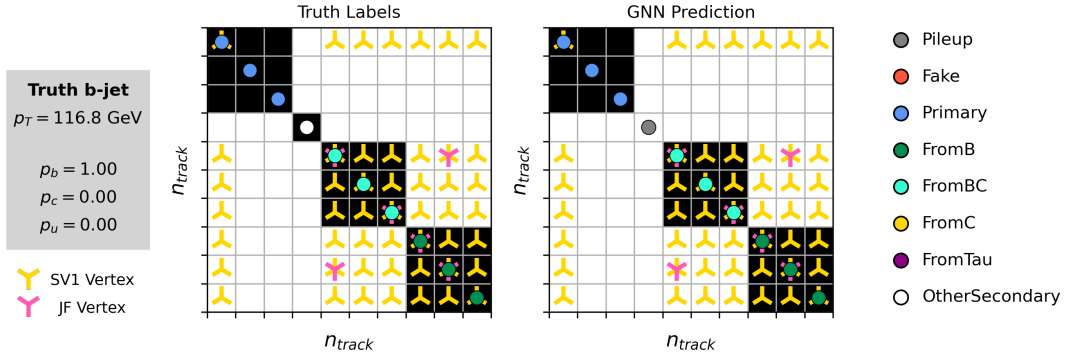


Figure 6.13: A schematic showing the truth track origin and vertex information (left) compared with the predictions from GN1 (right). The diagrams show the truth (left) and predicted (right) structure of a b -jet. The true and predicted origins of the tracks is shown by the coloured circles along the diagonal. The shaded black boxes show the groupings of tracks into different vertices. Vertices reconstructed by SV1 and JetFitter are also marked. Class probabilities p_b , p_c and p_u are rounded to three significant figures. GN1 improves over SV1 and JetFitter by successfully determining the origins and vertex compatibility of all the tracks in the jet with the exception of the truth OtherSecondary track, which is misidentified as pile-up.

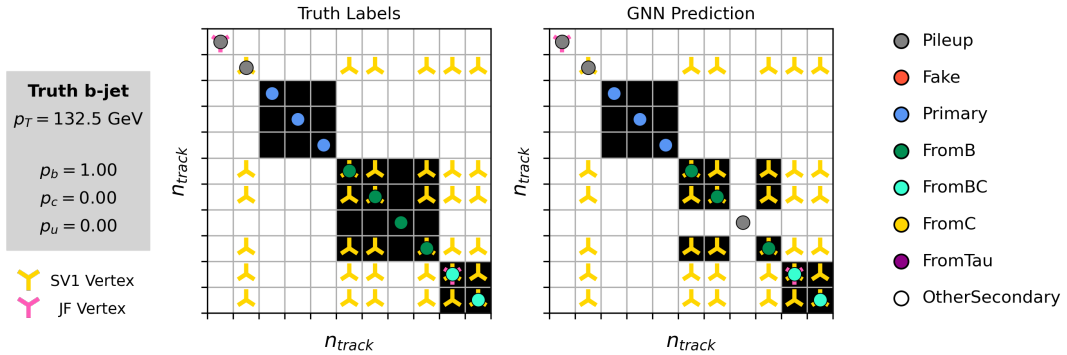


Figure 6.14: A schematic showing the truth track origin and vertex information (left) compared with the predictions from GN1 (right). The diagrams show the truth (left) and predicted (right) structure of a b -jet. The true and predicted origins of the tracks is shown by the coloured circles along the diagonal. The shaded black boxes show the groupings of tracks into different vertices. Vertices reconstructed by SV1 and JetFitter are also marked. Class probabilities p_b , p_c and p_u are rounded to three significant figures. GN1 improves over SV1 and JetFitter by successfully determining the origins and vertex compatibility of all but one tracks in the jet.

1829 There are several caveats to a comparison of the vertexing tools which are a result
1830 of the different approaches they take to vertexing. SV1 and JetFitter are designed
1831 to only find secondary vertices in the jet, whereas GN1 is also trained to determine
1832 which tracks in the jet belong to the primary vertex. To account for this the GN1
1833 vertex with the largest number of predicted primary tracks is excluded from the
1834 vertex finding efficiency calculation. While JetFitter and GN1 aim to resolve each
1835 displaced vertex inside the jet, such that secondary vertices from b -hadron decays
1836 are found separately to tertiary vertices from $b \rightarrow c$ decay chains, SV1 by design
1837 attempts to find a single inclusive vertex per jet. This inclusive vertex groups tracks
1838 from the b -hadron decay itself (FromB) and tracks from $b \rightarrow c$ decays (FromBC). In
1839 order to fairly compare the performance of the different tools, both the exclusive and
1840 inclusive vertex finding efficiencies are studied. For the exclusive vertex finding case
1841 JetFitter and GN1 can be directly compared, while a comparison with SV1 is not
1842 possible due to the aforementioned design constraints. The inclusive vertex finding
1843 performance of all three tools can be compared using the procedure outlined below.

1844 The starting point for the secondary vertex finding efficiency in both the exclusive and
1845 inclusive cases is to select truth HF secondary vertices, defined as those containing
1846 only inclusive b -hadron decays. For exclusive HF vertex finding, these truth secondary
1847 HF vertices can be used directly as the denominator for the efficiency calculation.
1848 Meanwhile for the inclusive efficiency all such truth HF secondary vertices in the jet
1849 are merged into a single inclusive target vertex. Correspondingly, for the inclusive
1850 HF vertex finding case, the vertices found by JetFitter are merged into a single
1851 vertex, and the vertices found by GN1 which contain at least one predicted b -hadron
1852 decay track, are also merged. SV1 does not require any vertex merging. Only jets
1853 containing a single b -hadron at truth level are considered.

1854 Next, vertices in the jet found by the different vertexing tools are compared with
1855 the target truth vertices. The number of correctly and incorrectly assigned tracks is
1856 computed. In order to call a vertex efficient, it is required to contain at least 65% of
1857 the tracks in the corresponding truth vertex, and to have a purity of at least 50%.
1858 Single track vertices are required to have a purity of 100%. Additionally, for GN1
1859 only, at least one track in the vertex is required to have a predicted heavy flavour
1860 origin.

1861 Vertex finding efficiencies for b -jets in the $t\bar{t}$ sample are displayed as a function of
1862 p_T separately for the inclusive and exclusive approaches in Fig. 6.15. For b -jets in

the $t\bar{t}$ sample with $20 < p_T < 250$ GeV, the exclusive vertex finding efficiency of JetFitter and GN1 is relatively flat as a function of p_T . For the truth secondary vertices in this p_T region, JetFitter efficiently finds approximately 40% and GN1 finds approximately 55%. When finding vertices inclusively the vertex finding efficiency is generally higher. An increased dependence on p_T is also visible for JetFitter and SV1. As the jet p_T increases from 20 GeV to 100 GeV, the efficiency of JetFitter increases from 60% to 65%. In the same range, the efficiency of SV1 increases from 60% to 75%. GN1 displays less dependence on p_T than JetFitter and SV1, finding upwards of 80% of vertices in b -jets in this p_T region. For b -jets with $p_T > 100$ GeV, JetFitter finds approximately 65% of vertices, SV1 finds approximately 75% of vertices, and GN1 finds approximately 80% of vertices.

Fig. 6.16 compares the exclusive and inclusive HF vertex finding efficiencies for b -jets in the Z' sample. The inclusive vertex finding efficiency drops steeply with increasing p_T up until $p_T = 3$ TeV. GN1 outperforms SV1 and JetFitter across the p_T spectrum. In the first bin, the efficiency of GN1 is 65%, while the efficiencies of SV1 and JetFitter are around 55%. The efficiency of SV1 drops rapidly to almost zero above 3 TeV, while JetFitter and GN1 retain approximately 20% and 30% efficiency respectively. For the exclusive HF vertex finding efficiency, JetFitter finds 35% of vertices in the first bin, dropping to 20% of vertices above 2 TeV. GN1 finds 55% of vertices in the first bin, dropping to 30% above 2 TeV.

While Figs. 6.15 and 6.16 indicate that GN1 is able to successfully find displaced heavy flavour vertices in b -jets, it is also important to consider the vertexing performance inside light-jets. Light-jets may also contain real displaced vertices due to long lived secondary particles and material interactions. These tracks have a truth origin of OtherSecondary in the truth labelling scheme enumerated in see Table 5.1. The efficiency to reconstruct vertices comprised of OtherSecondary tracks can be computed in an analogous way to the heavy flavour vertexing efficiency, which is described above. Figs. 6.17 and 6.18 show the efficiency to reconstruct displaced OtherSecondary vertices in light-jets as a function of p_T for jets in the $t\bar{t}$ sample and jets in the Z' sample respectively. The figures demonstrate that GN1 is able to more effectively find such vertices in light-jets as compared with SV1 and JetFitter. Since the properties of the displaced vertices in light-jets are likely to be significantly different to heavy flavour vertices found in heavy flavour jets, the improved reconstruction of such vertices may help to differentiate between different flavour of jet.

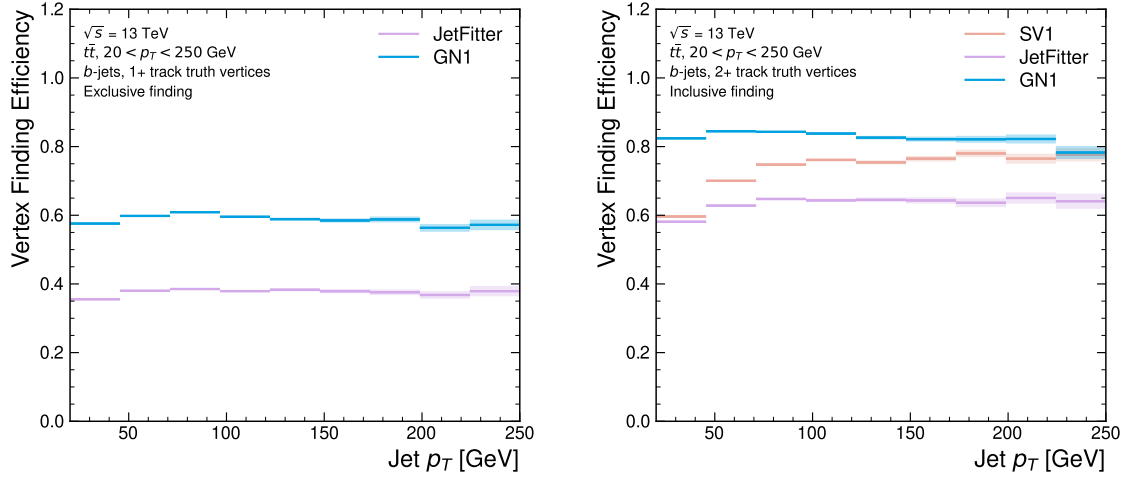


Figure 6.15: Heavy flavour vertex finding efficiency as a function of jet p_T for b -jets in the $t\bar{t}$ sample using the exclusive (left) and inclusive (right) vertex finding approaches. The exclusive vertexing approach includes single track vertices while the inclusive approach requires vertices to contain at least two tracks. Efficient vertex finding requires the recall of at least 65% of the tracks in the truth vertex, and allows no more than 50% of the tracks to be included incorrectly. Binomial error bands are denoted by the shaded regions.

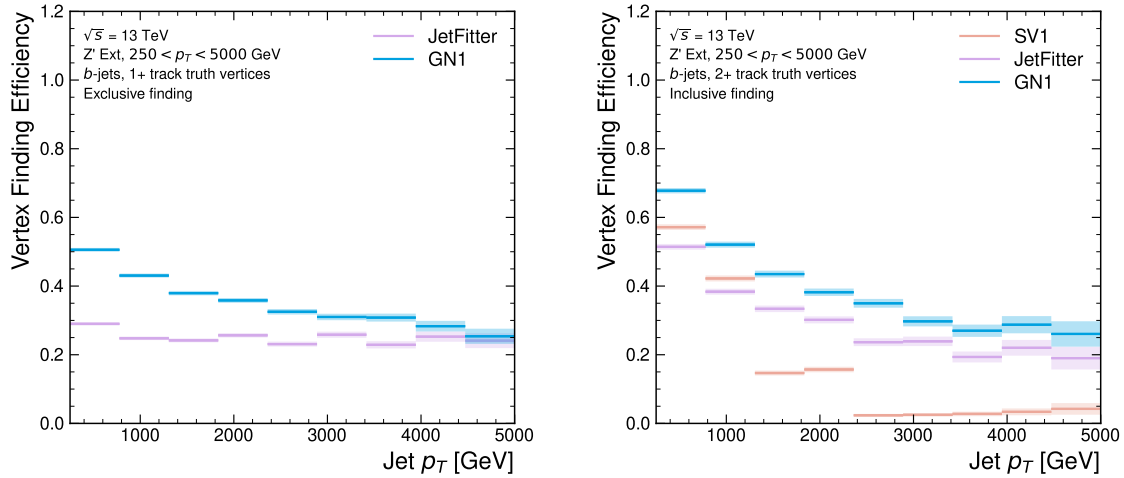


Figure 6.16: Heavy flavour vertex finding efficiency as a function of jet p_T for b -jets in the Z' sample using the exclusive (left) and inclusive (right) vertex finding approaches. The exclusive vertexing approach includes single track vertices while the inclusive approach requires vertices to contain at least two tracks. Efficient vertex finding requires the recall of at least 65% of the tracks in the truth vertex, and allows no more than 50% of the tracks to be included incorrectly. Binomial error bands are denoted by the shaded regions.

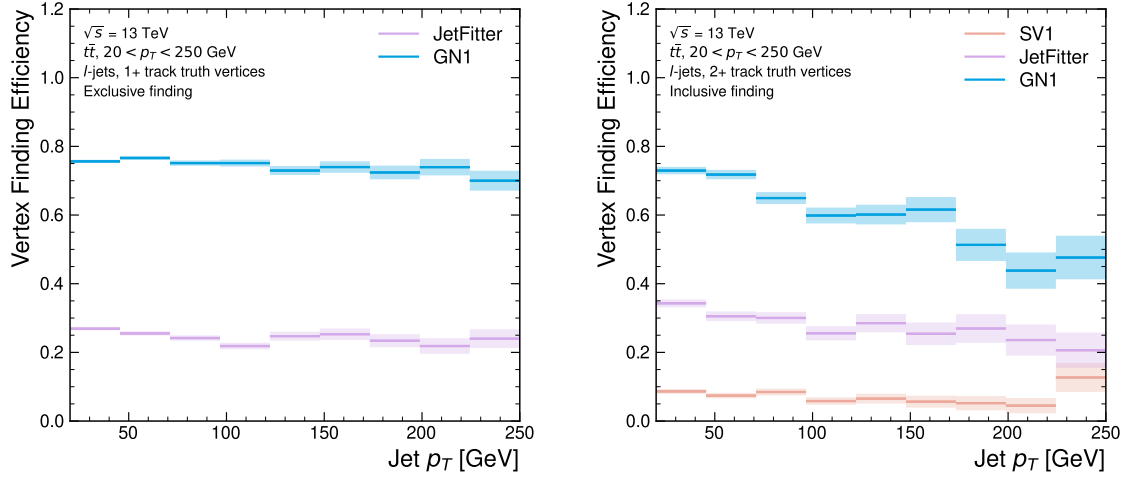


Figure 6.17: Vertex finding efficiency for other secondary decays as a function of jet p_T for light-jets in the $t\bar{t}$ sample using the exclusive (left) and inclusive (right) vertex finding approaches. The exclusive vertexing approach includes single track vertices while the inclusive approach requires vertices to contain at least two tracks. Efficient vertex finding requires the recall of at least 65% of the tracks in the truth vertex, and allows no more than 50% of the tracks to be included incorrectly. Binomial error bands are denoted by the shaded regions.

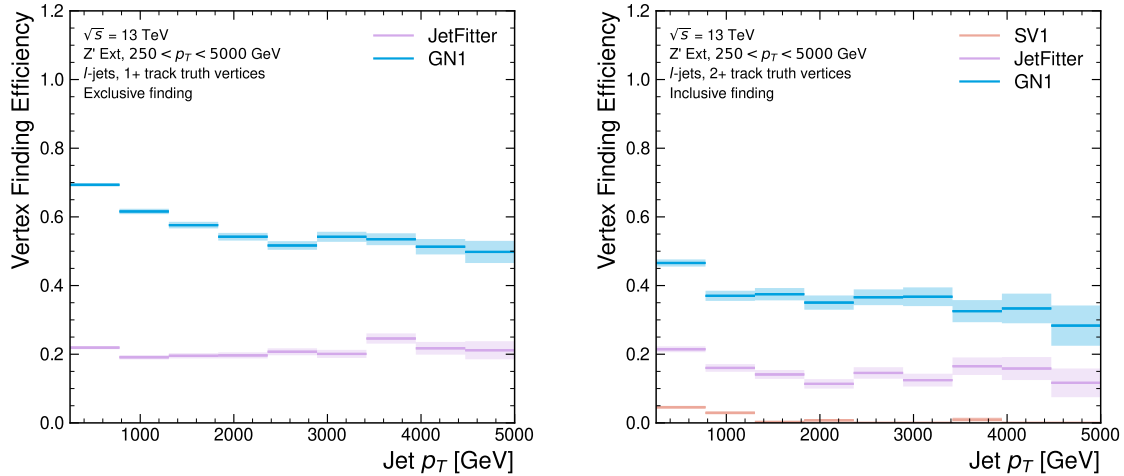


Figure 6.18: Vertex finding efficiency as a function of jet p_T for light-jets in the Z' sample using the exclusive (left) and inclusive (right) vertex finding approaches. The exclusive vertexing approach includes single track vertices while the inclusive approach requires vertices to contain at least two tracks. Efficient vertex finding requires the recall of at least 65% of the tracks in the truth vertex, and allows no more than 50% of the tracks to be included incorrectly. Binomial error bands are denoted by the shaded regions.

1897 Collectively, the results in this section demonstrate that GN1 is able to accurately
1898 group tracks by their spatial origin in both b -jets and light-jets. The purity of the
1899 found vertices was also investigated and was found to be comparable or better than
1900 that of SV1 and JetFitter.

1901 6.5.7 Track Classification Performance

1902 One of the two auxiliary training objectives used by GN1 is to predict the truth origin
1903 of each track associated to the jet. Since the equivalent information is not provided
1904 by any of the existing flavour tagging tools, a benchmark model used to predict the
1905 truth origin of each track is trained based on a standard multi-class feed-forward
1906 classification network. The benchmark model is trained on the same tracks used for
1907 the baseline GN1 training. The model uses precisely the same concatenated track-
1908 and-jet inputs as used by GN1, but processes only a single track at a time, meaning
1909 it cannot take into account the correlations between tracks when determining the
1910 track origin. The model is made up of five densely connected linear layers with 200
1911 neurons in each layer. The performance of the model was found to be insensitive to
1912 changes in the network structure.

1913 To measure the track classification performance, the area under the curve (AUC) of
1914 the receiver operating characteristic (ROC) curve is computed for each origin class,
1915 using a one-versus-all classification approach². The AUCs for the different truth
1916 origins are averaged using both an unweighted and a weighted mean. The unweighted
1917 mean treats the performance of each class equally, while the weighted mean uses
1918 as a weight the relative abundance of tracks of each class. The same approach is
1919 used to compute the precision, recall and F1 scores³. Table 6.3 demonstrates clearly
1920 that GN1 outperforms the MLP both at $20 < p_T < 250$ GeV for jets in the $t\bar{t}$ sample
1921 and at $250 < p_T < 5000$ GeV for jets in the Z' sample. For example, GN1 can reject
1922 65% of fake tracks in jets in the $t\bar{t}$ sample, while retaining more than 99% of good
1923 tracks (i.e. those tracks which are not fake). The GN1 model has two advantages
1924 over the MLP which can explain the performance improvement. Firstly, the graph

²One class is taken to be signal and the rest are taken as background, subsequently a binary classification approach is used.

³The precision is the fraction of selected tracks from the signal class. The recall, similar to the efficiency, is the fraction of tracks from the signal class which are selected. The F1 score is the harmonic mean of the precision and recall.

1925 neural network architecture enables the sharing of information between tracks. This
1926 is likely to be beneficial since the origins of different tracks within a jet are correlated.
1927 Secondly, the jet classification and vertexing objectives may be complementary to the
1928 track classification objective, and so the track classification performance is improved
1929 by the combined training of complementary objectives.

		AUC		Precision		Recall		F1	
		Mean		Weighted		Mean		Weighted	
		MLP	GN1	MLP	GN1	MLP	GN1	MLP	GN1
$t\bar{t}$	MLP	0.87	0.92	0.39	0.51	0.51	0.64	0.36	0.62
	GN1	0.95	0.95	0.71	0.82	0.56	0.70	0.51	0.74
Z'	MLP	0.90	0.94	0.36	0.84	0.47	0.72	0.31	0.76
	GN1	0.94	0.96	0.48	0.88	0.60	0.79	0.48	0.82

Table 6.3: The area under the ROC curves (AUC) for the track classification from GN1, compared to a standard multilayer perceptron (MLP) trained on a per-track basis. The unweighted mean AUC over the origin classes and weighted mean AUC (using as a weight the fraction of tracks from the given origin) is provided. GN1, which uses an architecture that allows track origins to be classified in a conditional manner as discussed in Section 6.4.3, outperforms the MLP model for both $t\bar{t}$ and Z' jets.

1930 Fig. 6.19 shows the track origin classification ROC curves for the different track
1931 origins for jets in both the $t\bar{t}$ and Z' samples. In order to improve visual readability
1932 of the plot, the curves for the heavy flavour truth origins (FromB, FromBC and
1933 FromC) have been combined (weighted by their relative abundance), as have the
1934 Primary and OtherSecondary origins. In jets in both the $t\bar{t}$ and Z' samples, the AUC
1935 of all the different origin groups exceeds 0.9, representing strong overall classification
1936 performance. In both samples fake tracks are the easiest to classify, followed by
1937 pile-up tracks. The FromC tracks which are c -hadron decay products, are the hardest
1938 to classify, possibly due to their similarity to both fragmentation tracks and b -hadron
1939 decay tracks, depending on the c -hadron species in question.

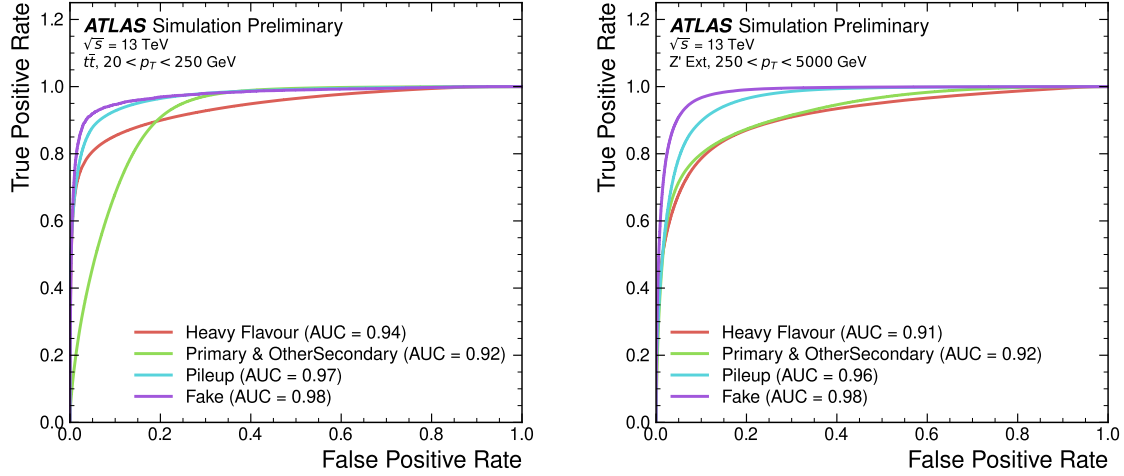


Figure 6.19: ROC curves for the different groups of truth origin labels defined in Table 5.1 for jets in the $t\bar{t}$ sample (left) and jets in the Z' sample (right). The FromB, FromBC and FromC labels have been combined, weighted by their relative abundance, into the Heavy Flavour category, and the Primary and OtherSecondary labels have similarly been combined into a single category. The mean weighted area under the ROC curves (AUC) is similar for both samples [3].

1940 6.6 Further Studies

1941 6.6.1 Looser Track Selection

1942 The track selections used to produce the main results are listed in Table 3.2. This
 1943 includes a selection on the number of shared silicon modules used to reconstruct the
 1944 track $N_{\text{shared}}^{\text{Si}}$. This value is calculated as

$$N_{\text{shared}}^{\text{Si}} = N_{\text{shared}}^{\text{Pix}} + N_{\text{shared}}^{\text{SCT}} / 2 \quad (6.10)$$

1945 where $N_{\text{shared}}^{\text{Pix}}$ is the number of shared pixel hits and $N_{\text{shared}}^{\text{SCT}}$ is the number of shared
 1946 SCT modules on a track. The nominal selection used elsewhere in this thesis is
 1947 $N_{\text{shared}}^{\text{Si}} < 2$. As the rate of shared hits is significantly higher for b -hadron decay
 1948 tracks than for other tracks, especially at high- p_T , this selection rejects a significant
 1949 proportion of these tracks.

1950 Figs. 6.20 and 6.21 show the result of training the GN1 tagger with the full relaxation
 1951 of this selection, i.e. allowing tracks with any number of shared hits. The shared hit

requirements applied by the ambiguity solver as part of track reconstruction (see Section 3.4.1) are still applied. In addition, the maximum allowed value of d_0 is increased from 3.5 mm to 5.0 mm. The results show that optimisation of the input track selection can lead to significant improvements in performance over the default selection. For the jets in the $t\bar{t}$ sample shown in Fig. 6.20, the effect of loosening the track selection is limited. This is expected due to the lower prevalence of shared hits at lower transverse momenta. However for jets in the Z' sample as shown in Fig. 6.21, the c -jet rejection improves with respect to the baseline GN1 model by 35%, while the light-jet rejection improves by 40% at the 20% b -jet WP. Relative improvements of a similar magnitude are also observed for GN1Lep.

6.6.2 High Level Trigger

The implementation of GN1 described in this chapter has been re-used in several other contexts, demonstrating its flexibility to easily provide good jet flavour tagging performance with minimal overhead. The model has been implemented as a b -jet tagger in the High Level Trigger (HLT) (see Section 3.3.4). The inputs to the model are the running on precision tracks⁴ and jet level quantities reconstructed after primary vertex reconstruction has been performed. Fig. 6.22 shows the performance of GN1 versus a comparable DL1d model [86], and two versions of DIPS [83], with EMTopo and PFlow jets (see Section 3.4.3) based on a low-precision region-of-interest based tracking pass, which is optimised for speed. The trigger implementation of GN1 improves upon the light-jet rejection of DL1d by 50% at the 60% b -jet WP for jets in the $t\bar{t}$ sample with $20 < p_T < 250$ GeV.

6.6.3 High Luminosity LHC

The model also demonstrates strong performance for the High Luminosity LHC (HL-LHC) using the proposed ITk inner tracking detector, as documented in Ref. [126]. Figs. 6.23 and 6.24 are reproduced from Ref. [126]. The results show that GN1 outperforms other existing flavour tagging algorithms when trained on an entirely different detector geometry, the ITk (see Section 3.3.1). When compared with

⁴Precision tracking refers to tracks reconstructed in the trigger using the same reconstruction algorithms as for the offline event reconstruction.

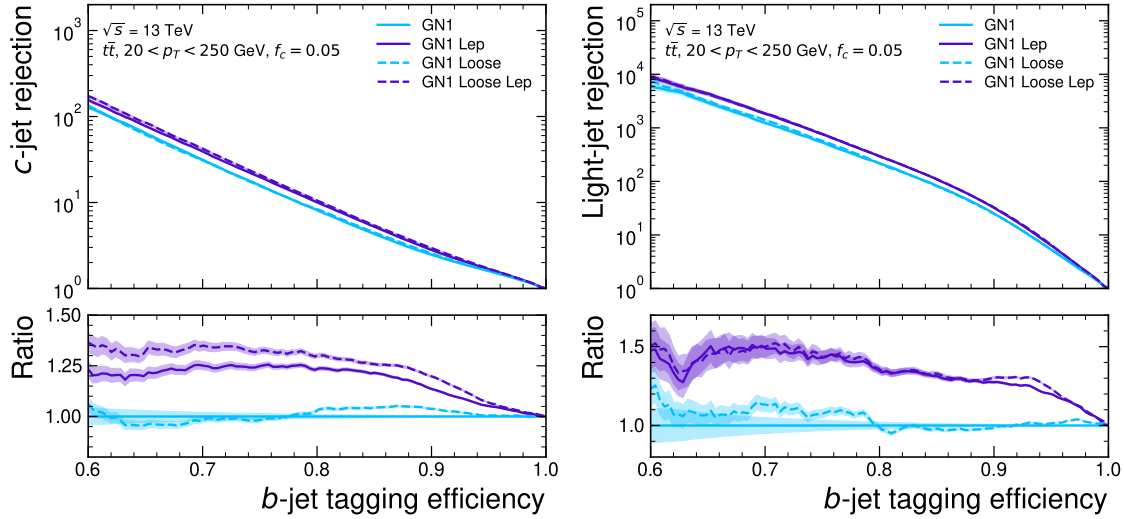


Figure 6.20: The c -jet (left) and light-jet (right) rejections as a function of the b -jet tagging efficiency for $t\bar{t}$ jets with $20 < p_T < 250$ GeV, for the looser track selection trainings of GN1. The ratio to the performance of the baseline GN1 model is shown in the bottom panels. A value of $f_c = 0.05$ is used for all models. Binomial error bands are denoted by the shaded regions.

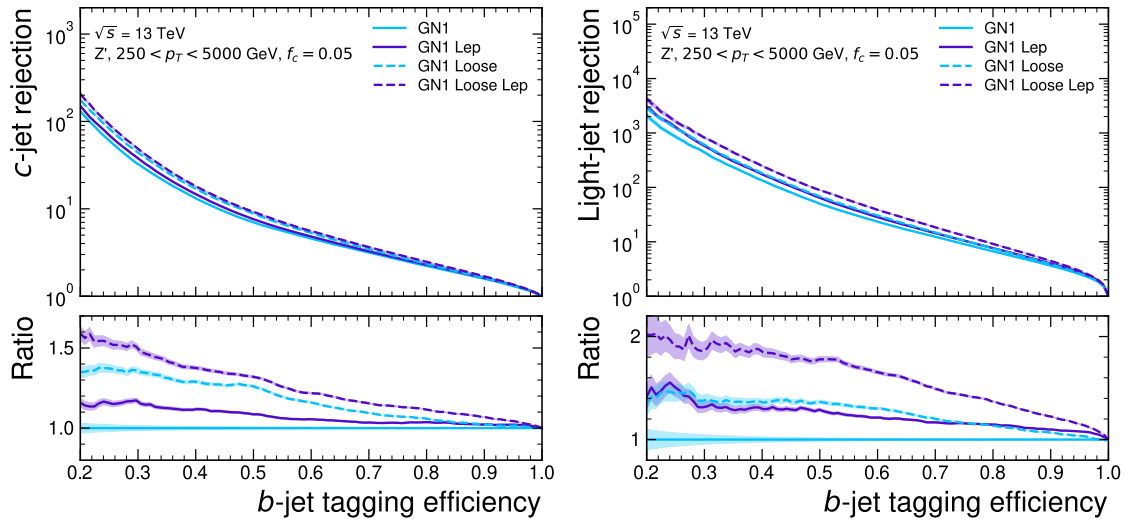


Figure 6.21: The c -jet (left) and light-jet (right) rejections as a function of the b -jet tagging efficiency for Z' jets with $250 < p_T < 5000$ GeV, for the looser track selection trainings of GN1. The ratio to the performance of the baseline GN1 model is shown in the bottom panels. A value of $f_c = 0.05$ is used for all models. Binomial error bands are denoted by the shaded regions.

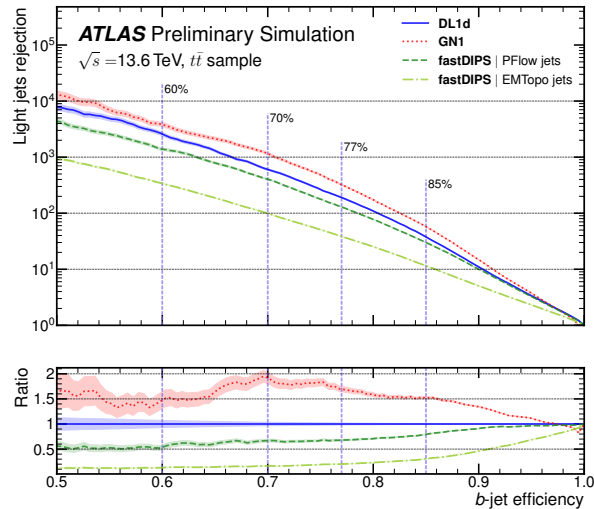


Figure 6.22: The HLT light-jet rejection as a function of the b -jet efficiency jets in the $t\bar{t}$ sample with $20 < p_T < 250 \text{ GeV}$ for events with a centre of mass energy $\sqrt{s} = 13.6 \text{ TeV}$ [125]. The ratio to the performance of the DL1d algorithm [86] is shown in the bottom panels. Binomial error bands are denoted by the shaded regions. The purple vertical dashed lines represent the most common working points used for b -tagging.

1980 DL1d [86], GN1 improves on the c -jet rejection (light-jet rejection) by a factor of ~ 2
1981 (~ 2.5) for jets in the $t\bar{t}$ sample at the 60% b -jet WP. Significant improvements in
1982 rejections are also observed for jets in the Z' sample.

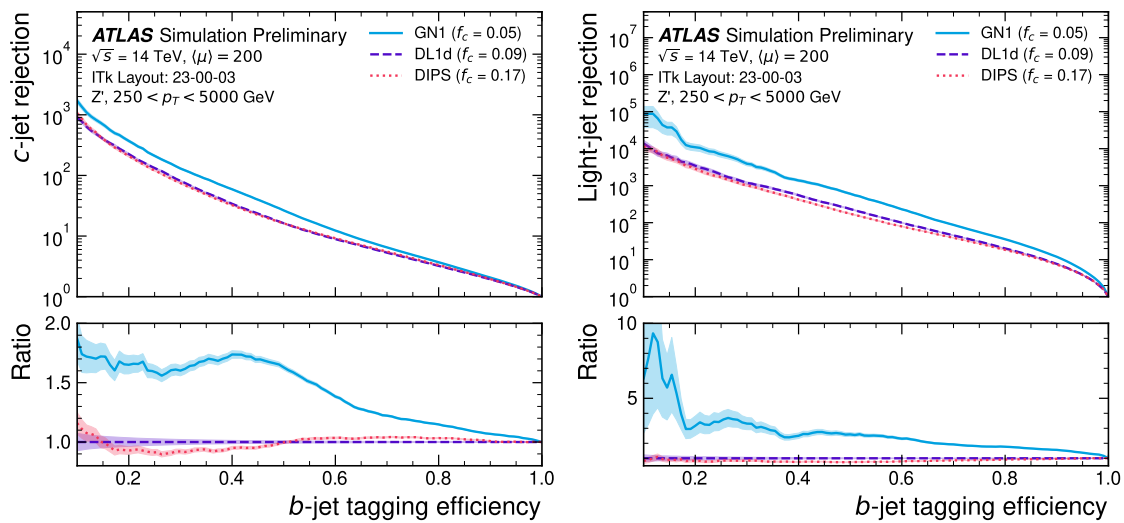
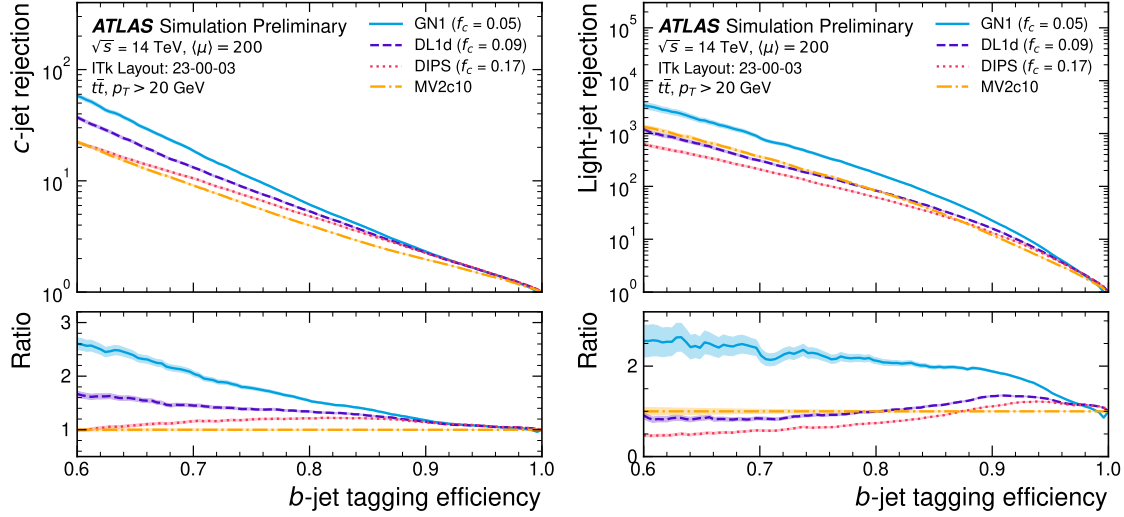
1983 6.7 Conclusion

1984 In this chapter a novel jet tagger, GN1, is presented. The model has a graph neural
1985 network architecture and is trained with auxiliary training objectives, which are
1986 shown to improve the performance of the basic model. GN1 significantly improves
1987 flavour tagging performance with respect to DL1r, the current default ATLAS flavour
1988 tagging algorithm, when compared in simulated collisions. GN1 improves c - and
1989 light-jet rejection for jets in the $t\bar{t}$ sample with $20 < p_T < 250$ GeV by factors of
1990 ~ 2.1 and ~ 1.8 respectively at a b -jet tagging efficiency of 70% when compared with
1991 DL1r. For jets in the Z' sample with $250 < p_T < 5000$ GeV, GN1 improves the
1992 c -jet rejection by a factor of ~ 2.8 and light-jet rejection by a factor of ~ 6 for a
1993 comparative b -jet efficiency of 30%.

1994 Previous multivariate flavour tagging algorithms relied on inputs from low-level
1995 tagging algorithms, whereas GN1 needs no such inputs, making it more flexible.
1996 It can be easily fully optimised via a retraining for specific flavour tagging use
1997 cases, as demonstrated with c -tagging and high- p_T b -tagging, without the need for
1998 time-consuming retuning of the low-level tagging algorithms. The model is also
1999 simpler to maintain and study due to the reduction in the number of constituent
2000 components.

2001 GN1 demonstrates improved track classification performance when compared with a
2002 simple per-track MLP. The model is also able to perform vertex finding, and prelimi-
2003 nary studies suggest it outperforms previous manually optimised approaches. The
2004 auxiliary track classification and vertex finding objectives are shown to significantly
2005 contribute to the performance in the jet classification objective, and, along with the
2006 more advanced graph neural network architecture, are directly responsible for the
2007 improvement over DL1r.

2008 GN1 has also been shown to perform well for b -tagging in the High Level Trigger,
2009 and in the projected environment for the upgraded High Luminosity LHC. The



2010 performance of the model at high- p_T can be improved by loosening the input track
2011 selection, which increases the number of b -hadron decay tracks that are inputted to
2012 the model.

2013 Preliminary validation of the model demonstrates that the level of discrepancy
2014 between different Monte Carlo event generators is similar to that seen for previous
2015 ATLAS ML based taggers such as DL1r, suggesting that the model has not learnt
2016 additional information that is specific to a single event generator. Initial comparisons
2017 between simulated events and data also show similar levels of agreement as for
2018 previous taggers [127].

2019 **Future Work**

2020 Further improvements in the b - and c -tagging performance are likely possible with
2021 a more thorough optimisation of the model architecture, and the integration of
2022 additional information from other parts of the ATLAS detector. The addition of
2023 other auxiliary training objectives, such as the prediction of the truth b -hadron decay
2024 radius and transverse momentum and the truth type of input tracks may also yield
2025 additional performance gains.

2026 Although the results demonstrate a significant performance improvement at high- p_T ,
2027 it is also possible that additional studies on further loosening the selection could yield
2028 further improved results. For example the selections on the number of number of
2029 holes and the longitudinal impact parameter could be further relaxed. The maximum
2030 number of tracks provided as input to the model could also be increased from the
2031 default value of 40. In order to validate the change from the default tracking setup,
2032 studies investigating the modelling uncertainties of the additional tracks need to be
2033 carried out.

2034 Given that GN1 exploits the input information in a more sophisticated way than
2035 DL1r, further studies are needed to confirm that the performance gain observed in
2036 these simulated samples is also observed in experimental data. Additional future
2037 work includes the full calibration of the model so it can be used by physics analyses.

2038 The flexible nature of the model means it can also be readily applied to other related
2039 problems outside of standard b - and c -tagging applications, as demonstrated in
2040 Section 6.6. Additional applications for the architecture include $X \rightarrow bb$ and $X \rightarrow cc$

2041 tagging. The model could also be repurposed as a pile-up jet or τ tagger, or general
2042 primary and secondary vertexing tool. Using a vertex fitting algorithm to compare
2043 the reconstructed vertex quantities with those from SV1 and JetFitter is left for
2044 future work.

2045 Chapter 7

2046 Boosted VHbb Analysis

2047 The Higgs boson, first observed by ATLAS and CMS at the LHC in 2012 [14, 15],
2048 is predicted by the Standard Model to decay primarily to a pair of b -quarks, with
2049 a branching fraction of 0.582 ± 0.007 for $m_H = 125$ GeV [26]. Observation of this
2050 decay mode was reported by ATLAS [79] and CMS [28] in 2018, establishing the
2051 first direct evidence for the Yukawa coupling of the Higgs boson to down-type quarks
2052 (see Section 2.2.2). The $H \rightarrow b\bar{b}$ process is also important for constraining the total
2053 decay width of the Higgs [128].

2054 Whilst the dominant Higgs production mechanism at the LHC is gluon-gluon fusion
2055 as outlined in Section 2.2.3, this mechanism has an overwhelming QCD multijet
2056 background and so overall sensitivity to the Higgs is low. The QCD multijet
2057 background refers to events containing one or more strongly produced jets which
2058 are not the decay product of heavy resonances, for example $g \rightarrow q\bar{q}$. In the $H \rightarrow b\bar{b}$
2059 gluon-gluon fusion channel the vast majority of events will contain only jets in the
2060 final state, and therefore it is extremely difficult to distinguish signal events from the
2061 overwhelming multijet background. The $H \rightarrow b\bar{b}$ observation therefore searched for
2062 Higgs bosons produced in association with a vector boson V (where V can be a W
2063 or Z boson) which subsequently decays leptonically. The leptonic final states allow
2064 for leptonic triggering whilst at the same time significantly reducing the multijet
2065 background.

2066 Two full Run 2 dataset analyses were carried out as a follow-up to the $H \rightarrow b\bar{b}$
2067 observation [79]. Similar to the observation, both measured the associated production
2068 of a Higgs with a vector boson, with the Higgs boson decaying to a pair of b -quarks.
2069 The first analysis [129] was focussed on the resolved phase-space, where the Higgs

2070 candidate is reconstructed as two distinct jets with radius parameter $R = 0.4$.
2071 The second analysis [130] was focussed on the boosted phase-space, where the
2072 Higgs candidate had a sufficiently large transverse momenta such that it can be
2073 reconstructed as a single jet with a radius parameter of $R = 1.0$. This chapter
2074 will focus on the latter analysis, which is referred to as the boosted VH , $H \rightarrow b\bar{b}$
2075 analysis.

2076 In this chapter, the boosted VH , $H \rightarrow b\bar{b}$ analysis is outlined in Section 7.1. An
2077 introduction to the systematic uncertainties used in the analysis is provided in
2078 Section 7.1.6. Detailed information about the modelling studies performed for
2079 the analysis are described in Section 7.3. The statistical treatment is detailed in
2080 Section 7.4, and the results of the analysis are presented in Section 7.5. This analysis
2081 has been published in Ref. [130]. Figures and tables from the published work are
2082 reproduced here.

2083 7.1 Analysis Overview

2084 The boosted VH , $H \rightarrow b\bar{b}$ analysis is focused on the high transverse momentum
2085 regime, which has the benefit of being more sensitive to physics beyond the Standard
2086 Model [131], but the disadvantage of being more challenging due to the increased
2087 difficulty in the accurate reconstruction of high transverse momentum physics objects
2088 (discussed in Chapter 4). In order to focus on the high- p_T regime, the reconstructed
2089 vector boson p_T^V is required to be $p_T^V > 250$ GeV (see Section 7.1.1). Events are
2090 also split into two p_T bins with the first bin covering $250 \text{ GeV} < p_T^V < 400 \text{ GeV}$ and
2091 the second covering $p_T^V > 400$ GeV, which allows the analysis to benefit from the
2092 improved signal-to-background in the high- p_T regime.

2093 The previous ATLAS analysis in Ref. [79] was primarily sensitive to vector bosons
2094 with a more modest p_T^V boost in the region of 150–300 GeV (for the 0- and 1-lepton
2095 channels) and 75–300 GeV (for the 2-lepton channel). In this regime, the Higgs
2096 candidate was reconstructed using a pair of jets with radius parameter of $R = 0.4$,
2097 called small- R jets. However in the high- p_T regime, the decay products of the Higgs
2098 boson become increasingly collimated and the small- R jets may not be individually
2099 resolved. In order to enhance the reconstruction of the Higgs boson candidate, this
2100 analysis uses a large- R jet with radius parameter $R = 1.0$ to reconstruct the Higgs

2101 boson candidate. The Higgs candidate is required to have exactly two ghost-associated
2102 and b -tagged variable-radius track-jets (b -track-jets). The candidate large- R jet is
2103 reconstructed using jet substructure techniques, in particular it is trimmed by
2104 removing soft and wide-angle components, which helps to remove particles from the
2105 underlying event and pile-up collisions [132]. Refer to Section 3.4.3 for more details
2106 on jet reconstruction.

2107 On top of the binning in p_T^V , selected events are further categorised into the 0-, 1-
2108 and 2-lepton channels depending on the number of charged leptons (electrons and
2109 muons) present in the reconstructed final state (also referred to as the 0L, 1L, and 2L
2110 channels respectively). The 0-lepton channel targets the $ZH \rightarrow \nu\nu b\bar{b}$ process, the
2111 1-lepton channel targets $WH \rightarrow \ell\nu b\bar{b}$, and the 2-lepton channel targets $ZH \rightarrow \ell\ell b\bar{b}$,
2112 where ℓ is an electron or muon and ν is a neutrino. Each channel has a dedicated
2113 set of selections which are listed in more detail in Section 7.1.2. Events in the 0- and
2114 1-lepton channels are further split depending on the number of additional small- R
2115 jets not matched to the Higgs candidate. The high-purity signal region (HP SR)
2116 has zero such jets, while the low-purity signal region (LP SR) has one or more, and
2117 therefore absorbs a larger number of background $t\bar{t}$ events. Maintaining a high purity
2118 signal region is important for the extraction of the signal yield. The 0- and 1-lepton
2119 channels also make use of a dedicated $t\bar{t}$ control region for jets with one or more
2120 additional b -tagged small- R jets, described in Section 7.1.3. A complete overview of
2121 the different analysis regions is given in Table 7.1.

2122 The large- R jet mass is used as the main discriminant in the analysis. The signal
2123 VH , $H \rightarrow b\bar{b}$ yields is extracted from a profile likelihood fit to the large- R jet mass
2124 over several signal and control analysis regions, which are described in Sections 7.1.2
2125 and 7.1.3. The diboson background VZ , $Z \rightarrow b\bar{b}$ yield is simultaneously extracted
2126 from the fit, and provides a cross check on the signal extraction. The fit model
2127 (described henceforth only as “the fit”) is described in more detail in described in
2128 Section 7.4.

2129 7.1.1 Object Reconstruction

2130 The presence of neutrinos in the $WH \rightarrow \ell\nu b\bar{b}$ and $ZH \rightarrow \ell\ell b\bar{b}$ signatures can be
2131 inferred from a momentum imbalance in the transverse plane (see Section 3.4.5). The

		Analysis Regions					
		250 < p_T^V < 400 GeV			$p_T^V \geq 400$ GeV		
Channel	0 add. b -track-jets		≥ 1 add. b -track-jets	0 add. b -track-jets		≥ 1 add. b -track-jets	
	0 add. small- R jets	≥ 1 add. small- R jets		0 add. small- R jets	≥ 1 add. small- R jets		
0-lepton	HP SR	LP SR	CR	HP SR	LP SR	CR	
1-lepton	HP SR	LP SR	CR	HP SR	LP SR	CR	
2-lepton	SR			SR			

Table 7.1: Summary of the definitions of the different analysis regions . Signal enriched regions are marked with the label SR. There are regions with relatively large signal purity (HP SR) and with low purity (LP SR). Background enriched control regions are marked with the label CR. The shorthand “add” stands for additional small- R jets, i.e. number of small- R jets not matched to the Higgs-jet candidate. The medium and high p_T^V regions are referred to as Mp_T^V and Hp_T^V , respectively [130].

vector boson transverse momentum p_T^V is reconstructed as the missing transverse energy E_T^{miss} in the 0-lepton channel, as the magnitude of the summed $\mathbf{E}_T^{\text{miss}}$ and charged-lepton momentum in the 1-lepton channel, and as the transverse momentum of the 2-lepton system in the 2-lepton channel.

Electrons and muons are reconstructed and identified as outlined in Section 3.4.4, and following the approach described in Ref. [79]. Leptons are required to satisfy the selections listed in Table 7.2. *Baseline* electrons are required to pass the looser likelihood-based identification selection described in Section 3.4.4, whilst *Signal* electrons are required to satisfy a tighter likelihood identification selection. *Baseline* muons are required to pass the ‘loose’ identification described in Ref. [51], while *signal* muons are required to pass the ‘medium’ identification working point. All signal leptons are required to additionally satisfy a $p_T > 27$ GeV selection criteria, except for muons in the 1-lepton channel where a cut of 25 GeV is used. The number of baseline leptons is used to categorise the event into the 0-, 1- or 2-lepton channels. The 1- and 2-lepton channels additionally require one signal lepton to be present.

The analysis makes use of large- R and variable-radius small- R track-jets, which are described in Section 3.4.3. The large- R jets are required to satisfy $p_T > 250$ GeV and $|\eta| < 2.0$, and are used to reconstruct the Higgs boson candidate, while small- R jets are used for b -tagging and for selection of the analysis region. These track-jets are

Variable	Electrons	Muons
p_T	$> 7 \text{ GeV}$	
$ \eta $	< 2.47	< 2.7
$s(d_0)$	< 5	< 3
$ z_0 \sin(\theta) $	$< 0.5 \text{ mm}$	

Table 7.2: Selections applied to baseline and signal electrons and muons. Signal leptons are additionally required to satisfy a $p_T > 27 \text{ GeV}$ (25 GeV in the 1-lepton channel).

required to have at least two constituent tracks with $p_T > 500 \text{ MeV}$ and $|\eta| < 2.5$, and must themselves satisfy $p_T > 10 \text{ GeV}$ and $|\eta| < 2.5$. The track-jets matched to the Higgs candidate are b -tagged using the MV2c10 b -tagging algorithm (see Chapter 4). The efficiency of the tagging algorithm is calibrated to events in data [133–135]. The jet tagging strategy relies on extensive studies into track-jet b -tagging in boosted topologies [136, 137].

7.1.2 Event Selection

An extensive list of selection cuts are applied to each event in order to reject background events whilst retaining as many signal events as possible. A full list of selection cuts applied to the different analysis regions is given in Table 7.3, while some key selections are listed below.

All channels require events with at least one large- R jet. The vector boson transverse momentum is also required to satisfy $p_T^V > 250 \text{ GeV}$. The Higgs candidate is chosen as the highest p_T large- R jet satisfying these requirements. As mentioned, the candidate large- R jet is required to have two ghost-associated and b -tagged variable-radius track-jets.

In the 0-lepton channel, trigger selections are applied using an E_T^{miss} trigger with a luminosity-dependent threshold that varied between $70\text{--}110 \text{ GeV}$ depending on the data taking period. In the 1-lepton electron sub-channel a combination of single electron triggers is used with minimum p_T thresholds between $24\text{--}26 \text{ GeV}$. In the muon sub-channel the same E_T^{miss} trigger as the 0-lepton channel is used. Since muons are not used for the E_T^{miss} trigger calculations, this is in effect a p_T requirement on

2173 the muon-neutrino system, which in the analysis phase space is more efficient than a
2174 single-muon trigger. The 2-lepton channel uses the same triggering strategy as the
2175 1-lepton channel. In all channels, the trigger selections applied are fully efficient for
2176 events selected using the full requirements in Table 7.3.

2177 The combined selections in Table 7.3 result in a signal efficiency ranging from 6–16%
2178 for the WH and ZH processes depending on the channel and p_T^V bin.

2179 7.1.3 Control Regions

2180 The $t\bar{t}$ process presents a major background in the 0- and 1-lepton channels. In these
2181 events, the Higgs candidate is often reconstructed from a correctly tagged b -jet from
2182 the top decay $t \rightarrow Wb$, and an incorrectly tagged c - or light-jet from the subsequent
2183 decay of the W , as shown in Fig. 7.1.

2184 The top quark decays to a W and a b -quark the vast majority of the time. Hence,
2185 the second top quark from the $t\bar{t}$ pair is also likely to result in a second tagged
2186 b -tagged track-jet outside of the large- R Higgs candidate. To ensure sufficient $t\bar{t}$
2187 rejection, 0- and 1-lepton channel signal regions are defined using a veto on events
2188 with b -tagged track-jets outside the Higgs candidate. These events are used to
2189 construct a control region (CR) which is enriched in $t\bar{t}$ events. The CR is used to
2190 constrain the normalisation of the $t\bar{t}$ background in the fit.

2191 7.1.4 Background Composition

2192 After the selections described in Section 7.1.2 the number of background events
2193 mimicking the VH , $H \rightarrow b\bar{b}$ signal is greatly reduced. However, the number of
2194 background events still greatly outnumbers that of signal events. The background
2195 processes are channel dependent. In the 0-lepton channel the dominant sources of
2196 backgrounds are Z +jets ($Z \rightarrow \nu\nu$) and $t\bar{t}$, with W +jets and diboson events being
2197 subdominant. W +jets contribute in the event of $W \rightarrow \tau\nu$, and subsequent hadronic
2198 decay of the τ or lack of successful reconstruction/selection of the leptonic decay
2199 products. $t\bar{t}$ and W +jets (with a leptonic decay of the W as in $W \rightarrow \ell\nu$) are
2200 dominant in the 1-lepton channel, while single-top is subdominant. In the 2-lepton
2201 channel, Z +jets ($Z \rightarrow \ell\ell$) is again dominant followed by ZZ diboson events.

Selection	0 lepton channel	1 lepton channel	2 leptons channel
Trigger	E_T^{miss}	e sub-channel μ sub-channel	e sub-channel μ sub-channel
Leptons	0 <i>baseline</i> leptons	Single electron 1 <i>signal</i> lepton $p_T > 27 \text{ GeV}$	Single electron 2 <i>baseline</i> leptons among which $p_T > 25 \text{ GeV}$ no second <i>baseline</i> lepton ≥ 1 <i>signal</i> lepton, $p_T > 27 \text{ GeV}$ both leptons of the same flavour -
E_T^{miss}	$> 250 \text{ GeV}$	$> 50 \text{ GeV}$	-
p_T^V		$p_T^V > 250 \text{ GeV}$	-
Large- R jets		at least one large- R jet, $p_T > 250 \text{ GeV}, \eta < 2.0$	
Track-jets		at least two track-jets, $p_T > 10 \text{ GeV}, \eta < 2.5$, matched to the leading large- R jet	
<i>b</i> -tagged jets		leading two track-jets matched to the leading large- R must be <i>b</i> -tagged (MV2c10, 70%)	
m_J			$> 50 \text{ GeV}$
$\min[\Delta\phi(\mathbf{E}_T^{\text{miss}}, \text{small-}R \text{ jets})]$	$> 30^\circ$		-
$\Delta\phi(\mathbf{E}_T^{\text{miss}}, H_{\text{cand}})$	$> 120^\circ$		-
$\Delta\phi(\mathbf{E}_T^{\text{miss}}, \mathbf{E}_{T,\text{trk}}^{\text{miss}})$	$< 90^\circ$		-
$\Delta y(V, H_{\text{cand}})$	-		$ \Delta y(V, H_{\text{cand}}) < 1.4$
$m_{\ell\ell}$			$66 \text{ GeV} < m_{\ell\ell} < 116 \text{ GeV}$
Lepton p_T imbalance			$(p_T^{\ell_1} - p_T^{\ell_2})/p_T^Z < 0.8$

Table 7.3: Event selection requirements for the boosted VH , $H \rightarrow b\bar{b}$ analysis channels and sub-channels [130]. Various channel dependent selections are used to maximise the signal efficiency and reduce the number of background events in each analysis region. The $\min[\Delta\phi(\mathbf{E}_T^{\text{miss}}, \text{small-}R \text{ jets})]$ selection is used to remove jets when the missing transverse momentum $\mathbf{E}_T^{\text{miss}}$ is pointing in the direction of the Higgs candidate, and the $\Delta\phi(\mathbf{E}_T^{\text{miss}}, \mathbf{E}_{T,\text{trk}}^{\text{miss}})$ is used to reject events where the calorimeter missing transverse momentum $\mathbf{E}_T^{\text{miss}}$ is not pointing in the direction of the track-based missing transverse momentum $\mathbf{E}_{T,\text{trk}}^{\text{miss}}$. The $\Delta y(V, H_{\text{cand}})$ quantifies the rapidity difference between the reconstructed vector boson and Higgs candidate (H_{cand}). $m_{\ell\ell}$ refers to the invariant mass of the two leptons, while $p_T^{\ell_1}$ and $p_T^{\ell_2}$ refer to the p_T of the first and second leptons, respectively.

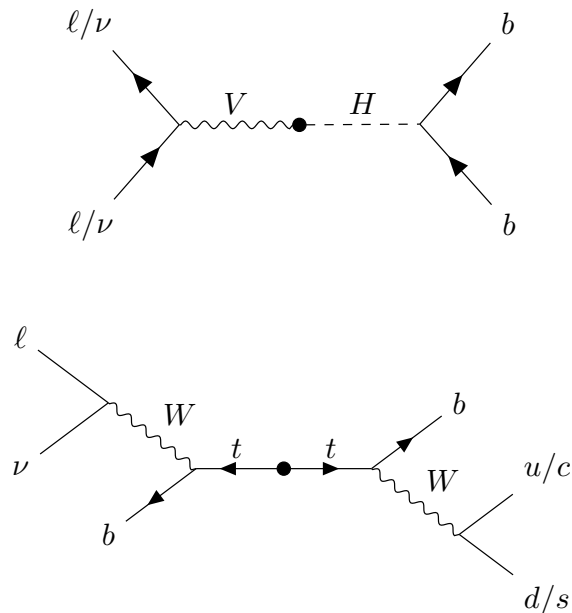


Figure 7.1: Diagrams of the signal process (top) and $t\bar{t}$ background (bottom). The object to the right of centre are reconstructed within the large- R jet. For the $t\bar{t}$ background, the large- R jet contains a mistagged c -jet or (less often) a mistagged light-jet. The contribution in the 0-lepton channel results from hadronically decaying τ lepton, or a electron or muon which is out of the analysis acceptance. For the $t\bar{t}$ background process to be in the signal region, the b -jet on the left hand side must either be not within acceptance, not reconstructed, or not tagged.

- 2202 The diboson background VV consists primarily of WZ and ZZ events in which the
2203 Z decays to a pair of b -quarks. This process very closely matches the signal, with a
2204 resonant peak occurring at $m_Z = 91\text{ GeV}$. As it is a well understood process, the
2205 diboson background can be used as a cross-check on the Higgs results.
- 2206 The $t\bar{t}V$, $t\bar{t}H$ and multijet backgrounds are negligible in the analysis phase space
2207 after the selections have been applied, with the exception of the 1-lepton electron
2208 sub-channel, in which multijet background is not negligible. The multijet background
2209 in this region is generally made up of events where the isolated leptonic signature
2210 has been mimicked by either a jet or electron from a semi-leptonic heavy flavour
2211 decay, where the electron has escaped the jet.
- 2212 The contributions from the different backgrounds are modelled using Monte Carlo
2213 event generators and the uncertainties associated with these samples are studied in
2214 Section 7.3. The multijet background is modelled using a data-driven technique.

2215 7.1.5 Data & Simulated Samples

- 2216 Data from centre-of-mass energy $\sqrt{s} = 13\text{ TeV}$ proton-proton collisions at the LHC
2217 recorded over the course of Run 2 (between 2015 and 2018) were used for the analysis.
2218 The resulting dataset corresponds to a total integrated luminosity of 139 fb^{-1} .
- 2219 An overview of the MC simulated samples used in the analysis is given in Table 7.4.
2220 These samples are used to model the signal and background processes relevant to the
2221 analysis, with the exception of the multijet background which is modelled using a
2222 data-driven technique. Data and simulated events are reconstructed using the same
2223 algorithms, and a reweighting is applied to the simulated events in order to match
2224 the pile-up distribution observed in the data.

2225 7.1.6 Overview of Systematic Uncertainties

- 2226 Systemic uncertainties are extensively employed to reflect assumptions and inaccura-
2227 cies in the various inputs used by the fit. Two main types of systematic uncertainty
2228 are considered: experimental and modelling. Experimental uncertainties arise due
2229 to the imperfect modelling of the reconstruction algorithms (in particular the jet
2230 reconstruction and b -tagging algorithms), and due to the imperfect modelling of

Process	ME generator	ME PDF	PS and Hadronisation	UE model tune	Cross-section order
Signal ($m_H = 125$ GeV and $b\bar{b}$ branching fraction set to 58%)					
$qg \rightarrow W H \rightarrow \ell\nu b\bar{b}$	POWHEG-Box v2 [138] + GoSam [140] + MiNLO [141, 142]	NNPDF3.0NLO ^(*) [91]	Pythia 8.212 [93]	AZNLO	NNLO(QCD) + NLO(EW) [143–149]
$qq \rightarrow ZH \rightarrow \nu\nu b\bar{b}/\ell\ell b\bar{b}$	POWHEG-Box v2 + GoSam + MiNLO	NNPDF3.0NLO ^(*)	Pythia 8.212	AZNLO	NNLO(QCD) ^(†) + NLO(EW)
$gg \rightarrow ZH \rightarrow \nu\nu b\bar{b}/\ell\ell b\bar{b}$	POWHEG-Box v2	NNPDF3.0NLO ^(*)	Pythia 8.212	AZNLO	NLO+ NLL [150–154]
Top quark ($m_t = 172.5$ GeV)					
$t\bar{t}$	POWHEG-Box v2 [138, 155]	NNPDF3.0NLO	Pythia 8.230	A14 [94]	NNLO+NNLL [156]
s -channel	POWHEG-Box v2 [138, 157]	NNPDF3.0NLO	Pythia 8.230	A14	NLO [158]
t -channel	POWHEG-Box v2 [138, 157]	NNPDF3.0NLO	Pythia 8.230	A14	NLO [159]
Wt	POWHEG-Box v2 [138, 160]	NNPDF3.0NLO	Pythia 8.230	A14	Approximate NNLO [161]
Vector boson + jets					
$W \rightarrow \ell\nu$	SHERPA 2.2.1 [162–165]	NNPDF3.0NNLO	SHERPA 2.2.1 [166, 167]	Default	NNLO [168]
$Z/\gamma^* \rightarrow \ell\ell$	SHERPA 2.2.1	NNPDF3.0NNLO	SHERPA 2.2.1	Default	NNLO
$Z \rightarrow \nu\nu$	SHERPA 2.2.1	NNPDF3.0NNLO	SHERPA 2.2.1	Default	NNLO
Diboson					
$qq \rightarrow WW$	SHERPA 2.2.1	NNPDF3.0NNLO	SHERPA 2.2.1	Default	NLO
$qq \rightarrow WZ$	SHERPA 2.2.1	NNPDF3.0NNLO	SHERPA 2.2.1	Default	NLO
$qq \rightarrow ZZ$	SHERPA 2.2.1	NNPDF3.0NNLO	SHERPA 2.2.1	Default	NLO
$gg \rightarrow VV$	SHERPA 2.2.2	NNPDF3.0NNLO	SHERPA 2.2.2	Default	NLO

Table 7.4: Signal and background processes with the corresponding generators used for the nominal samples [130]. If not specified, the order of the cross-section calculation refers to the expansion in the strong coupling constant (α_s). ^(*) The events were generated using the first PDF in the NNPDF3.0NLO set and subsequently reweighted to the PDF4LHC15NLO set [169] using the internal algorithm in POWHEG-BOX v2. ^(†) The NNLO(QCD)+NLO(EW) cross-section calculation for the $pp \rightarrow ZH$ process already includes the $gg \rightarrow ZH$ contribution. The $qg \rightarrow ZH$ process is normalised using the cross-section for the $pp \rightarrow ZH$ process, after subtracting the $gg \rightarrow ZH$ contribution. An additional scale factor is applied to the $qg \rightarrow VH$ processes as a function of the transverse momentum of the vector boson, to account for electroweak (EW) corrections at NLO. This makes use of the VH differential cross-section computed with HAWK [170, 171].

pile-up and other effects, as described in Section 7.2. Modelling uncertainties arise due to the imperfections in the Monte-Carlo generators used to model the signal and background events. In order to observe a certain process, for example VH , $H \rightarrow b\bar{b}$, an increase in the number of observed events with respect to the background-only hypothesis is looked for. The excess is often relatively small against the total number of background events, and hence accurate modelling of the expected number of background and signal events is crucial for successfully performing the analysis.

7.2 Experimental Uncertainties

The main experimental uncertainties in the analysis are due to the modelling of following sources:

- The small- R jet energy scale and resolution, which are informed by in situ calibration studies [69].
- The large- R jet energy and mass scales and resolutions. The scales are calibrated as described in Ref. [73], and an uncertainty of 2% and 20% is applied for the jet energy and mass resolutions, respectively.
- b -tagging uncertainties, which are computed separately for b -, c - and light-flavour jets as described in the data-based calibration studies in Refs. [133–135]. An additional extrapolation uncertainty is added to account for jets with transverse momenta above that which is accessible in the calibration analyses.
- Uncertainties associated with the lepton energy and momentum scales, and reconstruction and identification efficiencies.
- Uncertainty on the pile-up models which are used in the simulated samples, described in Ref. [172].
- Uncertainties associated with the reconstruction of the missing transverse energy E_T^{miss} , as described in Ref. [78].
- Uncertainty on the total recorded integrated luminosity, as described in Ref. [40].

The impact of these uncertainties on the analysis can be found in Table 7.16.

2258 7.3 Background Modelling

2259 Particular care is paid to the uncertainties on the modelling predictions as discussed
2260 in the following sections. The *Nominal* MC samples are used as a reference to
2261 which different variations can be compared. The nominal samples are chosen as the
2262 best possible representation of the underlying physical process. *Alternative* samples
2263 are used to understand inaccuracies that may be present in the nominal samples.
2264 Some aspect of the nominal model is varied, and the discrepancy with respect to
2265 the nominal model is quantified. The discrepancy is used to estimate a systematic
2266 uncertainty associated with the model parameter which was varied. The alternate
2267 samples are sometimes obtained via internal weight variations or parameterisation
2268 methods, rather than by re-running the simulation. This is discussed in more detail
2269 in Section 7.3.3.

2270 Modelling systematics can have several impacts, including affecting the overall
2271 normalisation for different processes, the relative acceptances between different
2272 analysis regions (i.e. migrations between HP and LP SRs, between the SR and
2273 CR, and between p_T^V bins), and the shapes of the m_J distributions. For each
2274 source of uncertainty, acceptance and shape uncertainties are therefore derived.
2275 Acceptance uncertainties account for the uncertainty in the overall number of events
2276 in each channel, and for the relative numbers of events in the various analysis
2277 regions. Meanwhile, shape uncertainties account for the uncertainty on the kinematic
2278 distributions of the events, but not overall normalisations. They are measured for
2279 the shape of the large- R jet mass distribution, since this is the variable used in the
2280 fit to data.

2281 In this section, truth tagging, the method used to ensure sufficient numbers of jets
2282 are available to calculate uncertainties, is described in Section 7.3.1. The different
2283 sources of background modelling uncertainty which have been assessed are described
2284 in Section 7.3.2, and details of their implementations are found in Section 7.3.3.
2285 Full descriptions of the modelling uncertainties applied for the $V+jets$ and diboson
2286 backgrounds are given in Section 7.3.4 and Section 7.3.5, respectively.

2287 7.3.1 Truth Tagging

2288 Modelling studies involving c - and light-jets is hampered by the low number of events
2289 available after the analysis selection is applied, due to the high rejection rates of the
2290 b -tagging algorithm MV2c10. For modelling studies, truth tagging (TT) is therefore
2291 employed to ensure sufficient numbers of jets are available to calculate uncertainties.
2292 TT works by computing a 2-dimensional efficiency map using the jet p_T and η . The
2293 two leading track-jets associated to the large- R jet are weighted based on their
2294 probability to pass the b -tagging selection, rather than being required to explicitly
2295 pass the b -tagging requirement. The probability to pass the b -tagging selection is
2296 parameterised by the jet p_T and η , and is extracted using a pre-calculated efficiency
2297 map.

2298 7.3.2 Sources of Systematic Modelling Uncertainties

2299 This section briefly describes the different sources of uncertainty in the analysis, and
2300 how each is implemented.

2301 QCD Scales

2302 The $V+jets$ matrix element calculations contains infrared and ultraviolet divergences.
2303 These are handled by introducing arbitrary parameters corresponding to the renormalisation scale (μ_R) and factorisation scale (μ_F). Physical observables are not
2304 dependent on these parameters when using the infinite perturbation series expansion,
2305 however at some fixed order in QCD a limited is present. To assess the impact of
2306 this, both μ_R and μ_F are independently varied from their nominal values by factors
2307 of 0.5 and 2 to account for higher order corrections to the calculation of the matrix
2308 element used to simulate the process.

2310 PDF Sets

2311 Parton distribution functions (PDFs) specify the probability of finding a parton with
2312 a given momentum inside a hadron (in this case, colliding protons). PDFs have
2313 to be derived from data and are a significant source of uncertainty in analyses of

hadronic collision data. There are three sources of PDF uncertainties: the statistical and systematic errors on the underlying data used to derive the PDFs, the theory which is used to describe them (which is based on some fixed order perturbative QCD expansion), and finally the procedure which is used to extract the PDFs from the data. PDF-related uncertainties were derived following Ref. [169]. This involves considering 100 PDF replicas which, when combined, form a central value and associated uncertainty, and also in parallel direct changes to the central values of PDFs using the MMHT2014 [173] and CT14NLO [174] PDF sets.

Event Generator

The choice of parton shower (PS) and underlying event (UE) generators can affect the analysis outcome. Changing these models modifies several aspects of the event generation at the same time, such as the accuracy of matrix element predictions and different approaches to parton showering. This change tends to lead to the largest discrepancy with respect to the nominal samples.

Resummation and Merging Scales

Resummation is a technique used in QCD to help cope with calculations involving disparate energy scales, and involves the introduction of an associated resummation scale, the choice of which introduces some systematic uncertainty into the model. Parton showering models are accurate when simulating low- p_T radiation, however inaccuracies start to arrive when simulating hard emissions. To combat this, parton showering models utilise more precise matrix element calculations above some momentum threshold. The choice of threshold, or *merging scale* introduces some uncertainty into the final result. Resummation (QSF) and merging (CKKW) scale variations are available for a subset of the SHERPA samples. The number of available events is significantly lower than the number of events in the nominal sample, and no statistically significant discrepancy with respect to the nominal samples is observed. The corresponding uncertainties and therefore neglected.

7.3.3 Implementation of Variations

Modelling variations are implemented in various ways, depending on the associated uncertainty. Table 7.5 lists the different sources of uncertainty described in Section 7.3.2 and for each lists the implementation.

Source of Uncertainty	Implementation
Renormalisation scale (μ_R)	Internal weights
Factorisation scale (μ_F)	Internal weights
PDF set	Internal weights
Parton Shower (PS) models	Alternative samples
Underlying Event (UE) models	Alternative samples
Resummation scale (QSF)	Parameterisation
Merging scale (CKKW)	Parameterisation

Table 7.5: Different sources of uncertainty (i.e. variations in the model) considered for the $V+jets$ background, and the corresponding implementation. For each uncertainty, acceptance and shape uncertainties are derived.

As production of large numbers of MC events is computationally expensive, a technique in state of the art simulation packages is to store some sources of variation as internal weights, which can be generated alongside the nominal samples, saving computation time. The nominal sample then effectively contains information about an ensemble of different samples, corresponding to different model parameters, which are accessible via reweightings.

While the inclusion of internal weight variation in some MC event generators has decreased simulation times and increased available statistics, there are currently some sources of systematic uncertainty that are unable to be stored as internal weight variations due to technical limitations in some of these generators. Two examples are the choice of resummation and merging scales. A method to parameterise the systematic variation using one sample, and to then apply this parameterisation to another sample, has been developed by ATLAS [175]. This method was used to derive resummation and merging uncertainties for the nominal SHERPA 2.2.1 sample, using a previous SHERPA 2.1 alternate sample. The resulting uncertainties were studied and found to be negligible in comparison with systematics from other sources.

7.3.4 Vector Boson + Jets Modelling

- After event selection, the $V+jets$ background is a dominant background in all three analysis channels as described in Section 7.1.4. The $V+jets$ samples are split into categories depending on the truth flavour of the track-jets which are ghost-associated to the large- R jet Higgs candidate. The categories are $V+bb$, $V+bc$, $V+bl$, $V+cc$, $V+cl$, $V+ll$, and $V+hf$ refers collectively to the bb , bc , bl , and cc categories. $V+bb$ is dominant generally accounting for 80% of the events, while $V+hf$ accounts for around 90% of the events. The full flavour composition breakdown for each channel and analysis region are given in Tables 7.6, 7.8 and 7.9.
- The nominal MC event generator used for $V+jets$ events is SHERPA 2.2.1, while MADGRAPH5_AMC@NLO+PYTHIA8 (which uses a different parton showering model) is used as an alternative generator.

Sample	Mp_T^V HP SR	Hp_T^V HP SR	Mp_T^V LP SR	Hp_T^V LP SR	Mp_T^V CR	Hp_T^V CR
Wbb	$79.3\% \pm 4.4\%$	$75.0\% \pm 8.6\%$	$77.4\% \pm 2.5\%$	$71.7\% \pm 4.5\%$	$68.0\% \pm 7.6\%$	$63.5\% \pm 14.0\%$
Wbc	$6.6\% \pm 0.9\%$	$3.4\% \pm 1.7\%$	$6.2\% \pm 0.5\%$	$5.3\% \pm 0.9\%$	$14.5\% \pm 3.2\%$	$3.4\% \pm 3.2\%$
Wbl	$3.9\% \pm 0.9\%$	$11.4\% \pm 3.5\%$	$4.5\% \pm 0.5\%$	$8.7\% \pm 1.4\%$	$9.8\% \pm 2.2\%$	$9.1\% \pm 3.8\%$
Wcc	$5.1\% \pm 1.7\%$	$6.8\% \pm 2.4\%$	$7.1\% \pm 1.0\%$	$6.3\% \pm 1.4\%$	$4.2\% \pm 2.4\%$	$12.3\% \pm 7.0\%$
Wcl	$2.3\% \pm 1.4\%$	$2.4\% \pm 2.1\%$	$3.4\% \pm 0.7\%$	$5.2\% \pm 1.5\%$	$2.6\% \pm 1.5\%$	$3.4\% \pm 2.1\%$
Wl	$2.9\% \pm 1.0\%$	$0.9\% \pm 1.6\%$	$1.3\% \pm 0.7\%$	$2.8\% \pm 0.7\%$	$0.9\% \pm 0.6\%$	$8.4\% \pm 5.1\%$
Events	187.5 ± 7.7	38.2 ± 3.1	429.5 ± 10.0	97.8 ± 4.2	33.8 ± 2.5	8.3 ± 1.2

Table 7.6: 0-lepton $W+jets$ nominal sample flavour composition and total event yield [176]. Mp_T^V refers to the medium p_T^V region, and Hp_T^V refers to the high p_T^V region (see Table 7.1).

Sample	Mp_T^V HP SR	Hp_T^V HP SR	Mp_T^V LP SR	Hp_T^V LP SR	Mp_T^V CR	Hp_T^V CR
Wbb	$77.2\% \pm 2.6\%$	$72.4\% \pm 4.3\%$	$77.8\% \pm 1.8\%$	$69.3\% \pm 2.5\%$	$64.6\% \pm 4.9\%$	$53.5\% \pm 6.3\%$
Wbc	$7.4\% \pm 0.7\%$	$7.3\% \pm 1.1\%$	$6.6\% \pm 0.4\%$	$6.3\% \pm 0.6\%$	$13.7\% \pm 1.9\%$	$16.4\% \pm 3.7\%$
Wbl	$4.0\% \pm 0.5\%$	$6.7\% \pm 1.1\%$	$5.1\% \pm 0.3\%$	$8.7\% \pm 0.8\%$	$10.3\% \pm 1.7\%$	$14.6\% \pm 3.0\%$
Wcc	$6.2\% \pm 1.1\%$	$5.5\% \pm 1.7\%$	$6.6\% \pm 0.6\%$	$6.4\% \pm 0.7\%$	$4.5\% \pm 1.7\%$	$9.5\% \pm 3.0\%$
Wcl	$3.6\% \pm 0.8\%$	$4.2\% \pm 1.8\%$	$2.8\% \pm 0.5\%$	$6.2\% \pm 0.8\%$	$4.6\% \pm 1.2\%$	$4.4\% \pm 1.5\%$
Wl	$1.5\% \pm 0.5\%$	$3.9\% \pm 1.3\%$	$1.1\% \pm 0.2\%$	$3.1\% \pm 0.5\%$	$2.3\% \pm 1.2\%$	$1.6\% \pm 0.6\%$
Events	477.1 ± 11.7	147.5 ± 6.4	784.7 ± 12.3	301.8 ± 7.2	68.7 ± 3.5	26.9 ± 2.0

Table 7.7: 1-lepton $W+jets$ nominal sample flavour composition and total event yield [176]. Mp_T^V refers to the medium p_T^V region, and Hp_T^V refers to the high p_T^V region (see Table 7.1).

Channel	Mp_T^V HP SR	Hp_T^V HP SR	Mp_T^V LP SR	Hp_T^V LP SR	Mp_T^V CR	Hp_T^V CR
Zbb	84.56%	81.84%	82.37%	76.06%	66.12%	63.18%
Zbc	6.03%	6.98%	5.80%	7.46%	15.04%	14.30%
Zbl	4.06%	6.55%	3.83%	6.59%	12.66%	12.81%
Zcc	3.68%	3.40%	5.82%	3.75%	3.36%	3.38%
Zcl	1.23%	0.44%	1.47%	3.97%	1.82%	4.95%
Zl	0.44%	0.78%	0.70%	2.16%	1.00%	1.38%
Events	259.91 ± 4.86	66.12 ± 2.04	420.45 ± 5.73	141.97 ± 2.50	43.49 ± 1.73	16.07 ± 0.83

Table 7.8: 0-lepton $Z+jets$ nominal sample flavour composition and total event yield [176]. Mp_T^V refers to the medium p_T^V region, and Hp_T^V refers to the high p_T^V region (see Table 7.1).

Channel	Mp_T^V	Hp_T^V	p_T^V inclusive
Zbb	80.80%	76.95%	79.76%
Zbc	8.10%	6.26%	7.60%
Zbl	4.95%	7.06%	5.52%
Zcc	3.97%	4.46%	4.10%
Zcl	1.61%	3.60%	2.14%
Zll	0.57%	1.68%	0.87%
Events	115.49 ± 2.42	42.42 ± 1.27	157.92 ± 2.73

Table 7.9: 2-lepton $Z+jets$ nominal sample flavour composition and total event yield [176]. Mp_T^V refers to the medium p_T^V region, and Hp_T^V refers to the high p_T^V region (see Table 7.1).

$V+jets$ Acceptance Uncertainties

Several different types of acceptance uncertainties have been calculated and implemented as nuisance parameters in the fit. These account for the uncertainty in the overall number of events in each channel, and for the migration of events between different analysis regions. The acceptance uncertainties relevant to the $V+jets$ processes are summarised below.

- **Overall normalisation:** only relevant where normalisation cannot be left unconstrained (or “floating”, i.e. determined as part of the fit). The $V+hf$ component is left floating in the fit, with independent normalisations used for $W+hf$ and $Z+hf$. The normalisations are mainly determined by the 1-lepton (for $W+hf$) and 2-lepton (for $Z+hf$) regions respectively and then extrapolated to the 0-lepton channel. The negligible $V+jets$ backgrounds were constrained to their cross-sections in the fit.
- **SR-to-CR relative acceptance:** the uncertainty on the relative number of $V+jets$ events in the signal and control regions.
- **HP-to-LP relative acceptance:** the uncertainty on the relative number of $V+jets$ events in the HP and LP SRs.
- **Medium-to-high p_T^V relative acceptance:** the uncertainty on the relative number of $V+jets$ events in the medium and high p_T^V bins.
- **Flavour relative acceptance:** for each flavour $V+xx$, where $xx \in \{bc, bl, cc\}$ the ratio of $V+xx/V+bb$ events is calculated. This corresponds to the uncertainty on the heavy flavour composition of the $V+hf$ background.
- **Channel relative acceptance:** the uncertainty on the relative number of $V+jets$ events between the channels.

The uncertainties arising from the different sources described in Section 7.3.2 are summed in quadrature to give a total uncertainty on each region. A summary of the different acceptance uncertainties that were derived and subsequently applied in the fit are given in Table 7.10. An effort has been made, wherever possible, to harmonise similar uncertainties across different analysis regions and channels.

V+jets Acceptance Uncertainties				
Boson	W		Z	
Channel	0L	1L	0L	2L
SR-to-CR	90% [†]	40% [†]	40%	-
HP-to-LP SR		18%	18%	-
Medium-to-high p_T^V	30%	10%*	10%	
Channel relative acceptance	20%	-	16%	-
Vbc/Vbb		30%		
Vbl/Vbb		30%		
Vcc/Vbb		20%		
Vcl Norm.		30%		
VI Norm.		30%		

Table 7.10: $V+jets$ acceptance uncertainties [176]. $W+jets$ SR and CR uncertainties marked with a superscript † are correlated. The 1L $W+jets$ medium-to-high p_T^V uncertainty marked by * is applied as independent and uncorrelated NPs in both HP and LP signal regions.

$V+jets$ Shape Uncertainties

In order to derive shape uncertainties for a given background or signal process, normalised distributions of the reconstructed large- R Higgs candidate jet mass m_J are compared for the nominal sample and variations. For each variation, the ratio of the variation to nominal is calculated, the up and down variations are symmetrised, and an analytic function is used to parameterise the ratio. If different analysis regions or channels show the same pattern of variation, a common uncertainty is assigned.

An example of a significant source of uncertainty, arising from the choice of factorisation scale μ_R is shown in Fig. 7.2. The HP SRs in the medium and high p_T^V bins are shown for the 0-lepton channel for the $W+hf$ and $Z+hf$ jet backgrounds. The 0- and 1-lepton channels for the $W+hf$ contribution and the 0- and 2-lepton channels for the $Z+jets$ contribution were found to have compatible shapes in m_J , and so were jointly measured. An exponential function $e^{p_0 + p_1 x} + p_2$ has been fitted to the ratio of the normalised distributions. The magnitude of the variation is p_T^V dependent, and so separate uncertainties are implemented in the fit for each p_T^V region.

²⁴¹⁷ The shape uncertainties for μ_R were derived on the SRs but are also applied to the
²⁴¹⁸ CRs, as the low statistics in the CRs make it difficult to derive dedicated shape
²⁴¹⁹ uncertainties. All the shape uncertainties are fully correlated across regions.

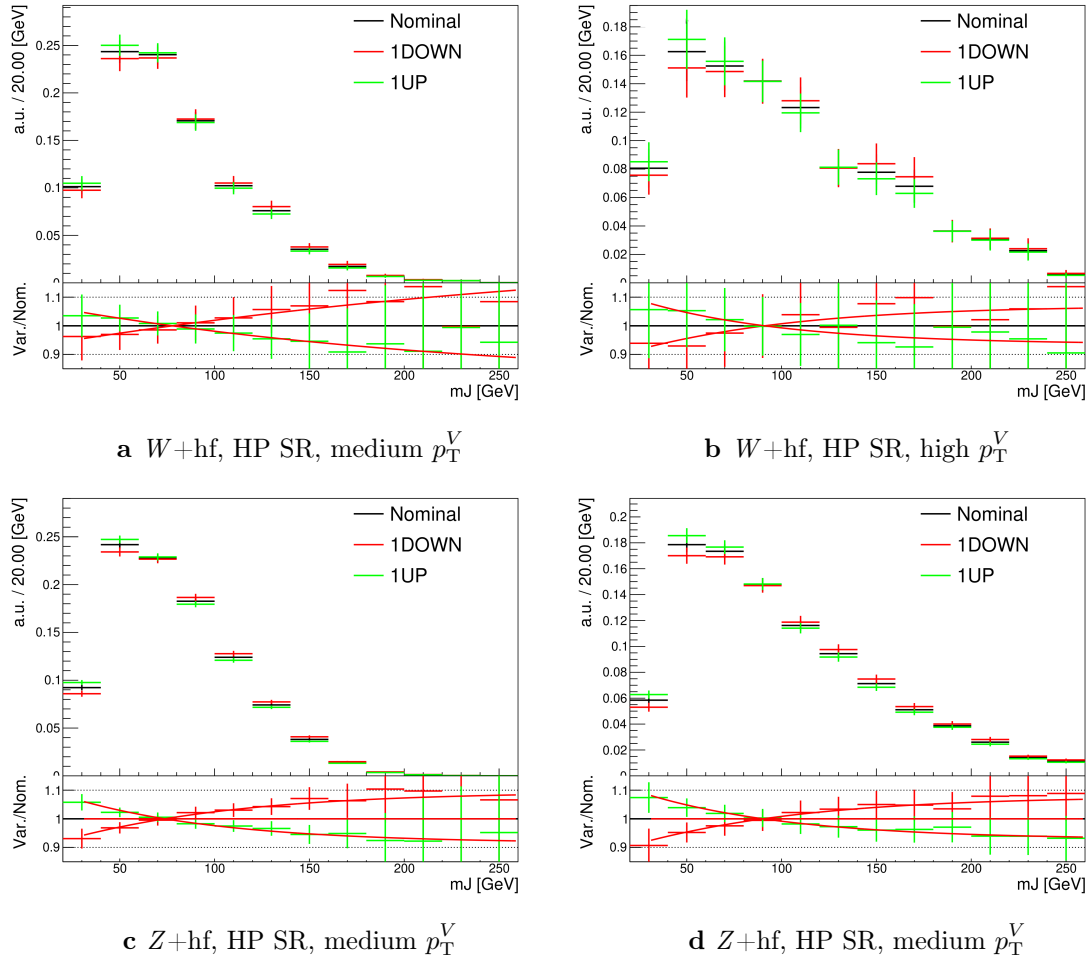


Figure 7.2: Leading large- R jet mass for the Z and $W+hf$ processes in the HP SR of the 0-lepton channel [176]. The renormalisation scale μ_r has been varied by a factor of 0.5 (1DOWN) and 2 (1UP). An exponential function is fitted to the ratio between the nominal and alternate samples.

²⁴²⁰ As an example where no significant deviation is seen, a comparison of the m_J shapes
²⁴²¹ between SHERPA and MADGRAPH is shown in Fig. 7.3. The plots are split by process
²⁴²² and channel, but merged in SR and p_T^V bins reflecting similarities between the m_J
²⁴²³ shapes and variations. Due to the lack of statistically significant variation between
²⁴²⁴ the samples, no additional shape uncertainty was added to the fit in this case.

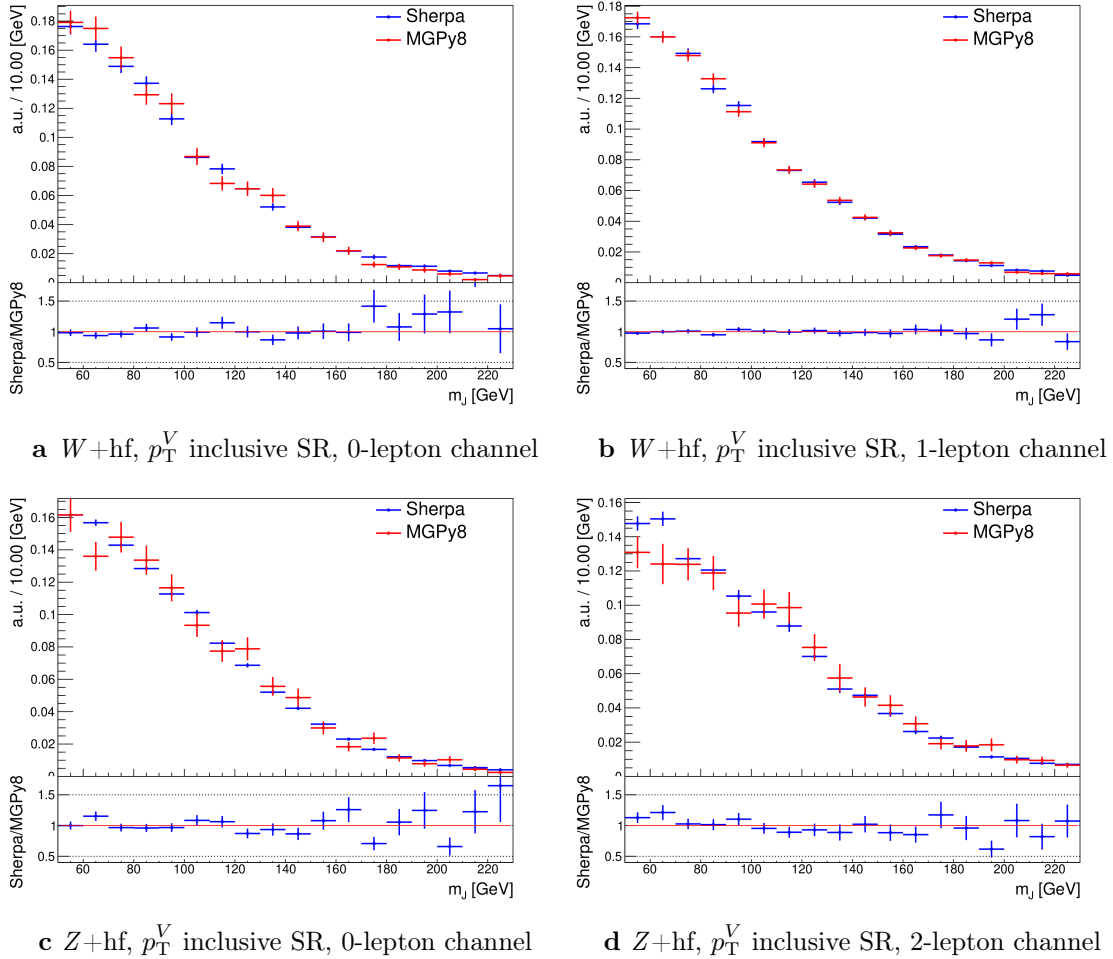


Figure 7.3: Leading large- R jet m_J inclusive in p_T^V for the $V+hf$ process modelled using both the SHERPA + PYTHIA8 (blue) and MADGRAPH + PYTHIA8 (red) samples [176].

2425 The impacts of variations in the factorisation scale μ_F and the choice of PDF set on
2426 m_J shape were also found to be negligible in comparison with μ_R and are hence no
2427 additional uncertainty was added to the fit.

2428 7.3.5 Diboson Modelling

2429 The procedure to derive the uncertainties for the diboson background generally
2430 follows that of $V+jets$.

2431 The nominal diboson samples are generated using SHERPA 2.2.1 (except for $gg \rightarrow VV$
2432 which uses SHERPA 2.2.2) with the NNPDF3.0NNLO tune. alternate samples were
2433 generated using POWHEG interfaced with PYTHIA8, using the AZNLO shower tune
2434 with the CTEQ6L1 PDFs [177]. Unlike SHERPA, POWHEG models the off-shell Z
2435 contribution at NLO.

2436 Acceptance and shape uncertainties are derived in an analogous fashion to $V+jets$
2437 as described below.

2438 Diboson Acceptance Uncertainties

2439 Diboson acceptance uncertainties are summarised in Table 7.11. Variations from
2440 μ_R , μ_F , PDF choice and an alternative generator are considered and are combined
2441 via a sum in quadrature as described in Section 7.3.4. The largest modification to
2442 the nominal acceptance is from the POWHEG+PYTHIA8 alternate sample. Since
2443 the diboson contribution to the $t\bar{t}$ control region is negligible, no SR-to-CR relative
2444 acceptance uncertainty is necessary.

2445 For the WZ contribution, uncertainties are derived using the 1-lepton channel
2446 and applied to all three channels. The 1-lepton channel was used as it has the
2447 largest amount of available statistics, with the compatibility checked between the
2448 derived uncertainties and the other channels. An additional 8% channel migration
2449 uncertainty is applied on the WZ 0-lepton channel. For the ZZ contribution, the
2450 normalisation uncertainty is calculated using the 2-lepton channel and applied to all
2451 three channels. The 0- and 1-lepton channels were found to have a similar HP-to-LP
2452 relative acceptance uncertainty of 18%. The 1-lepton medium-to-high p_T^V relative
2453 acceptance is estimated using the 2-lepton channel, since the 1-lepton channel had

2454 an insufficient number of events to estimate the uncertainty directly. 30% and
2455 18% channel migration uncertainties are applied in the 0- and 1-lepton channels
2456 respectively.

2457 Since the contribution from WW is negligible, dedicated studies are not performed,
2458 but a 25% normalisation uncertainty is applied in all the three channels which is
2459 based on the modelling studies performed for the previous analysis [79].

Diboson Acceptance Uncertainties						
Bosons	WZ			ZZ		
Channel	0L	1L	2L	0L	1L	2L
Normalisation	16%			10%		
HP-to-LP SR	18%		18%		-	
Medium-to-high p_T^V	10%		6%		18%	
Channel Relative acceptance	8%	-	30%	18%	-	-

Table 7.11: Diboson acceptance uncertainties [176]. All uncertainties except channel extrapolation uncertainties are fully correlated between the ZZ and WZ processes and channels.

2460 Diboson Shape Uncertainties

2461 Diboson shape uncertainties are derived in a similar fashion to $V+jets$. Only the
2462 uncertainties associated with the systematic variations of μ_R and the alternate event
2463 generator have a non-negligible impact on the m_J shape. Variation of μ_R produces
2464 consistent m_J shape changes across all regions and channels, and hence only a single
2465 associated uncertainty is derived, shown in Fig. 7.4. A hyperbolic tangent is fitted
2466 to the symmetrised ratio.

2467 In the 2-lepton channel, no significant shape differences between the nominal and
2468 alternate was observed. The comparison between the nominal SHERPA and alternate
2469 POWHEG+PYTHIA8 samples is shown in Fig. 7.5 for the 0- and 1-lepton channels
2470 for both the WZ and ZZ processes. For these channels, the shape of m_J varies in
2471 opposite directions in the LP and HP signal regions. Shapes are similar between
2472 p_T^V bins, the 0- and 1-lepton channels and for WZ and ZZ . In order to reduce the
2473 effects of statistical fluctuations on the fitted shape, these regions are merged before

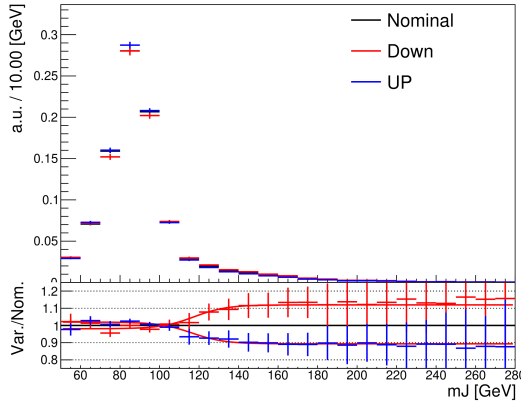


Figure 7.4: Leading large- R jet mass distribution for the combined WZ and ZZ processes, inclusive across all signal regions and lepton channels [176]. The renormalisation scale μ_R has been varied by a factor of 2 (UP) and 0.5 (DOWN). The red and blue curves show the fitted results of the hyperbolic tangent function.

2474 deriving the shape uncertainty. A third order polynomial is fitted to the ratio, and
 2475 this function transitions to a constant piecewise function in the high mass region
 2476 to accurately represent the shape. Dependence on the event generator was found
 2477 to be negligible within statistical uncertainty in the 2-lepton channel, and so no
 2478 uncertainty was applied. All diboson shape uncertainties are fully correlated in the
 2479 fit.

2480 7.3.6 $t\bar{t}$ and single-top Modelling

2481 The main features of the systematic uncertainties on the remaining two modelled
 2482 backgrounds, $t\bar{t}$ and single-top, are described below.

2483 The modelling of the $t\bar{t}$ background uses a POWHEG+PYTHIA8 nominal sample.
 2484 Two alternate samples were considered: POWHEG+HERWIG7 (providing an alternate
 2485 parton shower model) and MADGRAPH5+PYTHIA8.2 (providing an alternate hard
 2486 scatter model). Effects of initial and final state radiation (ISR and FSR, respectively)
 2487 were assessed using internal weight variations in the nominal sample. Acceptance and
 2488 shape uncertainties were derived for each of the variations. The largest contribution
 2489 for the acceptance uncertainties is due to the matrix element calculation, with the
 2490 parton showering model being second. The ISR and FSR acceptance uncertainties

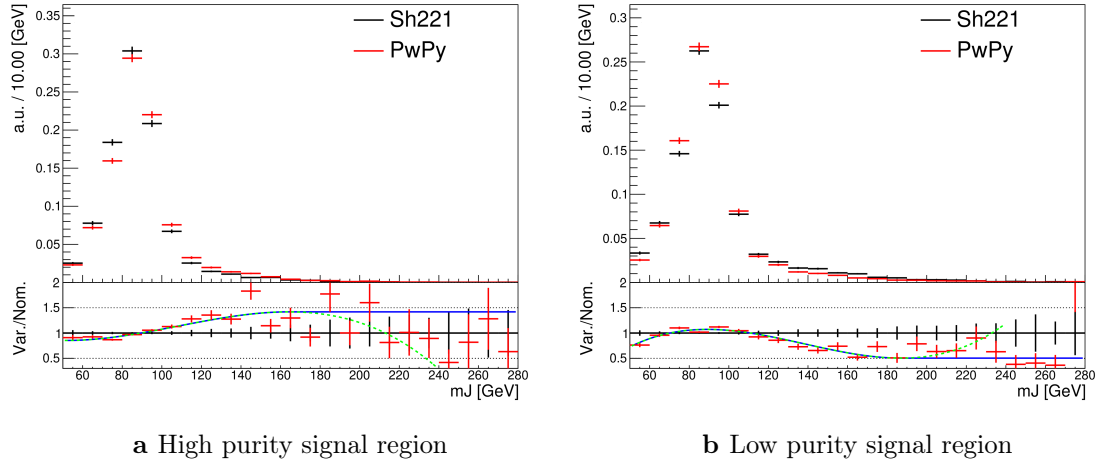


Figure 7.5: Comparison of the shapes of the large- R jet mass m_J between SHERPA (Sh221) (black) and POWHEG+PYTHIA8 (PwPy) (red) samples from the WZ and ZZ processes in high and low purity signal regions, integrated over p_T^V regions and the 0- and 1-lepton channels [176]. The dashed green line shows the fitted third order polynomial function and the blue lines show the function after protection is added in the high mass region.

were found to be subdominant. For the shape uncertainties, only the ISR and parton showering variations have non-negligible impacts on the m_J shape.

The dominant process contributing to the single-top background is Wt production for the 0- and 1-lepton channels. The same nominal and alternate generators are used as for the $t\bar{t}$ background. Again, ISR and FSR variations are obtained from internal weight variations in the nominal sample. At higher orders in QCD, diagrams contributing to the Wt production process can also be found in leading-order $t\bar{t}$ production processes. To account for the arising interference effects, the diagram removal (DR) scheme in Ref. [178] was employed for the nominal sample. The uncertainty on the DR scheme was assessed using an alternate sample using a diagram subtraction (DS) method which removes interference at the generator level. The largest sources of acceptance and shape uncertainties were due to this DS-DR variation.

7.3.7 Signal Modelling

The modelling of the systematic uncertainties affecting the signal processes follows the procedure described in Refs. [26, 179, 180]. The $qq \rightarrow VH$ signal samples are

2507 generated with POWHEG Box v2 +GoSAM at next-to-leading order (NLO) accuracy
2508 in QCD. An additional $gg \rightarrow ZH$ sample is generated using POWHEG BOX v2 at
2509 leading order (LO) in QCD. In both cases, the generated events are interfaced with
2510 PYTHIA 8 for the parton showering modelling. An alternate HERWIG7 sample is used
2511 to assess the uncertainty on the parton showering model. Recommended systematic
2512 uncertainties on the signal production cross-sections and $H \rightarrow b\bar{b}$ branching ratio
2513 from the LHC Higgs Cross Section Working Group are applied [181, 182]. This
2514 includes acceptance and shape uncertainties arising from missing higher-order QCD
2515 and electroweak corrections, PDF uncertainties, renormalisation and factorisation
2516 scales, and alternate parton showering model.

2517 7.4 Statistical Treatment

2518 A binned global maximum-profile-likelihood fit of the m_J distribution is performed
2519 to extract information on the signal, combining all the analysis regions defined
2520 in Table 7.1. The signal strength $\mu = \sigma/\sigma_{\text{SM}}$ is defined as the ratio between the
2521 observed and predicted cross-sections, where $\mu = 0$ corresponds to the background-
2522 only hypothesis and $\mu = 1$ corresponds to the SM prediction. This is a parameter of
2523 interest (POI) which acts to scale the total number of signal events, and is determined
2524 during the fit procedure.

2525 The present analysis makes use of two POIs. The first, μ_{VH}^{bb} , is the signal strength
2526 for the VH , $H \rightarrow b\bar{b}$ process, the primary process under investigation. The diboson
2527 production strength μ_{VZ}^{bb} for the VZ , $Z \rightarrow b\bar{b}$ process is measured simultaneously and
2528 provides a validation of the analysis apparatus used for the primary $H \rightarrow b\bar{b}$ measure-
2529 ment. Alongside the two POIs, the predictive model depends on several parameters
2530 which are not the primary target of measurement, and represent the systematic
2531 uncertainties discussed previously. These parameters are called nuisance parameters
2532 (NPs), collectively referred to as θ . Freely floating background normalisations are
2533 implemented as NPs and are also extracted during the fitting processes.

2534 7.4.1 Likelihood Function

2535 The statistical setup treats each bin as a Poisson counting experiment and is based on
 2536 the ROOSTATS framework [183]. The combined likelihood over N bins is constructed
 2537 as the product of Poisson probabilities in each bin. Considering the simplified case
 2538 of a single signal strength parameter μ , and neglecting sources of systematic or
 2539 statistical uncertainty, this is given by

$$\mathcal{L}(\mu) = \prod_{i=1}^N \frac{(\mu s_i + b_i)^{n_i}}{n_i!} \exp[-(\mu s_i + b_i)], \quad (7.1)$$

2540 where s_i (b_i) is the expected number of signal (background) events in bin i , and n_i is
 2541 the number of observed data events in bin i .

2542 Treatment of Uncertainties

2543 Systematic uncertainties can modify the predicted signal and background yields s_i
 2544 and b_i . Each source of systematic uncertainty is taken into account by adding an
 2545 additional NP θ_j to the likelihood in the form of a Gaussian cost function. The
 2546 combined effect of the NPs is then

$$\mathcal{L}(\theta) = \prod_{j=1}^{N_\theta} \frac{1}{\sqrt{2\pi\sigma_j}} \exp\left[\frac{-(\theta_j - \hat{\theta}_j)^2}{2\sigma_j^2}\right], \quad (7.2)$$

2547 where N_θ is the number of NPs, θ_j is the nominal value of the j th NP, $\hat{\theta}_j$ is the fitted
 2548 value, and σ_j is the corresponding associated prior uncertainty on the NP. As the
 2549 fitted value $\hat{\theta}_j$ deviates from its nominal value, a cost is introduced. The presence of
 2550 NPs modifies the likelihood as

$$\mathcal{L}(\mu) \rightarrow \mathcal{L}(\mu, \theta) = \mathcal{L}(\mu)\mathcal{L}(\theta). \quad (7.3)$$

2551 The predicted signal and background yields are also modified by the presence of the
 2552 NPs with

$$s_i \rightarrow s_i(\theta), \quad b_i \rightarrow b_i(\theta). \quad (7.4)$$

2553 For NPs which are left freely floating in the fit, no corresponding Gaussian constraints
 2554 are added to the likelihood.

2555 The pull of a NP is defined as the difference between the fitted value $\hat{\theta}_j$ and the
 2556 nominal value θ_j , divided by the uncertainty on the NP σ_j . To obtain the uncertainty
 2557 on the pull of a NP, the following procedure is used. The Hessian matrix \mathbf{H} is
 2558 calculated as

$$\mathbf{H} = \begin{bmatrix} \frac{\partial^2 \mathcal{L}}{\partial \theta_1^2} & \frac{\partial^2 \mathcal{L}}{\partial \theta_1 \partial \theta_2} & \dots & \frac{\partial^2 \mathcal{L}}{\partial \theta_1 \partial \theta_n} \\ \frac{\partial^2 \mathcal{L}}{\partial \theta_2 \partial \theta_1} & \frac{\partial^2 \mathcal{L}}{\partial \theta_2^2} & \dots & \frac{\partial^2 \mathcal{L}}{\partial \theta_2 \partial \theta_n} \\ \vdots & \vdots & \ddots & \vdots \\ \frac{\partial^2 \mathcal{L}}{\partial \theta_n \partial \theta_1} & \frac{\partial^2 \mathcal{L}}{\partial \theta_n \partial \theta_2} & \dots & \frac{\partial^2 \mathcal{L}}{\partial \theta_n^2} \end{bmatrix}. \quad (7.5)$$

2559 Taking the inverse of the Hessian matrix \mathbf{H}^{-1} yields the covariance matrix, from
 2560 which the post-fit uncertainties on the different NPs can be extracted. If the post-fit
 2561 uncertainty is smaller than the nominal uncertainty, additional information about
 2562 the NP has been extracted by the fit, and NP is said to be *constrained*.

2563 Following Ref. [184], the statistical uncertainty on the simulated events is implemented
 2564 using a dedicated NP for each bin which can scale the background yield in that bin.
 2565 Statistical NPs are also implemented using a Gaussian constraint.

2566 Smoothing and Pruning

2567 To simplify the fit to reduce and improve its robustness, systematic uncertainties
 2568 are smoothed and pruned. Smoothing accounts for the large statistical uncertainty
 2569 present in some samples that can lead to unphysical fluctuations in the shape
 2570 systematics. The smoothing procedure relies on the assumption that the impact of
 2571 systematics should be approximately monotonic and correlated between neighbouring
 2572 bins.

2573 In addition to smoothing, pruning is the process of removing from the fit those
 2574 systematics which only have a very small effect. This improves the stability of the
 2575 fit by reducing the number of degrees of freedom. Acceptance uncertainties are
 2576 pruned in a given region if they have a variation of less than 0.5%, or if the up and
 2577 down variations have the same sign in that region. Shape uncertainties are pruned
 2578 in a given region if the deviation in each bin is less than 0.5% in that region. In
 2579 addition, acceptance and shape uncertainties are neglected in a given region for any
 2580 background which makes up less than 2% of the total background in that region.

2581 Fit Procedure and Statistical Tests

2582 The best-fit value of μ , denoted $\hat{\mu}$, is obtained via an unconditional maximisation of
 2583 the likelihood. The likelihood is also used to construct a statistical test which can
 2584 confirm or reject the background-only hypothesis. The test statistic q_μ is constructed
 2585 from the profile likelihood ratio,

$$q_\mu = -2 \ln \frac{\mathcal{L}(\mu, \hat{\theta}_\mu)}{\mathcal{L}(\hat{\mu}, \hat{\theta})} \quad (7.6)$$

2586 where $\hat{\mu}$ and $\hat{\theta}$ are chosen to maximise the likelihood \mathcal{L} , and the profile value $\hat{\theta}_\mu$ is
 2587 obtained from a conditional maximisation of the likelihood for a specific choice of
 2588 $\mu = 0$ corresponding to the background-only hypothesis.

2589 The test statistic is used to construct a p -value which is used to probe the background-
 2590 only hypothesis. The p -value is typically reported in terms of the significance Z ,
 2591 defined as the number of standard deviations for a Gaussian Normal distribution
 2592 which will produce a one-sided tail integral equal to the p -value, as in

$$p = \int_Z^\infty \frac{1}{\sqrt{2\pi}} e^{-x^2/2} dx = 1 - \Phi(Z). \quad (7.7)$$

2593 Typically a value of $Z = 3$ constitutes *evidence* of a processes, while $Z = 5$ is
 2594 required for a *discovery*, or *observation*. Alongside the p -value, the best-fit value of
 2595 the signal strength $\hat{\mu}$ and its corresponding uncertainty are quoted, and compared to
 2596 their expected values. More detail on the statistical methodology can be found in
 2597 Ref. [185].

2598 7.4.2 Background Normalisations

2599 The backgrounds which can be constrained by the fit are left freely floating and
 2600 the corresponding normalisation factors are extracted. Normalisation factors (NF),
 2601 represent the value by which the predicted normalisations are scaled, and are im-
 2602 plemented for the dominant backgrounds ($t\bar{t}$, $Z+hf$, $W+hf$). The NFs are also
 2603 subdivided into different regions of phase-space for $t\bar{t}$, given it is possible to obtain
 2604 a strong constraint in the individual channels. This also removes the need for an
 2605 extrapolation uncertainty.

2606 The normalisations and shapes of all other backgrounds, with the exception of the
 2607 multijet background which is estimated using a data driven technique, are initialised
 2608 using the nominal samples and the state-of-the art process normalisations, as outlined
 2609 in Table 7.4.

2610 7.4.3 Asimov Dataset & Expected Results

2611 The Asimov dataset is constructed by replacing the data with the sum of the signal
 2612 and background predictions $n_i = s_i + b_i$. A fit to this dataset using the nominal
 2613 values of the NPs from the simulation will recover the input values and is useful for
 2614 studying the expected result, in addition to constraints on and correlations between
 2615 the NPs.

2616 Alternatively, a conditional fit to the Asimov dataset can be performed using values
 2617 of the background NPs which are determined from an unconditional fit to data. The
 2618 signal NPs and POIs are fixed at their nominal values from the SM simulation. The
 2619 result of this fit can be used to calculate expected (median) significances given a
 2620 more realistic background model, which can be compared to their observed values,
 2621 as is done in Section 7.5.2.

2622 7.5 Results

2623 In the present analysis, the two signal strength parameters μ_{VH}^{bb} and μ_{VZ}^{bb} are extracted
 2624 from a simultaneous maximisation of the likelihood described in Section 7.4. The
 2625 results of the analysis are summarised in this section. Post-fit m_J distributions are

2626 shown in Section 7.5.1. The observed signal strengths are given in Section 7.5.2,
2627 along with observed and expected significances. Finally in Section 7.5.3 the impact
2628 of systematic uncertainties on the results is examined.

2629 7.5.1 Post-fit Results

2630 In addition to the observed significance and signal strength, it is also necessary to
2631 study the post-fit m_J yields and distributions to compare the level of the agreement
2632 between the simulation (using the best-fit values of the signal strength $\hat{\mu}$ and the
2633 NP $\hat{\theta}$) and the data. The best-fit values $\hat{\mu}$ and $\hat{\theta}$ are obtained from an unconditional
2634 fit to data over all analysis regions. The post-fit background normalisation factors
2635 extracted from the unconditional fit to data fit are shown in Table 7.12, and the
2636 post-fit yields are presented in Table 7.13, Table 7.14, and Table 7.15 for the 0-, 1-
2637 and 2-lepton channels, respectively.

Process	Normalisation factor
$t\bar{t}$ 0-lepton	0.88 ± 0.10
$t\bar{t}$ 1-lepton	0.83 ± 0.09
$W+\text{hf}$	1.12 ± 0.14
$Z+\text{hf}$	1.32 ± 0.16

Table 7.12: Factors applied to the nominal normalisations of the $t\bar{t}$, $W+\text{hf}$, and $Z+\text{hf}$ backgrounds, as obtained from the likelihood fit [130]. The errors represent the combined statistical and systematic uncertainties.

2638 Post-fit m_J distributions are given for the signal regions in the 0-, 1- and 2-lepton
2639 channels in Fig. 7.6. The LP and HP regions are merged for the 0- and 1-lepton
2640 channels for the sake of simplicity. In general there is a good level of agreement
2641 between the simulation and data, indicating the fit model is performing as expected.
2642 Fig. 7.7 shows the post-fit plots for the $t\bar{t}$ control regions. Again, a good level of
2643 agreement is observed given the statistical uncertainties on the distributions.

Processes	$250 \text{ GeV} < p_T^V \leq 400 \text{ GeV}$			$p_T^V > 400 \text{ GeV}$		
	HP	LP	CR	HP	LP	CR
Signal	21.93±11.17	18.99±9.76	1.05±0.54	5.69±2.88	5.85±3.01	0.33±0.17
W+t	14.70±5.37	45.55±19.44	17.18±8.09	2.03±0.98	8.93±6.33	3.76±2.49
other t+X	0.79±0.03	3.18±0.66	4.51±1.28	-	0.66±0.03	0.11±0.00
$t\bar{t}$	75.19±13.60	423.85±36.12	539.21±31.39	7.54±1.77	38.20±6.75	44.07±7.43
VZ	77.01±17.09	87.70±19.36	6.16±1.56	17.30±4.10	28.77±6.55	2.79±0.72
WW	-	2.15±0.05	0.24±0.01	0.33±0.02	1.80±0.06	-
Whf	100.78±20.01	331.31±59.54	29.97±21.85	20.19±6.24	59.82±17.91	6.61±5.09
Wcl	5.13±2.31	8.44±3.24	0.46±0.01	0.99±0.69	2.77±1.14	0.19±0.07
Wl	5.61±3.93	4.61±2.45	0.16±0.00	1.41±2.06	2.67±1.67	0.57±0.36
Zhf	318.76±35.27	548.71±61.84	76.97±21.47	86.79±10.63	184.99±21.43	25.76±7.43
Zcl	3.97±1.63	6.74±2.68	0.83±0.02	-	6.36±2.73	0.93±0.41
Zl	1.34±0.67	3.61±2.14	0.42±0.01	1.05±0.63	3.68±2.47	0.29±0.16
Data	623	1493	683	146	330	85
Background	603±25	1466±36	676±25	138±9	339±15	85±7

Table 7.13: Post-fit yields in the 0-lepton channel. Combined statistical and systematic uncertainties are shown [176].

Processes	$250 \text{ GeV} < p_T^V \leq 400 \text{ GeV}$			$p_T^V > 400 \text{ GeV}$		
	HP	LP	CR	HP	LP	CR
Signal	24.23±12.34	18.02±9.29	0.88±0.45	7.84±3.96	7.50±3.87	0.39±0.20
W+t	64.35±21.12	159.95±75.14	73.44±29.96	16.40±7.31	53.28±41.74	21.16±15.36
other t+X	1.92±0.48	16.33±0.31	21.89±6.18	0.13±0.01	1.70±0.06	3.95±1.40
$t\bar{t}$	234.76±30.21	1189.51±75.91	1758.08±57.99	50.87±7.34	226.85±23.98	340.61±25.32
VZ	35.94±8.87	56.30±13.98	4.93±1.38	8.63±2.30	20.02±5.29	2.61±0.84
WW	-	6.48±1.63	-	-	4.35±1.32	0.93±0.03
Whf	265.13±27.68	617.81±63.56	59.91±21.90	91.42±11.51	238.81±29.53	26.55±9.84
Wcl	7.33±2.95	13.81±5.65	2.10±0.04	6.23±2.49	10.17±4.09	0.63±0.02
Wl	2.99±1.47	5.66±3.39	0.65±0.01	2.21±1.35	7.67±4.98	0.31±0.01
Zhf	10.16±1.24	24.61±2.46	3.45±0.41	2.12±0.30	6.56±0.79	0.98±0.12
Zcl	0.02±0.00	0.75±0.02	-	-	0.33±0.01	0.02±0.00
Zl	-	0.49±0.01	0.03±0.00	0.30±0.19	0.23±0.01	0.02±0.00
ggWW	-	0.35±0.01	0.27±0.01	0.15±0.02	0.33±0.01	-
MultiJet	17.04±8.87	44.29±22.82	21.78±11.22	7.81±4.50	21.85±12.73	7.86±4.01
Data	668	2161	1946	185	597	410
Background	640±26	2136±44	1947±43	186±11	592±21	406±18

Table 7.14: Post-fit yields in the 1-lepton channel. Combined statistical and systematic uncertainties are shown [176].

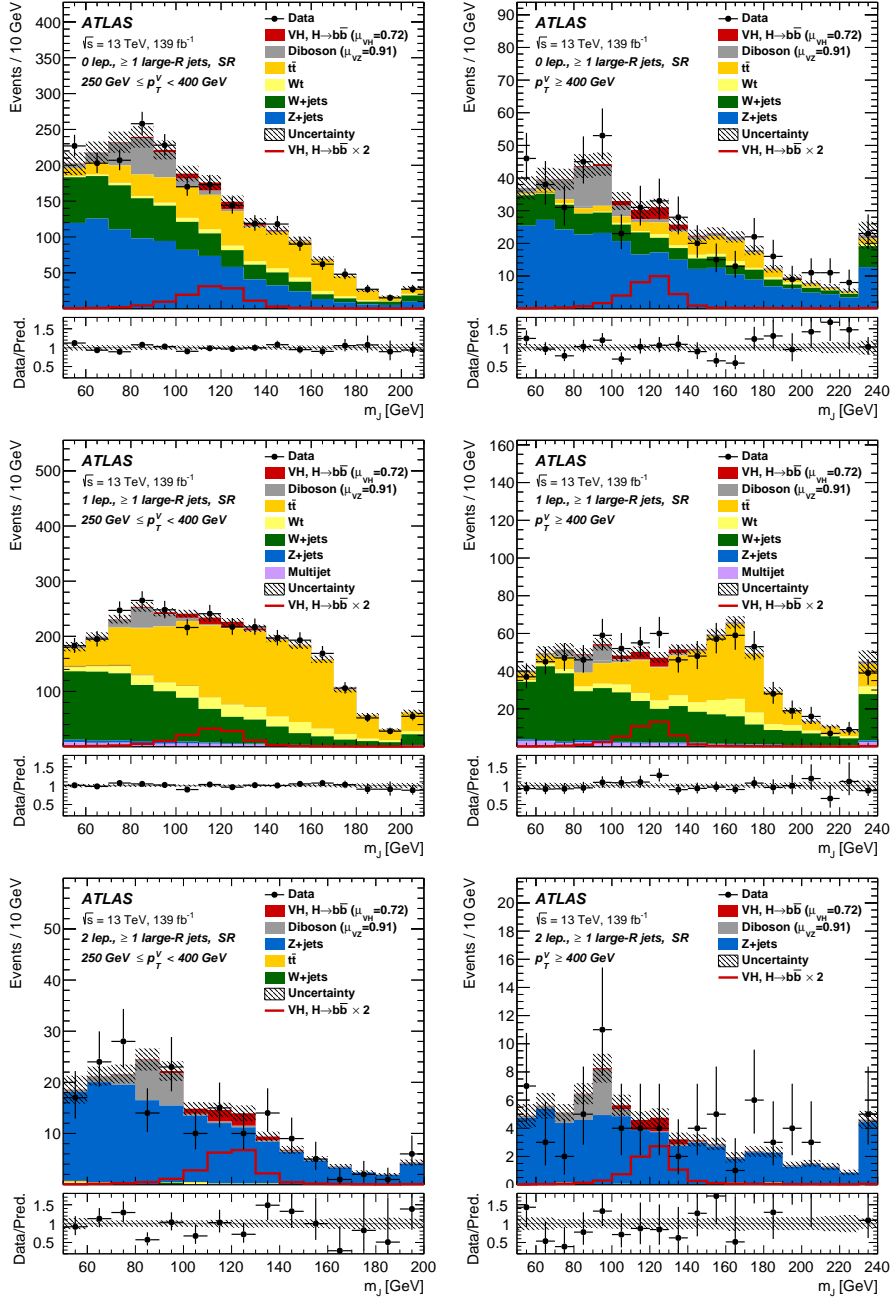


Figure 7.6: The m_J post-fit distributions in (top) the 0-, (middle) 1- and (bottom) 2-lepton SRs for (left) $250 \text{ GeV} < p_T^V < 400 \text{ GeV}$ and (right) $p_T^V \geq 400 \text{ GeV}$. The LP and HP regions are merged for the 0-lepton and 1-lepton channels. The fitted background contributions are shown as filled histograms. The Higgs boson signal ($m_H = 125 \text{ GeV}$) is shown as a filled histogram and is normalised to the signal yield extracted from data ($\mu_{VH}^{bb} = 0.72$), and as an unstacked unfilled histogram, scaled by the SM prediction times a factor of two. The size of the combined on the sum of the fitted signal and background is shown in the hatched band. The highest bin contains the overflow [130].

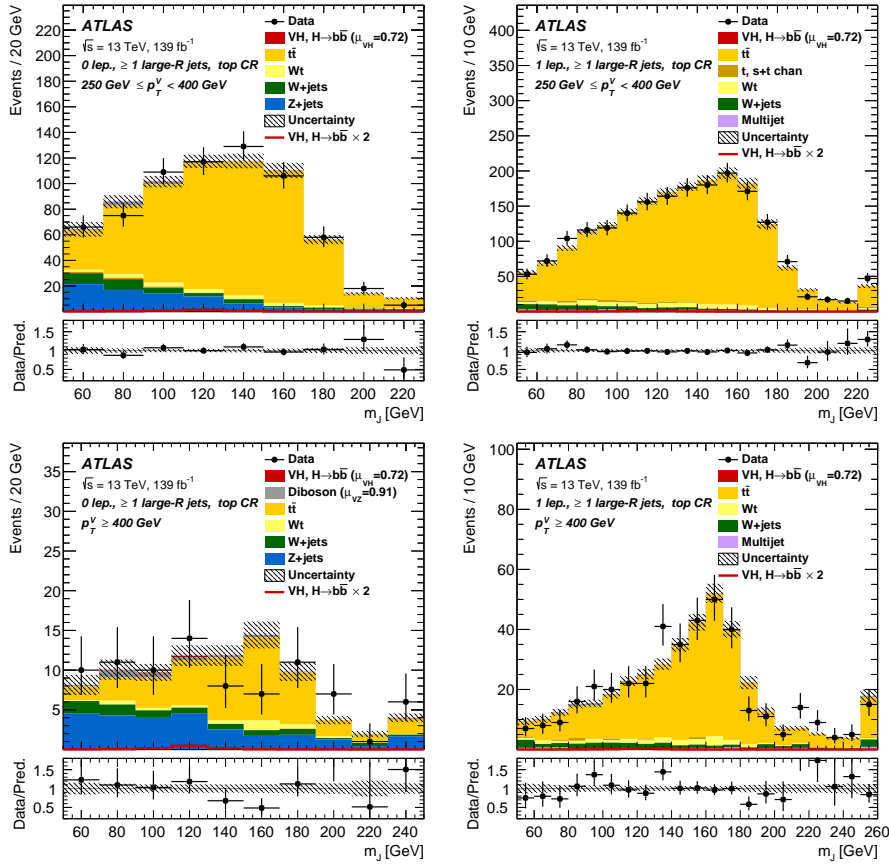


Figure 7.7: The m_J post-fit distributions in the $t\bar{t}$ control region for (top) the 0-lepton channel and the 1-lepton channel for $250 \text{ GeV} < p_T^V < 400 \text{ GeV}$ and (bottom) the 0-lepton channel and the 1-lepton channel for $p_T^V > 400 \text{ GeV}$. The background contributions after the likelihood fit are shown as filled histograms. The Higgs boson signal ($m_h = 125 \text{ GeV}$) is shown as a filled histogram on top of the fitted backgrounds normalised to the signal yield extracted from data ($\mu_{VH}^{bb} = 0.72$), and unstacked as an unfilled histogram, scaled by the SM prediction times a factor of 2. The size of the combined statistical and systematic uncertainty for the sum of the fitted signal and background is indicated by the hatched band. The highest bin in the distributions contains the overflow [130].

Processes	$250 \text{ GeV} < p_T^V \leq 400 \text{ GeV}$	$p_T^V > 400 \text{ GeV}$
	SR	SR
Signal	7.62 ± 3.88	2.79 ± 1.41
W+t	1.28 ± 0.39	-
t̄t	1.64 ± 0.35	0.45 ± 0.10
VZ	19.90 ± 4.86	7.49 ± 2.05
Whf	0.41 ± 0.07	0.07 ± 0.01
Zhf	150.94 ± 12.72	57.15 ± 5.81
Zcl	2.20 ± 0.91	1.80 ± 0.76
Zl	0.94 ± 0.67	1.01 ± 0.67
Data	179	73
Background	177 ± 12	68 ± 6

Table 7.15: Post-fit yields in the 2-lepton channel. Combined statistical and systematic uncertainties are shown [176].

2644 7.5.2 Observed Signal Strength & Significance

2645 The measured signal strength is computed as the ratio between the measured signal
 2646 yield to the prediction from the SM. The combined result for all three lepton channels
 2647 and all analysis regions is given for μ_{VH}^{bb} in Eq. (7.8), and for μ_{VZ}^{bb} in Eq. (7.9). Both
 2648 results include a full breakdown of the systematic and statistical uncertainties.

$$\mu_{VH}^{bb} = 0.72^{+0.39}_{-0.36} = 0.72^{+0.29}_{-0.28}(\text{stat.})^{+0.26}_{-0.22}(\text{syst.}) \quad (7.8)$$

2649

$$\mu_{VZ}^{bb} = 0.91^{+0.29}_{-0.23} = 0.91 \pm 0.15(\text{stat.})^{+0.24}_{-0.17}(\text{syst.}) \quad (7.9)$$

2650 The results for μ_{VH}^{bb} and μ_{VZ}^{bb} are consistent with the expectation from the SM. The
 2651 μ_{VH}^{bb} measurement is dominated by statistical uncertainty, while the μ_{VZ}^{bb} measurement
 2652 is dominated by systematic sources of uncertainty. The measured signal strength
 2653 for μ_{VZ}^{bb} corresponds to an observed significance of 2.1 standard deviations, with an
 2654 expected (median) significance given the SM prediction of 2.7 standard deviations.
 2655 The diboson observed (expected) signal strength significance is 5.4 (5.7). These results
 2656 are summarised in Fig. 7.8, which shows the weighted and background-subtracted m_J
 2657 distribution. A clear signal excess is visible around the Higgs mass of $m_H = 125 \text{ GeV}$.

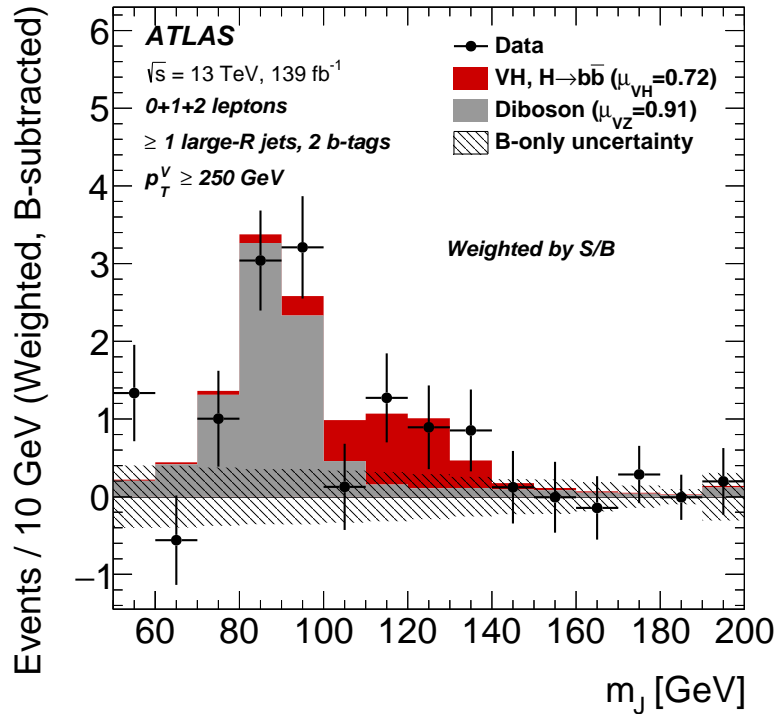


Figure 7.8: m_J distribution in data after subtraction of all backgrounds except for the WZ and ZZ diboson processes. The contributions from all lepton channels and signal regions are summed and weighted by their respective values of the ratio of fitted Higgs boson signal and background yields. The expected contribution of the associated WH and ZH production of a SM Higgs boson with $m_H = 125$ GeV is shown scaled by the measured combined signal strength ($\mu_{VH}^{bb} = 0.72$). The diboson contribution is normalised to its best-fit value of $\mu_{VZ}^{bb} = 0.91$. The size of the combined statistical and systematic uncertainty is indicated by the hatched band. This error band is computed from a full signal-plus-background fit including all the systematic uncertainties defined in Section 7.3, except for the VH/VZ experimental and theory uncertainties [130].

2658 **Compatibility Studies**

2659 Alongside the standard 2-POI fit, a (3+1)-POI fit can be performed by splitting μ_{VH}^{bb}
2660 into three separate POIs, one for each channel. A simultaneous fit to the channel
2661 specific signal strengths can then be performed, which allows a comparison of the
2662 contributions from each channel. Fig. 7.9 compares the best-fit signal strengths.
2663 The 0- and 1-lepton channels show a signal strength which is consistent with the
2664 SM prediction, while the 2-lepton channel shows a small deviation within the 1σ
2665 uncertainty. Overall, good compatibility is observed via a χ^2 test with a corresponding
2666 p -value of 49%.

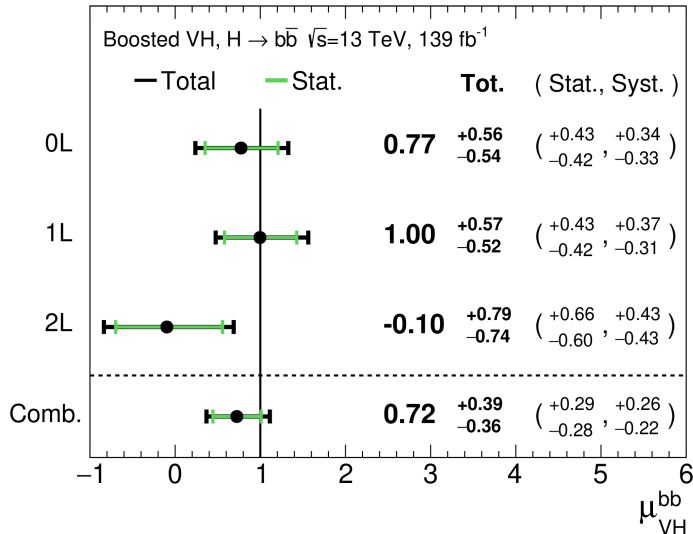


Figure 7.9: Signal strength compatibility test between the (3+1)-POI fit (with the three lepton channels fit separately) and the default (1+1)-POI fit. The compatibility of the three channels is evaluated via a χ^2 difference test and results in a p -value of 49% [130].

2667 **7.5.3 Impact of Systematics**

2668 The impact of systematic uncertainties on the final fitted value $\hat{\mu}^{bb}$ can be studied
2669 using the NP rankings, and the uncertainty breakdown.

2670 Fig. 7.10 shows the NP ranking, which is used to visualise which NPs have the largest
2671 impact on the sensitivity to the fitted POI. To obtain the ranking, a likelihood scan
2672 is performed for each NP θ_j . First, an unconditional fit is used to determine $\hat{\theta}_j$.

2673 The NP is then fixed to its post-fit value varied by $\pm 1\sigma$, the fit is repeated and the
2674 difference between the best-fit value of the POI, $\Delta\hat{\mu}_{VH}^{bb}$, is calculated, and used to
2675 rank the NPs. In addition, the pulls and constraints for the highest ranked NPs are
2676 also shown.

2677 The experimental uncertainty on the signal large- R jet mass resolution (JMR) has
2678 the largest impact. JMR and jet energy scale (JES) uncertainties also have large
2679 impacts for the $V+jets$ and for the diboson backgrounds. The freely-floating $Z+hf$
2680 normalisation is the second highest ranked NP, and is heavily constrained by the
2681 fit. The VZ POI μ_{VZ}^{bb} is also a significant NP when considering the primary μ_{VH}^{bb}
2682 measurement.

2683 The NP ranking highlights individual NPs which have a large impact on the POI
2684 measurement sensitivity. Complementary information is provided at a higher level
2685 by considering the overall impact of different groups of systematics. The groups
2686 are constructed from NPs which have similar physical origins. The impact of each
2687 group is calculated by running a fit with all the NPs in the given group fixed to their
2688 nominal values. The uncertainty on the POI extracted from this fit is subtracted in
2689 quadrature from the uncertainty on the POI from the nominal fit, and the resulting
2690 values are provided as the impact for each group. The total systematic impact
2691 is the difference in quadrature between the nominal uncertainty on μ_{VH}^{bb} and the
2692 estimated impact for the combined statistical uncertainties. The “data stat only”
2693 group fixes all NPs at their nominal value, while the total statistical impact fixes all
2694 NPs except floating normalisations. The floating normalisations group fixes only the
2695 NPs associated with normalisation which are left floating in the fit.

2696 The full breakdown for the observed impact of uncertainties on the μ_{VH}^{bb} signal
2697 strength is provided in Table 7.16. The uncertainty on μ_{VH}^{bb} is dominated by com-
2698 bined statistical effects (0.28), although the combined impact of systematics (0.24) is
2699 of a comparable size. The signal largest group is the data stat uncertainty (0.25),
2700 demonstrating that the analysis would benefit from an increased integrated lumi-
2701 nosity or improved efficiency to select signal events (recall from Section 7.1.2 the
2702 signal efficiency is in the range of 10%). Of the experimental systematic sources of
2703 uncertainty, the dominant impact is from the experimental uncertainties associated
2704 with the simulation of large- R jets (0.13). Other experimental sources of uncertainty
2705 are small in comparison. Modelling uncertainties also have a large contribution to the
2706 overall systematic uncertainty. The biggest contribution to the overall uncertainty

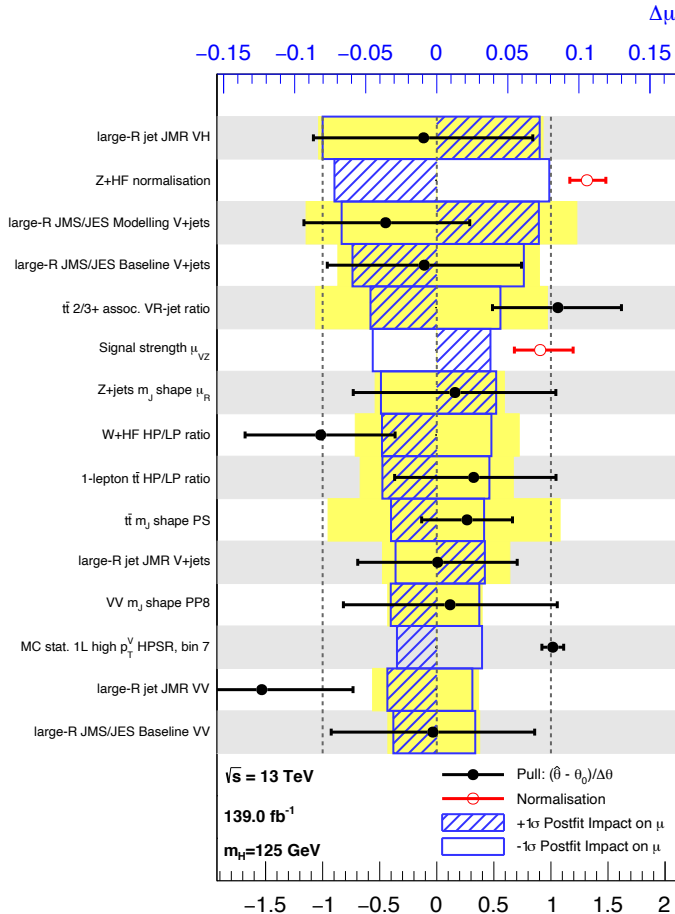


Figure 7.10: Impact of systematic uncertainties on the fitted VH signal-strength parameter $\hat{\mu}_{VH}^{\text{bb}}$ sorted in decreasing order. The boxes show the variations of $\hat{\mu}$, referring to the top x -axis, when fixing the corresponding individual nuisance parameter to its post-fit value modified upwards or downwards by its post-fit uncertainty, i.e. $\hat{\theta} \pm \sigma_{\hat{\theta}}$, and repeating the fit. The impact of up- and down-variations can be distinguished via the dashed and plane box fillings. The yellow boxes show the pre-fit impact (top x -axis) by varying each nuisance parameter by ± 1 . The filled circles show the deviation of the fitted value for each nuisance parameter, $\hat{\theta}$, from their nominal input value θ_0 expressed in standard deviations with respect to their nominal uncertainties $\Delta\theta$ (bottom x -axis). The error bars show the post-fit uncertainties on $\hat{\theta}$ with respect to their nominal uncertainties. The open circles show the fitted values and uncertainties of the normalization parameters that are freely floating in the fit. Pre-fit, these parameters have a value of one [176].

Source of uncertainty	Signed impact	Avg. impact
Total	+0.388 / -0.356	0.372
Statistical	+0.286 / -0.280	0.283
↪ Data stat only	+0.251 / -0.245	0.248
↪ Floating normalisations	+0.096 / -0.092	0.094
Systematic	+0.261 / -0.219	0.240
<hr/>		
Experimental uncertainties		
Small- R jets	+0.041 / -0.034	0.038
Large- R jets	+0.161 / -0.105	0.133
E_T^{miss}	+0.008 / -0.007	0.007
Leptons	+0.013 / -0.007	0.010
b -tagging	b -jets	+0.028 / -0.004
	c -jets	+0.012 / -0.011
	light-flavour jets	+0.009 / -0.007
	extrapolation	+0.004 / -0.005
Pile-up	+0.001 / -0.002	0.001
Luminosity	+0.019 / -0.007	0.013
<hr/>		
Theoretical and modelling uncertainties		
Signal	+0.073 / -0.026	0.050
Backgrounds	+0.106 / -0.095	0.100
↪ $Z + \text{jets}$	+0.049 / -0.047	0.048
↪ $W + \text{jets}$	+0.059 / -0.056	0.058
↪ $t\bar{t}$	+0.037 / -0.032	0.035
↪ Single top quark	+0.031 / -0.023	0.027
↪ Diboson	+0.034 / -0.029	0.032
↪ Multijet	+0.009 / -0.009	0.009
↪ MC statistical	+0.091 / -0.092	0.092

Table 7.16: Breakdown of the absolute contributions to the uncertainty on the signal strength μ_{VH}^{bb} obtained from the (1+1)-POI fit. The average impact represents the average between the positive and negative uncertainties on μ_{VH}^{bb} . The sum in quadrature of the systematic uncertainties attached to the categories differs from the total systematic uncertainty due to correlations [176].

²⁷⁰⁷ is the combined statistical uncertainty on the simulated samples (0.09). Out of the
²⁷⁰⁸ backgrounds, the $W+\text{jets}$ and $Z+\text{jets}$ have the highest (0.06) and second-highest
²⁷⁰⁹ (0.05) impact respectively.

2710 7.5.4 STXS Interpretation

2711 The Simplified Template Cross Sections (STXS) framework provides a common
 2712 categorisation of candidate Higgs boson events according to certain truth-level
 2713 properties of the production mode under study [26, 186]. The STXS framework is
 2714 designed to be independent of the decay mode of the Higgs boson, and is therefore
 2715 well suited to the combination of measurements between different decay channels
 2716 and experiments.

2717 The STXS cross sections are independently measured for the ZH and WH production
 2718 modes following the approach described in [179]. For each production mode, two
 2719 bins in the truth vector boson transverse momentum $p_T^{V,t}$ are considered, $250 \text{ GeV} <$
 2720 $p_T^{V,t} < 400 \text{ GeV}$ and $p_T^{V,t} \geq 400 \text{ GeV}$, leading to four independent analysis regions.
 2721 Events from the simulated signal samples are categorised into the regions and used
 2722 to estimate the expected cross section times branching ratio $\sigma \times B$ in each region,
 2723 where

$$B = B(H \rightarrow b\bar{b}) \times B(V \rightarrow \text{leptons}), \quad (7.10)$$

2724 A simultaneous fit of the four cross section times branching ratios is performed.
 2725 The uncertainties described in Section 7.3 are reused for the STXS fit, with the
 2726 exception of the theoretical uncertainties on the signal cross section and branching
 2727 ratios. The result from the fit is shown in Section 7.5.4 and compared with the
 2728 expected prediction from the SM. The expected and observed results agree within
 2729 the given uncertainties.

2730 7.6 Conclusion

2731 The analysis of the associated production of vector bosons with boosted Higgs bosons
 2732 decaying to a pair of b -quarks using large- R jets is presented. The Higgs candidate is
 2733 reconstructed as a large- R jet in order to improve sensitivity in the boosted regime
 2734 in which the Higgs decay products are significantly collimated. The analysis is
 2735 performed using 139 fb^{-1} of proton–proton collision data at $\sqrt{s} = 13 \text{ TeV}$ collected
 2736 throughout the duration of Run 2 of the LHC.

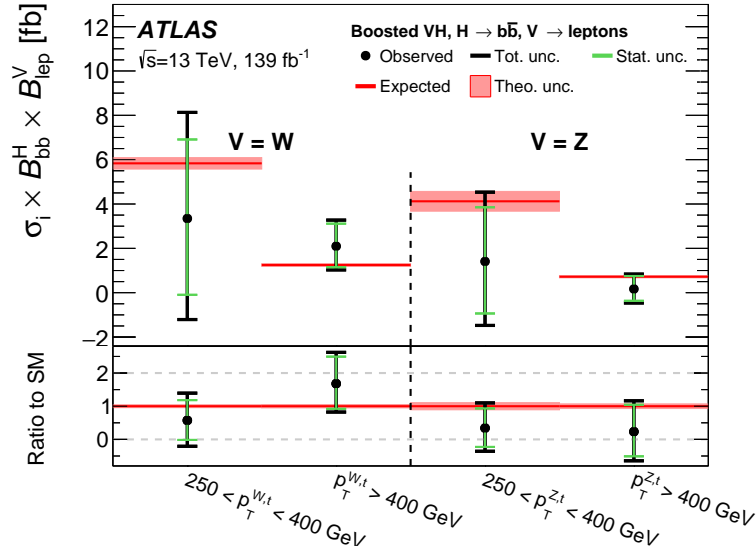


Figure 7.11: Measured VH simplified template cross sections times the $H \rightarrow b\bar{b}$ and $V \rightarrow \text{leptons}$ branching fractions in the medium and high $p_T^{V,t}$ bins [130].

In comparison with the null hypothesis, the Standard Model (SM) VH , $H \rightarrow b\bar{b}$ process is found to have an observed significance of 2.1 standard deviations, whereas the corresponding expected significance is 2.7 standard deviations. The VH , $H \rightarrow b\bar{b}$ process is measured simultaneously with the diboson VZ , $Z \rightarrow b\bar{b}$ process, which provide a cross-check for the main analysis. The observed (expected) significance for the diboson process is 5.4 (5.7).

The results are interpreted in the context of the STXS framework. The cross sections for the WH and ZH processes are measured in two p_T^V bins, and are found to agree with the SM prediction within the given uncertainties. At the time of publication, the results are the most precise measurements of the WH and ZH , $H \rightarrow b\bar{b}$ cross sections in the high p_T^V regime.

The statistical and systematic sources of uncertainty contribute a similar amount to the overall uncertainty on the result. This analysis would therefore likely benefit greatly from the improved b -tagging efficiency at high- p_T enabled by GN1 as discussed in Chapter 6, due to the associated reduction in statistical uncertainty provided by the increased number of events used in the analysis.

The large- R jet mass resolution is found to be the dominant source of systematic uncertainty on the μ_{VH}^{bb} measurement. An improved method of reconstructing the

2755 large- R jet mass, for example by using a machine learning based regression approach,
2756 possibly as an additional auxiliary task to GN1 (see Chapter 6), could reduce the
2757 systematic uncertainty on the μ_{VH}^{bb} measurement. Statistical uncertainty could be
2758 reduced by increasing the integrated luminosity used to perform the analysis by
2759 combining with Run 3 data.

2760 **Chapter 8**

2761 **Conclusion**

2762 **8.1 Summary**

2763 The current understanding of particle physics contains many unanswered questions,
2764 and improving our understanding of the Standard Model is a promising way to
2765 attempt to answer some of them. One of the key particles which may enhance this
2766 understanding is the Higgs boson, which was first observed only a decade ago and
2767 remains under intense scrutiny at the LHC. Given it's propensity to decay to heavy
2768 flavour b -quarks, reconstructing and identifying b -jets is of crucial importance to
2769 improving our understanding in this area. As discussed in Chapter 4, this task
2770 becomes increasingly difficult at high transverse momenta.

2771 One of the effects that hampered tracking and b -tagging performance at high- p_{T} was
2772 identified to be the increased rate of fake tracks. To address this issue, an algorithm
2773 was developed which is able to successfully identify fake tracks within jets 45% of
2774 the time, with a minimal loss of signal tracks of 1.2%. Removal of such tracks was
2775 found to improve the light-jet mistagging rate of the SV1 and JetFitter algorithms
2776 by up to 20% at high transverse momentum.

2777 A novel approach to b -tagging, GN1 was also developed using a Graph Neural Network
2778 (GNN) architecture. The model is encouraged to learn the topology of the jet through
2779 vertexing and track classification auxiliary tasks. As a single end-to-end trained
2780 model, GN1 simplifies the complexity of the flavour tagging pipeline and is able to
2781 achieve superior performance to the current state-of-the-art algorithms, which rely
2782 on a two-tiered approach. Compared with DL1r, GN1 improves the light-jet rejection

2783 by a factor of ~ 1.8 for jets in the $t\bar{t}$ sample with $20 < p_T < 250$ GeV at the 70%
2784 b -jet WP and by a factor of ~ 6 for jets in the Z' sample with $250 < p_T < 5000$ GeV
2785 for a corresponding b -jet efficiency of 30%. GN1 also demonstrates a significant
2786 improvement in the discrimination between b - and c -jets, which also contributes to
2787 improved c -tagging performance. In the high- p_T regime, GN1 improves the b -jet
2788 tagging efficiency by 100% for a fixed light-jet rejection of 100. Initial validation of
2789 the model in data has been performed. The level of agreement between the simulation
2790 and data that is observed is similar to previous flavour tagging algorithms. GN1 has
2791 been successfully deployed in the ATLAS High Level Trigger, and shows promising
2792 performance when trained on high pile-up samples corresponding to the HL-LHC
2793 conditions. Ultimately the improved jet tagging performance enabled by the new
2794 algorithm will have a large impact across a broad spectrum of the ATLAS physics
2795 programme.

2796 This thesis demonstrates that even with suboptimal track reconstruction in this
2797 regime, it is possible to make algorithmic advancements to the flavour tagging pipeline
2798 to improve the identification of b -jets. This work has impacts for any analysis which
2799 relies on the identification of b -jets, including those which are sensitive to the Higgs
2800 boson.

2801 Analysis of VH , $H \rightarrow b\bar{b}$ events was also carried out with 139 fb^{-1} of Run 2
2802 ATLAS at $\sqrt{s} = 13$ TeV. Various background modelling uncertainties were derived
2803 and investigations into the fit model were carried out. The analysis observed a
2804 signal strength of $\mu_{VH}^{bb} = 0.72^{+0.39}_{-0.36} = 0.72^{+0.29}_{-0.28}(\text{stat.})^{+0.26}_{-0.22}(\text{syst.})$ corresponding to an
2805 observed (expected) significance of 2.1σ (2.7σ). The result was validated using a
2806 simultaneous fit to the VZ , $Z \rightarrow b\bar{b}$ process, which acts as a cross check to validate
2807 the primary analysis. The results of the analysis are the most precise measurements
2808 available in the high- p_T for the VH , $H \rightarrow b\bar{b}$ process. The high- p_T region is of
2809 particular interest as it is a region of phase space with good sensitivity to new physics.

2810 8.2 Future Work

2811 Additional algorithmic improvements are likely to yield further improved flavour
2812 tagging performance. Aside from these, large improvements to the flavour tagging
2813 performance at high- p_T will be possible if the b -hadron decay track reconstruction

efficiency and accuracy is improved. Investigations into such improvements, for example loosening the track reconstruction requirements in high- p_T environments, are currently ongoing.

At the moment only the tracks from the Inner Detector and kinematic information about the jet are provided as inputs to the tagging algorithms. In Chapter 6 it was shown that the addition of a simple track-level variable corresponding to the ID of the reconstruction lepton to the model improved tagging performance. However there is still untapped potential in the form of additional information from the full parameters of the reconstructed leptons (making full use of the Calorimeters and Muon Spectrometer), the calorimeter clusters, and even the individual clusters which are used to reconstruct tracks. Providing such additional inputs to the model is likely to complement the information provided by the tracks and further improve performance.

Additional auxiliary training objectives may yield improved performance and also help to add to the explainability of the model. Regression of jet-level quantities such as the transverse momentum and mass, in addition to the truth b -hadron decay length are promising targets.

The GN1 architecture can be easily optimised for new use cases and topologies, as demonstrated by the studies described in Section 6.6. Other opportunities include a model with only cluster-based inputs, which could be used for a fast trigger preselection on jets without the need to run the computationally expensive tracking algorithms, or improved primary vertexing and pile-up jet tagging algorithms.

For an improved analysis of the VH , $H \rightarrow b\bar{b}$ process, the following considerations could be taken into account. Firstly, the addition of Run 3 data will provide a significant increase in statistics and a corresponding reduction in statistical uncertainties. Improved b -tagging, enabled by the GN1 model, will also improve the sensitivity of the analysis through improvements in the signal-to-background ratio. A dedicated $X \rightarrow bb$ version of GN1 which is trained to identify the flavour of large- R jets directly would also be of benefit. Improvements in signal-to-background ratio could also be further improved through the use of a dedicated MVA to select signal events, rather than relying on a series of selection cuts. Finally, the dominant systematic uncertainties relating to the modelling of large- R jets could be reduced via improved reconstruction and calibration techniques.

₂₈₄₇

Bibliography

- ₂₈₄₈ [1] A. Buckley, *A class for typesetting academic theses*, (2010). <http://ctan.tug.org/tex-archive/macros/latex/contrib/heptesis/heptesis.pdf>.
- ₂₈₄₉
- ₂₈₅₀ [2] J. Shlomi, S. Ganguly, E. Gross, K. Cranmer, Y. Lipman, H. Serviansky et al.,
₂₈₅₁ *Secondary vertex finding in jets with neural networks*, *The European Physical Journal C* 81 (2021) .
- ₂₈₅₂
- ₂₈₅₃ [3] ATLAS Collaboration, *Graph Neural Network Jet Flavour Tagging with the ATLAS Detector*, ATL-PHYS-PUB-2022-027 (2022).
- ₂₈₅₄
- ₂₈₅₅ [4] L. Morel, Z. Yao, P. Cladé and S. Guellati-Khélifa, *Determination of the fine-structure constant with an accuracy of 81 parts per trillion*, *Nature* 588 (2020)
₂₈₅₆ pp. 61–65.
- ₂₈₅₇
- ₂₈₅₈ [5] T. Sailer, V. Debierre, Z. Harman, F. Heiße, C. König, J. Morgner et al.,
₂₈₅₉ *Measurement of the bound-electron g-factor difference in coupled ions*, *Nature* 606
₂₈₆₀ (2022) pp. 479–483.
- ₂₈₆₁
- ₂₈₆₂ [6] CDF collaboration, *Observation of top quark production in $\bar{p}p$ collisions*, *Phys. Rev. Lett.* 74 (1995) pp. 2626–2631 [[hep-ex/9503002](#)].
- ₂₈₆₃
- ₂₈₆₄ [7] D0 collaboration, *Observation of the top quark*, *Phys. Rev. Lett.* 74 (1995)
pp. 2632–2637 [[hep-ex/9503003](#)].
- ₂₈₆₅
- ₂₈₆₆ [8] S. W. Herb et al., *Observation of a Dimuon Resonance at 9.5-GeV in 400-GeV Proton-Nucleus Collisions*, *Phys. Rev. Lett.* 39 (1977) pp. 252–255.
- ₂₈₆₇
- ₂₈₆₈ [9] UA1 collaboration, *Experimental Observation of Isolated Large Transverse Energy Electrons with Associated Missing Energy at $\sqrt{s} = 540$ GeV*, *Phys. Lett. B* 122
₂₈₆₉ (1983) pp. 103–116.
- ₂₈₇₀
- ₂₈₇₁ [10] DONUT collaboration, *Observation of tau neutrino interactions*, *Phys. Lett. B* 504 (2001) pp. 218–224 [[hep-ex/0012035](#)].

- 2872 [11] F. Englert and R. Brout, *Broken Symmetry and the Mass of Gauge Vector Mesons*,
2873 *Phys. Rev. Lett.* 13 (1964) pp. 321–323.
- 2874 [12] P. W. Higgs, *Broken Symmetries and the Masses of Gauge Bosons*, *Phys. Rev. Lett.*
2875 13 (1964) pp. 508–509.
- 2876 [13] G. S. Guralnik, C. R. Hagen and T. W. B. Kibble, *Global Conservation Laws and*
2877 *Massless Particles*, *Phys. Rev. Lett.* 13 (1964) pp. 585–587.
- 2878 [14] ATLAS Collaboration, *Observation of a new particle in the search for the Standard*
2879 *Model Higgs boson with the ATLAS detector at the LHC*, *Phys. Lett. B* 716 (2012)
2880 p. 1 [[1207.7214](#)].
- 2881 [15] CMS Collaboration, *Observation of a new boson at a mass of 125 GeV with the CMS*
2882 *experiment at the LHC*, *Phys. Lett. B* 716 (2012) p. 30 [[1207.7235](#)].
- 2883 [16] Particle Data Group collaboration, *Review of Particle Physics*, *PTEP* 2022 (2022)
2884 p. 083C01.
- 2885 [17] C. N. Yang and R. L. Mills, *Conservation of isotopic spin and isotopic gauge*
2886 *invariance*, *Phys. Rev.* 96 (1954) pp. 191–195.
- 2887 [18] S. L. Glashow, *Partial Symmetries of Weak Interactions*, *Nucl. Phys.* 22 (1961)
2888 pp. 579–588.
- 2889 [19] S. Weinberg, *A Model of Leptons*, *Phys. Rev. Lett.* 19 (1967) pp. 1264–1266.
- 2890 [20] A. Salam, *Weak and Electromagnetic Interactions*, *Proceedings of the 8th Nobel*
2891 *symposium*, Ed. N. Svartholm, Almqvist & Wiksell, 1968, Conf. Proc. C680519
2892 (1968) pp. 367–377.
- 2893 [21] T. D. Lee and C. N. Yang, *Question of parity conservation in weak interactions*,
2894 *Phys. Rev.* 104 (1956) pp. 254–258.
- 2895 [22] C. S. Wu, E. Ambler, R. W. Hayward, D. D. Hopper and R. P. Hudson, *Experimental*
2896 *test of parity conservation in beta decay*, *Phys. Rev.* 105 (1957) pp. 1413–1415.
- 2897 [23] R. L. Garwin, L. M. Lederman and M. Weinrich, *Observations of the failure of*
2898 *conservation of parity and charge conjugation in meson decays: the magnetic moment*
2899 *of the free muon*, *Phys. Rev.* 105 (1957) pp. 1415–1417.
- 2900 [24] Y. Nambu, *Quasi-particles and gauge invariance in the theory of superconductivity*,
2901 *Phys. Rev.* 117 (1960) pp. 648–663.

- 2902 [25] J. Goldstone, *Field theories with « superconductor » solutions*, *Il Nuovo Cimento*
2903 (1955-1965) 19 (1961) pp. 154–164.
- 2904 [26] LHC Higgs Cross Section Working Group collaboration, *Handbook of LHC Higgs*
2905 *Cross Sections: 4. Deciphering the Nature of the Higgs Sector*, [[1610.07922](#)].
- 2906 [27] ATLAS Collaboration, *Observation of $H \rightarrow b\bar{b}$ decays and VH production with the*
2907 *ATLAS detector*, [ATLAS-CONF-2018-036](#) (2018).
- 2908 [28] CMS Collaboration, *Observation of Higgs Boson Decay to Bottom Quarks*, *Phys.*
2909 *Rev. Lett.* 121 (2018) p. 121801 [[1808.08242](#)].
- 2910 [29] L. Evans and P. Bryant, *LHC Machine*, *JINST* 3 (2008) p. S08001.
- 2911 [30] The ALICE Collaboration, *The ALICE experiment at the CERN LHC*, *Journal of*
2912 *Instrumentation* 3 (2008) pp. S08002–S08002.
- 2913 [31] CMS Collaboration, *The CMS experiment at the CERN LHC*, *JINST* 3 (2008)
2914 p. S08004.
- 2915 [32] The LHCb Collaboration, *The LHCb detector at the LHC*, *Journal of*
2916 *Instrumentation* 3 (2008) pp. S08005–S08005.
- 2917 [33] ATLAS Collaboration, *The ATLAS Experiment at the CERN Large Hadron Collider*,
2918 *JINST* 3 (2008) p. S08003.
- 2919 [34] ATLAS Collaboration, *Integrated luminosity summary plots for 2011-2012 data*
2920 *taking*, (2022). <https://twiki.cern.ch/twiki/bin/view/AtlasPublic/LuminosityPublicResults>.
- 2922 [35] ATLAS Collaboration, *Public ATLAS Luminosity Results for Run-2 of the LHC*,
2923 (2022). <https://twiki.cern.ch/twiki/bin/view/AtlasPublic/LuminosityPublicResultsRun2>.
- 2925 [36] CERN, *The accelerator complex*, (2012).
2926 <http://public.web.cern.ch/public/en/research/AccelComplex-en.html>.
- 2927 [37] G. C. Strong, *On the impact of selected modern deep-learning techniques to the*
2928 *performance and celerity of classification models in an experimental high-energy*
2929 *physics use case*, [[2002.01427](#)].
- 2930 [38] ATLAS Collaboration, *Atlas track reconstruction – general overview*, (2022).
2931 <https://atlassoftwaredocs.web.cern.ch/trackingTutorial/idoverview/>.

- 2932 [39] ATLAS Collaboration, *Performance of b-jet identification in the ATLAS experiment*,
2933 *JINST* 11 (2016) p. P04008 [[1512.01094](#)].
- 2934 [40] ATLAS Collaboration, *Luminosity determination in pp collisions at $\sqrt{s} = 13 \text{ TeV}$*
2935 *using the ATLAS detector at the LHC*, *ATLAS-CONF-2019-021* (2019).
- 2936 [41] ATLAS Collaboration, *ATLAS Detector and Physics Performance: Technical Design*
2937 *Report, Volume 1*, ATLAS-TDR-14; CERN-LHCC-99-014, Geneva (1999).
2938 <https://cds.cern.ch/record/391176>.
- 2939 [42] ATLAS Collaboration, *Status of the ATLAS Experiment*, Tech. Rep., Geneva (2010).
2940 <https://cds.cern.ch/record/1237407>.
- 2941 [43] ATLAS Collaboration, *ATLAS Inner Tracker Pixel Detector: Technical Design*
2942 *Report*, ATLAS-TDR-030; CERN-LHCC-2017-021 (2017).
2943 <https://cds.cern.ch/record/2285585>.
- 2944 [44] ATLAS Collaboration, *ATLAS Inner Tracker Strip Detector: Technical Design*
2945 *Report*, ATLAS-TDR-025; CERN-LHCC-2017-005 (2017).
2946 <https://cds.cern.ch/record/2257755>.
- 2947 [45] ATLAS Collaboration, *The inner detector*, (2022).
2948 <https://atlas.cern/Discover/Detector/Inner-Detector>.
- 2949 [46] ATLAS Collaboration, *ATLAS Insertable B-Layer: Technical Design Report*,
2950 ATLAS-TDR-19; CERN-LHCC-2010-013 (2010).
2951 <https://cds.cern.ch/record/1291633>.
- 2952 [47] B. Abbott et al., *Production and integration of the ATLAS Insertable B-Layer*,
2953 *JINST* 13 (2018) p. T05008 [[1803.00844](#)].
- 2954 [48] ATLAS Collaboration, *Operation and performance of the ATLAS semiconductor*
2955 *tracker*, *JINST* 9 (2014) p. P08009 [[1404.7473](#)].
- 2956 [49] ATLAS Collaboration, *Calorimeter*, (2022).
2957 <https://atlas.cern/Discover/Detector/Calorimeter>.
- 2958 [50] ATLAS Collaboration, *ATLAS Tile Calorimeter: Technical Design Report*,
2959 ATLAS-TDR-3; CERN-LHCC-96-042, Geneva (1996).
2960 <https://cds.cern.ch/record/331062>.
- 2961 [51] ATLAS Collaboration, *Muon reconstruction performance of the ATLAS detector in*
2962 *proton–proton collision data at $\sqrt{s} = 13 \text{ TeV}$* , *Eur. Phys. J. C* 76 (2016) p. 292

- 2963 [1603.05598].
- 2964 [52] ATLAS Collaboration, *Muon spectrometer*, (2022).
2965 <https://atlas.cern/Discover/Detector/Muon-Spectrometer>.
- 2966 [53] ATLAS Collaboration, *Performance of the ATLAS trigger system in 2015*, *Eur. Phys. J. C* 77 (2017) p. 317 [1611.09661].
- 2968 [54] ATLAS Collaboration, *The ATLAS Collaboration Software and Firmware*,
2969 *ATL-SOFT-PUB-2021-001* (2021).
- 2970 [55] T. Cornelissen, M. Elsing, S. Fleischmann, W. Liebig and E. Moyse, *Concepts, Design and Implementation of the ATLAS New Tracking (NEWT)*, .
- 2972 [56] ATLAS Collaboration, *The Optimization of ATLAS Track Reconstruction in Dense Environments*, *ATL-PHYS-PUB-2015-006* (2015).
- 2974 [57] ATLAS Collaboration, *Performance of the ATLAS track reconstruction algorithms in dense environments in LHC Run 2*, *Eur. Phys. J. C* 77 (2017) p. 673 [1704.07983].
- 2976 [58] ATLAS Collaboration, *A neural network clustering algorithm for the ATLAS silicon pixel detector*, *JINST* 9 (2014) p. P09009 [1406.7690].
- 2978 [59] R. Jansky, *Truth Seeded Reconstruction for Fast Simulation in the ATLAS Experiment*, Ph.D. Thesis, Innsbruck U., 2013.
2979 <https://cds.cern.ch/record/1625231>.
- 2981 [60] ATLAS Collaboration, *Reconstruction of primary vertices at the ATLAS experiment in Run 1 proton–proton collisions at the LHC*, *Eur. Phys. J. C* 77 (2017) p. 332 [1611.10235].
- 2984 [61] ATLAS Collaboration, *ATLAS b-jet identification performance and efficiency measurement with $t\bar{t}$ events in pp collisions at $\sqrt{s} = 13$ TeV*, *Eur. Phys. J. C* 79 (2019) p. 970 [1907.05120].
- 2987 [62] ATLAS Collaboration, *Secondary vertex finding for jet flavour identification with the ATLAS detector*, *ATL-PHYS-PUB-2017-011* (2017).
- 2989 [63] M. Cacciari, G. P. Salam and G. Soyez, *The anti- k_t jet clustering algorithm*, *JHEP* 04 (2008) p. 063 [0802.1189].
- 2991 [64] M. Cacciari, G. P. Salam and G. Soyez, *Fastjet user manual*, *Eur.Phys.J. C*72 (2012) p. 1896 [1111.6097].

- 2993 [65] M. Cacciari, G. P. Salam and G. Soyez, *The Catchment Area of Jets*, *JHEP* **04**
2994 (2008) p. 005 [[0802.1188](#)].
- 2995 [66] ATLAS Collaboration, *Tagging and suppression of pileup jets with the ATLAS*
2996 *detector*, [ATLAS-CONF-2014-018](#) (2014).
- 2997 [67] ATLAS Collaboration, *Topological cell clustering in the ATLAS calorimeters and its*
2998 *performance in LHC Run 1*, *Eur. Phys. J. C* **77** (2017) p. 490 [[1603.02934](#)].
- 2999 [68] ATLAS Collaboration, *Jet reconstruction and performance using particle flow with*
3000 *the ATLAS Detector*, *Eur. Phys. J. C* **77** (2017) p. 466 [[1703.10485](#)].
- 3001 [69] ATLAS Collaboration, *Jet energy scale measurements and their systematic*
3002 *uncertainties in proton–proton collisions at $\sqrt{s} = 13\text{ TeV}$ with the ATLAS detector*,
3003 *Phys. Rev. D* **96** (2017) p. 072002 [[1703.09665](#)].
- 3004 [70] J. M. Butterworth, A. R. Davison, M. Rubin and G. P. Salam, *Jet Substructure as a*
3005 *New Higgs Search Channel at the Large Hadron Collider*, *Phys. Rev. Lett.* **100** (2008)
3006 p. 242001 [[0802.2470](#)].
- 3007 [71] ATLAS collaboration, *Measurement of the associated production of a Higgs boson*
3008 *decaying into b-quarks with a vector boson at high transverse momentum in pp*
3009 *collisions at $\sqrt{s} = 13\text{ TeV}$ with the ATLAS detector*, *Phys. Lett. B* **816** (2021)
3010 p. 136204 [[2008.02508](#)].
- 3011 [72] ATLAS collaboration, *Performance of jet substructure techniques for large- R jets in*
3012 *proton-proton collisions at $\sqrt{s} = 7\text{ TeV}$ using the ATLAS detector*, *JHEP* **09** (2013)
3013 p. 076 [[1306.4945](#)].
- 3014 [73] ATLAS Collaboration, *In situ calibration of large-radius jet energy and mass in*
3015 *13 TeV proton–proton collisions with the ATLAS detector*, *Eur. Phys. J. C* **79** (2019)
3016 p. 135 [[1807.09477](#)].
- 3017 [74] D. Krohn, J. Thaler and L.-T. Wang, *Jets with Variable R* , *JHEP* **06** (2009) p. 059
3018 [[0903.0392](#)].
- 3019 [75] ATLAS Collaboration, *Variable Radius, Exclusive- k_T , and Center-of-Mass Subjet*
3020 *Reconstruction for Higgs($\rightarrow b\bar{b}$) Tagging in ATLAS*, [ATL-PHYS-PUB-2017-010](#)
3021 (2017).
- 3022 [76] ATLAS Collaboration, *Improved electron reconstruction in ATLAS using the*
3023 *Gaussian Sum Filter-based model for bremsstrahlung*, [ATLAS-CONF-2012-047](#) (2012).

- 3024 [77] ATLAS Collaboration, *Electron efficiency measurements with the ATLAS detector*
3025 *using the 2015 LHC proton–proton collision data*, **ATLAS-CONF-2016-024** (2016).
- 3026 [78] ATLAS Collaboration, *Performance of missing transverse momentum reconstruction*
3027 *with the ATLAS detector using proton–proton collisions at $\sqrt{s} = 13 \text{ TeV}$* , **Eur. Phys.**
3028 **J. C** **78** (2018) p. 903 [[1802.08168](#)].
- 3029 [79] ATLAS Collaboration, *Observation of $H \rightarrow b\bar{b}$ decays and VH production with the*
3030 *ATLAS detector*, **Phys. Lett. B** **786** (2018) p. 59 [[1808.08238](#)].
- 3031 [80] ATLAS Collaboration, *Observation of Higgs boson production in association with a*
3032 *top quark pair at the LHC with the ATLAS detector*, **Phys. Lett. B** **784** (2018) p. 173
3033 [[1806.00425](#)].
- 3034 [81] ATLAS Collaboration, *Search for new resonances in mass distributions of jet pairs*
3035 *using 139 fb^{-1} of pp collisions at $\sqrt{s} = 13 \text{ TeV}$ with the ATLAS detector*, **JHEP** **03**
3036 (2020) p. 145 [[1910.08447](#)].
- 3037 [82] ATLAS Collaboration, *Identification of Jets Containing b -Hadrons with Recurrent*
3038 *Neural Networks at the ATLAS Experiment*, **ATL-PHYS-PUB-2017-003** (2017).
- 3039 [83] ATLAS Collaboration, *Deep Sets based Neural Networks for Impact Parameter*
3040 *Flavour Tagging in ATLAS*, **ATL-PHYS-PUB-2020-014** (2020).
- 3041 [84] ATLAS Collaboration, *Expected performance of the ATLAS b -tagging algorithms in*
3042 *Run-2*, **ATL-PHYS-PUB-2015-022** (2015).
- 3043 [85] ATLAS Collaboration, *Optimisation and performance studies of the ATLAS*
3044 *b -tagging algorithms for the 2017-18 LHC run*, **ATL-PHYS-PUB-2017-013** (2017).
- 3045 [86] ATLAS collaboration, *ATLAS flavour-tagging algorithms for the LHC Run 2 pp*
3046 *collision dataset*, [[2211.16345](#)].
- 3047 [87] P. Nason, *A new method for combining nlo qcd with shower monte carlo algorithms*,
3048 *Journal of High Energy Physics* **2004** (2004) p. 040–040.
- 3049 [88] S. Frixione, G. Ridolfi and P. Nason, *A positive-weight next-to-leading-order monte*
3050 *carlo for heavy flavour hadroproduction*, *Journal of High Energy Physics* **2007** (2007)
3051 p. 126–126.
- 3052 [89] S. Frixione, P. Nason and C. Oleari, *Matching nlo qcd computations with parton*
3053 *shower simulations: the powheg method*, *Journal of High Energy Physics* **2007** (2007)
3054 p. 070–070.

- 3055 [90] S. Alioli, P. Nason, C. Oleari and E. Re, *A general framework for implementing nlo*
3056 *calculations in shower monte carlo programs: the powheg box*, *Journal of High Energy*
3057 *Physics* **2010** (2010) .
- 3058 [91] NNPDF collaboration, *Parton distributions for the LHC run II*, *JHEP* **04** (2015)
3059 p. 040 [[1410.8849](#)].
- 3060 [92] ATLAS Collaboration, *Studies on top-quark Monte Carlo modelling for Top2016*,
3061 *ATL-PHYS-PUB-2016-020* (2016).
- 3062 [93] T. Sjöstrand, S. Ask, J. R. Christiansen, R. Corke, N. Desai, P. Ilten et al., *An*
3063 *introduction to PYTHIA 8.2*, *Comput. Phys. Commun.* **191** (2015) p. 159
3064 [[1410.3012](#)].
- 3065 [94] ATLAS Collaboration, *ATLAS Pythia 8 tunes to 7 TeV data*,
3066 *ATL-PHYS-PUB-2014-021* (2014).
- 3067 [95] R. D. Ball et al., *Parton distributions with LHC data*, *Nucl. Phys. B* **867** (2013)
3068 p. 244 [[1207.1303](#)].
- 3069 [96] D. J. Lange, *The EvtGen particle decay simulation package*, *Nucl. Instrum. Meth. A*
3070 **462** (2001) p. 152.
- 3071 [97] ATLAS Collaboration, *The ATLAS Simulation Infrastructure*, *Eur. Phys. J. C* **70**
3072 (2010) p. 823 [[1005.4568](#)].
- 3073 [98] GEANT4 Collaboration, S. Agostinelli et al., *GEANT4 – a simulation toolkit*, *Nucl.*
3074 *Instrum. Meth. A* **506** (2003) p. 250.
- 3075 [99] B. R. Webber, *Fragmentation and hadronization*, *Int. J. Mod. Phys. A* **15S1** (2000)
3076 pp. 577–606 [[hep-ph/9912292](#)].
- 3077 [100] Particle Data Group collaboration, *Review of particle physics*, *Phys. Rev. D* **98**
3078 (2018) p. 030001.
- 3079 [101] ATLAS Collaboration, *Comparison of Monte Carlo generator predictions for bottom*
3080 *and charm hadrons in the decays of top quarks and the fragmentation of high p_T jets*,
3081 *ATL-PHYS-PUB-2014-008* (2014).
- 3082 [102] Nazar Bartosik, *Diagram showing the common principle of identification of jets*
3083 *initiated by b-hadron decays*, (2022).
3084 https://en.m.wikipedia.org/wiki/File:B-tagging_diagram.png.
- 3085 [103] ATLAS Collaboration, *Tracking efficiency studies in dense environments*, (2022).

- 3086 <https://atlas.web.cern.ch/Atlas/GROUPS/PHYSICS/PLOTS/IDTR-2022-03/>.
- 3087 [104] S. Adorni Braccesi Chiassi, *Vector Boson Tagging in the Context of the Search for
3088 New Physics in the Fully Hadronic Final State*, Ph.D. Thesis, Geneva U., 2021.
3089 [10.13097/archive-ouverte/unige:158558](https://archive-ouverte.unige.ch/unige:158558).
- 3090 [105] E. Boos et al., *Generic user process interface for event generators*, [[hep-ph/0109068](https://arxiv.org/abs/hep-ph/0109068)].
- 3091 [106] J. Alwall, A. Ballestrero, P. Bartalini, S. Belov, E. Boos, A. Buckley et al., *A
3092 standard format for Les Houches Event Files*, *Computer Physics Communications*
3093 **176** (2007) pp. 300–304.
- 3094 [107] K. Hornik, M. Stinchcombe and H. White, *Multilayer feedforward networks are
3095 universal approximators*, *Neural Networks* **2** (1989) pp. 359–366.
- 3096 [108] D. E. Rumelhart, G. E. Hinton and R. J. Williams, *Learning representations by
3097 back-propagating errors*, *nature* **323** (1986) pp. 533–536.
- 3098 [109] W. McCulloch and W. Pitts, *A logical calculus of the ideas immanent in nervous
3099 activity*, *The bulletin of mathematical biophysics* **5** (1943) pp. 115–133.
- 3100 [110] J. Hopfield, *Neural networks and physical systems with emergent collective
3101 computational abilities*, in *Spin Glass Theory and Beyond: An Introduction to the
3102 Replica Method and Its Applications*, pp. 411–415, World Scientific, (1987).
- 3103 [111] A. F. Agarap, *Deep Learning using Rectified Linear Units (ReLU)*, *arXiv e-prints*
3104 (2018) p. [arXiv:1803.08375](https://arxiv.org/abs/1803.08375) [[1803.08375](https://arxiv.org/abs/1803.08375)].
- 3105 [112] S. Elfwing, E. Uchibe and K. Doya, *Sigmoid-Weighted Linear Units for Neural
3106 Network Function Approximation in Reinforcement Learning*, *arXiv e-prints* (2017)
3107 p. [arXiv:1702.03118](https://arxiv.org/abs/1702.03118) [[1702.03118](https://arxiv.org/abs/1702.03118)].
- 3108 [113] Y. A. LeCun, L. Bottou, G. B. Orr and K.-R. Müller, *Efficient backprop*, in *Neural
3109 networks: Tricks of the trade*, pp. 9–48, Springer, (2012).
- 3110 [114] D. P. Kingma and J. Ba, *Adam: A Method for Stochastic Optimization*, *arXiv
3111 e-prints* (2014) [[1412.6980](https://arxiv.org/abs/1412.6980)].
- 3112 [115] H. Serviansky, N. Segol, J. Shlomi, K. Cranmer, E. Gross, H. Maron et al.,
3113 *Set2Graph: Learning Graphs From Sets*, *arXiv e-prints* (2020) p. [arXiv:2002.08772](https://arxiv.org/abs/2002.08772)
3114 [[2002.08772](https://arxiv.org/abs/2002.08772)].
- 3115 [116] P. W. Battaglia, J. B. Hamrick, V. Bapst, A. Sanchez-Gonzalez, V. Zambaldi,
3116 M. Malinowski et al., *Relational inductive biases, deep learning, and graph networks*,

- 3117 *arXiv e-prints* (2018) p. arXiv:1806.01261 [[1806.01261](#)].
- 3118 [117] M. Zaheer, S. Kottur, S. Ravanbakhsh, B. Poczos, R. Salakhutdinov and A. Smola,
3119 *Deep Sets*, *arXiv e-prints* (2017) p. arXiv:1703.06114 [[1703.06114](#)].
- 3120 [118] ATLAS Collaboration, *Muon reconstruction performance in early $\sqrt{s} = 13$ TeV data*,
3121 **ATL-PHYS-PUB-2015-037** (2015).
- 3122 [119] ATLAS Collaboration, *Electron reconstruction and identification in the ATLAS*
3123 *experiment using the 2015 and 2016 LHC proton–proton collision data at*
3124 $\sqrt{s} = 13$ TeV, *Eur. Phys. J. C* **79** (2019) p. 639 [[1902.04655](#)].
- 3125 [120] D. Hwang, J. Park, S. Kwon, K.-M. Kim, J.-W. Ha and H. J. Kim, *Self-supervised*
3126 *Auxiliary Learning with Meta-paths for Heterogeneous Graphs*, *arXiv e-prints* (2021)
3127 [[2007.08294](#)].
- 3128 [121] S. Brody, U. Alon and E. Yahav, *How Attentive are Graph Attention Networks?*,
3129 *arXiv e-prints* (2021) [[2105.14491](#)].
- 3130 [122] A. Vaswani, N. Shazeer, N. Parmar, J. Uszkoreit, L. Jones, A. N. Gomez et al.,
3131 *Attention Is All You Need*, *arXiv e-prints* (2017) [[1706.03762](#)].
- 3132 [123] D. P. Kingma and J. Ba, *Adam: A Method for Stochastic Optimization*, *arXiv*
3133 *e-prints* (2014) [[1412.6980](#)].
- 3134 [124] J. Bai, F. Lu, K. Zhang et al., *ONNX: Open neural network exchange*, (2019).
3135 <https://github.com/onnx/onnx>.
- 3136 [125] ATLAS Collaboration, *Performance of Run 3 HLT b-tagging with fast tracking,*
3137 *Public b-Jet Trigger Plots for Collision Data*, (2022).
3138 [https://twiki.cern.ch/twiki/bin/view/AtlasPublic/
3139 BJetTriggerPublicResults#Performance_of_Run_3_HLT_b_taggi](https://twiki.cern.ch/twiki/bin/view/AtlasPublic/BJetTriggerPublicResults#Performance_of_Run_3_HLT_b_taggi).
- 3140 [126] ATLAS Collaboration, *Neural Network Jet Flavour Tagging with the Upgraded*
3141 *ATLAS Inner Tracker Detector at the High-Luminosity LHC*,
3142 **ATL-PHYS-PUB-2022-047** (2022).
- 3143 [127] ATLAS Collaboration, *Jet flavour tagging with GN1 and DL1d. generator*
3144 *dependence, run 2 and run 3 data agreement studies*, (2023).
3145 <https://atlas.web.cern.ch/Atlas/GROUPS/PHYSICS/PLOTS/FTAG-2023-01/>.
- 3146 [128] R. Lafaye, T. Plehn, M. Rauch, D. Zerwas and M. Duhrssen, *Measuring the Higgs*
3147 *Sector*, *JHEP* **08** (2009) p. 009 [[0904.3866](#)].

- 3148 [129] ATLAS Collaboration, *Measurements of WH and ZH production in the $H \rightarrow b\bar{b}$*
3149 *decay channel in pp collisions at 13 TeV with the ATLAS detector*, *Eur. Phys. J. C*
3150 **81** (2021) p. 178 [[2007.02873](#)].
- 3151 [130] ATLAS Collaboration, *Measurement of the associated production of a Higgs boson*
3152 *decaying into b -quarks with a vector boson at high transverse momentum in pp*
3153 *collisions at $\sqrt{s} = 13$ TeV with the ATLAS detector*, *Phys. Lett. B* **816** (2021)
3154 p. 136204 [[2008.02508](#)].
- 3155 [131] K. Mimasu, V. Sanz and C. Williams, *Higher order QCD predictions for associated*
3156 *Higgs production with anomalous couplings to gauge bosons*, *JHEP* **08** (2016) p. 039
3157 [[1512.02572](#)].
- 3158 [132] ATLAS Collaboration, *Performance of jet substructure techniques for large- R jets in*
3159 *proton–proton collisions at $\sqrt{s} = 7$ TeV using the ATLAS detector*, *JHEP* **09** (2013)
3160 p. 076 [[1306.4945](#)].
- 3161 [133] ATLAS Collaboration, *Measurements of b -jet tagging efficiency with the ATLAS*
3162 *detector using $t\bar{t}$ events at $\sqrt{s} = 13$ TeV*, *JHEP* **08** (2018) p. 089 [[1805.01845](#)].
- 3163 [134] ATLAS Collaboration, *Calibration of light-flavour b -jet mistagging rates using*
3164 *ATLAS proton–proton collision data at $\sqrt{s} = 13$ TeV*, *ATLAS-CONF-2018-006*
3165 (2018).
- 3166 [135] ATLAS Collaboration, *Measurement of b -tagging efficiency of c -jets in $t\bar{t}$ events using*
3167 *a likelihood approach with the ATLAS detector*, *ATLAS-CONF-2018-001* (2018).
- 3168 [136] ATLAS Collaboration, *Flavor Tagging with Track-Jets in Boosted Topologies with the*
3169 *ATLAS Detector*, *ATL-PHYS-PUB-2014-013* (2014).
- 3170 [137] ATLAS Collaboration, *Identification of boosted Higgs bosons decaying into b -quark*
3171 *pairs with the ATLAS detector at 13 TeV*, *Eur. Phys. J. C* **79** (2019) p. 836
3172 [[1906.11005](#)].
- 3173 [138] S. Alioli, P. Nason, C. Oleari and E. Re, *A general framework for implementing NLO*
3174 *calculations in shower Monte Carlo programs: the POWHEG BOX*, *JHEP* **06** (2010)
3175 p. 043 [[1002.2581](#)].
- 3176 [139] ATLAS collaboration, *Measurement of the Z/γ^* boson transverse momentum*
3177 *distribution in pp collisions at $\sqrt{s} = 7$ TeV with the ATLAS detector*, *JHEP* **09**
3178 (2014) p. 145 [[1406.3660](#)].
- 3179 [140] G. Cullen, N. Greiner, G. Heinrich, G. Luisoni, P. Mastrolia, G. Ossola et al.,

- 3180 *Automated one-loop calculations with GoSam*, *Eur. Phys. J. C* 72 (2012) p. 1889
3181 [[1111.2034](#)].
- 3182 [141] K. Hamilton, P. Nason and G. Zanderighi, *MINLO: multi-scale improved NLO*,
3183 *JHEP* 10 (2012) p. 155 [[1206.3572](#)].
- 3184 [142] G. Luisoni, P. Nason, C. Oleari and F. Tramontano, *$HW^\pm/HZ + 0$ and 1 jet at*
3185 *NLO with the POWHEG BOX interfaced to GoSam and their merging within*
3186 *MiNLO*, *JHEP* 10 (2013) p. 083 [[1306.2542](#)].
- 3187 [143] M. L. Ciccolini, S. Dittmaier and M. Krämer, *Electroweak radiative corrections to*
3188 *associated WH and ZH production at hadron colliders*, *Phys. Rev. D* 68 (2003)
3189 p. 073003 [[hep-ph/0306234](#)].
- 3190 [144] O. Brein, A. Djouadi and R. Harlander, *NNLO QCD corrections to the*
3191 *Higgs-strahlung processes at hadron colliders*, *Phys. Lett. B* 579 (2004) pp. 149–156
3192 [[hep-ph/0307206](#)].
- 3193 [145] G. Ferrera, M. Grazzini and F. Tramontano, *Associated Higgs-W-Boson Production*
3194 *at Hadron Colliders: a Fully Exclusive QCD Calculation at NNLO*, *Phys. Rev. Lett.*
3195 107 (2011) p. 152003 [[1107.1164](#)].
- 3196 [146] O. Brein, R. V. Harlander, M. Wiesemann and T. Zirke, *Top-quark mediated effects*
3197 *in hadronic Higgs-Strahlung*, *Eur. Phys. J. C* 72 (2012) p. 1868 [[1111.0761](#)].
- 3198 [147] G. Ferrera, M. Grazzini and F. Tramontano, *Higher-order QCD effects for associated*
3199 *WH production and decay at the LHC*, *JHEP* 04 (2014) p. 039 [[1312.1669](#)].
- 3200 [148] G. Ferrera, M. Grazzini and F. Tramontano, *Associated ZH production at hadron*
3201 *colliders: The fully differential NNLO QCD calculation*, *Phys. Lett. B* 740 (2015)
3202 pp. 51–55 [[1407.4747](#)].
- 3203 [149] J. M. Campbell, R. K. Ellis and C. Williams, *Associated production of a Higgs boson*
3204 *at NNLO*, *JHEP* 06 (2016) p. 179 [[1601.00658](#)].
- 3205 [150] L. Altenkamp, S. Dittmaier, R. V. Harlander, H. Rzehak and T. J. E. Zirke,
3206 *Gluon-induced Higgs-strahlung at next-to-leading order QCD*, *JHEP* 02 (2013) p. 078
3207 [[1211.5015](#)].
- 3208 [151] B. Hespel, F. Maltoni and E. Vryonidou, *Higgs and Z boson associated production via*
3209 *gluon fusion in the SM and the 2HDM*, *JHEP* 06 (2015) p. 065 [[1503.01656](#)].
- 3210 [152] R. V. Harlander, A. Kulesza, V. Theeuwes and T. Zirke, *Soft gluon resummation for*

- 3211 *gluon-induced Higgs Strahlung*, *JHEP* 11 (2014) p. 082 [[1410.0217](#)].
- 3212 [153] R. V. Harlander, S. Liebler and T. Zirke, *Higgs Strahlung at the Large Hadron*
3213 *Collider in the 2-Higgs-doublet model*, *JHEP* 02 (2014) p. 023 [[1307.8122](#)].
- 3214 [154] O. Brein, R. V. Harlander and T. J. E. Zirke, *vh@nnlo – Higgs Strahlung at hadron*
3215 *colliders*, *Comput. Phys. Commun.* 184 (2013) pp. 998–1003 [[1210.5347](#)].
- 3216 [155] S. Frixione, G. Ridolfi and P. Nason, *A positive-weight next-to-leading-order Monte*
3217 *Carlo for heavy flavour hadroproduction*, *JHEP* 09 (2007) p. 126 [[0707.3088](#)].
- 3218 [156] M. Czakon and A. Mitov, *Top++: A program for the calculation of the top-pair*
3219 *cross-section at hadron colliders*, *Comput. Phys. Commun.* 185 (2014) p. 2930
3220 [[1112.5675](#)].
- 3221 [157] S. Alioli, P. Nason, C. Oleari and E. Re, *NLO single-top production matched with*
3222 *shower in POWHEG: s- and t-channel contributions*, *JHEP* 09 (2009) p. 111
3223 [[0907.4076](#)].
- 3224 [158] N. Kidonakis, *Next-to-next-to-leading logarithm resummation for s-channel single top*
3225 *quark production*, *Phys. Rev. D* 81 (2010) p. 054028 [[1001.5034](#)].
- 3226 [159] N. Kidonakis, *Next-to-next-to-leading-order collinear and soft gluon corrections for*
3227 *t-channel single top quark production*, *Phys. Rev. D* 83 (2011) p. 091503 [[1103.2792](#)].
- 3228 [160] E. Re, *Single-top Wt-channel production matched with parton showers using the*
3229 *POWHEG method*, *Eur. Phys. J. C* 71 (2011) p. 1547 [[1009.2450](#)].
- 3230 [161] N. Kidonakis, *Two-loop soft anomalous dimensions for single top quark associated*
3231 *production with a W^- or H^-* , *Phys. Rev. D* 82 (2010) p. 054018 [[1005.4451](#)].
- 3232 [162] T. Gleisberg, S. Höche, F. Krauss, M. Schönherr, S. Schumann, F. Siegert et al.,
3233 *Event generation with SHERPA 1.1*, *JHEP* 02 (2009) p. 007 [[0811.4622](#)].
- 3234 [163] E. Bothmann et al., *Event generation with Sherpa 2.2*, *SciPost Phys.* 7 (2019) p. 034
3235 [[1905.09127](#)].
- 3236 [164] F. Cascioli, P. Maierhöfer and S. Pozzorini, *Scattering Amplitudes with Open Loops*,
3237 *Phys. Rev. Lett.* 108 (2012) p. 111601 [[1111.5206](#)].
- 3238 [165] T. Gleisberg and S. Höche, *Comix, a new matrix element generator*, *JHEP* 12 (2008)
3239 p. 039 [[0808.3674](#)].
- 3240 [166] S. Schumann and F. Krauss, *A parton shower algorithm based on Catani–Seymour*

- 3241 *dipole factorisation*, *JHEP* 03 (2008) p. 038 [[0709.1027](#)].
- 3242 [167] S. Höche, F. Krauss, M. Schönher and F. Siegert, *QCD matrix elements + parton*
3243 *showers. The NLO case*, *JHEP* 04 (2013) p. 027 [[1207.5030](#)].
- 3244 [168] S. Catani, L. Cieri, G. Ferrera, D. de Florian and M. Grazzini, *Vector Boson*
3245 *Production at Hadron Colliders: a Fully Exclusive QCD Calculation at NNLO*, *Phys.*
3246 *Rev. Lett.* 103 (2009) p. 082001 [[0903.2120](#)].
- 3247 [169] J. Butterworth et al., *PDF4LHC recommendations for LHC Run II*, *J. Phys. G* 43
3248 (2016) p. 023001 [[1510.03865](#)].
- 3249 [170] A. Denner, S. Dittmaier, S. Kallweit and A. Mück, *Electroweak corrections to*
3250 *Higgs-strahlung off W/Z bosons at the Tevatron and the LHC with Hawk*, *JHEP* 03
3251 (2012) p. 075 [[1112.5142](#)].
- 3252 [171] A. Denner, S. Dittmaier, S. Kallweit and A. Mück, *HAWK 2.0: A Monte Carlo*
3253 *program for Higgs production in vector-boson fusion and Higgs strahlung at hadron*
3254 *colliders*, *Comput. Phys. Commun.* 195 (2015) pp. 161–171 [[1412.5390](#)].
- 3255 [172] ATLAS Collaboration, *Measurement of the Inelastic Proton–Proton Cross Section at*
3256 $\sqrt{s} = 13\text{ TeV}$ *with the ATLAS Detector at the LHC*, *Phys. Rev. Lett.* 117 (2016)
3257 p. 182002 [[1606.02625](#)].
- 3258 [173] L. A. Harland-Lang, A. D. Martin, P. Motylinski and R. S. Thorne, *Parton*
3259 *distributions in the LHC era: MMHT 2014 PDFs*, *Eur. Phys. J. C*75 (2015) p. 204
3260 [[1412.3989](#)].
- 3261 [174] S. Dulat, T.-J. Hou, J. Gao, M. Guzzi, J. Huston, P. Nadolsky et al., *New parton*
3262 *distribution functions from a global analysis of quantum chromodynamics*, *Phys. Rev.*
3263 D93 (2016) p. 033006 [[1506.07443](#)].
- 3264 [175] J. K. Anders and M. D’Onofrio, *V+Jets theoretical uncertainties estimation via a*
3265 *parameterisation method*, Tech. Rep. ATL-COM-PHYS-2016-044, Geneva (2016).
3266 <https://cds.cern.ch/record/2125718>.
- 3267 [176] ATLAS Collaboration, *Search for the Standard Model Higgs boson produced in*
3268 *association with a vector boson and decaying to a pair of b-quarks using large-R jets*,
3269 ATL-COM-PHYS-2019-1125 (2019).
- 3270 [177] J. Pumplin et al., *New generation of parton distributions with uncertainties from*
3271 *global qcd analysis*, *JHEP* 07 (2002) p. 012 [[0201195](#)].

- 3272 [178] S. Frixione, E. Laenen, P. Motylinski, C. White and B. R. Webber, *Single-top*
3273 *hadroproduction in association with a W boson*, *JHEP* 07 (2008) p. 029 [[0805.3067](#)].
- 3274 [179] ATLAS Collaboration, *Measurement of VH, H → bb* production as a function of the
3275 *vector-boson transverse momentum in 13 TeV pp collisions with the ATLAS detector*,
3276 *JHEP* 05 (2019) p. 141 [[1903.04618](#)].
- 3277 [180] ATLAS Collaboration, *Evidence for the H → bb* decay with the ATLAS detector,
3278 *JHEP* 12 (2017) p. 024 [[1708.03299](#)].
- 3279 [181] LHC Higgs Cross Section Working Group, S. Dittmaier, C. Mariotti, G. Passarino
3280 and R. Tanaka (Eds.), *Handbook of LHC Higgs Cross Sections: 2. Differential*
3281 *Distributions*, *CERN-2012-002* (2012) [[1201.3084](#)].
- 3282 [182] LHC Higgs Cross Section Working Group, *Handbook of LHC Higgs Cross Sections: 3.*
3283 *Higgs Properties*, *CERN-2013-004* (2013) [[1307.1347](#)].
- 3284 [183] L. Moneta, K. Belasco, K. Cranmer, S. Kreiss, A. Lazzaro, D. Piparo et al., *The*
3285 *roostats project*, *arXiv preprint arXiv:1009.1003* (2010) .
- 3286 [184] R. Barlow and C. Beeston, *Fitting using finite Monte Carlo samples*, *Comput. Phys.*
3287 *Commun.* 77 (1993) pp. 219–228.
- 3288 [185] G. Cowan, K. Cranmer, E. Gross and O. Vitells, *Asymptotic formulae for*
3289 *likelihood-based tests of new physics*, *Eur. Phys. J. C* 71 (2011) p. 1554 [[1007.1727](#)].
- 3290 [186] J. R. Andersen et al., *Les Houches 2015: Physics at TeV Colliders Standard Model*
3291 *Working Group Report*, [[1605.04692](#)].

3292 List of figures

<small>3293</small>	2.1	The Higgs potential $V(\phi)$ of the complex scalar field singlet $\phi = \phi_1 + i\phi_2$, with a choice of $\mu^2 < 0$ leading to a continuous degeneracy in the true vacuum states. A false vacuum is present at the origin.	<small>3294</small> 21
<small>3295</small>			
<small>3296</small>	2.2	Higgs boson production cross sections as a function of Higgs mass (m_H) at $\sqrt{s} = 13$ TeV [26]. Uncertainties are shown in the shaded bands. At $m_H = 125$ GeV, Higgs boson production is dominated by gluon-gluon fusion, vector boson fusion, associated production with vector bosons, and top quark fusion.	<small>3297</small> 26
<small>3298</small>			
<small>3299</small>			
<small>3300</small>			
<small>3301</small>	2.3	Diagrams for the four main Higgs boson production modes at the LHC for a Higgs mass $m_H = 125$ GeV at a centre of mass energy $\sqrt{s} = 13$ TeV.	<small>3302</small> 26
<small>3303</small>			
<small>3304</small>			
<small>3305</small>			
<small>3306</small>			
<small>3307</small>	2.4	Higgs boson branching ratios as a function of Higgs mass (m_H) at $\sqrt{s} = 13$ TeV [26]. Uncertainties are shown in the shaded bands. At $m_H = 125$ GeV, the Higgs predominantly decays to a pair of b -quarks, around 58% of the time. The leading subdominant decay mode is to a pair of W bosons.	<small>3308</small> 27
<small>3309</small>			
<small>3310</small>			
<small>3311</small>	3.1	An overview of the CERN accelerator complex [36]. The LHC is fed by a series of accelerators starting with Linac2 (or Linac4 from 2020). Next are the Proton Synchrotron Booster, the Proton Synchrotron, and finally the Super Proton Synchrotron which injects protons into the LHC.	<small>3312</small> 30
<small>3313</small>			
<small>3314</small>	3.2	The coordinate system used at the ATLAS detector, showing the locations of the four main experiments located at various points around the LHC. The 3-vector momentum $\mathbf{p} = (p_x, p_y, p_z)$ is shown by the red arrow. Reproduced from Ref. [37].	<small>3315</small> 31

3315	3.3 The track parameterisation used at the ATLAS detector. Five coordinates $(d_0, z_0, \phi, \theta, q/p)$ are specified, defined at the track's point of closest approach to the nominal interaction point at the origin of the coordinate system. The figure shows the three-momentum \mathbf{p} and the transverse momentum p_T (defined in Eq. (3.2)). The basis vectors e_x , e_y and e_z are also shown. Reproduced from Ref. [38].	33
3321	3.4 Delivered, recorded, and usable integrated luminosity as a function of time over the course of Run 2 [35]. A total of 139 fb^{-1} of collision data is labelled as good for physics, meaning all sub-detector systems were operating nominally.	35
3325	3.5 Average pile-up profiles measured by ATLAS during Run 2 [35].	35
3326	3.6 A 3D model of the entire ATLAS detector [42]. Cutouts to the centre of the detector reveal the different sub-detectors which are arranged in concentric layers around the nominal interaction point.	36
3329	3.7 A 3D model of the ATLAS ID showing the pixel, SCT and TRT sub- detectors [45].	37
3331	3.8 A cross-sectional view of the ATLAS ID, with the radii of the different barrel layers shown [38].	38
3333	3.9 A schematic cross-sectional view of the ATLAS IBL [46].	39
3334	3.10 The ATLAS calorimeters [49]. The ECal uses LAr-based detectors, while the HCal uses mainly scintillating tile detectors. In the forward region the HCal also includes the LAr hadronic end-caps.	41
3337	3.11 The ATLAS muon spectrometer [52].	43
3338	3.12 Particles (left) which have enough separation will leave charge depositions which are resolved into separate clusters. Sufficiently close particles (right) can lead to merged clusters. Their combined energy deposits are recon- structed as a single merged cluster [57].	47
3342	3.13 A sketch of electron reconstruction using the ATLAS detector [77]. Electron reconstruction makes use of the entire ID and the calorimeters.	52

3344	3.14 An overview of different high and low level taggers used in ATLAS. The low level taggers are IPxD, SV1 and JetFitter, and RNNIP and DIPS [61, 62, 82, 83]. The outputs of these taggers are fed into the high-level taggers DL1, DL1r and DL1d [85, 86].	55
3348	4.1 The truth b -hadron decay radius L_{xy} as a function of truth transverse momentum p_T for reconstructed b -jets in Z' events. Error bars show the standard deviation. The pixel layers are shown in dashed horizontal lines.	59
3351	4.2 Diagram of a typical b -jet (blue) which has been produced in an event alongside two light jets (grey) [102]. The b -hadron has travelled a significant distance (pink dashed line) from the primary interaction point (pink dot) before its decay. The large transverse impact parameter d_0 is a characteristic property of the trajectories of b -hadron decay products.	59
3356	4.3 At lower p_T (left) the decay length of the b -hadron is on average reduced, and the decay tracks are less collimated. At higher p_T (right) the b -hadron decay length increases and the resulting decay tracks are more collimated and have less distance over which to diverge before reaching detector elements. As a result, the ID may be unable to resolve charged depositions from different particles, resulting merged clusters.	61
3362	4.4 b -hadron decay track reconstruction efficiency as a function of truth b -hadron p_T [103]. Nominal track reconstruction is shown in black, while the track reconstruction efficiency for track candidates (i.e. the pre-ambiguity solver efficiency) is shown in green. For high- p_T b -hadrons, the ambiguity solver is overly aggressive in its removal of b -hadron decay tracks. Suggestions for the improvement of the track reconstruction efficiency in this regime by the loosening of cuts in the ambiguity solver are shown in blue and red.	62
3369	4.5 Hit multiplicities on the IBL (left) and the pixel layers (right) as a function of the p_T of the reconstructed track for tracks in jets in a Z' sample at $\sqrt{s} = 13$ TeV. Tracks from the weak decay of the b -hadron are shown in red, while fragmentation tracks (which are prompt) are in blue. Baseline tracks are those produced in the standard reconstruction described in Section 3.4.1, while pseudotrack represent the ideal performance of the ATLAS detector and are described in Section 3.4.1.	63

3376	4.6	The fraction of IBL (left) and B-layer (right) hits which are shared on 3377 <i>b</i> -hadron decay tracks as a function of the production radius of the <i>b</i> -hadron 3378 decay product for tracks in jets in a Z' sample at $\sqrt{s} = 13$ TeV. Pseudotacks 3379 represent the ideal performance given the ATLAS detector, see Section 3.4.1.	65
3380	4.7	The average number of good (left) and wrong (right) IBL hits as a function 3381 of <i>b</i> -hadron p_T for tracks using baseline tracking (black) and the modified 3382 version of the outlier removal procedure (red).	67
3383	4.8	(left) <i>b</i> -hadron decay track d_0 pulls ($d_0/s(d_0)$) for baseline and modified 3384 GX2F tracks. (right) The absolute value of the d_0 pull as a function of the 3385 truth <i>b</i> -hadron transverse momentum.	68
3386	5.1	A diagram displaying the logical flow of a single neuron with three inputs 3387 x_i^j . Each input is multiplied by a weight θ_j , and the resulting values are 3388 summed. A bias term θ_0 is added, and the result z is passed to an activation 3389 function. Each neuron can be thought of as a logistic regression model. .	71
3390	5.2	The output of several common choices for the activation function $g(z)$ of 3391 an artificial neuron. The input z is the output of the dot product between 3392 the activation and the weights, plus a bias term.	72
3393	5.3	Rate of fake tracks as a function of jet transverse momentum (left) and 3394 $\Delta R(\text{track}, \text{jet})$ (right) for jets in the Z' sample. The rate of fake tracks 3395 increases significantly as a function of p_T , and also increases as the distance 3396 to the jet axis decreases.	75
3397	5.4	The light-jet efficiency of the low level tagger SV1 for jets in the Z' sample 3398 with $250 < p_T < 5000$ GeV, as a function of <i>b</i> -jet efficiency. The nominal 3399 tracking setup (black) is shown alongside the case where fake tracks which 3400 are not from the decay of a <i>b</i> -hadron are removed. The light-jet efficiency 3401 is decreased, demonstrating that the presence of fake tracks is detrimental 3402 to the algorithm performance.	76

3403	5.5 (left) Normalised histograms of the fake track classification model output separated for signal and fake tracks, and further separated by those tracks which are from the decay of a b -hadron. (right) The ROC curve for all tracks (solid line) and tracks from the decay of a b -hadron (dashed line). The plots show tracks in the combined $t\bar{t}$ and Z' testing sample. The model is able to successfully discriminate between signal and fake tracks, and shows a very similar performance when looking specifically at tracks from the decay of a b -hadron.	79
3411	5.6 (left) Normalised histogram of the b -hadron track identification model output separated for tracks from the decay of a b -hadron and tracks from other sources. The two groups are further separated into those tracks which are fake. (right) The ROC curve for all tracks (solid line). The plots show tracks in the combined $t\bar{t}$ and Z' testing sample.	81
3416	5.7 The effect of applying the fake track identification algorithm together with the b -hadron decay track identification on the jet tagging performance of SV1 for jets in the Z' sample with $250 \text{ GeV} < p_T < 400 \text{ GeV}$ (left) and $400 \text{ GeV} < p_T < 1 \text{ TeV}$ (right). The nominal SV1 light-jet rejection (black) is compared to two working points of fake track removal, labelled “A” (red) and “B” (orange), which represent two different 2D working points of the track classification tools. Removal of fake tracks based on truth information is shown by the green curves.	82
3424	6.1 Comparison of the existing flavour tagging scheme (left) and GN1 (right). The existing approach utilises low-level algorithms (shown in blue), the outputs of which are fed into a high-level algorithm (DL1r). Instead of being used to guide the design of the manually optimised algorithms, additional truth information from the simulation is now being used as auxiliary training targets for GN1. The solid lines represent reconstructed information, whereas the dashed lines represent truth information [3]. . .	85
3431	6.2 The flow of information through a graph neural network layer for (left) a full implementation of the layer and (right) a deep sets model [117]. Reproduced from Ref. [116].	88

3434	6.3 The inputs to GN1 are the two jet features ($n_{\text{jf}} = 2$), and an array of 3435 n_{tracks} , where each track is described by 21 track features ($n_{\text{tf}} = 21$). The 3436 jet features are copied for each of the tracks, and the combined jet-track 3437 vectors of length 23 form the inputs of GN1 [3].	93
3438	6.4 The network architecture of GN1. Inputs are fed into a per-track initialisa- 3439 tion network, which outputs an initial latent representation of each track. 3440 These representations are then used to populate the node features of a 3441 fully connected graph network. After the graph network, the resulting node 3442 representations are used to predict the jet flavour, the track origins, and 3443 the track-pair vertex compatibility [3].	93
3444	6.5 Comparison between the DL1r and GN1 b -tagging discriminant D_b for jets 3445 in the $t\bar{t}$ sample. The 85% WP and the 60% WP are marked by the solid 3446 (dashed) lines for GN1 (DL1r), representing respectively the loosest and 3447 tightest WPs typically used by analyses. A value of $f_c = 0.018$ is used in the 3448 calculation of D_b for DL1r and $f_c = 0.05$ is used for GN1. The distributions 3449 of the different jet flavours have been normalised to unity area [3].	98
3450	6.6 The c -jet (left) and light-jet (right) rejections as a function of the b -jet 3451 tagging efficiency for jets in the $t\bar{t}$ sample with $20 < p_{\text{T}} < 250 \text{ GeV}$. The 3452 ratio with respect to the performance of the DL1r algorithm is shown in 3453 the bottom panels. A value of $f_c = 0.018$ is used in the calculation of D_b 3454 for DL1r and $f_c = 0.05$ is used for GN1 and GN1Lep. Binomial error bands 3455 are denoted by the shaded regions. The x -axis range is chosen to display 3456 the b -jet tagging efficiencies usually probed in these regions of phase space [3].	101
3457	6.7 The c -jet (left) and light-jet (right) rejections as a function of the b -jet 3458 tagging efficiency for jets in the Z' sample with $250 < p_{\text{T}} < 5000 \text{ GeV}$. The 3459 ratio with respect to the performance of the DL1r algorithm is shown in 3460 the bottom panels. A value of $f_c = 0.018$ is used in the calculation of D_b 3461 for DL1r and $f_c = 0.05$ is used for GN1 and GN1Lep. Binomial error bands 3462 are denoted by the shaded regions. The x -axis range is chosen to display 3463 the b -jet tagging efficiencies usually probed in these regions of phase space [3].	101

3464	6.8 The b -jet tagging efficiency for jets in the $t\bar{t}$ sample (left) and jets in the Z' sample (right) as a function of jet p_T with a fixed light-jet rejection of 100 in each bin. A value of $f_c = 0.018$ is used in the calculation of D_b for DL1r and $f_c = 0.05$ is used for GN1 and GN1Lep. GN1 demonstrates improved performance with respect to DL1r across the p_T range shown. Binomial error bands are denoted by the shaded regions [3].	102
3465		
3466		
3467		
3468		
3469		
3470	6.9 The b -jet (left) and light-jet (right) rejections as a function of the c -jet tagging efficiency for $t\bar{t}$ jets with $20 < p_T < 250$ GeV. The ratio to the performance of the DL1r algorithm is shown in the bottom panels. Binomial error bands are denoted by the shaded regions. The x -axis range is chosen to display the c -jet tagging efficiencies usually probed in these regions of phase space [3].	104
3471		
3472		
3473		
3474		
3475		
3476	6.10 The b -jet (left) and light-jet (right) rejections as a function of the c -jet tagging efficiency for Z' jets with $250 < p_T < 5000$ GeV. The ratio to the performance of the DL1r algorithm is shown in the bottom panels. Binomial error bands are denoted by the shaded regions. The x -axis range is chosen to display the c -jet tagging efficiencies usually probed in these regions of phase space [3].	104
3477		
3478		
3479		
3480		
3481		
3482	6.11 The c -jet (left) and light-jet (right) rejections as a function of the b -jet tagging efficiency for $t\bar{t}$ jets with $20 < p_T < 250$ GeV, for the nominal GN1, in addition to configurations where no (GN1 No Aux), only the track classification (GN1 TC) or only the vertexing (GN1 Vert) auxiliary objectives are deployed. The ratio to the performance of the DL1r algorithm is shown in the bottom panels. A value of $f_c = 0.018$ is used in the calculation of D_b for DL1r and $f_c = 0.05$ is used for GN1 [3].	106
3483		
3484		
3485		
3486		
3487		
3488		
3489	6.12 The c -jet (left) and light-jet (right) rejections as a function of the b -jet tagging efficiency for Z' jets with $250 < p_T < 5000$ GeV, for the nominal GN1, in addition to configurations where no (GN1 No Aux), only the track classification (GN1 TC) or only the vertexing (GN1 Vert) auxiliary objectives are deployed. The ratio to the performance of the DL1r algorithm is shown in the bottom panels. A value of $f_c = 0.018$ is used in the calculation of D_b for DL1r and $f_c = 0.05$ is used for GN1 [3].	106
3490		
3491		
3492		
3493		
3494		
3495		

3496	6.13 A schematic showing the truth track origin and vertex information (left) compared with the predictions from GN1 (right). The diagrams show the truth (left) and predicted (right) structure of a b -jet. The true and predicted origins of the tracks is shown by the coloured circles along the diagonal. The shaded black boxes show the groupings of tracks into different vertices. Vertices reconstructed by SV1 and JetFitter are also marked. Class probabilities p_b , p_c and p_u are rounded to three significant figures. GN1 improves over SV1 and JetFitter by successfully determining the origins and vertex compatibility of all the tracks in the jet with the exception of the truth OtherSecondary track, which is misidentified as pile-up.	108
3506	6.14 A schematic showing the truth track origin and vertex information (left) compared with the predictions from GN1 (right). The diagrams show the truth (left) and predicted (right) structure of a b -jet. The true and predicted origins of the tracks is shown by the coloured circles along the diagonal. The shaded black boxes show the groupings of tracks into different vertices. Vertices reconstructed by SV1 and JetFitter are also marked. Class probabilities p_b , p_c and p_u are rounded to three significant figures. GN1 improves over SV1 and JetFitter by successfully determining the origins and vertex compatibility of all but one tracks in the jet.	108
3515	6.15 Heavy flavour vertex finding efficiency as a function of jet p_T for b -jets in the $t\bar{t}$ sample using the exclusive (left) and inclusive (right) vertex finding approaches. The exclusive vertexing approach includes single track vertices while the inclusive approach requires vertices to contain at least two tracks. Efficient vertex finding requires the recall of at least 65% of the tracks in the truth vertex, and allows no more than 50% of the tracks to be included incorrectly. Binomial error bands are denoted by the shaded regions. . .	111
3522	6.16 Heavy flavour vertex finding efficiency as a function of jet p_T for b -jets in the Z' sample using the exclusive (left) and inclusive (right) vertex finding approaches. The exclusive vertexing approach includes single track vertices while the inclusive approach requires vertices to contain at least two tracks. Efficient vertex finding requires the recall of at least 65% of the tracks in the truth vertex, and allows no more than 50% of the tracks to be included incorrectly. Binomial error bands are denoted by the shaded regions. . .	111

3529	6.17 Vertex finding efficiency for other secondary decays as a function of jet p_T 3530 for light-jets in the $t\bar{t}$ sample using the exclusive (left) and inclusive (right) 3531 vertex finding approaches. The exclusive vertexing approach includes single 3532 track vertices while the inclusive approach requires vertices to contain at 3533 least two tracks. Efficient vertex finding requires the recall of at least 65% 3534 of the tracks in the truth vertex, and allows no more than 50% of the tracks 3535 to be included incorrectly. Binomial error bands are denoted by the shaded 3536 regions.	112
3537	6.18 Vertex finding efficiency as a function of jet p_T for light-jets in the Z' sample 3538 using the exclusive (left) and inclusive (right) vertex finding approaches. 3539 The exclusive vertexing approach includes single track vertices while the 3540 inclusive approach requires vertices to contain at least two tracks. Efficient 3541 vertex finding requires the recall of at least 65% of the tracks in the truth 3542 vertex, and allows no more than 50% of the tracks to be included incorrectly. 3543 Binomial error bands are denoted by the shaded regions.	112
3544	6.19 ROC curves for the different groups of truth origin labels defined in Table 5.1 3545 for jets in the $t\bar{t}$ sample (left) and jets in the Z' sample (right). The 3546 FromB, FromBC and FromC labels have been combined, weighted by their 3547 relative abundance, into the Heavy Flavour category, and the Primary and 3548 OtherSecondary labels have similarly been combined into a single category. 3549 The mean weighted area under the ROC curves (AUC) is similar for both 3550 samples [3].	115
3551	6.20 The c -jet (left) and light-jet (right) rejections as a function of the b -jet 3552 tagging efficiency for $t\bar{t}$ jets with $20 < p_T < 250$ GeV, for the looser track 3553 selection trainings of GN1. The ratio to the performance of the baseline 3554 GN1 model is shown in the bottom panels. A value of $f_c = 0.05$ is used for 3555 all models. Binomial error bands are denoted by the shaded regions.	117
3556	6.21 The c -jet (left) and light-jet (right) rejections as a function of the b -jet 3557 tagging efficiency for Z' jets with $250 < p_T < 5000$ GeV, for the looser track 3558 selection trainings of GN1. The ratio to the performance of the baseline 3559 GN1 model is shown in the bottom panels. A value of $f_c = 0.05$ is used for 3560 all models. Binomial error bands are denoted by the shaded regions.	117

3561	6.22 The HLT light-jet rejection as a function of the b -jet efficiency jets in the $t\bar{t}$ sample with $20 < p_T < 250$ GeV for events with a centre of mass energy $\sqrt{s} = 13.6$ TeV [125]. The ratio to the performance of the DL1d algorithm [86] is shown in the bottom panels. Binomial error bands are denoted by the shaded regions. The purple vertical dashed lines represent the most common working points used for b-tagging.	118
3562		
3563		
3564		
3565		
3566		
3567	6.23 The c -jet rejection (left) and light-jet rejection (right) for the upgraded HL-LHC ATLAS detector with $\langle \mu \rangle = 200$ as a function of the b -jet efficiency for jets in the $t\bar{t}$ sample with $20 < p_T < 250$ GeV for events with a centre of mass energy $\sqrt{s} = 14$ TeV [126]. The ratio to the performance of the DL1d algorithm is shown in the bottom panels. Binomial error bands are denoted by the shaded regions. The purple vertical dashed lines represent the most common working points used for b-tagging.	120
3568		
3569		
3570		
3571		
3572		
3573		
3574	6.24 The c -jet rejection (left) and light-jet rejection (right) for the upgraded HL-LHC ATLAS detector with $\langle \mu \rangle = 200$ as a function of the b -jet efficiency for jets in the Z' sample with $250 < p_T < 5000$ GeV for events with a centre of mass energy $\sqrt{s} = 14$ TeV [126]. The ratio to the performance of the DL1d algorithm is shown in the bottom panels. Binomial error bands are denoted by the shaded regions.	120
3575		
3576		
3577		
3578		
3579		
3580	7.1 Diagrams of the signal process (top) and $t\bar{t}$ background (bottom). The object to the right of centre are reconstructed within the large- R jet. For the $t\bar{t}$ background, the large- R jet contains a mistagged c -jet or (less often) a mistagged light-jet. The contribution in the 0-lepton channel results from hadronically decaying τ lepton, or a electron or muon which is out of the analysis acceptance. For the $t\bar{t}$ background process to be in the signal region, the b -jet on the left hand side must either be not within acceptance, not reconstructed, or not tagged.	130
3581		
3582		
3583		
3584		
3585		
3586		
3587		
3588	7.2 Leading large- R jet mass for the Z and $W + \text{hf}$ processes in the HP SR of the 0-lepton channel [176]. The renormalisation scale μ_r has been varied by a factor of 0.5 (1DOWN) and 2 (1UP). An exponential function is fitted to the ratio between the nominal and alternate samples.	142
3589		
3590		
3591		
3592	7.3 Leading large- R jet m_J inclusive in p_T^V for the $V + \text{hf}$ process modelled using both the SHERPA +PYTHIA8 (blue) and MADGRAPH +PYTHIA8 (red) samples [176].	143
3593		
3594		

3595	7.4 Leading large- R jet mass distribution for the combined WZ and ZZ processes, inclusive across all signal regions and lepton channels [176]. The renormalisation scale μ_R has been varied by a factor of 2 (UP) and 0.5 (DOWN). The red and blue curves show the fitted results of the hyperbolic tangent function.	146
3600	7.5 Comparison of the shapes of the large- R jet mass m_J between SHERPA (Sh221) (black) and POWHEG+PYTHIA8 (PwPy) (red) samples from the WZ and ZZ processes in high and low purity signal regions, integrated over p_T^V regions and the 0- and 1-lepton channels [176]. The dashed green line shows the fitted third order polynomial function and the blue lines show the function after protection is added in the high mass region.	147
3606	7.6 The m_J post-fit distributions in (top) the 0-, (middle) 1- and (bottom) 2-lepton SRs for (left) $250 \text{ GeV} < p_T^V < 400 \text{ GeV}$ and (right) $p_T^V \geq 400 \text{ GeV}$. The LP and HP regions are merged for the 0-lepton and 1-lepton channels. The fitted background contributions are shown as filled histograms. The Higgs boson signal ($m_H = 125 \text{ GeV}$) is shown as a filled histogram and is normalised to the signal yield extracted from data ($\mu_{VH}^{bb} = 0.72$), and as an unstacked unfilled histogram, scaled by the SM prediction times a factor of two. The size of the combined on the sum of the fitted signal and background is shown in the hatched band. The highest bin contains the overflow [130].	155
3616	7.7 The m_J post-fit distributions in the $t\bar{t}$ control region for (top) the 0-lepton channel and the 1-lepton channel for $250 \text{ GeV} < p_T^V < 400 \text{ GeV}$ and (bottom) the 0-lepton channel and the 1-lepton channel for $p_T^V > 400 \text{ GeV}$. The background contributions after the likelihood fit are shown as filled histograms. The Higgs boson signal ($m_h = 125 \text{ GeV}$) is shown as a filled histogram on top of the fitted backgrounds normalised to the signal yield extracted from data ($\mu_{VH}^{bb} = 0.72$), and unstacked as an unfilled histogram, scaled by the SM prediction times a factor of 2. The size of the combined statistical and systematic uncertainty for the sum of the fitted signal and background is indicated by the hatched band. The highest bin in the distributions contains the overflow [130].	156

3659 List of tables

<small>3660</small>	2.1 The fermions of the SM [16]. Three generations of particles are present. Also present (unlisted) are the antiparticles, which are identical to the particles up to a reversed charge sign.	15
<small>3663</small>	2.2 The bosons of the SM [16]. The photon, weak bosons and gluons are gauge bosons arising from gauge symmetries, and carry the four fundamental forces of the SM. The recently discovered Higgs boson is the only fundamental scalar particle in the SM.	16
<small>3667</small>	3.1 Overview of the different LHC runs [34, 35]. The average number of interac- tions per bunch-crossing is denoted as $\langle \mu \rangle$ (see Section 3.2.3), and is here averaged over the entire run. The luminosity is the peak instantaneous luminosity. Numbers for Run 3 are preliminary and are only provided to give an indication of expected performance.	29
<small>3672</small>	3.2 Quality selections applied to tracks, where d_0 is the transverse IP of the track, z_0 is the longitudinal IP with respect to the PV and θ is the track polar angle (see Section 3.2.2 for the IP definitions). Silicon hits are hits on the pixel and SCT layers. Shared hits are hits used on multiple tracks which have not been classified as split by the cluster-splitting neural networks [57]. A hole is a missing hit, where one is expected, on a layer between two other hits on a track.	46

3679	5.1 Truth origins which are used to categorise the physical process that led to the production of a track. Tracks are matched to charged particles using the truth-matching probability [57]. A truth-matching probability of less than 0.75 indicates that reconstructed track parameters are likely to be mismeasured and may not correspond to the trajectory of a single charged particle. The “OtherSecondary” origin includes tracks from photon conversions, K_S^0 and Λ^0 decays, and hadronic interactions.	75
3686	5.2 Input features to the fake track classification NN. Basic jet kinematics, along with information about the reconstructed track parameters and constituent hits are used. Shared hits, are hits used on multiple tracks which have not been classified as split by the cluster-splitting neural networks [57], while split hits are hits used by multiple tracks which have been identified as merged, and therefore split.	77
3692	5.3 Hyperparameter for the track classification model	78
3693	5.4 Good and fake track selection efficiencies for the combined $t\bar{t}$ and Z' samples. Two working points are defined, cutting on the NN output at 0.06 and 0.12.	80
3695	5.5 Cut values for the fake and b -hadron decay track MVAs for the two defined working points. Working point “B” cuts more aggressively on the MVA outputs than WP “A”, removing more fake tracks but resulting in an increased loss of signal tracks (which here are all b -hadron decay tracks).	81
3699	6.1 Input features to the GN1 model. Basic jet kinematics, along with information about the reconstructed track parameters and constituent hits are used. Shared hits, are hits used on multiple tracks which have not been classified as split by the cluster-splitting neural networks [57], while split hits are hits used on multiple tracks which have been identified as merged. A hole is a missing hit, where one is expected, on a layer between two other hits on a track. The track leptonID is an additional input to the GN1Lep model [3].	90
3706	6.2 A summary of GN1’s different classification networks used for the various training objectives, adapted from Ref. [3]. The hidden layers column contains a list specifying the number of neurons in each layer. ReLU activation is used through the network [111].	95

3710	6.3 The area under the ROC curves (AUC) for the track classification from GN1, compared to a standard multilayer perceptron (MLP) trained on a per-track basis. The unweighted mean AUC over the origin classes and weighted mean AUC (using as a weight the fraction of tracks from the given origin) is provided. GN1, which uses an architecture that allows track origins to be classified in a conditional manner as discussed in Section 6.4.3, outperforms the MLP model for both $t\bar{t}$ and Z' jets.	114
3711		
3712		
3713		
3714		
3715		
3716		
3717	7.1 Summary of the definitions of the different analysis regions . Signal enriched regions are marked with the label SR. There are regions with relatively large signal purity (HP SR) and with low purity (LP SR). Background enriched control regions are marked with the label CR. The shorthand “add” stands for additional small- R jets, i.e. number of small- R jets not matched to the Higgs-jet candidate. The medium and high p_T^V regions are referred to as Mp_T^V and Hp_T^V , respectively [130].	126
3718		
3719		
3720		
3721		
3722		
3723		
3724	7.2 Selections applied to baseline and signal electrons and muons. Signal leptons are additionally required to satisfy a $p_T > 27$ GeV (25 GeV in the 1-lepton channel).	127
3725		
3726		
3727	7.3 Event selection requirements for the boosted VH , $H \rightarrow b\bar{b}$ analysis channels and sub-channels [130]. Various channel dependent selections are used to maximise the signal efficiency and reduce the number of background events in each analysis region. The $\min[\Delta\phi(\mathbf{E}_T^{\text{miss}}, \text{small-}R \text{ jets})]$ selection is used to remove jets when the missing transverse momentum $\mathbf{E}_T^{\text{miss}}$ is pointing in the direction of the Higgs candidate, and the $\Delta\phi(\mathbf{E}_T^{\text{miss}}, \mathbf{E}_{T, \text{trk}})$ is used to reject events where the calorimeter missing transverse momentum $\mathbf{E}_T^{\text{miss}}$ is not pointing in the direction of the track-based missing transverse momentum $\mathbf{E}_{T, \text{trk}}^{\text{miss}}$. The $\Delta y(V, H_{\text{cand}})$ quantifies the rapidity difference between the reconstructed vector boson and Higgs candidate (H_{cand}). $m_{\ell\ell}$ refers to the invariant mass of the two leptons, while $p_T^{\ell_1}$ and $p_T^{\ell_2}$ refer to the p_T of the first and second leptons, respectively.	129
3728		
3729		
3730		
3731		
3732		
3733		
3734		
3735		
3736		
3737		
3738		

3739	7.4 Signal and background processes with the corresponding generators used for the nominal samples [130]. If not specified, the order of the cross-section calculation refers to the expansion in the strong coupling constant (α_s). (★) The events were generated using the first PDF in the NNPDF3.0NLO set and subsequently reweighted to the PDF4LHC15NLO set [169] using the internal algorithm in POWHEG-Box v2. (†) The NNLO(QCD)+NLO(EW) cross-section calculation for the $pp \rightarrow ZH$ process already includes the $gg \rightarrow ZH$ contribution. The $qq \rightarrow ZH$ process is normalised using the cross-section for the $pp \rightarrow ZH$ process, after subtracting the $gg \rightarrow ZH$ contribution. An additional scale factor is applied to the $qq \rightarrow VH$ processes as a function of the transverse momentum of the vector boson, to account for electroweak (EW) corrections at NLO. This makes use of the VH differential cross-section computed with HAWK [170, 171].	132
3751	7.5 Different sources of uncertainty (i.e. variations in the model) considered for the $V+jets$ background, and the corresponding implementation. For each uncertainty, acceptance and shape uncertainties are derived.	137
3754	7.6 0-lepton $W+jets$ nominal sample flavour composition and total event yield [176]. Mp_T^V refers to the medium p_T^V region, and Hp_T^V refers to the high p_T^V region (see Table 7.1).	138
3758	7.7 1-lepton $W+jets$ nominal sample flavour composition and total event yield [176]. Mp_T^V refers to the medium p_T^V region, and Hp_T^V refers to the high p_T^V region (see Table 7.1).	138
3760	7.8 0-lepton $Z+jets$ nominal sample flavour composition and total event yield [176]. Mp_T^V refers to the medium p_T^V region, and Hp_T^V refers to the high p_T^V region (see Table 7.1).	139
3763	7.9 2-lepton $Z+jets$ nominal sample flavour composition and total event yield [176]. Mp_T^V refers to the medium p_T^V region, and Hp_T^V refers to the high p_T^V region (see Table 7.1).	139
3766	7.10 $V+jets$ acceptance uncertainties [176]. $W+jets$ SR and CR uncertainties marked with a superscript † are correlated. The 1L $W+jets$ medium-to-high p_T^V uncertainty marked by * is applied as independent and uncorrelated NPs in both HP and LP signal regions.	141
3770	7.11 Diboson acceptance uncertainties [176]. All uncertainties except channel extrapolation uncertainties are fully correlated between the ZZ and WZ processes and channels.	145

3773	7.12 Factors applied to the nominal normalisations of the $t\bar{t}$, $W+\text{hf}$, and $Z+\text{hf}$ backgrounds, as obtained from the likelihood fit [130]. The errors represent the combined statistical and systematic uncertainties.	153
3776	7.13 Post-fit yields in the 0-lepton channel. Combined statistical and systematic uncertainties are shown [176].	154
3778	7.14 Post-fit yields in the 1-lepton channel. Combined statistical and systematic uncertainties are shown [176].	154
3780	7.15 Post-fit yields in the 2-lepton channel. Combined statistical and systematic uncertainties are shown [176].	157
3782	7.16 Breakdown of the absolute contributions to the uncertainty on the signal strength μ_{VH}^{bb} obtained from the (1+1)-POI fit. The average impact represents the average between the positive and negative uncertainties on μ_{VH}^{bb} . The sum in quadrature of the systematic uncertainties attached to the categories differs from the total systematic uncertainty due to correlations [176].	162